THERMAL PERFORMANCE ANALYSIS OF FLAT-PLATE SOLAR COLLECTOR BY USING CARBON AND METAL BASED NANOFLUIDS

NAVEED AKRAM

FACULTY OF ENGINEERING
UNIVERSITY OF MALAYA
KUALA LUMPUR

2021

THERMAL PERFORMANCE ANALYSIS OF FLAT-PLATE SOLAR COLLECTOR BY USING CARBON AND METAL BASED NANOFLUIDS

NAVEED AKRAM

THESIS SUBMITTED IN FULFILMENT OF THE REQUIREMENT FOR THE DEGREE OF DOCTOR OF PHILOSOPHY

FACULTY OF ENGINEERING
UNIVERSITY OF MALAYA
KUALA LUMPUR

2021

UNIVERSITY OF MALAYA

ORIGINAL LITERARY WORK DECLARATION

Name of Candidate: NAVEED AKRAM

Matric No: KVA170030 /17028677/1

Name of Degree: Doctor of Philosophy

Title of Thesis: Thermal performance analysis of flat-plate solar collector by using carbon and metal based nanofluids

Field of Study: ENERGY

I do solemnly and sincerely declare that:

(1) I am the sole author/writer of this Work.
(2) This Work is original.
(3) Any use of any work in which copyright exists was done by way of fair dealing and for permitted purposes and any excerpt or extract from, or reference to or reproduction of any copyright work has been disclosed expressly and sufficiently and the title of the Work and its authorship have been acknowledged in this Work.
(4) I do not have any actual knowledge, nor do I ought reasonably to know that the making of this work constitutes an infringement of any copyright work.
(5) I hereby assign all and every right in the copyright to this Work to the University of Malaya ("UM"), who henceforth shall be owner of the copyright in this Work and that any reproduction or use in any form or by any means whatsoever is prohibited without the written consent of UM having been first had and obtained.
(6) I am fully aware that if in the course of making this Work, I have infringed any copyright whether intentionally or otherwise, I may be subject to legal action, or any other action as may be determined by UM.

Candidate's Signature Date:01-07-2021

Subscribed and solemnly declared before,

Witness's Signature Date:

Name:

Designation:

ABSTRACT

Thermal performance analysis of flat-plate solar collector by using carbon and metal based nanofluids were carried out in this study. Different nanomaterials such as, graphene nanoplatelets (GNPs) with SSAs of 750 m^2/g, iron nanoparticles (Fe_3O_4) (< 9 nm), zinc oxide (ZnO) (< 50 nm), and silicon dioxide (SiO_2) (10-20 nm) based aqueous nanofluids were synthesized at the weight concentrations range of 0.025% to 0.2%. Thermodynamic properties and colloidal stability of the nanofluids were thoroughly investigated. The overall performance of FPSC was analyzed using commercial ANSYS fluent 16.2 and was validated experimentally. Experiments were performed following ASHRAE indoor standard; where the inlet temperatures range of 30 - 50 °C; flow rates of 0.8, 1.2 and 1.6 kg/min; and heat flux intensities of 597, 775 and 988 W/m^2 were maintained.

In this investigation the nanofluids were synthesized by probe sonication method. The maximum colloidal stability of nanofluid was obtained at 60 min ultrasonication time for the graphene nanoplatelets. Non-covalent functionalization with surfactants enhanced stability but created unnecessary foam. The undesired phenomena were avoided by covalent functionalization of the suspensions such as, clove-treated GNPs (CGNPs) and polyethylene glycol-treated Fe_3O_4. Successful functionalization was later confirmed through different characterization methods. Present investigation results revealed that the success of suspension stability was dependent on nanomaterial and weight concentrations, in the present case it was observed the suspension weight concentration of 0.9543 for PEG- Fe_3O_4, at 0.1wt.% nanofluid concentration. Thermophysical properties of the synthesized nanofluids were enhanced. The temperature was directly proportional to the thermal conductivity and indirectly proportional to the viscosity, density, and specific heat of the nanofluids. The noticeable increase in thermal conductivity was up to 25.68% at 0.1wt.% CGNPs. The measured thermal conductivity

of CGNPs showed good agreement with the model of Lu-Li. The maximum increment in viscosity of nanofluid was 24.05% for SiO_2, followed by 22.4% and 12% for PEG- Fe_3O_4 and CGNPs. The measured viscosity is well-matched with the Batchelor and Einstein model with a maximum deviation of 6.1%. The deviation in measured density is up to 0.08% higher and well-matched with Pak & Cho equation, while the specific heat deviation reduced up to 1.54% and showed good agreement with Xuan & Roetzel equation.

The efficiency of FPSC is directly proportional to the heat flux intensity and flow rate and inversely proportional to the inlet fluid temperature. As the concentration of nanoparticles increased, the experimental values of AP and TW were decreased about 8.07% and 8.23%, respectively, in comparison with the water data, while efficiency was increased up to 18.2% at 0.1 wt.% CGNPs. Experimental results of efficiency, AP, and TW for water were well matched with the ANSYS Fluent results with the highest differences of 3.22%, 2.21%, and 2.48%, respectively. On the other hand, for CGNPs nanofluid, the maximum differences were 8.20%, 2.70%, and 1.88% respectively. The performance index was higher than one for all the nanofluids and increased up to 1.142 for 0.1wt.% CGNPs nanofluid. All the nanofluids have higher positive effectiveness effects than the negative pressure drops effects. Consequently, the investigated nanofluids can be used to enhance the thermal efficiency of FPSCs and at 0.1wt.% the CGNPs nanofluid provided the highest performance which could be considered superior to others.

Keywords: Solar collector, Efficiency, Thermophysical, Heat Transfer, Nanofluids.

ABSTRAK

Analisis prestasi termal pengumpul suria plat rata dengan menggunakan karbon dan nanofluid berasaskan logam telah dilakukan dalam kajian ini. Bahan nano yang berbeza seperti, graphene nanoplatelet (CGNPs) dengan SSA sebanyak 750 m^2/g, nanopartikel besi (Fe_3O_4) (< 9 nm), zink oksida (ZnO) (< 50 nm), dan silikon dioksida (SiO_2) (10-20 nm) berasaskan cecair nano akueus telah dimaksimumkan pada julat kepekatan berat sebanyak 0.025% hingga 0.2%. Sifat termodinamik dan kestabilan larutan nano telah disiasat dengan teliti. Prestasi keseluruhan FPSC dianalisis menggunakan ANSYS fluent 16.2 komersial dan disahkan secara eksperimen. Ujikaji dilakukan mengikut piawaian ASHRAE; di mana Julat suhu masuk 30-50 ºC; kadar aliran 0.8, 1.2 dan 1.6 kg/min; dan fluks haba secara intensif 597, 775 dan 988 W/m^2 dikekalkan.

Dalam kajian ini, cecair nano telah disoriskan oleh kaedah ultrasonik. Koloidal maksimum bagi cecair nano telah diperolehi setelah 60 min diproses dengan ultrasonik untuk graphene nanoplatelet. Fungsian bukan kovalen dengan surfaktan stabil yang dipertingkatkan tetapi mencipta buih yang tidak perlu. Fenomena yang tidak diingini telah dielakkan oleh kovalen fungsian daripada penggantungan seperti, Clove-terawat yang dirawat (CGNPs) dan polietilena glycol-dirawat Fe_3O_4. Fungsian yang berjaya kemudiannya disahkan melalui kaedah Pencirian yang berbeza. Keputusan siasatan menunjukkan bahawa kejayaan kestabilan penggantungan adalah bergantung kepada nanomaterial dan kepekatan, dalam kes sekarang, ia telah diperhati penggantungan berat kepekatan 0.9543 untuk PEG- Fe_3O_4, pada 0.1 wt.% daripada penumpuan nanofluid. Sifat termofisikal daripada cecair nano telah dispertingkatkan. Suhu itu secara langsung berkadar kepada kekonduksian terma dan tidak langsung kepada kelikatan, ketumpatan, dan haba khusus nanofluids. Peningkatan yang ketara dalam kekonduksian terma adalah sehingga 25.68% pada 0.1 wt.% CGNPs. Kekonduksian terma CGNPs yang diukur

menunjukkan persetujuan yang baik dengan model Lu-Li. Peningkatan maksimum dalam kelikatan nanofluid adalah 24.05% untuk SiO2, diikuti 22.4% dan 12% untuk PEG- Fe_3O_4 dan CGNPs. Kelikatan diukur mempunyai padanan yang baik dengan model Batchelor dan Einstein dengan sisihan maksimum sebanyak 6.1%. Peningkatan ketumpatan diukur adalah sehingga 0.08% dan baik dipadankan dengan Pak & Cho persamaan, manakala haba tertentu berkurangan sehingga 1.54% dan menunjukkan perjanjian yang baik dengan Xuan & Roetzel persamaan.

Kecekapan FPSC adalah berkadar secara langsung kepada keamatan fluks haba dan kadar aliran dan berkadar songsang secara terbalik kepada suhu masuk cecair. Sebagai kepekatan nanopartikel meningkat, nilai eksperimen AP dan TW telah menurun kira-kira 8.07% dan 8.23%, masing-masing, berbanding dengan data air, manakala kecekapan meningkat sehingga 18.2% pada 0.1 wt.% CGNPs. Keputusan eksperimen kecekapan, AP, dan TW untuk air dengan baik dipadankan dengan hasil yang fasih ANSYS dengan perbezaan tertinggi sebanyak 3.22%, 2.21%, dan 2.48%, masingmasing. Sebaliknya, untuk CGNPs nanofluid, perbezaan maksimum adalah 8.20%, 2.70%, dan 1.88%. Indeks prestasi adalah lebih tinggi daripada satu untuk semua nanofluid dan meningkat kepada 1.142 untuk 0.1 wt.% CGNPs nanofluid. Semua nanofluid mempunyai kesan keberkesanan positif yang lebih tinggi daripada kesan titisan tekanan negatif. Oleh itu, yang disiasat nanofluid boleh digunakan untuk meningkatkan kecekapan terma FPSCs, dan 0.1 wt.% CGNPs nanofluid boleh dianggap lebih unggul kepada orang lain.

Kata kunci: Pengumpul suria, Kecekapan, Termofizik, Pemindahan Haba, Nanofluid.

ACKNOWLEDGMENTS

First and foremost, I would like to express my heartfelt thanks and gratitude to ALLAH Subhanahu wa ta'ala for his countless blessings throughout my life and for giving this opportunity to complete my Ph.D. degree successfully.

The utmost and heartiest words of thanks should go to my father and mother, who allowed me to study abroad and always pray for my success and best of my health with their every breath. I am highly indebted to my beloved sisters, uncles, and my friends for their moral support and sincere prayers. My sincere thanks go to my wife Hina Naveed and my daughters Anabia Fatima & Abeera Fatima for their endless love, sacrifice, full support, continuous encouragement to achieve the best in my life. Honestly, my efforts would not be meaningful without your existence in my life.

I would extend my deepest gratitude to my supervisors Prof. Dr. Kazi Md Salim Newaz, Dr. Mohd Nashrul, and Dr. Mohd Ridha, for accepting me as a Ph.D. student and their valuable suggestions, constructive discussions, support, and encouragement during my Ph.D. candidature at the University of Malaya. I would also like to express my gratitude and thanks to my uncle Muhammad Shakeel, colleagues, especially Engr. Uqab Munier Butt (late) and dedicate my work to him.

Finally, thanks are also presented to the Higher Education Commission (HEC) Pakistan for funding my Ph.D. study through scholarship and Mirpur University of Science and Technology (MUST) for giving me study leave. I want to pay my thanks to the University of Malaya, Malaysia, for providing the laboratory facilities and financial support for the experimental work to conduct this study.

TABLE OF CONTENTS

LIST OF FIGURES

LIST OF TABLES

LIST OF SYMBOLS AND ABBREVIATIONS

A_c	:	Collector area (m^2)
Al_2O_3	:	Aluminum oxide
AP	:	Absorber plate surface
ASHRAE	:	American Society of Heating, Refrigerating, and Air-Conditioning Engineers
C_p	:	Specific heat of fluid (J/kg K)
C_b	:	The conductance of bond (W/mK)
Cv	:	Coefficient of valve
CuO	:	Cooper oxide
CNT	:	Carbon nanotube
CTAB	:	Cetyl trimethylammonium bromide
DASC	:	Direct absorption solar collector
DPT	:	Differential pressure transmitter
DW	:	Distilled water
EG	:	Ethylene glycol
FPSC	:	Flat-plate solar collector
F_R	:	Heat removal factor
GNP	:	Graphene Nano platelet
G_S	:	Absorbed solar energy per m^2
G_T	:	Incident solar radiation (W/m^2)
HW	:	Hottel Whillier model
$\tilde{I}$	:	Alternating current
k	:	Thermal conductivity (W/m K)
$\dot{m}$	:	Mass flow rate (kg/s)
MWCNT	:	Multi-walled carbon nanotubes

n	:	Number of tubes
PI	:	Performance index
PV	:	Photovoltaic
PEG 400	:	Polyethylene glycol 400
PVD	:	Physical vapor deposition
Q_u	:	Useful heat gain (W)
Q	:	Heat transfer rate (W)
q	:	Heat transfer rate per unit length (W/m)
R	:	Reflectance
RTD	:	Resistance temperature detector
S	:	Absorbed solar radiation per unit area (W/m^2
SDBS	:	Sodium dodecyl benzene sulfonate
SDS	:	Sodium dodecyl sulfate
SSA	:	Specific surface area (m^2/g)
SiO_2	:	Silicon dioxide
SWCNT	:	Single-walled carbon nanotube
T	:	Temperature (°C)
TEM	:	Transmission electron microscope
thk	:	Thickness (m)
TiO_2	:	Titanium dioxide
TW	:	Wall temperature of riser tube (°C)
$(T_i-T_a)/G_T$	:	Reduced temperature parameter (m^2K/W)
U_L	:	Overall heat loss (W/m^2K)
UV-vis	:	Ultraviolet-visible spectrophotometry spectral analysis
V	:	The velocity of working fluid (m/s)
$\tilde{V}$	:	Alternating voltage (V)

x//d	:	Dimensionless axial distance
ZnO	:	Zinc oxide

Special character

α	:	Absorptance of collector
τ	:	The transmittance of solar energy
ε	:	Emittance
ϕ	:	Weight concentration
η	:	Efficiency of collector
φ	:	The tilt angle of the collector
μ	:	Viscosity (Pa. s)
ν	:	Specific volume (m^3/kg)
σ	:	Stefan Boltzmann constant
ρ	:	Density (kg/ m^3)
ω	:	Uncertainty

Subscripts

a	:	Ambient
ap	:	Absorber plate
b	:	bottom
bf	:	Base fluid
e	:	Edge
f	:	Fluid
g	:	glass
i	:	Inlet, inner, inside
ins	:	Insulation
nf	:	nanofluid

np	:	nanoparticles
o	:	Outlet, outer
p	:	particles
rt	:	Riser tube
t	:	top
w	:	wind

CHAPTER 1: INTRODUCTION

1.1 Renewable Energy

The population of the world is increasing day by day, and it is expected to be increased by 25% of the present in the first half of this century due to the modernization of lifestyle and the increment in population. Following this increase, the demand for energy will be doubled in the middle of this century, and it will be tripled at the end of this century (Soteris A Kalogirou, 2013). But fossil fuel resources are not enough to fulfill the expected demands. Climbing of fuel prices, reduction in fossil fuel resources and increase in greenhouse gas emissions are the main reasons for the researcher to go with eco-friendly energy resources, i.e., renewable energy to meet the projected demands (Alper & Oguz, 2016; Ohler & Fetters, 2014; Tugcu, Ozturk, & Aslan, 2012). Renewable energy resources include solar energy(Foster, Ghassemi, & Cota, 2009), Geothermal energy(AlZaharani, Dincer, & Naterer, 2013; Coskun, Oktay, & Dincer, 2012), Bio-energy (Jiaqiang et al., 2016; Soudagar et al., 2018), Marine energy(Zanuttigh, Angelelli, & Kofoed, 2013), etc.

Solar energy is one of the cleanest forms of renewable energy resources. So, considering environmental effects and easy availability at every place, the solar energy is considered one of the best forms of renewable energy resources (Soteris A Kalogirou, 2013; V. Verma & Kundan, 2013; Zanuttigh et al., 2013). In both the direct and indirect forms, solar energy is the best available source of renewable energy. From a 3.8×10^{23} kW of energy emitted by the Sun, nearly 1.08×10^{14} reaches on the surface of the earth. The rest is blocked by the atmosphere or reflected into space. If 0.1% of this available energy is harvested with a conversion efficiency of 10%, it could generate about 3000GW, which is around four times the total generation capacity of the world (Thirugnanasambandam, Iniyan, & Goic, 2010)

1.2 Solar Energy Collection

Methods for collecting solar energy can be categorized as photovoltaic systems (PV) and thermal systems, as shown in Figure 1.1. Thermal systems convert solar energy into thermal energy, while PV systems transform solar energy into electric energy. Whereas thermal systems can absorb over 95% of the incoming solar radiation, PV systems are restricted by their limited wavelengths range. Figure 1.2 presents the effective working wavelengths range for both types of solar systems at the air mass coefficient (AM) of 1.5. From which it can be concluded that the solar thermal system can utilize a higher percentage of incoming solar radiation than the photovoltaic system (Taylor, Phelan, Otanicar, Adrian, & Prasher, 2011). Therefore, the focus of this research is limited to the thermal type of solar collectors for the effective capture of solar radiation.

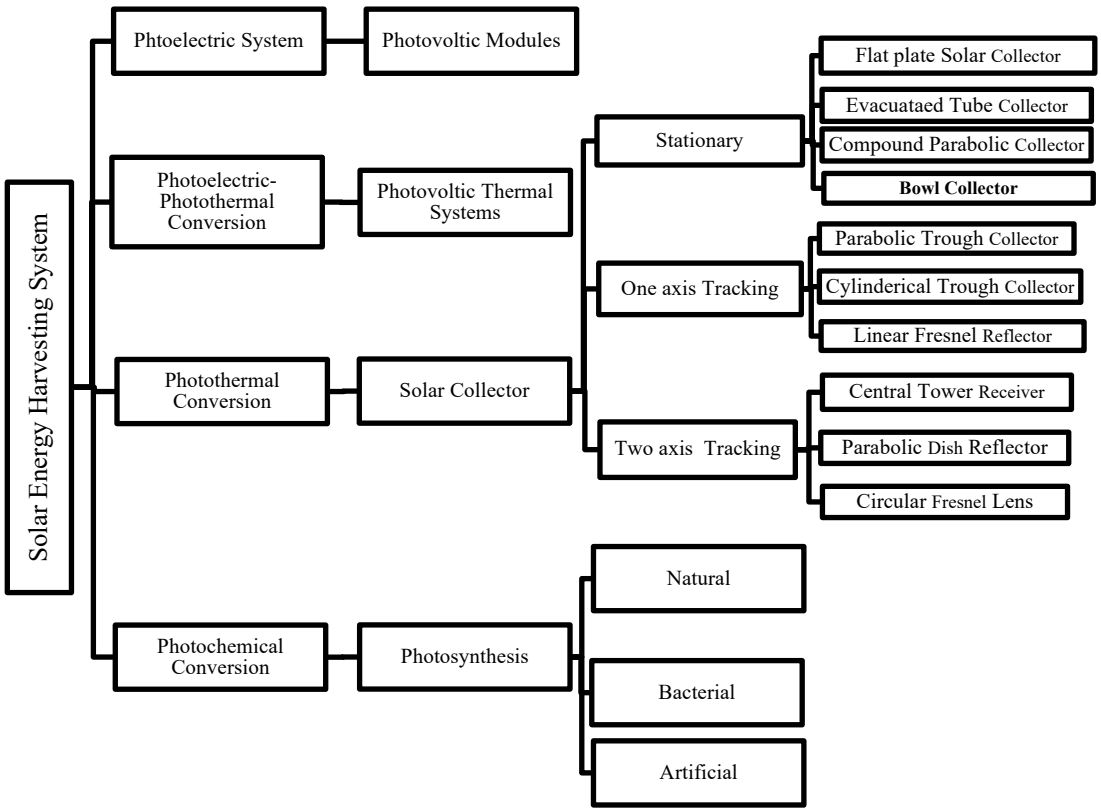

Figure 1.1 Type of Solar energy harvesting system

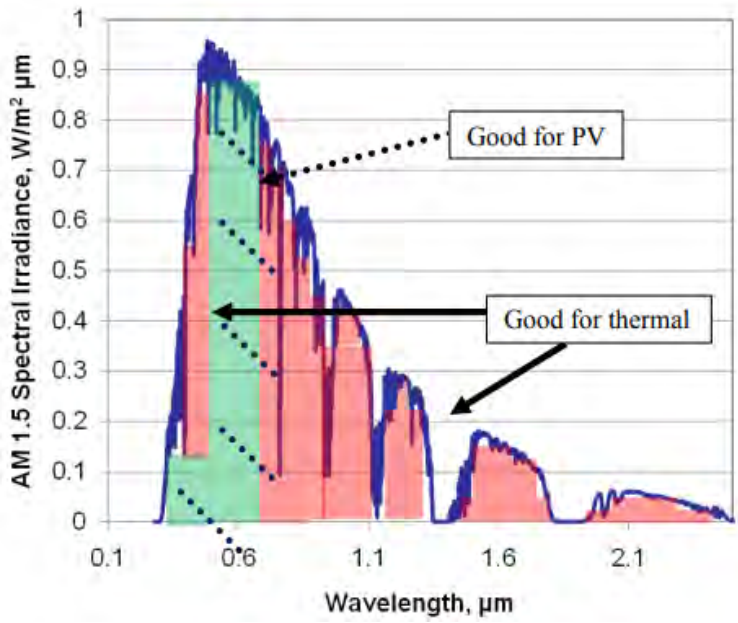

Figure 1.2 Spectrum for PV and Thermal system (R. Taylor, 2011)

1.3 Solar Thermal Collectors

The solar collector is a particular type of heat exchanger in which heat exchanges between radiant energy from a distance source and the working fluid flowing in the collector. The solar collectors are classified as concentrating and non-concentrating. Non-Concentrating is further subdivided into the flat plate solar collector and evacuated tube collector (Bogaerts & Lampert, 1983; Duffie & Beckman, 2013). Flat plate solar collector (FPSC) is the common type used to convert radiant energy into thermal energy by using an absorber plate. The surface of the absorber plate is black matte painted to absorb solar spectrum with minimum emissivity (Duffie & Beckman, 2013; H. Hottel & Woertz, 1942; Soteris A Kalogirou, 2013; Omid Mahian, Kianifar, Kalogirou, Pop, & Wongwises, 2013). Solar radiation struck on the absorber plate and converted into heat energy and then transferred to heat transfer fluid, which is flowing through the collector's tube. The schematic diagram of the FPSC is shown in Figure 1.3. The second type of flat plate collector is the direct absorption solar collector (DASC), no absorber plate is required, and here the incident rays fall directly on the working fluid and get absorbed (Khullar et al., 2012; Todd P Otanicar, Phelan, Prasher, Rosengarten, & Taylor, 2010; Phelan,

Otanicar, Taylor, & Tyagi, 2013; Sani et al., 2010; Taylor et al., 2011). The DASC was initially proposed by Minardi and Chuang (Minardi & Chuang, 1975). In DASC, operational fluid is allowing to flow between the top transparent surface and the bottom adiabatic surface, as shown in Figure 1.4. In this study, the investigation will be narrowed down to the research in the field of FPSCs.

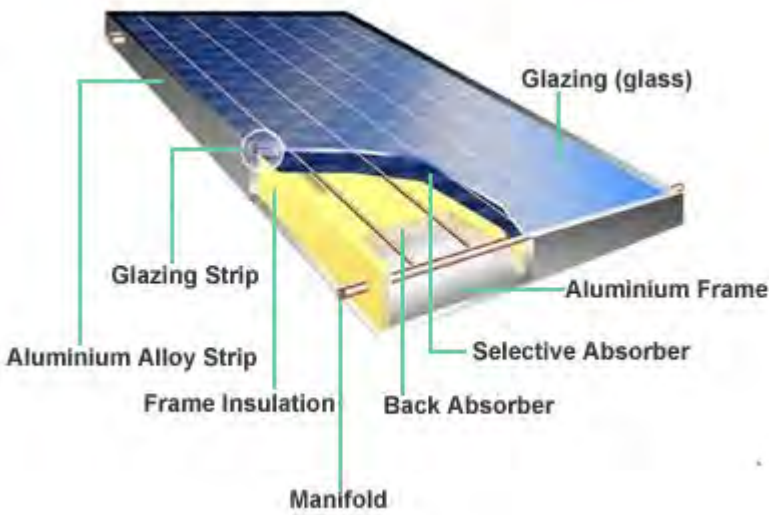

Figure 1.3 Schematic diagram of a flat plate solar collector (Efficiency, 2013)

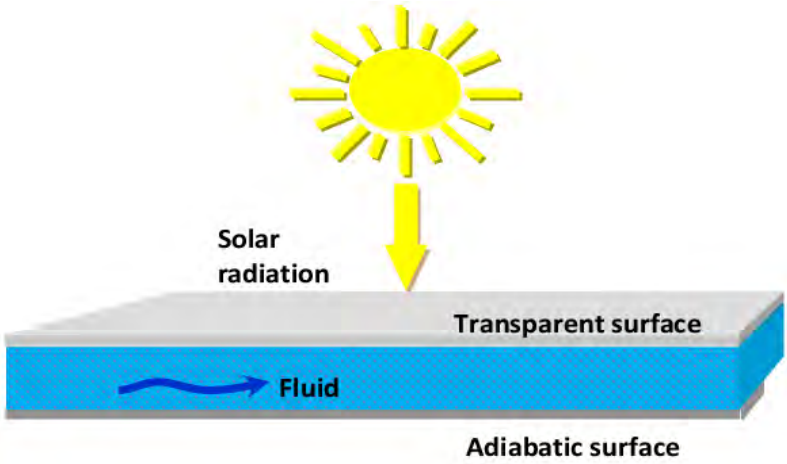

Figure 1.4 Schematic diagram of a direct absorption solar collector

1.4 Flat Plate Solar Collectors

The reason for the preference of FPSCs in comparison with other solar thermal collectors is relatively low manufacturing cost, the ability to collect both diffuse and beam radiation, and needless for any sun's tracking system. The absorber plate absorbs the central portion of the incoming solar radiation in FPSCs. To minimize the heat losses through conduction, the sides and bottom of the absorber plate are fully insulated. The glass cover of the collector reduces heat losses by convection (containments of an air layer) and radiation (translucent to sun's shortwave solar radiation). But, practically, it is non-transparent to the longwave thermal radiation emitted by the absorber plate (Soteris A Kalogirou, 2013). The conduits through which the operational fluid is flowing along with the collector, i.e., riser tubes, can either be an implicit part of the absorber plate or welded to it. The riser pipes are attached to wide header pipes on the two ends of the collector.

1.5 Problem statement

Conventional thermal fluids such as water, engine oil, and ethylene/propylene glycol play an essential role in the various engineering processes and mechanical equipment, for example, power generation, air-conditioning, chemical production, heating and cooling processes, electronic appliances, spaces, nuclear system cooling, transportation, and in the microelectronics field. Thermal properties of these conventional working fluids are deficient as compared to the solids, so heat transfer rate in thermal applications are comparatively low (Daungthongsuk & Wongwises, 2007; Duangthongsuk & Wongwises, 2010; M. Gupta, Singh, Kumar, & Said, 2017). Efficiency and compactness of mechanical equipment are improved by uplifting heat transfer properties of the working fluids, and it will also lead to reducing capital and operating costs (Maiga, Palm, Nguyen, Roy, & Galanis, 2005).

The performance of FPSCs can be improved by using different methods such as, by applying different coatings on the absorber plate (Anderson, Duke, & Carson, 2010; Oliva, Maldonado, Díaz, & Montalvo, 2013), varying the flow rates (Z. Chen, Furbo, Perers, Fan, & Andersen, 2012), and considering different configurations and tilt angle of the FPSCs (Akhtar & Mullick, 2007; Bakari, Minja, & Njau, 2014; Bisen, Dass, & Jain, 2011b; Ho & Chen, 2006; Ibrahim, Fardoun, Younes, & Ibrahim, 2018; Khalifa & Jabbar, 2010b; Martín, Pinar, & García, 2011; Skeiker, 2009; Xiaowu & Ben, 2005). However, the simplest way to increase the efficiency of FPSCs is to replace the conventional working fluid with the new class of fluids, i.e., "Nanofluids" (S. U. Choi & Eastman, 1995) for increasing the heat transfer rate from the absorber plate to the operational fluid (Abdin et al., 2013; Balaji, Khan, Kumar, Iniyan, & Goic, 2019; FS Javadi, R Saidur, & M Kamalisarvestani, 2013b; Khullar & Tyagi, 2010; Omid Mahian et al., 2013; Xiaowu & Ben, 2005; Wenhua Yu, David M France, Jules L Routbort, & Stephen US Choi, 2008b).

The present research aims to investigate, experimentally, and theoretically, the performance of flat-plate solar collectors using carbon and metal based nanofluids as working fluid. Nanofluids based on carbon could be synthesized using bio-facial method as well as conventional method, while in-situ oxidation method could be used to synthesize the iron nanoparticles. By considering weather conditions of Malaysia, i.e., intermittent cloudy weather, there is a massive fluctuation in solar radiations (irradiance) (Nawayseh, Farid, Omar, & Sabirin, 1999), the outdoor testing results are not reliable in such conditions. Moreover, the cost of outdoor testing simulator for solar applications is very high (Codd, Carlson, Rees, & Slocum, 2010; Garrido, Aichmayer, Wang, & Laumert, 2017). Considering these factors, in the present study the FPSC could be fabricated with the adhesive heater fixed to the top surface of the absorber plate for indoor testing. This heater can generate constant heat flux analogous to that of solar radiation at

the surface of the collector (Badran, Mustafa, Dawood, & Ghazzawi, 2008; Balaji et al., 2019).

1.6 Research Objectives

The objectives of the present research can be summarized as:

1. To synthesize water based nanofluids with conventional and novel bio-facial & in-situ oxidation functionalization processes, investigation of their colloidal stability and the synthesis parameters affecting thermal properties.
2. To investigate the thermophysical properties of carbon and metal-based nanofluids and comparison of them with the available models/correlation values of thermophysical properties to choose the best reliable and accurate model/correlation for each of the thermophysical properties.
3. To develop a computational simulation using ANSYS R16.2 software on nanofluid-based FPSC at the steady-state condition. To compare the experimental and simulated data at different heat flux intensities, inlet temperatures, mass flow rates, and weight concentrations for validating the experimentally collected data for water and water-based nanofluids.
4. To design and fabricate the experimental setup for studying the effects of carbon and metal base nanofluids as operational fluids on the performance of FPSC. To collect the experimental results at different conditions of heat flux intensity, collector inlet temperature, mass flux rate, and weight concentration of nanoparticles in the base fluid and evaluate the performances of the solar collector.

1.7 Organization of Thesis

This dissertation consists of five chapters and organized as follows. “Chapter 1” is the introduction that provides background about the area of this study, highlights the current

problems that motivated this research, and clarifies the objectives through which the aim of the present study can be achieved. “Chapter 2” is the literature review that comprehensively surveys the previously published work related to this field of study, which can be categorized as description and parts of FPSC, preparation of nanofluids, thermophysical properties of nanofluids; and thermal performance of nanofluid base FPSCs. “Chapter 3” is a methodology that concerns about materials, devices, and methods used in this study for preparation, characterization, thermophysical properties measurements, and evaluation of colloidal stability of nanofluids. In addition, the experimental test setup that is built and used for the investigation of the thermal performance of FPSC using nanofluid as operational fluid is fully described. “Chapter 4” is results and discussion which presents the data obtained from different sources and compares such water versus nanofluid, experimental versus correlated, or analytical data. All data are shown in the form of tables and figures. Finally, “Chapter 5” is the conclusions and recommendations in which the essential outcomes of this study are summarized with a proposal for future work inf this research area.

CHAPTER 2: LITERATURE REVIEW

2.1 Introduction

By increasing the heat transfer rate from the absorber surface to the operating fluid and then from the working fluid to the end-user, the thermal efficiency of flat-plate solar collectors is improved. The heat transfer rate can improve by using nanofluid as an alternative of conventional working fluid because nanofluids have improved thermophysical properties than conventional fluid. However, some important variables ought to be considered for the productive utilization of nanofluids in FPSCs. The first consideration is the preparation of nanofluid; it is the primary step to improve the thermal conductivity of fluids by using nanoparticles. Nanofluids synthesis is not simple as to make a mixture of liquid and solid; due to high surface to volume ratio, nanoparticles aggregate over time. Agglomeration of nanoparticles results is not only settling and blockage inflow channels but also reduces the thermal conductivity of nanofluids. So, the stability of suspending nanoparticles in base fluid should be investigated thoroughly (Behi & Mirmohammadi, 2012; Hordy, Rabilloud, Meunier, & Coulombe, 2014; Pantzali, Mouza, & Paras, 2009; Saidur, Leong, & Mohammad, 2011). The second consideration is the cost of nanofluids. For this purpose, nanoparticles which have high thermal conductivity should be used for the synthesis of nanofluids. Due to the high thermal conductivity and low concentration of nanoparticles, nanofluids have a notable effect on cost reduction and enhance the heat transfer coefficient. This approach also affects the stability of nanofluids because of the low concentrations of dispersed nanoparticles, and the nanofluids are more stable (Behi & Mirmohammadi, 2012). Another positive effect of low concentration of dispersed nanoparticles is the lower level of enhancement of the viscosity of the nanofluids which is the prime concern of pumping power and pressure drop (Omid Mahian, Kianifar, Sahin, & Wongwises, 2015; Sadri,

Hosseini, Kazi, Bagheri, Ahmed, et al., 2017). Nanofluids with higher concentrations have higher viscosities (J. Li, Li, & Wang, 2002). The pressure drop is another crucial factor associated with a fluid flowing that should be considered for operating applications (Hosseini et al., 2018). An increase in the viscosity of nanofluids causes an increase in pressure drop, which later refers to the pumping power requirement, which is one of the disadvantages of the nanofluids (Duangthongsuk & Wongwises, 2010; Razi, Akhavan-Behabadi, & Saeedinia, 2011). Based on the considerations, this chapter will cover the main components of FPSCs, the preparation methods of nanofluids, the techniques for enhancement, and evaluation of the stability of nanofluids in addition to thermophysical properties. Furthermore, the previous investigation reported in the field of nanofluid based flat plate solar collector will be thoroughly reviewed.

2.2 Description of FPSCs

In this section, a brief description of the main parts of FPSCs, along with their materials used for fabrication and functions, will be presented.

2.2.1 Glazing

The FPSCs consist of one or more transparent cover, which is crafted from plastic or glass. Such cover is designed to shield the absorber plate and to minimize heat losses from the solar collector surface. The cover of the collector reduces heat losses by convection (containments of an air layer) and radiation (translucent to sun's shortwave solar radiation range between 0.3 to 2.5μm). But practically, it is non-transparent to the long-wavelength thermal radiations (greater than 3 μm) emitted by absorber plate. The glazing of FPSCs has similar behavior to the glass of greenhouse (Bourges, Rabl, Leide, Carvalho, & Collares-Pereira, 1991; Soteris A Kalogirou, 2013). Therefore, for the

selection of collector's cover, optical properties get considerable importance (Hood & Meyer, 1994; Ting, 1981).

The principal features of the glazing are absorptance, reflectance, and transmittance of solar energy, which are absorbed, reflected, and the transmitted portion of incoming solar radiation, respectively. The absorptance, reflectance, and transmittance are represented as $\alpha_g, R_g,$ and τ_g respectively and linked together according to the law of conservation of energy, as shown in equation 2.1 (Duffie & Beckman, 2013).

$$\alpha_g + R_g + \tau_g = 1 \tag{2.1}$$

The most extensively used material for glazing of FPSC is glass, which may be attributed to its high transmittance of greater than 90% of the incoming solar radiation and opaqueness for solar radiation emitted from the top surface of absorber plate. The main drawbacks of glass glazing are that it is brittle, expensive, and has a high density (Amrutkar, Ghodke, & Patil, 2012; Bourges et al., 1991; Gillett & Moon, 1985; Köhl et al., 2005).

The effect of the glazed material thickness (glass) on the FPSC's performance was investigated by R Bakari et al. (2014). The glass thickness was 3,4, 5, and 6 mm and used in four 0.72 m^2 FPSCs as a transparent shield. The results reveal that varying the glazing thickness affected the FPSC's efficiency; the maximum efficiency was noted for 4 mm glass thickness. Another essential factor is spacing between glazing and absorber plate, Kalogirou (2009) specified that for spacing between glazing and absorber plate in the range of 15-40. In the present research, the transparent cover was selected with a 4 mm thick and 15 mm gap between the absorber plate and glass cover.

2.2.2 Absorber plate and riser tubes

The purpose of the absorber plate is to absorb the maximum possible radiation after transmitting by FPSC glazing hits on the surface region of the absorber plate. It will minimize the heat losses, and to transfer the received energy to the working fluid flowing in riser tubes (Amrutkar et al., 2012; Duffie & Beckman, 2013). The absorber plate is made of single or composite materials. The selection of materials depends upon the material's thermal conductivity, cost, weight, and availability. The common materials used for fabrication of absorber plate are Aluminium, Copper, stainless steel, mild steel, and plastics (Duffie & Beckman, 2013; Gillett & Moon, 1985; Soteris A Kalogirou, 2013).

The performance of the collector has a noticeable effect due to the bond between the absorber plate and riser tube. A good bond will provide a better heat transfer rate from the absorber to working fluid flowing in the rise tubes. Different types of methods, like press-fitting, brazing, and high-temperature soldering, are used for bonding. So, the selection of the bonding system is critical because it resists both high temperature and temperature cycling (Badran et al., 2008; Gillett & Moon, 1985).

Using an electric resistance heater to emulate the energy input to the absorber plate from solar radiation, Badran et al. (2008) examined the bonding efficiency from the absorber plate to the raiser tube of five locally developed FPSCs. All the samples were enclosed with 5-cm thick insulation to eliminate energy losses. Through evaluating the generated heat flux of the electric heater and the energy transferred to the working fluid, the bond conductance was calculated and found to be in the range of 6.3-1.8 W/mK. From all the samples tested, the one that was manufactured using the press-fit method showed the highest conductance value.

In the present study, a 2 mm copper absorber plate and 12.7 mm copper riser tubes were used to manufacturing the FPSC. The riser tubes and absorber plate are solder bonded all over the contact length.

2.2.3 Thermal insulation

The heat losses on the FPSC's back and sides are minimized by insulation materials. The four important factors that should be considered for the selection of insulation materials are thermal conductivity of materials, durability in the existence of moisture, resistance to heat, and cost of materials. Polyurethane foam, glass wool and mineral wool are the most common materials used for isolation (Gillett & Moon, 1985).

2.3 Analysis of FPSC

The systematic evaluation of the FPSC is a complicated topic. Duffie & Beckman (2013) offered a fairly simple analysis with optimistic results. The current research follows Whillier (1953,1977) and Hottel & Whillier (1958) basic derivation, as cited in Duffie & Beckman (2013). This model represents the important variables and shows how they are linked and how they affect the thermal efficiency of FPSC. Equation 2.2 from the analysis is known as Hottel-Whillier (HW) or Hottel-Whillier-Bliss (HWB) equation (Soteris A Kalogirou, 2013; Munich, 2013), this is most commonly used equation to find out useful heat gain for the solar collector. This equation has two parts, one is heat gain term, and the second is a heat loss term.

$$Q_u = A_c F_R S - A_c F_R U_L (T_{in} - T_a) \quad (2.2)$$

Where,

Q_u= Useful heat gain

A_c= Area of collector (m^2)

F_R= Heat removal factor

S = Absorbed solar energy per m^2

U_L= Overall heat loss

T_{in}= Inlet fluid temperature (K)

T_a= Ambient temperature (K)

The absorbed solar energy per unit area (S) is vital for estimating the performance of FPSC. The calculation of absorbed solar energy by absorber plate in term of the transmittance-absorptance product ($\tau\alpha$) is explained as (Duffie & Beckman, 2013):

$$S = G_T(\tau_g \alpha_{ap}) \quad (2.3)$$

Where, G_T = Impacted solar radiation (W/m^2)

τ_g= Transmittance of the glass cover

α_{ap}= Absorptance of the absorber plate

By considering the fluid inlet temperature of the solar collector, the Hottel-Whillier equation is used for measuring the energy gain in FPSC. However, this equation may have some possibilities of errors when the fluid inlet temperature is matched to the ambient temperature, then the second term of the equation reduces to zero, which means there occurred no convective heat losses.

Munich (2013) proposed a better model for the thermal efficiency of a FPSC, which was based on replacing the fluid inlet temperature of solar collectors in the HW equation with an average temperature of the collector and log mean temperature difference for heat

transfer fluid in the collector. The replacement of these two parameters instead of fluid inlet temperature revealed that no considerable effect was found as compared to the original Hottel-Whillier equation.

(K. J. S. E. Ong, 1974) carried out the theoretical and experimental analysis of the thermal performance of a flat plate solar collector. A finite difference method is used for numerical work, while experimental tests were performed on the experimental heater, which incorporated a FPSC design. Some defects were highlighted from the inaccurate assumption of the mean temperatures of various components. However, a sufficient qualitative and quantitative agreement between theoretical and experimental findings was obtained during the principal insulation phase.

(Ong, 1976) had improved his existing model to predict the thermal performance of the thermosiphon flow solar collector. The whole structure was divided into a finite number of parts, and a growing section had a uniform mean temperature. By observing the energy balance for each section, the mean temperature of each segment was determined by finite difference equations. A good agreement between experimental and theoretical data was obtained during the main part of the day.

An experimental comparative study of the implementation of conventional solar collectors and storage solar domestic hot water systems was conducted by (Khalifa & Jabbar, 2010a). The storage device consists of six copper tubes with a diameter of 80 mm, which are connected in series and act concurrently as a tank and absorber. The efficiency factor, overall heat loss coefficient, heat removal factor, temperature distribution along the pipe surface are calculating by using modified equations derived from the Hottel-Whillier-Bliss basic derivation. A strong consensus was achieved between the theoretical model and experimental results. Moreover, storage type collectors showed better

efficiency than the conventional one. Therefore, it is concluded from these previous studies that the Hottel-Whillier model presented by Duffie and Beckman is acceptable for the steady-state operation of the FPSC. In the present study, this model is used for mathematical modeling with some modifications.

The heat losses have a direct effect on the thermal efficiency of FPSC; the calculation of these heat losses is essential for the estimation of the exact thermal performance of FPSC. Among all heat losses, the top heat loss had a significant contribution to the total heat losses. (Bisen, Dass, & Jain, 2011a) conduct an analytical study to measure the top heat loss coefficient of flat-plate solar collectors. Hollan & Buchberg correlations were used for natural convective heat transfer. The ambient temperature, absorber plate temperature, and wind-heat transfer coefficient were measured with suggested correlations, and their effect on top heat loss was evaluated by using MATLAB. From the result, it was concluded that the top heat loss coefficient was increased as the wind-heat transfer coefficient, ambient & absorber plate temperature increased.

(Bhatt, Gaderia, & Channiwala, 2011) investigate the top loss coefficient of solar flat-plate collectors at different tilt angles. The top heat loss coefficient has a major impact on the useful energy gain of FPSC, although the sides and bottom losses happened, those losses are not significant as top losses. The results reveal that the thermal performance of FPSC is mainly concern with top heat loss, and it also showed that top heat loss has a direct relation with absorber plate temperature and tilt angle.

The effects of flow inside riser conduits, insolation, the emissivity of glazing material, ambient temperature, incline angle, and absorber plate temperature on top heat loss coefficient were evaluated experimentally and theoretically by (Sekhar, Sharma, & Rao, 2009). All experiments were performed by considering these parameters under

laboratory conditions. The results reveal that the emissivity of the absorber plate had shown a considerable effect on the top loss coefficient, while the incline angle had an insignificant impact. The performance of FPSC was found to enhance with increment in ambient temperature.

(Klein, 1975) developed an empirical relation to calculate the top heat loss coefficient of FPSCs with selective and non-selective coated absorber plates at a different tilt angle. This equation is an extension of Hottel & Woertz's (1942) empirical relation, which was only design for non-selective coating of absorber plates (as cited Klein 1975). This relation is represented as;

$$U_t = \frac{\left(T_p - T_a\right)A}{\frac{N}{\left(\frac{C}{T_p}\right)\left[\frac{\left(\left(T_p - T_a\right)\right)}{(N+f)}\right]^{0.33}} + \frac{1}{h_w}} + \frac{\sigma\left({T_p}^4 - {T_a}^4\right)A}{\frac{1}{\varepsilon_p + 0.05N(1-\varepsilon_p)} + \frac{2N+f-1}{\varepsilon_g}} \qquad (2.4)$$

where,

C = 365.9(1-0.00883s+0.0001298s^2)

$f = (1 - 0.04h_w + 0.0005{h_w}^2)(1 + 0.091N)$

σ = Stefan-Boltzman constant

s = tilt angle of collector

h_w= wind heat transfer coefficient (5.7 + 3.8V) where V is the velocity of air at the surface of the collector

ε_p = emittance of glazing

ε_p = emittance of the absorber plate

N = Number of the glass cover

Klein (1979) as mentioned in Duffie and Beckman 2013, modify his previous empirical relation to calculate the top heat loss of FPSC. This equation is effective for a range of mean absorber plate temperature from ambient to 200 °C with $\pm$0.3 W/m^{2}K ambiguity.

$$U_t = \left(\frac{N}{\left(\frac{C}{T_{pm}}\right)\left[\frac{\left(\left(T_{pm} - T_a\right)\right)}{(N+f)}\right]^e} + \frac{1}{h_w} \right)^{-1} + \frac{\sigma\left(T_{pm} + T_a\right)\left({T_{pm}}^2 + {T_a}^2\right)}{\frac{1}{\varepsilon_p + 0.00591 N h_w} + \frac{2N + f - 1 + 0.133\varepsilon_p}{\varepsilon_g} - N} \quad (2.5)$$

where,

C = 520(1-0.000051 β^2) for 0° < β < 70°

f = (1+0.089h_w −0.1166$h_w\varepsilon_p$)(1+0.07866N)

e = 0.430(1-100/T_{pm})

(Khoukhi & Maruyama, 2006) proposed a mathematical model to evaluate the thermal efficiency of collector with a black absorber plate. The optical constants of glass cover proposed by (Rubin, 1985) were used. The model used (Klein, 1975) equation to calculate the top heat loss coefficient, and the results revealed a virtually straight profile for the effectiveness of FPSC when convection is dominant in comparison of radiation. Based

on a previous study, it can be concluded that Klein's (1979) empirical relation as quoted in (Duffie & Beckman, 2013) was suitable for estimating the top heat loss coefficient in present study.

Later, ASHRAE developed their standard 93-2003 by extended the work of (H. C. Hottel, & Whillier, A., 1958). This standard is introduced for outdoor as well as indoor testing of the solar collector. According to ASHRAE (A. Standard, 2003), the flow rates were varied from 0.8 -1.6 liter/min. The inlet temperature is in tune between 30 – 65 °C. The ambient temperature for all data periods must be less than 30 °C. The angle of the solar collector was adjusted between 30 and 60 degree. The minimum heat flux at the surface of the collector received from radiation was 790 W/m². ASHRAE Standard 93-2003 was followed in the present study, so the flow rates used in this study were 0.8, 1.20, and 1.60 kg/s-m². The inlet temperature was in the range of 30°C to 50°C. All the experiments were conducted at steady-state conditions, and different heat flux rates analogous to the solar radiations were used to find out the thermal efficiency of FPSC.

2.4 Nanofluid as Working fluid

The solids, in particular metals form, have a hundred times higher thermal conductivities as compared to the liquids. Several studies have focused on the thermal performance of solid particles suspending in fluids. The initial suspended particle size was a millimeter or micrometer (Ahuja, 1975; Sohn & Chen, 1981). However, these millimeters or micrometer-sized particles in early studies cause some problems such as poor suspension, low stability, and channel clogging. A way to solve these problems could be the introduction of nanometer-sized particles (1-100 nm). Suspension of nanometric size particles in a base fluid is called nanofluid, and the term "Nanofluid" was first introduced by (S. U. Choi & Eastman, 1995). Nanofluids are more stable, having

high thermal conductivity, which reducing the pumping power and showing better rheological properties (Yujin Hwang et al., 2008; Sadri, Hosseini, Kazi, Bagheri, Zubir, et al., 2017; W. Yu & Xie, 2012).

2.5 Synthesis of nanofluid

Nanofluids synthesis is not simple as to make a mixture of liquid and solid; there are two methods for the preparation of nanofluids, single-step method, and two-step method (Behi & Mirmohammadi, 2012; Keblinski, Eastman, & Cahill, 2005; Raj & Subudhi, 2018; Taylor et al., 2011). A detailed description of these methods is presented in the next sections.

2.5.1 One-step method

In the single-step method, preparation of nanoparticles and synthesis of nanofluids are done in a single step by physical vapor deposition (PVD) (Eastman, Choi, Li, Yu, & Thompson, 2001; Rashidi, Mahian, Languri, & Calorimetry, 2018). The one-step method is suitable for metal-based nanofluids because it prevents oxidation of metal nanoparticles (Wenhua Yu, David M France, Jules L Routbort, & Stephen US Choi, 2008c). High dispersion stability of nanofluid can be obtained by this method due to reduced agglomeration of nanoparticles (Behi & Mirmohammadi, 2012; A Ghadimi, Rahman Saidur, & HSC Metselaar, 2011b; Taylor et al., 2011). However, there are some limitations for this method such as, it is only applicable to fluids with low vapor pressure, and can only be used for synthesizing nanofluids in small scale, and relatively expensive (Y. Li, Tung, Schneider, & Xi, 2009; R. Taylor, 2011; W. Yu & Xie, 2012). Lin, Tsai, & Wang (2006) prepared Cu-water nanofluid using a one-step method for the first time. (Kumar, Meenakshi, Narashimhan, Srikanth, & Arthanareeswaran, 2009) prepared ethylene glycol-based Cu nanofluids using in situ one-step technique. Using this method,

they improve the thermal conductivity of Cu-EG nanofluid up to 0.6 $Wm^{-1}K^{-1,}$ while this value is 0.256 $Wm^{-1}K^{-1}$ for previous reported study (H.-t. Zhu, Lin, & Yin, 2004).

2.5.2 Two-step method

In the two-step method nanoparticle, nanotubes or nanofibers are produced by inert gas condensation, chemical vapor deposition, and mechanical alloying techniques in dry powder form in the first step and then dispersed into the base fluid in a second step (Hong, Yang, & Choi, 2005). As in this technique, the preparation of nanoparticles and the synthesis of nanofluids are separately done; agglomeration of particles may take place during drying, storage, and transportation of nanoparticles (Colangelo, Favale, De Risi, & Laforgia, 2013; Y. Li et al., 2009). The graphical representation of preparation methods is shown in Figure 2.1. Due to high surface to volume ratio nanoparticles aggregate over time. Agglomeration of nanoparticles results is not only settling and blockage inflow channels but also reduces the thermal conductivity of nanofluids. So, the stability of suspending nanoparticles in base fluid should be investigated thoroughly (Behi & Mirmohammadi, 2012; Hordy et al., 2014; Pantzali, Mouza, et al., 2009; Saidur et al., 2011). The stability of nanofluid can be improved by adding a surfactant, surface modification, and ultrasonic vibration. Still, the most cost-effective and long-term stability method is the addition of a surfactant that is a non-covalent functionalization method (Behi & Mirmohammadi, 2012). All these methods will be discussed in the following sections.

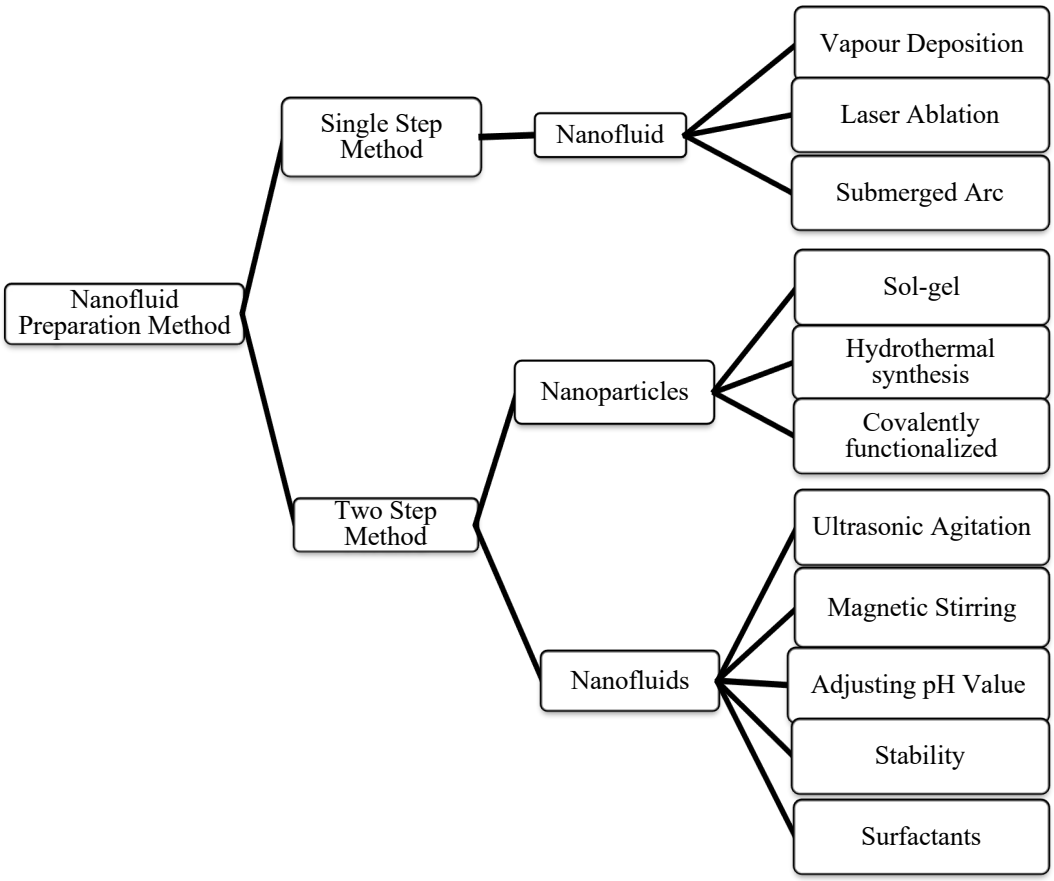

Figure 2.1 Classification of Nano-fluid preparation method

2.6 Stability of nanofluids

Producing a stable nanofluid is very important for its use as a working fluid in a heat transfer application. The colloidal stability is no longer be affected by buoyancy and gravity or any other body forces when nanoscale particles are dispersed in the base fluid. The stability of nanofluid will mainly be governed by Brownian motion, which is defined as "the random movement of nanoparticles inside the mixture caused by molecular interactions"(Mahmood, 2012; Vandsburger, 2009). In the next section, methods for evaluation and enhancing the stability of nanofluids are presented.

2.6.1 Measurement of the stability of nanofluids

Many techniques are used to measure the stability of nanofluids, such as zeta-potential, sediment photograph capturing, and ultraviolet-visible spectrophotometry spectral analysis (UV-vis). An overview of these techniques is given below.

2.6.1.1 Zeta potential analysis

It is defined as the "Electric potential in the interfacial double layer at the location of the slipping plane versus a point in the bulk fluid away from the interface, and it shows the potential difference between the dispersion medium and the stationary layer of the fluid attached to the dispersed particle" (W. Yu, Xie, H., & Chen, L., 2012). The researchers evaluate the colloidal stability of the nanofluid by using zeta-potential as one of the procedures, and it's based on the electrophoretic behavior of prepared nanofluid (H. Zhu et al., 2007). An excellent feature of zeta-potential is that its value can directly link to the colloidal stability of nanofluid (Amiri et al., 2015; Amrollahi, Rashidi, Emami Meibodi, & Kashefi, 2009). The high zeta potential values (positive or negative) are electrically stabilized; on the other side, low values (positive or negative) tend to coagulate. So, if the value of zeta-potential is less than 30 mV than it will considered to be unstable. The zeta-potential between 30 mV to 60 mV are good stable and values (positive or negative) higher than 60 mV shows exceptional stability (Vandsburger, 2009; W. Yu, Xie, H., & Chen, L., 2012).

2.6.1.2 Sediment photograph capturing method

The estimation of colloidal stability for nanofluids by this method considered the most simple and dependable method. The picture should be captured for the sample at a regular interval, and a thorough comparison between successive photos, sedimentation will be visible and be evaluated. This is a time-consuming method that required a long time for

monitoring the sample (A Ghadimi et al., 2011b; Wail Sami Sarsam, Ahmad Amiri, SN Kazi, & A Badarudin, 2016b)

2.6.1.3 UV- spectrophotometry spectral analysis

UV- vis spectroscopy provides a quantitative analysis of stability; it is due to the absorbed light of nanofluid. By measuring the values of light absorbance for the base fluid (water) and the freshly prepared nanofluid, a linear relation can be obtained between the concentration of the supernatant nanoparticles and the light absorbance. The superiority of this method is its appropriateness for all the viscosities of base fluids, while zeta-potential has limitations in this regard (A Ghadimi et al., 2011b; W. Yu, Xie, H., & Chen, L., 2012). (Linqin Jiang, Lian Gao, & Jing Sun, 2003a) were first proposed the UV-vis spectroscopy as a suitable method for measuring the stability of nanofluids.

2.6.2 Improving the colloidal stability of nanofluids

The stability of nanofluids is the major problem for researchers; it has the characteristics to agglomerate over a period of time due to van der Walls forces (Gyoung-Ja Lee & Chang Kyu Rhee, 2014; Teng et al., 2011). Addition of surfactant, Surface modification, and ultrasonic vibration are three main techniques for enhancing the stability of nanofluids (Behi & Mirmohammadi, 2012; A Ghadimi et al., 2011b; W. Yu, Xie, H., & Chen, L., 2012). The first two procedures were used to enhance the dispersity of nanometer-sized particles in colloidal suspensions by preventing or minimizing the agglomeration of nanoparticles. The third method was used to augment the colloidal stability by breaking down the agglomerated nanoparticles instead of preventing their formation. Many researchers have used all these methods to improve the colloidal stability of nanofluids (Yulong Ding et al., 2007; He, Wang, Zeng, & Zheng, 2013; Huang et al., 2009; X. Li et al., 2008; X.-j. Wang & Zhu, 2009; Wen & Ding, 2005; Yousefi,

Shojaeizadeh, Veysi, & Zinadini, 2012; D. Zhu et al., 2009) , while others just applied one technique such as (Azari, Kalbasi, Derakhshandeh, & Rahimi, 2013; Chandrasekar, Suresh, & Bose, 2010; Lee et al., 2008; W. Yu, Xie, Chen, & Li, 2009) or two techniques such as (Assael, Metaxa, Arvanitidis, Christofilos, & Lioutas, 2005; Chaji et al., 2013; L. Chen, Xie, Li, & Yu, 2008; Drzazga, Gierczycki, Dzido, & Lemanowicz, 2013; Azadeh Ghadimi & Metselaar, 2013; Halelfadl, Maré, & Estellé, 2014; Yujin Hwang et al., 2008; Y Hwang, Park, Lee, & Jung, 2006; Jiang et al., 2003a; Kahani, Heris, & Mousavi, 2013; M. E. Meibodi et al., 2010; Todd Phillip Otanicar, 2009; Todd P Otanicar et al., 2010; Pak & Cho, 1998; Pantzali, Kanaris, Antoniadis, Mouza, & Paras, 2009; Sani et al., 2010; R. A. Taylor, 2011; Taylor et al., 2011; Vijayakumaar, Shankar, & Babu, 2013; Yousefi, Veisy, Shojaeizadeh, & Zinadini, 2012; Yousefi, Veysi, Shojaeizadeh, & Zinadini, 2012).

2.6.2.1 Use of surfactants

The stability of suspending nanoparticles in base fluid should be investigated thoroughly (Behi & Mirmohammadi, 2012; Hordy et al., 2014; Pantzali, Mouza, et al., 2009; Saidur et al., 2011). The stability of nanofluid can be improved with different methods, but the most cost-effective and long-term stability method is the addition of a surfactant that is a non-covalent functionalization method (Behi & Mirmohammadi, 2012; W. Yu & Xie, 2012). The surfactant addition is a very simple method to avoid or reduce sedimentation and agglomeration of nanoparticles by changing the nature of the surface of nanoparticles from hydrophobic to hydrophilic. Heating and cooling are regular processes in heat exchange systems; surfactants tend to create forms in such situations. So, the addition of surfactant not only contaminate the working fluids but also decreases the thermal conductivity and provides adverse effects on the viscosity of the nanofluids (Aravind et al., 2011; L. Chen et al., 2008; Mingzheng, Guodong, Jian, Lei, & Lijun,

2012; W. Yu & Xie, 2012). Surfactants are categorized according to the structure of the head:

- Cationic surfactants are those in which the head has positively charged head groups such as cetyltrimethylammonium bromide (CTAB).
- Anionic surfactants are those in which the head has negatively charged head group such as (SDS) sodium dodecyl sulfate, (GA) gum Arabic, and (SDBS) sodium dodecylbenzene sulfonate.
- Nonionic surfactants are those in which the head doesn't have any charge group, such as Triton X-100.
- Amphoteric surfactants are those in which pH value specifies the charge of the head.

Selecting the correct concentration of surfactants has equal importance as selecting the right surfactant for any application. There is sufficient concentration of surfactant required to get the high stability of nanofluid as this concentration produce an adequate coating of nanoparticles capable of inducing enough electrostatic repulsion to counteract the van der Waals forces (Goodwin, 2004; Linqin Jiang, Lian Gao, & Jing Sun, 2003b; W. Yu & Xie, 2012).

2.6.2.2 Surface modification method

Due to the formulation of foam and loss of stability at high temperatures, the surfactant is not reliable for many applications. Therefore, the surface modification method is used, which is also known as covalently functionalized nanoparticles, also called a surfactant-free method. This method not only showed better and long term colloidal stability but also enhanced the thermal conductivity of nanofluids when it used in heat transfer application (Aravind et al., 2011; L. Chen et al., 2008).

Every attempt was made to prepare a nanofluid with highly dispersed nanoparticles adorned with a hydrophilic group in the base fluid. Nanofluid with high dispersibility can be obtained by using functionalized nanoparticles. It is due to the presence of dominating repulsive forces in nanoparticles. (Huang et al., 2009; Yujin Hwang et al., 2008).

(Sarsam, Amiri, Zubir, et al., 2016a) prepared water-based graphene nanoplatelets (GNPs) nanofluids by using covalent functionalization with the triethanolamine group. They prepared nanofluids with weight concentration of 0.025%,0.05%, 0.075%, and 0,1%. (Wail Sami Sarsam, Ahmad Amiri, SN Kazi, & A Badarudin, 2016a) also prepared non-covalent functionalized graphene nanoplatelets nanofluids by using SDBS, SDS, GA, and CTAB as surfactants with the same weight concentrations. Higher dispersion stability in water was obtain by the two functionalization methods in comparison with pristine GNPs. However, graphene nanoplatelets (GNPs) nanofluids containing surfactants showed more viscosity than covalently functionalized nanofluids. Thermal conductivity is also higher for covalently functionalized nanofluids than non-covalently functionalized nanofluids. (Yarmand, Gharehkhani, Shirazi, Amiri, Alehashem, Dahari, & Kazi, 2016) prepared water base nanofluids using covalent functionalization of carboxyl and hydroxyl groups with graphene nanoplatelets. They prepared three weight concentration of 0.02%, 0.06%, and 0.1%. After ten days, the sedimentation of the nanofluids was prepared was less than 7%.

2.6.2.3 Ultrasonication

Ultrasonication can enhance the colloidal stability of nanofluids that were prepared using functionalized or pristine nanoparticles, in the presence or absence of surfactants (Sarsam, Amiri, Kazi, et al., 2016a; Sarsam, Amiri, Zubir, et al., 2016a).

(Garg et al., 2009) investigate the effect of ultrasonic vibration time on the dispersion stability of 1 wt.% MWCNT nanofluid. Times of ultrasonication considered in this study were 20, 40, 60, and 80 min. Gum Arabic was used as a surfactant to disperse nanotubes in water. Ultrasonic vibration had double effects on the MWCNT nanofluid. The first one has enhanced the stability as ultrasonication time increased, and the other one was the thermal performance of MWCNT also increase as ultrasonication time increased. The optimal time for ultrasonication was noted 40 min after that, the thermal performance of MWCNT decreased. (Gyoung-Ja Lee & Chang Kyu Rhee, 2014) prepared water-based 0.1 wt.% titanium dioxide (TiO_2) nanofluid using a two-step method. Ultrasonic probe and bath, 0.1 wt.% SDS surfactant, and 25 mm nanoparticles were used. The highest colloidal stability was achieved at 3 hours ultrasonication. (Sarsam, Amiri, Kazi, et al., 2016a) prepared nineteen different samples of GNPs nanofluid by using four different surfactants and investigate the effect of ultrasonication times of 15, 30, 60, 90, and 120 min. The highest stability of 82% relative concentration after 60 days was achieved for 1-1 SDBS-GNPs sample at 60 min ultrasonication.

2.7 Thermo-physical properties of nanofluids

Thermophysical properties will be modified positively once nanoparticles are added for the use of nanofluids in different heat transfer applications. The adequacy of a nanofluid in any heat transfer application was related to the thermophysical properties of that nanofluid compared to the base fluid. Comprehensive knowledge of the effects of introducing nanoparticles to the base fluid on thermophysical properties is essential in the synthesis of a nanofluid with selected properties appropriate for a particular application of heat transfer (Leon, 2010; Zubir et al., 2016). Figure 2.2 shows the intricate connection between thermophysical properties and efficient nanofluid parameters. For all the weight

concentration of nanoparticles in nanofluid, the volumetric concentration can be determined using Equation 2.6 (Pak & Cho, 1998; Timofeeva, 2011).

$$\varphi_v = \frac{1}{(100/\varphi_m)(\rho_p/\rho_{bf}) + 1} \times 100 \tag{2.6}$$

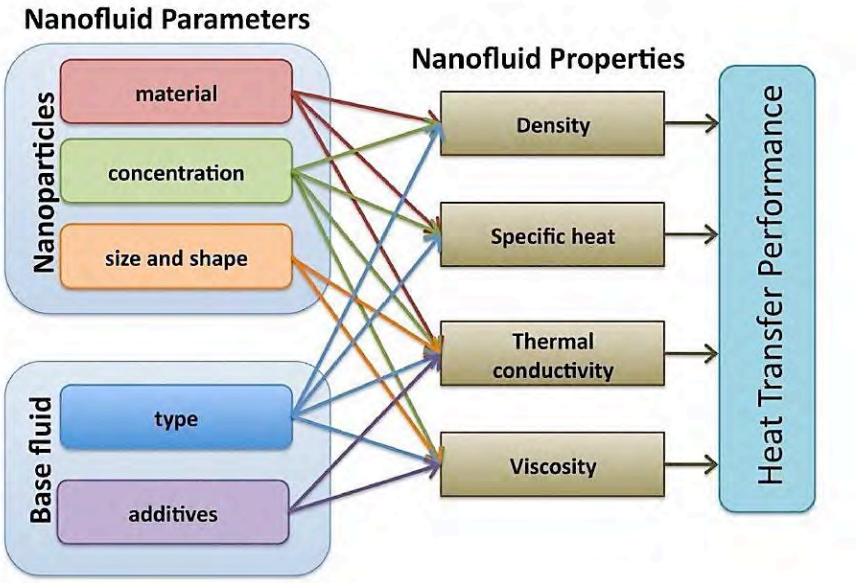

Figure 2.2 The link between thermo-physical characteristics and efficient nanofluid parameters (Timofeeva, 2011)

2.7.1 Specific heat and density of nanofluids

Using equation 2.7, actual useful heat energy gain is calculated, and it can also be calculated by taking the difference between heat energy absorbed and heat energy losses from the absorber plate is represented by equation 2.2. The specific heat of nanofluid can be calculated by using equation 2.8 (Xuan, Roetzel, & transfer, 2000). Where ρ, C_p and φ are density, specific heat and volume concentration of the nanoparticles respectively in the nanofluid suspension.

$$Q_u = \dot{m}C_p(T_i - T_a) = \rho V C_p(T_i - T_a) \tag{2.7}$$

$$\left(\rho C_p\right)_{nf} = \left(\rho C_p\right)_{nf}(\varphi) + \left(\rho C_p\right)_{bf}(1-\varphi) \tag{2.8}$$

The nanofluid density was evaluated by the help of Pak and Cho (1998) relation, which is represented by equation 2.9.

$$\rho_{nf} = \rho_{np}(\varphi) + \rho_{bf}(1-\varphi) \tag{2.9}$$

2.7.2 Thermal conductivity of nanofluids

In several engineering operations, conventional operational fluids like ethylene glycol, water, and engine oils have a comparatively meager heat conversion rate due to low thermal conductivity. Nanoparticles were applied to the fundamental liquids was a fresh concept to improve its thermal conductivity (Hong et al., 2005; Xuan et al., 2000; W. Yu et al., 2008c). Nano-particles dispersion has a significant impact on enhancing thermal conductivity by using less than 1 percent volume concentration of nanoparticles even 2.5 times in some cases (Eastman et al., 2001). There are several exciting features behind the selection of nanoparticles as possible candidates for dispersion in base liquids like elevated SSA, reduced particle power, and elevated mobility (S. K. Das, Choi, & Patel, 2006; S. K. Das, Putra, Thiesen, & Roetzel, 2003). Keblinski, Phillpot, Choi, & Eastman (2002) and Jeffrey A. Eastman, Phillpot, Choi, and Keblinski (2004) have proposed four possible mechanisms to explain the reasons for increasing the thermal conductivity of nanofluids.

- Liquid molecular level layering at the interface between fluid and particles
- Nanoparticles Brownian motion
- The nature of nanoparticle's thermal transport
- Nanoparticles cluster impacts

Previous studies have demonstrated that the thermal conductivity of nanofluids is based on various variables such as temperature, volume fraction, thermal conductivity of nanoparticles and parent liquid, nanoparticle geometry, interfacial heat strength, and specific surface area (SSA). Taking one or more variables into account, many researchers have established theoretical model and correlations to assess the thermal conductivity of nanofluid (S. Choi, Zhang, Yu, Lockwood, & Grulke, 2001; Eastman et al., 2001; Godson, Raja, Lal, & Wongwises, 2010; Huxtable et al., 2003; H. U. Kang, Kim, & Oh, 2006; Marconnet, Panzer, & Goodson, 2013; X.-Q. Wang & Mujumdar, 2008).

Maxwell (1881) (as mentioned in (Chandrasekar et al., 2010)) developed the first model for the calculation of thermal conductivity of a suspension containing liquid and solid. The model is shown in equation 2.10 and is adaptable for the comparatively low volume fraction. The particles must be uniform and randomly dispersed into the base fluid (Chandrasekar et al., 2010; Wenhua Yu, David M France, Jules L Routbort, & Stephen US Choi, 2008a). The thermal conductivity of the nanofluid can be evaluated by using equation 2.10 (Zhang, Gu, Fujii, & Science, 2007).

$$\frac{k_{nf}}{k_{bf}} = \frac{\left[k_{np} + 2k_{bf} + 2\varphi\left(k_{np} - k_{bf}\right)\right]}{\left[k_{np} + 2k_{bf} - \varphi\left(k_{np} - k_{bf}\right)\right]} \tag{2.10}$$

The thermal conductivity values determined from this model depend on the particle concentration, shape of nanoparticles, the thermal conductivity of nanoparticles, and base fluid thermal conductivity (Y. Li et al., 2009). For the spherical particles, a relatively high thermal conductivity and low volume fraction, this correlation can be written in an easier form (S. Choi et al., 2001; Gong, Bui, Papavassiliou, & Duong, 2014; Nan, Shi, & Lin, 2003; Timofeeva et al., 2007).

$$k_{nf} = k_{bf}(1 + 3\varphi) \tag{2.11}$$

The Maxwell equation failed to consider the effects of a few influence parameters on thermal conductivity values like particle shape and diameter, specific surface area, Brownian motion effect, and the thermal resistance between solid particles and the base fluid. Therefore, concerning experimental data, the expected thermal conductivity values did not meet. As a result, a series of models were proposed for modification and improvement in the Maxwell model-the Effective Middle Theory (EMT) (which in theory describes a medium based on its component volume and properties) taking more effective factors into account (Chandrasekar et al., 2010; W. Yu et al., 2008a). Hamilton & Crosser (1962) have modified the Maxwell model as represented in equation 2.12, by taking into consideration the effect of particle shape on the effective thermal conductivity of solid particles suspended in the base liquid.

$$k_{nf} = k_{bf} \frac{\left[k_{np} + (n-1)k_{bf} - (n-1)\varphi\left(k_{bf} - k_{np}\right)\right]}{\left[k_{np} + (n-1)k_{bf} - \varphi\left(k_{bf} - k_{np}\right)\right]} \tag{2.12}$$

Where,

φ = Volume fraction of nanoparticles

n = particle shape factor (3 for spherical)

k_{bf} = Thermal conductivity of host fluid (base fluid water) (W/m K)

k_{nf} = Thermal conductivity of nanofluid (W/m K)

k_{np} = Thermal conductivity of nanoparticles (W/m K)

The thermal conductivity of the base fluid can be calculated by using expression represented by equation 2.13 (Nieto de Castro et al., 1986).

$$k_{bf} = 0.6067\left[-1.26523 + 3.704\,\frac{T_{av}}{298} - 1.43955\left(\frac{T_{av}}{298}\right)^{2}\right] \tag{2.13}$$

Where, T_{av} is the logarithmic average temperature of the base fluid which is shown in equation 2.14

$$T_{av} = \frac{(T_{out} - T_{in})}{\ln\left[\frac{T_{out}}{T_{in}}\right]} \tag{2.14}$$

In the case of spherical particles without limitations of concentration of particles, the Bruggeman model is slightly better than any other model(Y Ding, Wen, & Williams, 2004; B.-X. Wang, Zhou, & Peng, 2003). The effects of the nanoparticle clustering were taken into consideration (B.-X. Wang et al., 2003). The Bruggeman model offers a binary blend of homogeneous spherical particles and represented as;

$$k_{eff} = \frac{1}{4}\left[(3\emptyset - 1)k_p + (2 - 3\emptyset)k_f\right] + \frac{k_f}{4}\sqrt{\Delta} \tag{2.15}$$

$$\Delta = \left[(3\emptyset - 1)^2\left(k_p/k_f\right)^2 + (2 - 3\emptyset)^2 + 2(2 + 9\emptyset - 9\emptyset^2)\left(k_p/k_f\right)\right] \tag{2.16}$$

Where k_{eff} represents the effective thermal conductivity, $\emptyset$ volume concentration of particles, k_p thermal conductivity of nanoparticles, and k_f thermal conductivity of the base fluid.

Lu-Lin (1996) presented a model for spherical and non-spherical particles. For spherical particles $\alpha = 10, a = 2.25, b = 2.27$; and for non-spherical s $\alpha = \infty, a = 3, b = 4.51$. The interaction of near and far filed pairs are considered. The model represented as:

$$\frac{k_e}{k_l} = 1 + a\emptyset + b\emptyset^2 \tag{2.17}$$

Timofeeva et al. (2007) prepared nanofluids using Al_2O_3 nanoparticles with 10, 20, and 40 nm diameter. The base fluid was water, and ethylene glycol, a two-step method was followed for synthesizing the nanofluids using 5-20 hrs. continuous bath sonication. The maximum improvement in thermal conductivity of water-based nanofluids was 24% at a 10% volume concentration of 40 nm nanoparticles. While thermal conductivity for EG-base nanofluids was enhanced by 29% at the same concentration, and the effect of the diameter of nanoparticles was insignificant. The effective medium theory (EMT) shows good agreement with thermal conductivity data.

(Hwang et al., 2007) prepared the nanofluids using oil, water, and EG as base fluid and CuO, MWCNT, and fullerene as nanomaterials. They investigated the thermal conductivity of nanofluids, and all the samples showed enhancement in thermal conductivity as concentration increased except water base fullerene sample. The thermal conductivity was found lower than water for water-based fullerene nanofluid, which confirmed the lower thermal conductivity of fullerene.

(Vajjha & Das, 2009) investigate the thermal conductivity of Al_2O_3, CuO, and ZnO nanofluids with up to 10% volume concentration, and EG-water (60:40) was used as base fluid. All the experiments were performed in the temperature range of 25-90 °C; the thermal conductivity of all nanofluids was increased as temperature and concentration increased. All the experimental data were compared with the available model and found an awful agreement. Consequently, new correlations were proposed and showed good agreement with experimental data.

(Sarsam, Amiri, Kazi, et al., 2016b) prepared nanofluids based on water using GNPs as nanoparticles. They used SDS, SDBS, CTAB, and GA as a surfactant. The thermal conductivities of nanofluids with weight concentrations 0.025%, 0.05%, 0.075%, and

0.1% were calculated experimentally using KD2 pro for the temperature range of 20-40 °C. The thermal conductivity increased as temperature increased, the highest thermal conductivity was found for 0.1 wt.% nanofluid in the presence of surfactants in order of GA, SDBS, and CTAB. Surfactant SDS showed the lowest improvement in thermal conductivity for all concentrations.

(Sarsam, Amiri, Zubir, et al., 2016b) investigate the thermal conductivity of TEA-GNPs nanofluid with different SSAs and concentrations. The highest thermal conductivity was found for TEA-GNPs 750 at 0.1% weight concentration. As the temperature increased from 20 to 40 °C the thermal conductivity increased from 0.673 to 0.752 W/m K. Four different models were considered for comparison of experimental data, out of four (Chu, Li, Dong, & Tang, 2012) was showed good agreement with experimental data.

(Sarsam et al., 2017) synthesized the nanofluid by using the covalent functionalization of MWCNT with β-Alanine. Four different concentrations were prepared, and two different outer diameters of MWCNT used. Later, experimental data were compared with theoretical models, and Nan et al. model were showed good agreement of data. The thermal conductivity of nanofluids increased as SSAs, weight concentration, and temperature increased. The highest increment in the thermal conductivity was found 12.2% and 14.74% for MWCNT with outer diameter 20-30 nm and less than 8 nm, respectively.

(Omer A Alawi, AR Mallah, SN Kazi, Nor Azwadi Che Sidik, & G Najafi, 2019a) synthesized nanofluids using PEG-GNPs, PEG-TGr, Al_2O_3, and SiO_2 as nanoparticles. The maximum enhancement in thermal conductivity was found 27.64% at 0.1% weight concentration.

2.7.3 Dynamic viscosity of nanofluids

For the use of nanofluids as better working fluids in specific applications for heat transfer, positive improvements in the thermophysical properties of traditional working fluids are required after the charge of nanoparticles. With the addition of nanoparticles, the thermal conductivity of the base fluids may increase; but the viscosity is adversely impacted. Viscosity and pumping power are essential economically in industrial and practical applications (Behi & Mirmohammadi, 2012). Therefore, the a nanofluid's rheological and heat transfer characteristics must be controlled because they have a direct influence on many applications as working fluid (Garg et al., 2009). Previous research has shown that the viscosity of nanofluids is based on various parameters like shear rate, the concentration of nanoparticles, temperature of nanofluids, and the size of nanoparticles. Several models in this area for estimating the viscosity of nanofluid were suggested and submitted by the researchers. (Y. Li et al., 2009).

Einstein's formula (1906), as cited in (Mahbubul, Saidur, & Amalina, 2012) and presented by equation 2.18, is one of the first correlations to evaluate the effective viscosity of a mixture suitable for low volume fractions (≤2%) of solid particles with spherical shapes. The formula of Einstein predicts underestimated viscosity values for higher volume fractions (Y. Li et al., 2009; Mahmood, 2012; Z. Said, Saidur, Sabiha, Rahim, & Anisur, 2015). Einstein's innovative research has been chiefly used as a source of several modified formulas for the evaluation of viscosity of particle suspension, based on the linear viscosity principle.

$$\frac{\mu_{nf}}{\mu_{bf}} = 1 + 2\emptyset_v \tag{2.18}$$

Brinkman (1952) amended and expanded Einstein's formula to predict the viscosity of mixtures with volume concentration (≤4%) of the particles. The new relation of the viscosity of the base fluid and nanofluid is represented as:

$$\frac{\mu_{nf}}{\mu_{bf}} = \frac{1}{(1-\emptyset_v)^{2.5}} \tag{2.19}$$

In Batchelor's modified formula (1977) as cited in (Y. Li et al., 2009), the impact of Brownian particle movement on viscosity was first represented as:

$$\frac{\mu_{nf}}{\mu_{bf}} = 1 + 2.5\emptyset_v + 6.5\emptyset^2 \tag{2.20}$$

The viscosity of nanofluid is calculated by using equation 2.21 for higher volume concentrations. (Corcione & Management, 2011).

$$\mu_{nf} = \frac{\mu_{bf}}{1 - 34.87\left(\frac{d_{np}}{d_{bf}}\right)^{-0.3} \varphi^{1.03}} \quad \varphi \leq 10\% \tag{2.21}$$

Where, d_{bf} is representing the molecular diameter of the base fluid:

$$d_{bf} = 0.1\left(\frac{6M}{\pi N \rho_{bfo}}\right)^{0.33} \tag{2.22}$$

Where M, N, and ρ_{bfo} are the molecular weight, Avogadro number, and density of the base fluid at 293K, respectively. While base fluid viscosity can be calculated by using equation 2.23 (Esfe et al., 2015).

$$\mu_{bf} = 2.414 \times 10^{-5}(10)^{\frac{247.8}{(T_{av}-140)}} \tag{2.23}$$

For a wide range of weight concentration of nanoparticles in nanofluids, the precise viscosity value is not estimated by almost any of the above standard models. A popular

technique for estimating nanofluid viscosity is, therefore, curved fitting (Y. Li et al., 2009; Mahmood, 2012).

(J. Li et al., 2002) investigate the viscosity of water-CuO nanofluid with weight concentration 0.02% - 0.1%, and temperature range 30-80 ℃. Results revealed that the viscosity of nanofluid affected with variation in temperature while weight concentration was not very noticeable.

(Prasher, Song, Wang, & Phelan, 2006) investigate the effect of volume concentration, temperature, particle diameter, and shear rate on the viscosity of PG-based Al_2O_3 nanofluid. A rheometer is used to measure the viscosity of nanofluids with volume concentrations of 0.5%, 2%, and 3%, temperature range 30-60 ℃, particle diameter 27, 40, and 50 nm at different shear rates. The viscosity of nanofluids was found to have a weak dependence on nanoparticle's diameter and temperature, and strong dependence on volume concentration.

(Nguyen et al., 2007) synthesized the water- Al_2O_3 and water-CuO nanofluids and investigate the effect of the temperature and nanoparticle diameter on viscosity on nanofluids using a viscometer. The volume concentration used in the range of 0.15%-13%, temperature range 25-75 ℃, and nanoparticles diameter was 36, 47 nm for Al_2O_3, and 29 nm for CuO were used. Results showed that the viscosity of nanofluid was not affected by nanoparticle size until ≤4% volume concentration; after that, Al_2O_3 nanofluid with 49 nm particle size showed higher viscosity. Water-CuO nanofluids displayed higher viscosity than water- Al_2O_3 nanofluids. The calculated values of viscosity using the formula of Einstein and other methods arising from the linear fluid theory were in bad agreement with experimental data for nanofluids.

The two-step technique was used to produce a volume concentration of 0.01%-0.3% of Al_2O_3 water-based nanofluids (Lee et al., 2008). The 30±5 nm Al_2O_3 nanoparticles were dispersed in the aqueous host liquid in different ultrasound times of 0, 5, 20, or 30 h. The viscosity of nanofluids decreased substantially as temperature increased and revealed non-linear relation with the volume concentration. Moreover, the formula of Einstein underestimated the values of viscosity predictions and displayed a linear relation with concentration.

(Sarsam, Amiri, Zubir, et al., 2016b) investigate the viscosity of TEA-GNPs nanofluid with different SSAs, weight concentrations, and temperatures. The maximum error of 1.04% was noted between experimental data and Arnold standard values. As the temperature increased from 20 to 40 °C, the viscosity decreased, and it grew as concentration and SSAs increased. Three different models were considered for comparison of experimental data; all the models underestimated the viscosity of nanofluids a new correlation was proposed as represented in equation 2.24:

$$\frac{\mu_{nf}}{\mu_{bf}} = 1 + 550\emptyset_v \tag{2.24}$$

(Sarsam et al., 2017) synthesized the nanofluid by using the covalent functionalization of MWCNT with β-Alanine. Four different concentrations range 0.025%-0.1% were prepared, and two different outer diameters of MWCNT used. The highest viscosity 25.69% was noted for weight concentration of 0.1% multi-wall Carbon nanotubes 20-30 nm.

(Alawi et al., 2019a) synthesized nanofluids using PEG-GNPs, PEG-TGr, Al_2O_3, and SiO_2 as nanoparticles. The viscosity of nanofluid increased as weight concentration increased and decreased with an increase in temperature. The maximum enhancement in

viscosity of PEG-GNPs, PEG-TGr, Al_2O_3, and SiO_2 nanofluids were 25%, 20%, 17%, and 15%, respectively.

2.8 Nanofluids as working fluid in flat-plate solar collectors

In the last decade, researchers have investigated both experimentally and theoretically the effect of concentration, diameter, preparation methods, and thermophysical properties (density, thermal conductivity, specific heat capacity, viscosity) of different nanofluids on the performance of FPSCs. In this section, we have focused on a review of studies on operational parameters, i.e., absorber fluids (nanofluids) effects on the efficiency of FPSCs.

The efficacy of FPSCs in steady-state conditions can be evaluated by energy balance that represents the incident solar radiation, which is divided into useful energy gain, thermal losses, and optical losses (Duffie & Beckman, 1980). The first mathematical model for evaluating the efficacy of FPSCs was suggested by Hottel and Whillier (H. Hottel & Woertz, 1942), which was later extended by ASHRAE for making a standard for testing the efficiency of FPSCs (A. J. A. S. o. H. Standard, 1977).

ASHRAE standards provide a method for indoor and outdoor testing of different solar collectors. The thermal performance of FPSCs can be tested by establishing the instantaneous efficiency of varying values of incident radiation, ambient temperature, and inlet temperature of the heat exchanging fluid. Instantaneous efficiency is defined as the ratio of useful energy gain to solar energy received by absorber plate as shown in equation 2.25

$$\eta_i = \frac{Q_u}{A_c\, G_T} \tag{2.25}$$

$$Q_u = A_c F_R[G_T(\tau\alpha) - U_L(T_i - T_a)] \tag{2.26}$$

So, the instantaneous efficiencies can be rewritten in different expressions as represented by the equations 2.27 to 2.29.

$$\eta_i = \frac{\rho V C_p(T_i - T_a)}{A_c\, G_T} \tag{2.27}$$

$$\eta_i = \frac{A_c F_R[G_T(\tau\alpha) - U_L(T_i - T_a)}{A_c\, G_T} \tag{2.28}$$

$$\eta_i = F_R(\tau\alpha) - F_R U_L \frac{T_i - T_a}{G_T} \tag{2.29}$$

Where, F_R represents the heat removal factor and its value can be calculated by using equation 2.30

$$F_R = \frac{\dot{m} C_p\left(T_{fo} - T_{fi}\right)}{A_c\left[I_c \tau\, \alpha - U_L\left(T_{fi} - T_o\right)\right]} \tag{2.30}$$

Where U_L is the overall losses of FPSCs, which is equal to the sum of the top, bottom, and edge losses. All these losses could be calculated by using equation 2.31 to 2.35

$$U_L = U_t + U_b + U_e \tag{2.31}$$

$$U_t = \left\{\frac{\frac{1}{N}}{\frac{C}{T_p}\left(\frac{T_p + T_a}{N + f}\right)^{0.33} + \frac{1}{h_a}}\right\} + \left\{\frac{\sigma\left(T_p + T_a\right)\left({T_p}^2 + {T_a}^2\right)}{\varepsilon_p + 0.5N\left(1 - \varepsilon_p\right) + \frac{2N + f - 1}{\varepsilon_g} - N}\right\} \tag{2.32}$$

Where,

$$C = 365.9 \times (1 - 0.00883\beta + 0.0001298\beta^2) \tag{2.33}$$

$$f = \left(1 + 0.04h_a + 0.0005{h_a}^2\right) \times (1 + 0.091N) \tag{2.34}$$

$$h_a = 5.7 + 3.8V \tag{2.35}$$

$$U_b = \frac{k_b}{x_b} \tag{2.36}$$

$$U_e = U_b \left(\frac{A_e}{A_c}\right) \tag{2.37}$$

To enhance the performance of the solar collector, it needs to improve the absorption of solar radiations and reduce heat losses (by conduction, convection, and radiation) from the absorber plate to the surroundings. Efficiency can also be improved by improvement in the heat transfer rate between the absorber plate and the operational fluid, then finally to the end-user (FS Javadi, R Saidur, & M Kamalisarvestani, 2013a). Therefore, use of nanofluid as working fluid in the solar collector is one of the ways to enhance the efficiency of the flat plate solar collector (Chaji et al., 2013; Javadi et al., 2013a; Z Said et al., 2015; M. A. Sharafeldin, Gróf, & Mahian, 2017; L Syam Sundar, Singh, & Sousa, 2014; Yousefi, Veisy, Shojaeizadeh, & Zinadini, 2012c).

2.8.1 Experimental studies on FPSCs by using nanofluids

Yousefi et al. (Yousefi, Shojaeizadeh, Veysi, & Zinadini, 2012a; Yousefi et al., 2012c; Yousefi, Veysi, Shojaeizadeh, & Zinadini, 2012b) investigated the effect of Al_2O_3/water, MWCNT/water, and pH variation with MWCNT/water nanofluids on the thermal performance of 2 m² FPSC. To enhance the stability of nanofluid, the Triton X-100 surfactant was used at 0.2 wt. % and 0.4 wt. % concentration of nanofluids. The flow rates were 1-3 liter/min. Experiments were performed by following the ASHRAE standard 93-86. The experimental results revealed that for Al_2O_3/water nanofluid, the maximum enhancement in the thermal efficiency of FPSC was noted 28.3 % at 0.2wt. % concentration with a surfactant. For MWCNT/water nanofluid, it was observed that at 0.2 wt. % concentration with surfactant the values of $F_R(\tau\alpha)$ and $F_R U_L$ factor improved by 47.76 % and 71.7 %, respectively. Moreover, there are effects of different pH values (3.5,

6.5, and 9.5) on the MWCNT/water, and the performance of FPSCs. The results showed that increasing or decreasing the values of pH from the isoelectric point gave a positive effect on the thermal performance of FPSCs, and the isoelectric point for MWCNT was noticed about 7.4.

The effect of using Cu synthesize/EG nanofluid as heat transfer fluid on the effectiveness of 0.67 m² FPSC was examined experimentally by (Zamzamian, KeyanpourRad, KianiNeyestani, & Jamal-Abad, 2014). Cu nanoparticle with the outer diameter of 10 nm and the weight concentrations of 0.2% - 0.3% were used. Nanofluid was synthesized without surfactant, and no information about stability was presented. The flow rate of nanofluid varied between 0.5 to 1.5 liter/min, and ASHRAE 93-2003 standard was used for the efficiency calculation. They used a copper absorber plate with a black coating, aluminum frame, and four riser tubes having 0.96 m length and 20 mm diameter. The efficiency of FPSC was decreased with a decrease in flow rate and increased with the increase in Cu-synthesized/ EG nanofluid concentration. Due to nanofluid, absorbed energy parameter $F_R(\tau\alpha)$ was increased for FPSC, and this parameter was highest at 1.5 liter/min. The remove energy parameter $F_R U_L$ was decreased with the increase of nanofluid concentration. So, an optimum point for FPSC efficiency could be reached for 0.3 wt. % Cu-synthesize/EG nanofluid at 1.5 liter/min flow rate, as shown in Figure 2.3.

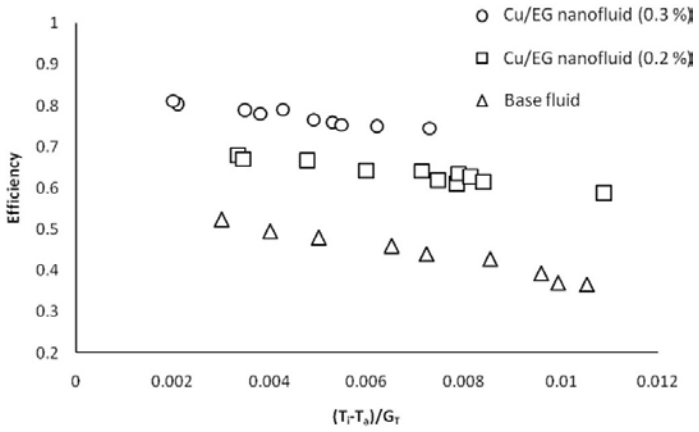

Figure 2.3 Variations of collector efficiency versus reduced temperature for the Cu/EG nanofluid at different concentrations and the base (Zamzamian et al., 2014).

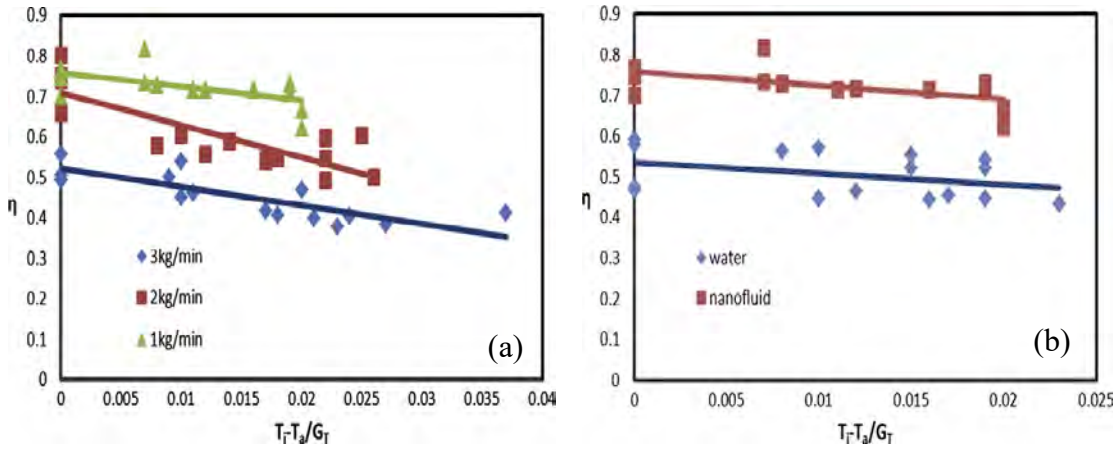

Figure 2.4 (a) Efficiency of solar collector for CuO/water nanofluid at different flow rates (b) Efficiency of solar collector for water and CuO/water nanofluid (A. J. Moghadam, Farzane-Gord, Sajadi, & Hoseyn-Zadeh, 2014)

Effect of CuO/water nanofluid on the performance and efficiency of FPSC was investigated experimentally by Moghadam et al. (2014) The volume fraction of CuO nanoparticles with a mean diameter of 40 nm was set 0.4. The mass flow rate of nanofluid in the experimental observation was varied from 1 to 3 kg/min. No surfactant was used for the preparation of nanofluid. Aluminum-based FPSC having 1.51 m² area, 22 mm, and 10 mm header and riser diameter respectively were used for experimental investigation. An electric pump was used for forced circulation in the test setup, where the tank capacity for fluid storage was kept 20 liters in this study. ASHRAE 93-2003

standard was followed for this study. Experimental results revealed that CuO/water nanofluid had improved the collector efficiency of about 21.8% at a 1 kg/min flow rate, as shown in Figure 2.4. This improved efficiency was 16.7% higher than that of water when compared with CuO/water nanofluid and water alone, as presented in Figure 2.4.

A FPSC of 2 m² area and absorber plates containing eight parallel copper strips of 8 mm inside diameter was fabricated by (He et al., 2015). $Cu - H_2O$ Nanofluid with mass fractions of 0.1 wt. % and 0.2wt. % and particle sizes 25 nm and 50 nm were prepared by a two-step method. To enhance the stability of the nanofluid SDBS surfactant was added, the pH value of nanofluid was adjusted at 8 by HCl and NaOH of analytical grades. Thermal efficiency was evaluated by ASHRAE standard 86-93. Experiments were conducted from 9:00 to 16:00 hrs. An external pump maintained the flow rate of nanofluid at 140 liters/hour, where the tank capacity used was at 100 liters. Heat gain, frictional resistance coefficient, and water temperature were also investigated in that study. The experimental results revealed that FPSC efficiency was increased up to 23.83 % by using $Cu - H_2O$ nanofluids (25 nm. 0.1 wt. %) as shown in Figure 2.5(a). With the increasing of nanoparticles size, the efficiency of the FPSC decreases as shown in Figure 2.5(b). The highest temperature and the highest heat gain of water in $Cu/water$ nanofluids (25 nm. 0.1 wt. %) were 12.24 % and 24.52 % respectively. The frictional resistance coefficient increment rate was less than 1%.

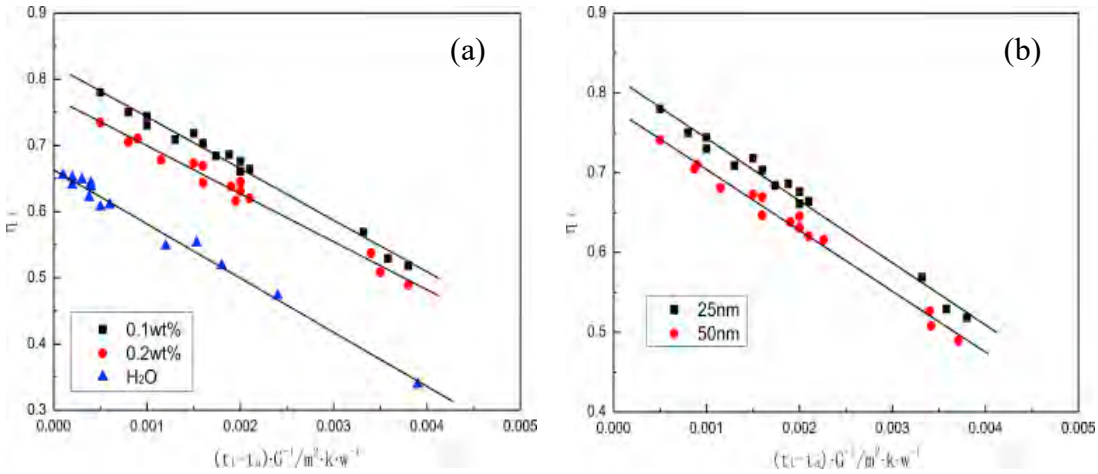

Figure 2.5 (a) Thermal efficiency of flat plate solar collector with Cu-water nanofluid at different weight concentration (b) Thermal efficiency of flat plate solar collector with Cu-water nanofluid at different size of Cu nanoparticles (He, Zeng, & Wang, 2015).

(Z Said et al., 2015) used TiO_2-H_2O nanofluid for improving the thermal efficiency of FPSC. Nanofluids were prepared by using TiO_2 nanoparticles of diameter 20 nm and 40 nm. The mass flow rates were varied from 0.5 to 1.5 kg/min, and the volume fractions were 0.1% and 0.3%. The sedimentation and thermophysical properties of the nanofluids were improved by using PEG 400 dispersant. Thermal efficiency was enhanced by 76.6% for 0.1 vol. % and 0.5 kg/min flow rate, whereas the exergy efficiency was improved by 16.9% for 0.1 vol. % and 0.5 kg/min flow rate. Pumping power and pressure drop of the nanofluid was close to the base fluid for the studied volume fraction of the nanoparticles.

(Michael & Iniyan, 2015) prepared the Copper Oxide/water nanofluid from Copper Acetate and conducted experiments to study the effect of nanofluid on the performance of a 2.184 m² FPSC. The stability of the CuO nanoparticles was checked with the addition of SDBS and Triton X-100 surfactant, where SDBS showed better stability after 3 days. SDBS was selected with 0.05 vol % in concentration. The thermal performance of FPSC was investigated both in forced circulation and in thermosyphon circulation. The flow

rate of natural (thermosyphon) circulation was considered 100 liters per day (LPD), and the maximum efficiency enhancement was 6.3 %, as shown in Figure 2.6. This enhancement of efficiency could be further improved with the effectiveness of the nanofluid.

Thermal efficiency and performance characteristics of FPSC having area 1.59 m² were investigated experimentally by (S. S. Meibodi, Kianifar, Niazmand, Mahian, & Wongwises, 2015). SiO_2/ Ethylene glycol (EG)-water was selected as nanofluid for the study. Experiments were conducted under ASHRAE standard 86-93 with volume fractions of 0.5%, 0.75%, and 1% nanoparticles, and the mass flow rates of the nanofluids were 0.018, 0.032, and 0.045 kg/s. Although SiO_2 nanoparticles have low thermal conductivity than the other considered nanoparticles, but still, they showed noticeable enhancement in thermal efficiency when suspended in EG-water, as presented in Figure 2.7. It was noticed that with the variation of the volume concentrations from 0 to 1%, the enhancement in the efficiency of FPSC varied from 4 to 8%. It was also observed that the efficiencies at the concentrations of 0.75% and 1% were very close to each other so, it was suggested to select 0.75 % concentration for its enhanced stability as nanofluid due to low particle loading.

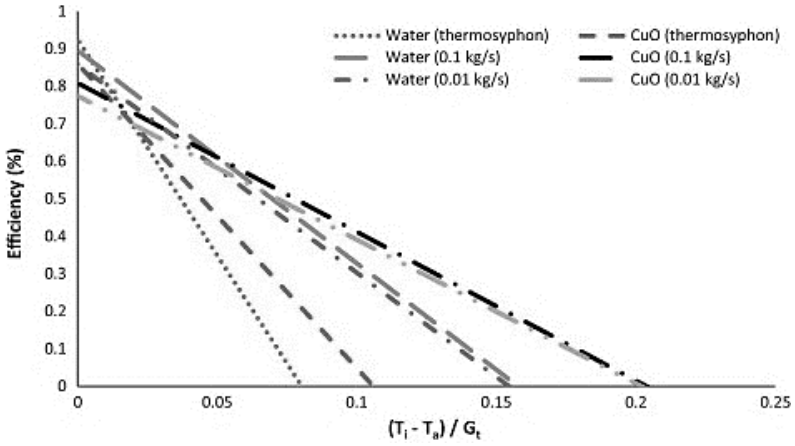

Figure 2.6 Efficiency of flat plate solar collector against reduced temperature parameter (Michael & Iniyan, 2015)

By using the same setup of the previous work (Z Said et al., 2015) investigated the effect of SWCNTs suspended in water on the thermos-physical properties of the fluid. To enhance the stability, SDS was used as a dispersant, ration used for SDS/SWCNTs particles was 1:1 where the nanofluid was found stable up to 30 days at the specified ratio. The concentrations for SWCNTs having a 1-3µm length and 1-2 nm diameter were 0.1 vol.% and 0.3 vol.% and at the flow rates were maintained at 0.5, 1.0, and 1.5 kg/min for the investigation. Thermal conductivity was increased linearly with the enhancement of concentration and temperature, while specific heat and viscosity were raised with the concentration but decreased with the increase in temperature. Energy and exergy efficacies were enhanced by 95.12 % and 26.25 % as compared to the water data. The low exergy efficiency shows that the used FPSC requires considerable improvement.

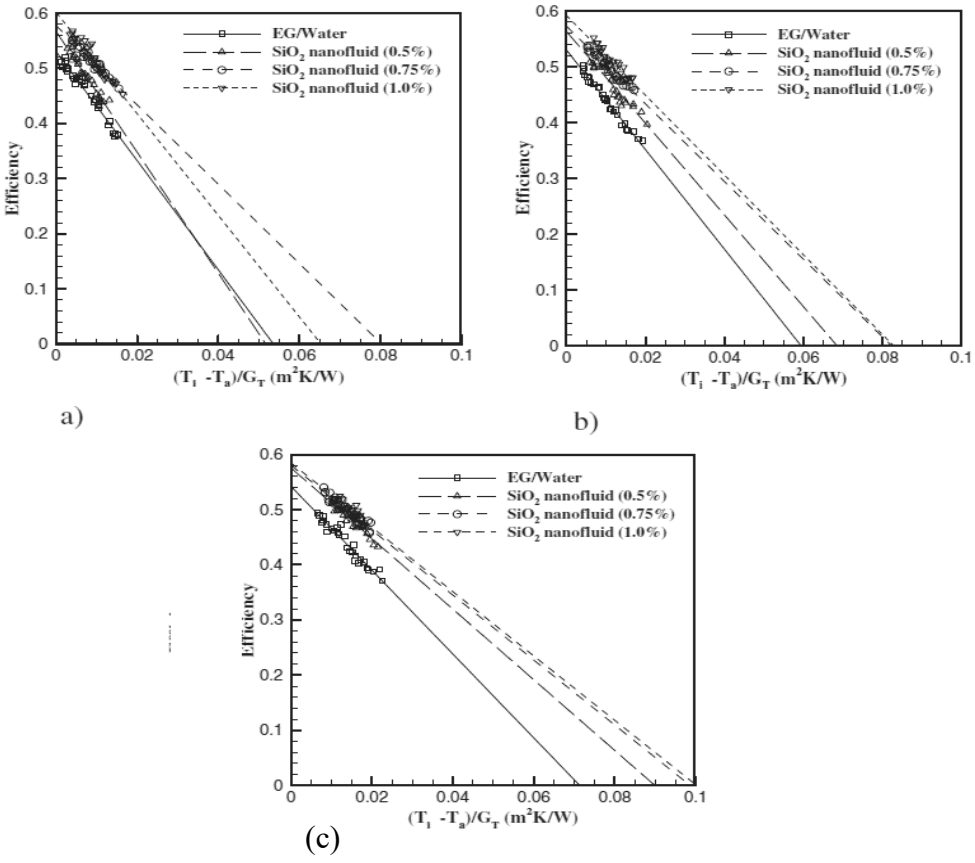

Figure 2.7 Efficiency of solar collector at different nanofluid concentrations and mass flow rates of (a) 0.018 kg/s (b) 0.032 kg/s (c) 0.045 kg/s (S. S. Meibodi et al., 2015)

The effect of using 15 nm Al_2O_3/H_2O nanofluid on the exergetic efficiency of 1.51 m² FPSC was studied by (Shojaeizadeh, Veysi, & Kamandi, 2015). The effect of different parameters like inlet temperature, ambient temperature, volume concentration, and the mass flow rate on FPSC's exergy efficiency was investigated and found optimum values for all these parameters. In that investigation, ASHRAE standard 93-2003 was used. To improve the stability of Al_2O_3/water nanofluid, SDBS was used as the surfactant and 0.090696%, 0.094583%, 0.10293%, 0.11057%, 0.117686%, 0.1244%, 0.13082%, 0.137% and 0.1423% were the volume concentrations of the nanofluids for that study with the flow rate maintained between 0.00727 to 0.01598 kg/s. By introducing nanofluid in FPSC, the maximum e gy efficiency was increased about 1%, and also the

corresponding optimum values of the mass flow rate of fluid and collector inlet fluid temperature were decreased by about 68% and 2%, respectively.

(Vakili, Hosseinalipour, Delfani, Khosrojerdi, & Karami, 2016) investigated the effect of graphene nanoplatelets nanofluid on FPSC for the domestic hot water system experimentally. European Standard EN 12975-2 was used for those experiments. A 60 × 60 cm² collector was used for four different types of nanofluids, including base fluid. The weight fraction and mass flow rate for that study was 0.0005, 0.001, 0.005 wt. % concentration and 0.0075, 0.015, 0.225 kg/s respectively. FPSC efficiency increased with flow rate, and the optimum flow rate was 0.015 kg/s, the increase in flow rate beyond this caused a decrease in collector efficiency. The zero-loss efficiency for 0.005 wt. %, 0.001 wt. % and 0.005 wt. % were 83.5 %, 89.7 %, and 93.2 % respectively, whereas this zero-loss efficiency for base fluid was 70% as shown in Figure 2.8

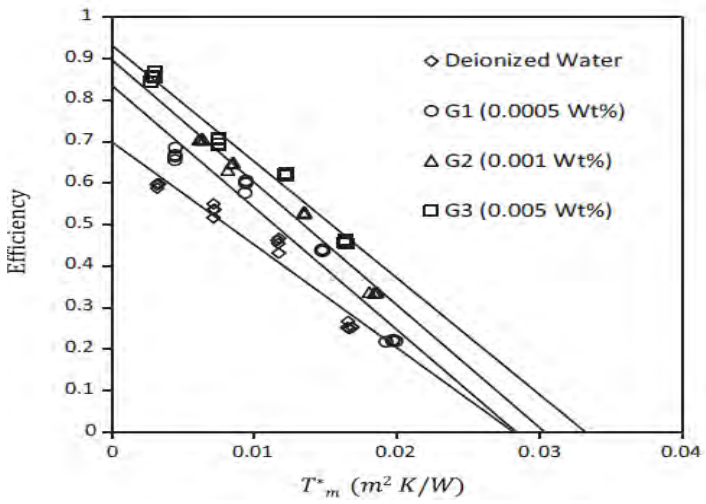

Figure 2.8 Effect of weight concentration on the efficiency of flat-plate solar collector at a flow rate of 0.015 kg/s (Vakili et al., 2016)

The impact of GNP on the efficiency of FPSC was investigated experimentally and theoretically by (Ahmadi, Ganji, & Jafarkazemi, 2016). Nanofluids with weight

concentrations of 0.01 % and 0.02 % and GNP having a structural length of less than 100 nm were prepared by a two-step method. Colloidal stability was tested with different pH values to prevent aggregation and sedimentation, and pH value 11.5 was selected for this study. The test was performed from 9:00 AM to 4:00 PM under ISO 9806 test standard. Efficiency of the collector (0.47 × 0.27 m) was increased 12.19% and 18.87% at 0.01 wt.% and 0.02 wt. % nanoparticles concentrations, respectively, as shown in Figure 2.9. The thermal conductivity of nanofluid with 0.02 wt.% also increased by 13% as compared to water data. The outlet temperature of the water heater reached 71 °C for 0.02 wt.% nanofluid, which is appropriate for household use.

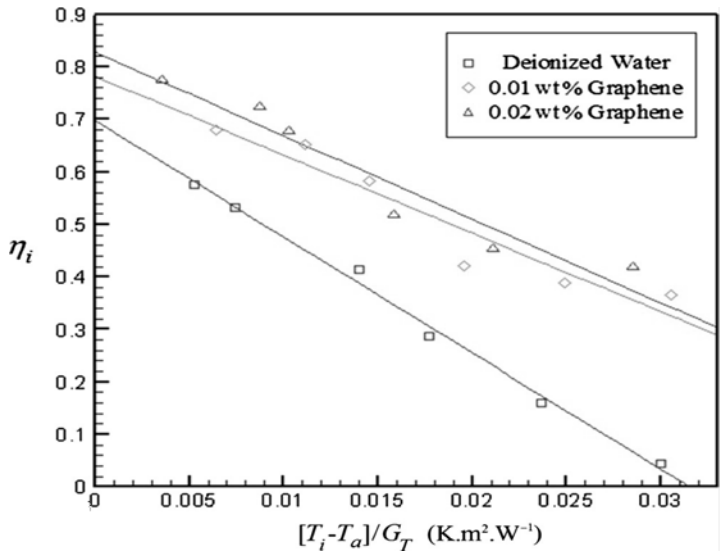

Figure 2.9 Thermal efficiency of flat plate solar collector for water and graphene-water nanofluids at different concentrations (Ahmadi et al., 2016)

Effect of SiO_2/H_2O nanofluid on the efficiency of a square (1m²) FPSC was investigated experimentally by (Noghrehabadi, Hajidavaloo, & Moravej, 2016). Nanofluid of weight fraction 1 % without surfactant used in this study. Tests were performed under ASHRAE standard 93 with different flow rates between 0.35 to 2.8 liter/min. Pumping power and pressure drop were not considered as high weight fraction

concentrations were used for the study. However, collector efficiency was enhanced with the application of nanofluid and increase with the enhancement of flow rate.

(S. K. Verma, Tiwari, & Chauhan, 2016) used 0.375 m² solar collectors for testing the effect of MgO/H_2O nanofluid of 40 nm diameter on the performance of a FPSC. Nanofluids were synthesized with concentrations of 0.25, 0.5, 0.75, 1.0, 1.25 and 1.5wt% in the presence of CTAB surfactant and the flow rates were 0.5, 1.0, 1.5, 2.0 and 2.5 liter/min. MgO/H_2O nanofluid was stable for 50 hours in the tank, and after that, sedimentation started. The parameters which were analyzed in the study were the thermal conductivity, energetic efficiency, Bejan number, pumping power, entropy generation, and reduction in the area of FPSC. Maximum thermal efficiency was observed at 0.75 vol.%, and it was 9.34 % at the flow rate of 1.5 l/min, as shown in Figure 2.10. At the same concentration and flow rate, energetic efficiency was 32.23%. Bejan number reached about 0.97 for the optimum concentration and flow rate. Pumping power loss of 0.75 vol.% and 1.5 vol.% was 6.84% and 12.84% respectively higher than the data for water alone. Economically, by using this nanofluid, the surface area of the FPSC was reduced about 12.5% compared to the data for water alone. (Vincely & Natarajan, 2016) studied the performance of a 2 m² FPSC using graphene oxide (GO) based nanofluid. No surfactant was used, and it was prepared by ultra-sonication of GO nanoparticles in a base fluid with mass concentrations of 0.005, 0.01, and 0.02. Nanofluid was stable for more than 60 days with no sedimentation. Thermal efficiency and heat transfer coefficient values were evaluated for nanofluid under laminar conditions. Improvement in thermal efficiency was noticed 7.3 % for GO nanofluid compared to the base fluid at a mass fraction of 0.02 % and the flow rate of 0.0167 kg/s as represented in Figure 2.11. The maximum heat removal factor for the same flow rate and concentration was noted at 28.3

%. Similarly, an increase in *h* values for GO nanofluid at the mass fractions of 0.005, 0.01, and 0.02 was 8.03%, 10.93%, and 11.5 %, respectively.

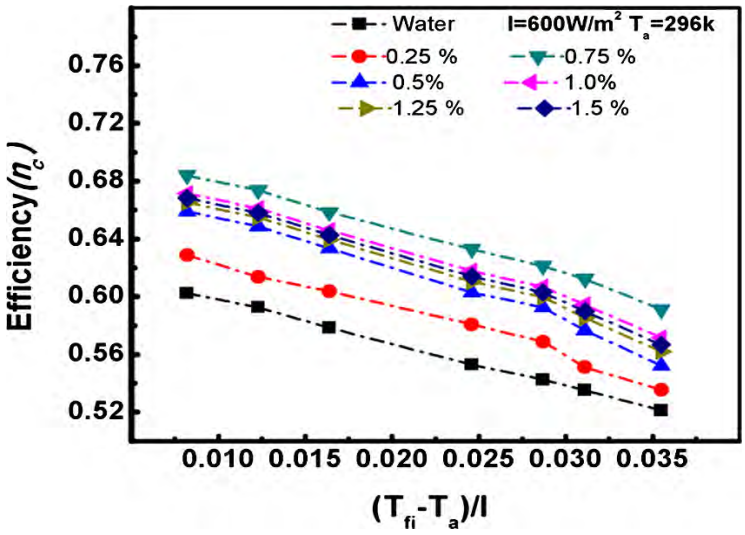

Figure 2.10 Effect of different concentration of MgO/H_2Onanofluid on thermal efficiency against reduced temperature parameter (S. K. Verma et al., 2016)

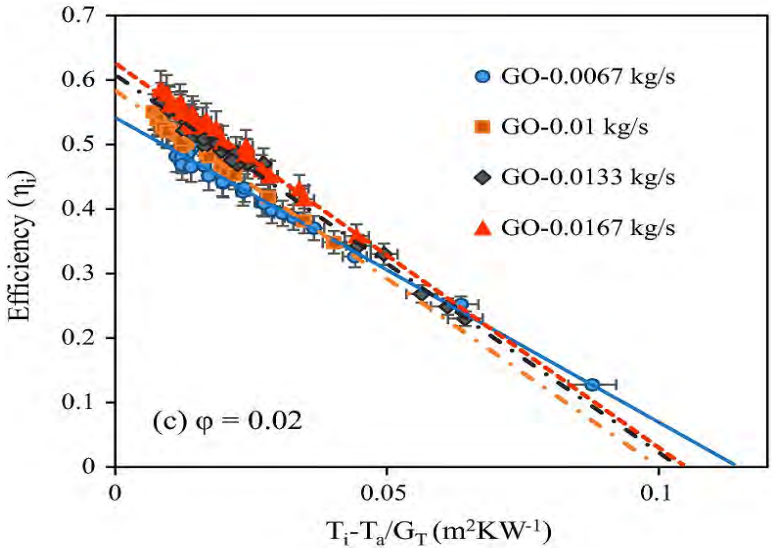

Figure 2.11 Effect of the mass flow rate of GO nanofluid on efficiency (Vincely & Natarajan, 2016)

(Kim, Kim, & Cho, 2017) Studied the effectiveness of a U-tube solar collector using Al_2O_3/H_2O nanofluid with nanoparticles sizes of 20, 50, and 100 nm. The thermal conductivity behavior of nanofluid was increased with the increase in concentration but decreased with the increase in particle size. At the ambient inlet temperature, the efficiency of the collector was 24.1% higher than the base fluid at the concentration of 1.0 vol. % and flow rate 0.047 kg/s for 20 nm-nanoparticles, which is 5.6% and 9.7 % higher when compared with the data at the volume concentration of 1.5% and 0.5%, respectively, as shown in Figure 2.12. For an equal concentration of Al_2O_3/water nanofluid, the highest efficiency for the collector, was 72.4 % at the size of the nanoparticles 20 nm, which is 3.05 % and 5.32 % higher than the data of the nanoparticles of sizes 50 nm and 100 nm respectively.

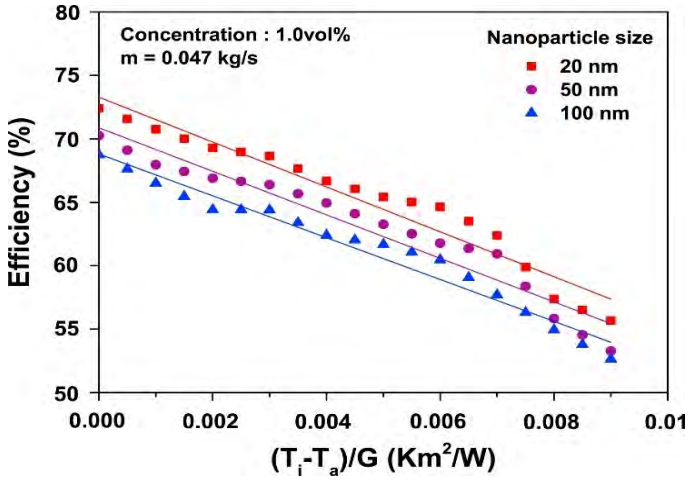

Figure 2.12 Variation of thermal efficiency of a solar collector as a function of nanoparticles size (Kim et al., 2017)

Experimental study on 0.375 m² FPSC for different nanofluids, SiO_2-H_2O, TiO_2-H_2O, Al_2O_3-H_2O, CuO-H_2O, Graphene/water, and MWCNTs-water were conducted by (S. K. Verma, Tiwari, & Chauhan, 2017). The effect of nanofluids on exergy efficiency, entropy generation, Bejan number, and thermal efficiency of FPSC was calculated

following ASHRAE standard 93-2003. Triton X-10 surfactant, volume fractions of 0.25, 0.50, 0.75, 1.0, 1.5 % and the mass flow rates of 0.01 to 0.05 kg/s were used for this study. Experiments showed that at a volume fraction of 0.75% and flow rate of 0.025kg/s the exergy efficiency of MWCNT/water nanofluid was enhanced 29.32% whereas 21.46%, 16.67%,10.86%, 6.97% and 5.74% enhancements were obtained for graphene/H_2O, CuO/H_2O, Al_2O_3/H_2O, TiO_2/H_2O and SiO_2/H_2O, respectively, as represented in Figure 2.13. A maximum drop in entropy generation was observed for MWCNTs, which is 65.55% followed by 57.89%, 48.32%, 36.84%, 24.49% and 10.04% for other nanofluids accordingly as mention in the previous results above. Thermal efficiency of FPSC was improved by 23.47%, 16.97%, 12.64%, 8.28%, 5.09% and 4.08% for MWCNTs/water, graphene/H_2O, CuO/H_2O, Al_2O_3/H_2O, TiO_2/H_2O and SiO_2/H_2O respectively.

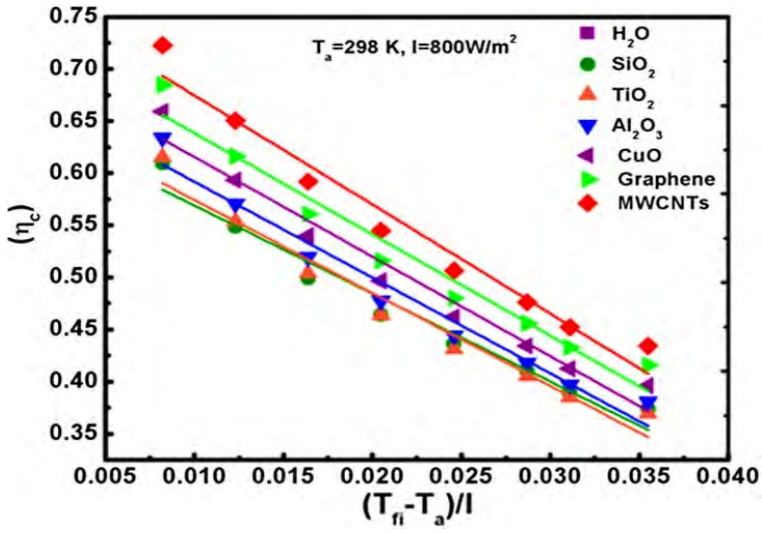

Figure 2.13 Experimental efficiency of solar collector against reduced temperature (S. K. Verma et al., 2017)

A (0.8 × 0.7 m²) FPSC with porous metal foam filled channel was used to find thermal efficiency of SiO_2/water nanofluid experimentally by (Jouybari, Saedodin, Zamzamian, Nimvari, & Wongwises, 2017). Nanoparticles of sizes 7, 20, 40 nm were used to synthesize nanofluid with volume fractions of 0.2%, 0.4%, and 0.6%. The thermal

efficiency of nanofluids was examined by ASHRAE standard 93-2003. Using nanofluid in metal porous foam channel, the maximum improvement in the thermal efficiency of FPSC was 8.1%. Based on experiments, it was found that the thermal efficiency was improved with the increase in concentration than the flow rate. Due to the use of porous media, the pressure drop of nanofluid was increased. For consideration of pressure drop and heat transfer enhancement, a Performance Evaluation Criterion (PEC) was evaluated for both the nanofluids and the porous media. Results reveal that the PEC value for nanofluid at the concentrations of 0.2 to 0.6% and the flow rate of 0.5 liter/min, was enhanced from 1.07 to 1.34. Finally, the effect of nanoparticles size on the performance was investigated by authors, and the results showed (Figure 2.14) that the efficiency curve slope parameter reduced with the decrease in nanoparticle size.

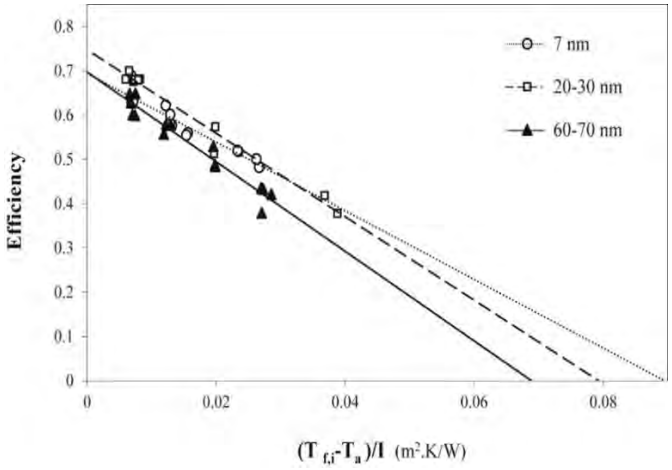

Figure 2.14 Effect of nanoparticles size on flat plate solar collector's efficiency (Jouybari et al., 2017)

(M. A. Sharafeldin et al., 2017) Conducted an experimental study using WO_3/H_2O nanofluid as the working fluid to find out the thermal efficiency of 2.009 × 1.009 m² FPSC. Nanofluids were prepared with the volume fractions of 0.0167%, 0.0333% and 0.0666% and the mass flux rate were 0.0156, 0.0183 and 0.0195 kg/s. The stability of

nanofluid was checked with zeta potential, where the nanofluids were found stable for 7 days. ASHRAE standard 93 was used for thermal efficiency. Results showed that the thermal performance of the collector was reached 71.87 % for 0.0666 vol. % concentration of nanofluid and at 0.0195 kg/s mass flux, as shown in Figure 2.15. Similarly, a 13.48% increase in the absorbed energy parameter was noticed for the same concentration and flow rate.

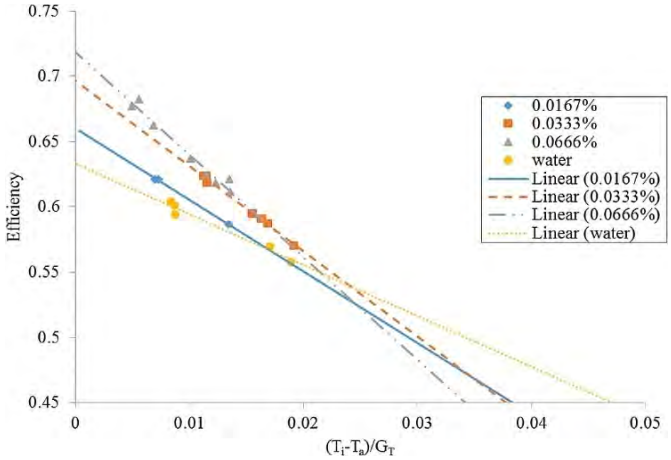

Figure 2.15 Efficiency of solar collector at the highest flow rate of 0.0195 kg/s (M. A. Sharafeldin et al., 2017)

The efficiency of FPSC and U-tube collector using Al_2O_3/H_2O nanofluid was investigated experimentally by (W. Kang, Shin, & Cho, 2017). In this study energy savings, CO_2 and SO_2 generated were calculated and compared with water data. Based on the experimental results it was noted that the performance of collectors improved with the enhancement of the concentration of $Al_2O_3/water$ nanofluid. Three concentrations were used in this study, with the volume percentages of 0.5, 1.0, and 1.5 %. The maximum efficiencies of FPSC and U-tube collector for 20 nm particles size Al_2O_3/H_2O nanofluid were 74.9% and 72.4%, respectively, at the volume fraction of 1.0 % and the flow rate of 0.047 kg/s, as shown in Figure 2.16. These improvements were 14.8 % and 10.7 % higher

than that of water data for FPSC and U-tube collectors, respectively. The coal, carbon dioxide, and sulfur dioxide generated were 189.99, 556.69, and 2.03 kg, respectively, less than that of using water. The electricity and its cost reduced by using nanofluid were 1546.56 kWh and 540.4 U. S dollar respectively for Germany.

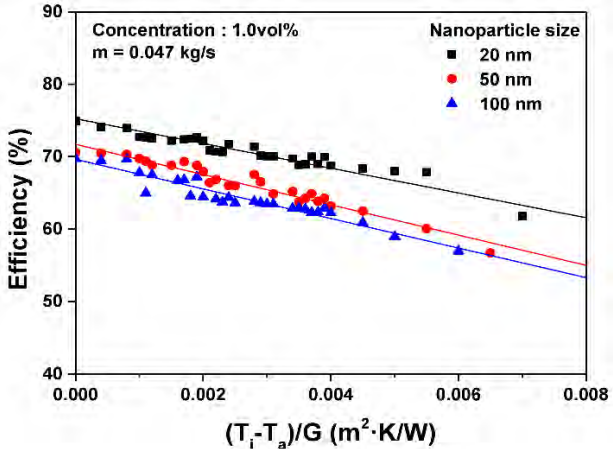

Figure 2.16 Thermal efficiency of flat plate solar collector (W. Kang et al., 2017)

(Stalin, Arjunan, Matheswaran, & Sadanandam, 2019) investigated the efficiency of the FPSC theoretically and experimentally by using CeO_2/H_2O nanofluid. The FPSC area of 2 m^2 and 100 liters per day capacity were fabricated for experimental study. Nanofluid with an average particle size of 25 nm, the volume concentration of 0.01 %, and the flow rate from 1 to 3 l/min was considered to carry out experiments as per ASHRAE standard 93. The efficiency improvement in FPSC by using CeO_2/H_2O nanofluid was 78.2 % at the flow rate of 2 l/min, which is 21.5 % higher than that of water data used at the same flow rate. The same enhancement in the efficiency of FPSC was observed theoretically with an error of $\pm$7.5 %. It was noticed that by increasing the flow rate between 2 to 3 lpm, the collector efficiency was reduced 4.4% due to the thermal properties of the nanofluid. Thus, based on the theoretical and experimental results it was observed that

using CeO_2/water nanofluid the collector area can be reduced by 25.2% as compared to water used as heat transfer liquid.

(L. S. Sundar, Singh, Punnaiah, & Sousa, 2018) fabricated a FPSC test setup of area 2 m² and observed that the thermal performance of FPSC could be enhanced by the passive heat transfer method, and the most effective passive approach is to improve the thermal conductivity of working fluid and its flow rate. Sunder et al. used Al_2O_3/H_2O nanofluid with particle size less than 20 nm and volume concentrations of 0.1% and 0.3%, SDBS used as a surfactant and observed that the nanofluid was stable for six months. Four different flow rates 0.033, 0.05, 0.066, and 0.083 kg/s were considered with twisted tape inserts of twist ratios 5, 10, and 15. The collector's efficiency was increased with the increase in mass flow rate and volume concentrations of nanoparticles. ASHRAE standard 93-86 was used for the experiments. Results showed that the heat transfer of collector enhanced for nanofluids at volume concentrations of 0.1 and 0.3 % at 0.083 kg/s flow rate were 9.4 % and 22 % respectively compared to water data. The heat transfer was further increased 37.73 % and 52.80 % for the volume concentrations of 0.1 and 0.3 % respectively for the collector with twisted tape H/D = 5 as compared to the collector without twisted tape. The maximum friction loss was observed 1.25-times for 0.3 vol. % nanofluid and twisted tape ratio H/D = 5 as compared to water data. Thermal effectiveness was 58 % for the plane collector, and it was increased to 76 % with the use of twisted tape ratio H/D = 5.

(M. Sharafeldin & Gróf, 2018) conducted an experimental study to determine the efficiency curves of FPSC with the use of CeO_2/water nanofluid. The stability of the nanofluid is shallow. In this case, three-volume fractions of 0.0167, 0.0333, and 0.0666 % with three mass flow rates of 0.015, 0.018, and 0.019 kg/s were used to find the

efficiency of FPSC of 2.027 m² area. ASHRAE standard 93-2003 was followed for experiments. Based on the experimental results, it was found that the maximum efficiency of the collector against the reduced temperature parameter was equal to 10.74 % at the nanofluid with a volume fraction of 0.066 % and the mass flow rate of 0.019 kg/s. The change in absorbed energy parameter was between 3.51 % and 10.74 %, and the recorded removal energy parameter was between 30.61 % and 191.8 %. The heat removal factor as a function of mass flow rate is represented in Figure 2.17.

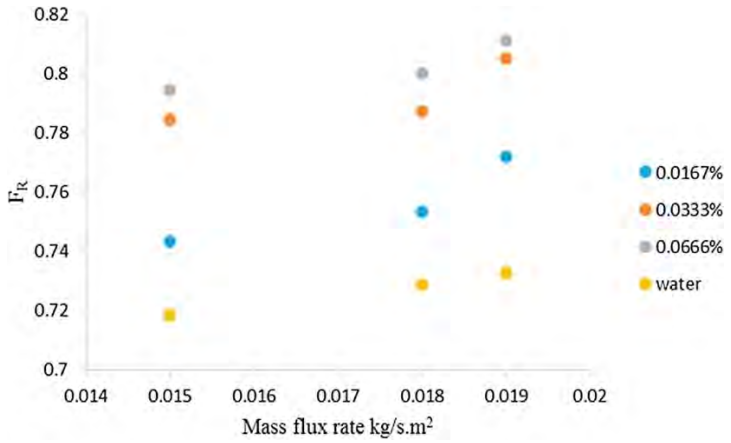

Figure 2.17 Value of heat removal factor as a function of the mass flux rate (M. Sharafeldin & Gróf, 2018)

(Farajzadeh, Movahed, & Hosseini, 2018) studied numerically and experimentally, the thermal performance of FPSC (1.85 m²) using Al_2O_3-water (20 nm 0.1 %), TiO_2-water (15 nm 0.1 %) and their mixture with equal concentration ratio. The nanofluids were prepared in a two-step method using CTAB as a surfactant. ASHRAE standard 93 and open-source Computational Fluid Dynamics (CFD) software were used for experimental and numerical investigations. Different volume flow rates of 1.5, 2.0, and 2.5 l/min were considered. Based on the experimental results it was observed an enhancement of the thermal efficiencies of Al_2O_3-water, TiO_2-water and their mixture at 0.1 wt. % as 19 %, 21 %, and 26 %, respectively, compared to the data of the standard working fluid (water).

The thermal efficiency of the mixture was increased as compared to the single nanofluid, as shown in Figure 2.18. Further increase in the concentration of the mixture from 0.1 wt.% to 0.2 wt.%, the thermal efficiency was enhanced by 5%. Since TiO_2 nanoparticles are expensive than Al_2O_3 nanoparticles, so using of their mixture is more economical with better efficiency.

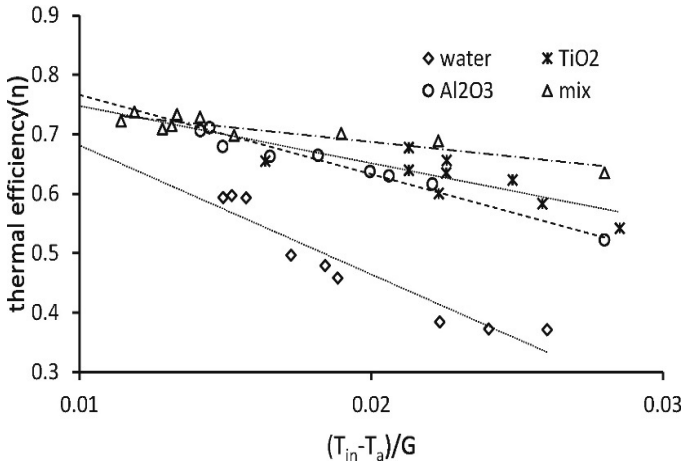

Figure 2.18 Efficiency of a solar collector with an individual and mixture form of nanofluids (Farajzadeh et al., 2018)

(Mirzaei, Hosseini, & Kashkooli, 2018) investigated the effect of Al_2O_3-water (20 nm 0.1 vol.%) nanofluid on the thermal efficiency of 1.51 m² FPSC at different flow rates of 1, 2, and 4 L/min. ASHRAE standard 86-93 were considered for this study. This study was conducted to find the optimum operating condition for Al_2O_3-water and the standard working fluid. Results reveal that adding nanoparticles in base fluid enhanced the thermal efficiency of FPSC. Thermal efficiency also increased with the increase in flow rate, and there is an optimum flow rate at which efficiency was maximum. Optimum flow rate for Al_2O_3-water nanofluid in this study was 2 l/min at which the thermal efficiency was 23.6% as compared to water data, as represented in Figure 2.19. There is no information recorded in this case about the stability of the used nanofluid.

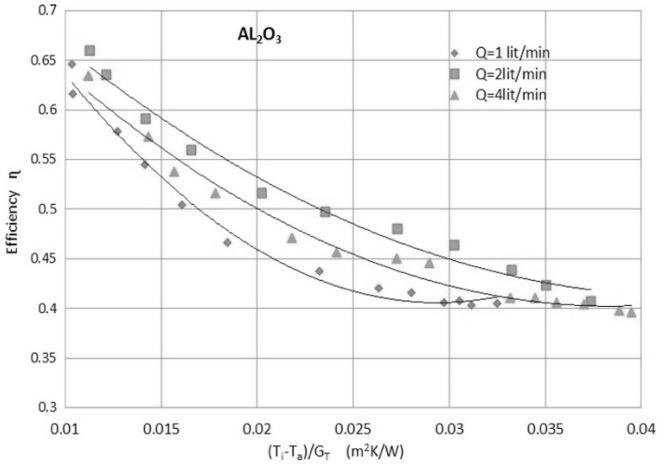

Figure 2.19 Efficiency of nanofluid at different flow rates (Mirzaei et al., 2018)

Some researchers (Alawi, Kamar, Mohammed, Mallah, & Hussein, 2020) utilized the PEG treated graphene which was covalently functionalized as absorbing material in a FPSC. They observed the thermophysical properties of different weight concentrations of nanofluids and used those nanofluids in FPSC. Some authors (Hussein et al., 2020) synthesized the hexagonal boron nitride treated MWCNT and GNPs and used them as working fluid in FPC. They reported 85% increment in efficiency of FPC. A group of researchers (Alawi et al., 2021) investigated the efficiency of solar collector using monolayer graphene and found 13% improvement in efficiency of collector in comparison with DI water.

2.8.2 Theoretical studies on FPSCs using nanofluids

The effect of using (Al_2O_3,TiO_2, CuO and SiO_2) nanoparticles dispersed in water in flat plate solar collector was theoretically analyzed by (Alim et al., 2013). In that study, the main parameters analyzed were exergy destruction, entropy generation, pressure drop, and heat transfer enhancement. Exergy destruction and entropy generation rate were recorded as the functions of nanoparticles volume concentration (1-4%) and flow rates (1- 4 liter/min). It can be realized that the entropy generation drops with the rise in volume

fraction and flow rate. This happened because, with the growth of the heat flux on the absorber plate, the irreversibility turned out as the governing effect. Based on the results, it was concluded that the heat transfer feature improved with the increase in the volume fraction of the nanoparticles. The evaluated friction factor of metal oxide nanofluids was close to that of the base fluid (water). Among all these nanoparticles, the CuO nanofluid reduced the entropy generation by 4.34% and improved the heat transfer coefficient by 22.15% theoretically. Due to the high-volume concentration of nanoparticles, a penalty in pumping power was noticed about 1.58 %.

(Faizal, Saidur, & Mekhilef, 2013) analyzed the effect of different concentrations (0.2 %, 0.4 %) of MWCNT/water nanofluid on the reduction in the size of the FPSC. The analysis was based on (Yousefi et al., 2012b) and (Foster et al., 2009) data. Different flow rates, mass fractions, and surfactants in nanofluid were considered in this study. However, only a single equation 2.36 was used to analyze the decrement in the size of FPSC, where no methodology was presented clearly. The analysis showed that 37 % decrement in the size of the FPSC was possible when MWCNT/H_2O nanofluid was used as compared to water data.

$$A_c = \frac{\dot{m} C_p (T_o - T_i)}{\eta_c \, G_T} \tag{2.38}$$

Furthermore, (Faizal, Saidur, Mekhilef, & Alim, 2013) analyzed the performance of the collector, and obtained a possible reduction in size, cost and embodied energy by utilizing Al_2O_3,TiO_2, CuO and SiO_2 nanoparticles dispersed in the base fluid for synthesizing nanofluid. The flow rates between 1 and 3.8 l/min and the volume fraction of 3 % were considered. Based on the calculations, it was observed that the thermal efficiency of the collector was enhanced by 38.5 % using CuO, while 28.8% for other metal oxides nanoparticles as compared to water for the same concentration. Reduction

in areas of the collector was calculated as 21.5, 21.6, 22.1 and 25.6 %, by using nanofluids of Al_2O_3, SiO_2, TiO_2 and CuO, respectively, as can be seen from Figure 2.20. The reduction in weights for 1000 units, the estimated values are 8618, 8625, 8857 and 10,239 kg for Al_2O_3, SiO_2, TiO_2 and CuO, respectively. The average values for the embodied energy and CO_2 were predicted 220 MJ and 170 kg, respectively. However, the volume concentration used in this study was higher than the previous research conducted by (Faizal, Saidur, & Mekhilef, 2013), where MWCNT/water with low concentration provided higher efficiency and a notable reduction in size.

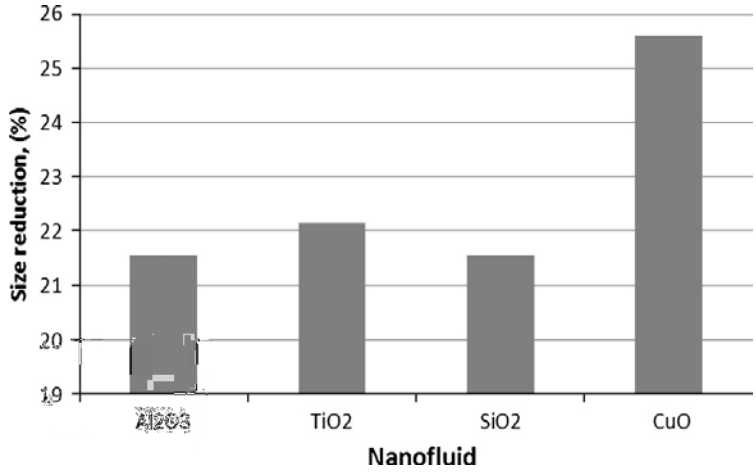

Figure 2.20 Percentage of size reduction of flat plate solar collector by using different nanofluids (Faizal, Saidur, Mekhilef, et al., 2013)

By the employed second law of thermodynamics, the effect of SWCNT, SiO_2, TiO_2 and Al_2O_3 nanofluids on the performance of a 1.51 m² FPSC were analyzed by (Z Said, Saidur, Rahim, & Alim, 2014) and found a similar pattern of performance enhancement. Entropy generation analysis is vital for the operation of a system at higher temperatures. The power output of a system can be increased by minimization of entropy generation; the entropy generation of SWCNT/water nanofluid was minimum compared to that of oxides based nanofluid. Therefore, the exergy output value of the SWCNT/water was

higher than that of the oxide-based nanofluid in the referred investigation. In both cases, the exergy destruction was lower for SWCNT/water nanofluid compared to those of other nanofluids. Furthermore, the heat transfer coefficient, pressure drop, and pumping power of nanofluids in FPSC were numerically investigated. SWCNT/water was selected as the best nanofluid than the metal oxides nanofluids. Results revealed that SWCNT/water reduced entropy generation by 4.34 %, and the enhanced heat transfer coefficient was 15.33% when compared with the water data obtained theoretically. The effect of pumping power and pressure drop were considered negligible as the pumping power penalty of using SWCNT/water in FPSC was found at 1.20%.

(O. Mahian, Kianifar, Sahin, & Wongwises, 2014) analytically analyzed the performance of a mini-channel based FPSC. They used four different nanofluids including Al_2O_3/H_2O, TiO_2/H_2O, Cu/H_2O, and SiO_2/H_2O with particles size 25 nm. The analysis was based on the first and second law of thermodynamics for turbulent flow with a volume concentration of 4% and the mass flow rate from 0.1 to 0.5 kg/s. According to the first law of thermodynamics, the results reveal that Al_2O_3/H_2O nanofluid showed the highest heat transfer coefficient value and the minimum value obtained for SiO_2/H_2O. Entropy generation rate for all the nanofluids used in this study was presented in Figure 2.21, and it was clear from the investigation that nanofluids instead of water lead to a reduction in entropy generation rate.

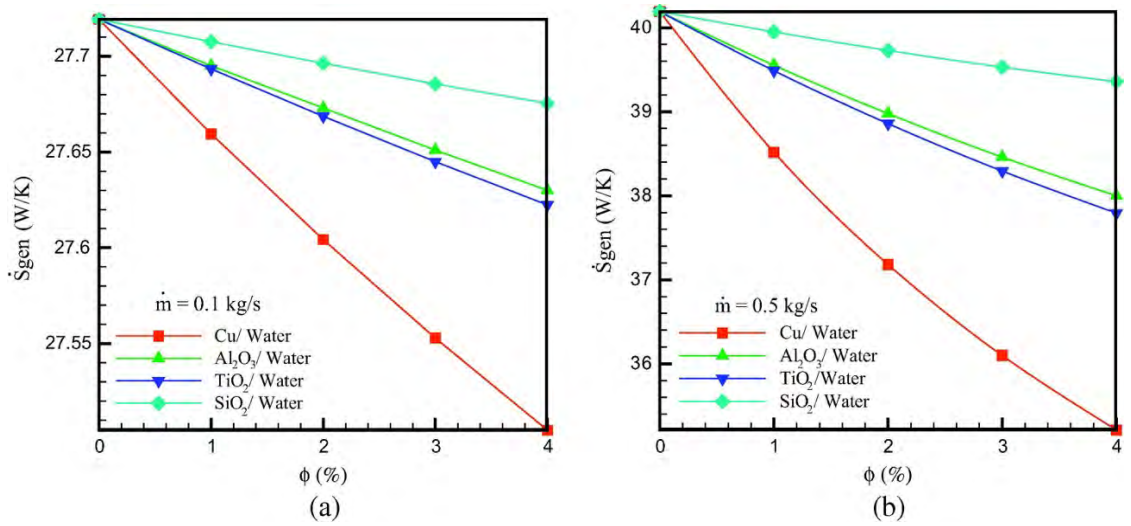

Figure 2.21 Variation of entropy generation rate for different nanofluids with different volume fractions (a) m = 0.1 kg/s (b) m = 0.5 kg/s (O. Mahian et al., 2014)

As the volume concentration of nanofluids was increased, the entropy generation was reduced. Analysis of the second law of thermodynamics revealed that the Cu/H_2O nanofluid produced the lowest entropy generation, it was also noticed that as TiO_2/H_2O nanofluid had less thermal conductivity than Al_2O_3/H_2O but the entropy generation of TiO_2/H_2O was lower than that of Al_2O_3/H_2O. Pressure drop decreased with the increase in volume fraction except SiO_2/H_2O nanofluid as it had low density than other nanofluids.

(Omid Mahian et al., 2015) conducted an analytical study to examine the effect of SiO_2/H_2O nanofluid on FPSC. SiO_2/water nanofluid with pH values of 5.8 and 6.5, and particle sizes of 12 and 16 nm with a volume concentration of 1 % were used to analyze the pressure drop, heat transfer coefficient, and entropy generation in a FPSC. Results showed that the highest heat transfer coefficient and collector efficiency were obtained from the Brinkman theoretical model instead of experimental value, as represented in Figure 2.22. It was also noticed that at 16 nm particle size, the increase in pH value caused a rise in entropy generation. At 12 nm particle size, the increase in pH value had decreased the entropy generation.

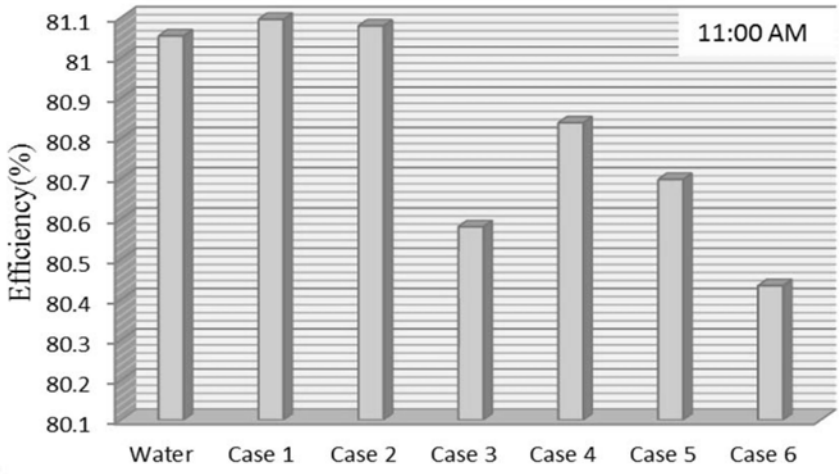

Figure 2.22 Thermal efficiency of solar collector for different case

(Omid Mahian et al., 2015)

(Shojaeizadeh & Veysi, 2016) conducted a study dealing with exergy efficiency optimization for Al_2O_3/H_2O nanofluid in FPSC using mathematical optimization (SQP) method. This study accounts for exergy efficiency optimization for two uncontrollable parameters ambient temperature and solar radiation. Furthermore, two cases were considered for this study, which was an open and closed loop. In open-loop fluid temperature at the inlet of the solar collector was independent of storage tank while in closed-loop, the storage tank was considered. Both cases were operated for the base fluid and Al_2O_3/H_2O nanofluid. The results of this study revealed that the optimum exergy efficiency for the collector inlet temperature, nanoparticles volume concentration, and mass flow rates decreased exponentially with the increase in T_a/G_t Values.

Using the test setup from their previous work Said et al. (2016a, 2016b) investigated the energy and exergy analysis of Al_2O_3/H_2O nanofluid, pH treated nanofluid (Al_2O_3, 13nm) (Z Said, Saidur, Sabiha, Hepbasli, & Rahim, 2016a) and the varying diameters of (13nm, 20nm) nanoparticles (Z Said, Saidur, & Rahim, 2016b) for FPSC. The volume fractions of 0.1% and 0.3% and the mass flow rates of 0.5 to 1.5 kg/min were used for the

investigation. Nanofluids were stable for more than 30 days. ASHRAE standard 93-2003 were used for the experiments. For pH treated Al_2O_3/water nanofluid the energy efficiency of FPSC was enhanced by 83.5% at 0.3 vol. % and 1.5 kg/min flow rate. Whereas exergy efficiency was improved by 20.3% at 0.1 vol. % and 1 kg/min flow rate. It could be noted that the thermal efficiency was 50% higher compared to the available data from the literature for the same nanofluid. For the different diameter sizes (13, 20 nm) of nanoparticles, the energy efficiency for 13 nm nanoparticles was higher than that of 20 nm nanoparticles, as shown in Figure 2.23. Energy efficiency enhanced for 13 nm particles was 73.7% at 0.1 vol. % and 1.5 kg/min.

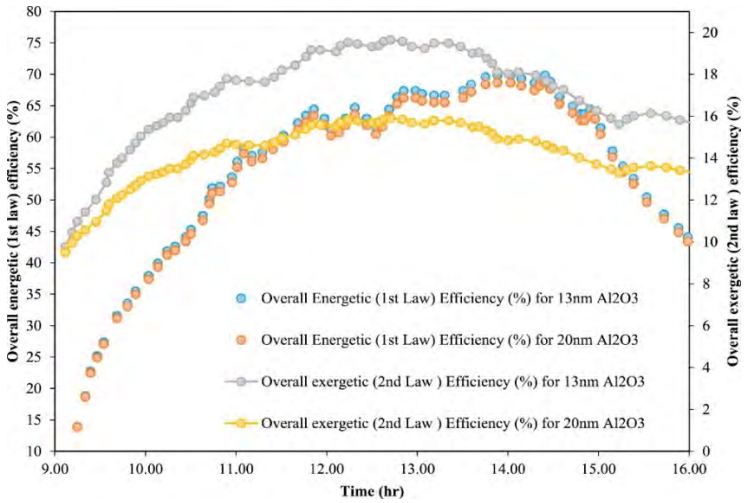

Figure 2.23 Variation in energetic and exergetic efficiencies against the testing period (Z Said et al., 2016b)

(Hajabdollahi & Premnath, 2017) performed thermos-economic modeling for FPSC using Al_2O_3/water nanofluid. They used the Particle Swarm algorithm to carry out the optimization of FPSC's total annual cost (TAC) and efficiency at different design parameters like mass flow rate, the number of the tube, collector length, collector width, insulation thickness, and particles volume concentration were considered for optimization. Al_2O_3/water nanofluid gave higher collector efficiency at a low flow rate.

Based on analysis it was observed that all the design parameters except the number of the tube should be at a lower magnitude for Al_2O_3/water nanofluid based FPSC. The number of the tubes between 5 to 8 with a diameter less than 10 mm were considered best for obtaining higher efficiency of the collectors. Results showed that using Al_2O_3/water nanofluid, the total annual cost can be reduced by 3.5 % along with the increase in efficiency by 2%.

In a numerical study, (M. C. Moghadam, Edalatpour, & Solano, 2017) examined the three-dimensional aluminum/water nanofluid based FPSC at 30° inclination angle by using ANSYS Fluent software. Al_2O_3/water nanofluid with various volume concentrations 0 - 4 % and particles of diameter 25-100 nm were considered. The coefficient of heat transfer from convection to conduction increased with the increase in Reynolds number and decreased with an increase in Richardson number and particle volume fraction. Results showed that the heat transfer coefficient increased between 45 and 58 % when nanofluid was introduced. The simulation also showed that entropy generation promptly rose with the increases in Reynolds number and decreased with the rise in Richardson number and nanofluid concentration. Pressure drop was considerable when Richardson's number was increased, at the particle size of 25 nm. The pressure drop value was lowered; even the Richardson number was considered constant. Compared to the previous literature, the efficiency of FPSC has improved by 2% in that study.

(Hawwash, Rahman, Nada, & Ookawara, 2018) conducted numerically and experimentally the research on the performance of FPSC using Alumina nanofluid. Alumina nanofluid with the surfactant Triton X-100 in the range of 0.1 to 3 vol. % was used for the study. ASHRAE standard and ANSYS 17 were used for the experimental and numerical investigations, respectively. Aluminum/water nanofluid enhanced FPSC's

efficiency by 3 to 18 % at the low to high-temperature differences. Pressure drop increased by 28 Pa, with the increase in volume concentrations from 0.1 to 3 %. The flow rate also affected the FPSC efficiency, and a 5.5 l/min flow rate was considered the best. The thermal efficiency of FPSC increased with the volume concentration, and it increased up to 0.5 %, and after that, a further increase in concentration caused a negative effect on the performance.

2.9 Summary

The updated literature available on the topic indicate that no study had been carried out on solar flat plate collectors using covalently and non-covalently functionalized nanoparticles. Appendix A.1 represents the overview of studies documented on the effectiveness of flat-plate solar collectors using different nanofluids. In the present research nanofluids were synthesized using bio-facial and conventional covalent functionalization method for graphene nanoparticles, in-situ oxidation covalent functionalization method for iron nanoparticle and surfactant treated method for zinc oxide nanoparticles. Sodium hexametaphosphate (SHMP) was used as a surfactant for metal oxides. Stability of nanofluids was checked with UV-vis spectroscopy. The thermophysical properties were evaluated and compared with the available theoretical model. The performance of functionalized carbon and metal oxides-based nanofluids used as working fluids in FPSC was evaluated in this research to assess the synergetic compatibility. The thermal performance of FPSC was evaluated using three different heat flux intensities, i.e., 597,775,988 W/m^2 at the mass flow rate of 0.8,1.2,1.6 kg/min. The inlet fluid temperatures were fixed at 30, 35, 40, 45 and 50°C. All the experiments were performed by using ASHRAE Standard 93-2003 for indoor testing. The inaccuracies of thermal efficiencies were measured in this study from the collected experimental data on a flat plate solar collector using an uncertainty mode.

CHAPTER 3: METHODOLOGY

3.1 Introduction

The current research aims to examine experimentally and numerically the impact of the use of water-dispersible nanomaterials, based on carbon, iron oxide, Zinc oxide, and Silicon dioxide, as working fluid on the efficiency of the flat-plate solar collector. This chapter aims to provide extensive information on the methodology used to meet and achieve the desired objective of this research. It involves comprehensive details on the preparation of nanofluid, characterization, materials, the stability of nanofluids, thermophysical characteristics, experimental configuration, numerical modeling, and test processes.

3.2 Materials

The materials used in this research are mentioned in the following parts. Distilled water in all nanofluids prepared in this research was used as the base liquid.

3.2.1 Nanomaterials

The specification of all nanomaterials used in this study are presented in the following section:

3.2.1.1 Graphene nanoplatelets (GNPs)

The pristine GNPs (supplier: XG Sciences, USA) specific surface area 750 m^2/g, thickness 2 nm, was used in the present study. The detailed specifications of graphene platelets are represented as Table 3.1given below:

Table 3.1 General specification of GNPs

Specification	Description
Supplier	XG Sciences, USA
Appearance	Powder

Colour	Black
Purity	99.5%
Density in bulk form	0.1 to 0.14 g/cm^3
Actual density	2.2 g/cm^3
SSA (Specific surface area)	750 m^2/g
Average thickness	2nm
Average lateral size	< 2nm
Thermal conductivity	3000 W/m. K

3.2.1.2 Iron nanoparticles

Iron nanoparticles were synthesized by using $FeCl_3$ and $FeCl_2$ as parent chloride. In 100 mL deionized water, $FeCl_3$ and $FeCl_2$ with a 1:1.5 molar ratio was dissolved. The solution was applied at a stirring speed of 600 rpm to a final pH 11 with ammonium hydroxide solution (3.0 M) of 5.0 mL /min. In an oxidizing environment, the reaction was performed at 80 °C and stirred for another 90 minutes. The magnetic decantation was used to separate the resulting black precipitation. Deionized water and ethanol used to rinse the precipitation. Finally, it was freeze-dried.

3.2.1.3 Silicon dioxide (SiO_2) and Zinc Oxide (ZnO) nanoparticles

Silicon dioxide (SiO_2) nanopowder was obtained from Sigma-Aldrich Co., Selangor, Malaysia, with an assay of 99.5 % and particle sizes ranging from 10 to 20 nm. SiO_2 nanofluids were prepared through dispersion in the base fluid. Distilled water was used as a base fluid for SiO_2 nanofluid preparation. The nanofluids of specific SiO_2 nanoparticles and the base fluids are formed by an ultrasonic agitator. Throughout the preparation process, no surfactant was added. In this case, the stable suspension was obtained after 30 minutes of intense sonication.

Zinc oxide is a spherical nanopowder with an assay of 97%, was purchased from Sigma-Aldrich Co., Selangor, Malaysia, and its particle size was less than 50 nm. Within a few

minutes, the ZnO nanoparticles sediment because of the insolubility of zinc oxide between water and particle dissipation. Therefore, surfactant (non-covalent) is used for the aqueous dispersion of ZnO nanoparticles. The stability of ZnO nanofluids is enhanced with sodium hexametaphosphate (SHMP) surfactant. SHMP was obtained from Sigma-Aldrich Co. of Selangor, Malaysia, with a purity of 96%. After a 60-minutes sonication cycle, the stable suspensions were brought in line with ZnO weight concentrations (wt.%). As seen in our sedimentation experiments, the most stable suspension in the weight percentage is 1:10 (SHMP: ZnO).

3.2.2 Chemicals

In the present study, different chemicals used to perform the covalent functionalization of pure nanoparticles to convert them from hydrophobic to hydrophilic behavior. The analytical grade chemicals used are $FeCl_3 \cdot 6H_2O$ (Iron (III) chloride, purity based on Trace Metals Analysis ≥ 99.998%), $FeCl_2 \cdot 4H_2O$ (Iron (II) chloride, purity based on Trace Metals Analysis ≥ 99.99%), Polyethylene glycol 200 (PEG), Ammonia (NH_3) (Purity ≥ 99.99%), Sulfuric acid (H_2SO_4), hydrogen peroxide (H_2O_2) and Nitric acid (HNO_3). All these chemicals are purchased from Sigma Aldrich Co., Selangor. Malaysia.

3.3 Nanofluid preparation

In this study, a two-step method was used to prepare all nanofluids, which were chosen based on the equipment available in the laboratory at the University of Malaya. An ultrasonication prob purchased from Sonics & Materials, Inc., USA (with a specification of 750W output power and 20 kHz frequency of power supply) and used to disperse the nanoparticles in the base fluid (distilled water). The temperature of the sample increased drastically during the sonification phase, and this increased temperature caused the water

evaporation from the sample, which later changed the weight concentration of the sample. Thus, to maintain an adequate temperature, a water bath was used.

3.4 Functionalization of nanomaterials

It is essential to improve the long-term stability of the nanomaterial in base fluids by covalent or non-covalent functionalization. The functionalization processes conducted in this research are summarized in two parts.

3.4.1 Covalent Functionalization

The covalent functionalization process that was implemented in this study for the different nanomaterials is described in the subsequent sections.

3.4.1.1 Eco-friendly Covalent functionalization of GNPs

An eco-friendly method for covalent functionalization of graphene nanoplatelets to enhance its suspension with dried clove buds for polar solvents is applied in this research. In this process, hydrogen peroxide and ascorbic acid, β-caryophyllene, eugenyl acetate, and eugenol (i.e., primary ingredients of cloves) (Parthasarathy, Chempakam, & Zachariah, 2008) are attached into GNPs. Hydrogen peroxide is a free radical oxidizer that creates non-toxic by-products with no chemical trace, and Ascorbic acid is the redox initiator. This method involves two phases: The first one is clove extract preparation, and the second one is functional operation. The clove extract in Figure 3.1 is illustrated. First, in 1000 ml of pre-heated (80 °C) distilled water (DI), 15 g of ground cloves added. Subsequently, homogenized the solution at 1200 rpm agitation rate and heated it for 30 minutes at 80 °C. The clove extract was eventually purified by a membrane of 45 μm polytetrafluoroethylene (PTFE).

The functionalization process was performed as: First, in one beaker, filled with 1000 ml of clove extract and 5 g pure GNPs poured into it. To get the homogeneous black suspension of GNPs, the mixture was stirred for 15 min. Then, 25 ml hydrogen peroxide has been inserted in the response mixture drop by drop during the whole time of the sonication. The reaction mixture has been ultra-sonicated for 10 minutes and then heated to 80 °C for 14 hours in reflux. At 14,000 rpm, the resultants were centrifuged, and the suspension constantly washed with a substantial quantity of distilled water until we got a neutral pH value. After that, we dried the sample in a vacuum oven with a temperature of 60 °C for day after day. Our clove treated GNPs are very stable, as anticipated, in an aqueous medium. The CGNP-water nanofluids were then synthesized as follows. DI water was used as our basic fluid in this research. An ultrasonication time of 10 min was selected for good dispersion of CGNP in DI water. CGNP-water nanofluids with four different concentrations i.e. 0.025, 0.050, 0.075, and 0.1 wt.% were prepared for further study.

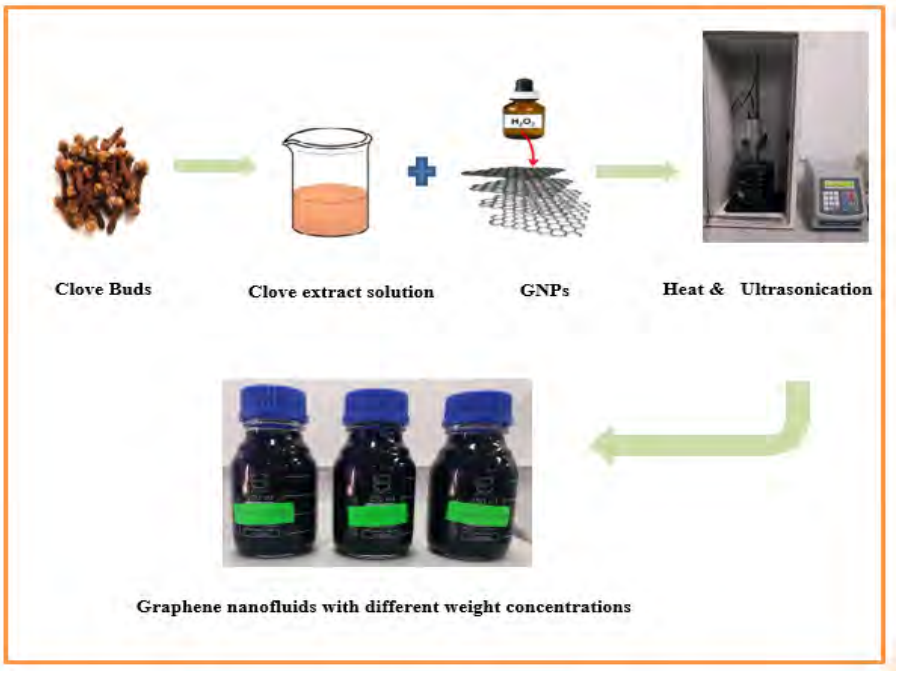

Figure 3.1 Preparation of clove treated GNPs (CGNPs)

3.4.1.2 Conventional (acid treated) covalent funtionalization of GNPs

Acidic treatment was done to introduce the carboxyl and hydroxyl group on the surface of GNPs (750 m2/g). Make a 1:3 solution of HNO_3 and H_2SO_4 in the first step. Add 5 g GNPs (750 m^2/g) in the strong acid solution and put the final product under bath sonication for 3hrs at plus rate 3s ON 2s OFF. The suspension solution is then pouring on the Teflon reaction vessel and put it into the industrial microwave for 15 min under 700W and 90^oC (Milestone MicroSYNTH programmable microwave system). The final suspension is then cool down at room temperature and filtered through 45 μm polytetrafluoroethylene membrane, washed several times with DI water to attained neutral pH values. The resultant sample is then dry overnight at 40^oC in a vacuum oven (Yarmand, Gharehkhani, Shirazi, Amiri, Alehashem, Dahari, Kazi, et al., 2016).

3.4.1.3 Covalent functionalization of Fe_3O_4

The synthesis of PEG-Fe_3O_4 nanoparticles was carried out by using the in-situ functionalization method. $FeCl_3$ and $FeCl_2$ were used as parent chloride. In 100 mL deionized water, $FeCl_3$ and $FeCl_2$ with a 1:1.5 molar ratio was dissolved, followed by the addition of 50 mL PEG. The solution was applied at a stirring speed of 600 rpm to a final pH 11 with ammonium hydroxide solution (3.0 M) of 5.0 mL/min. In an oxidizing environment, the reaction was performed at 80 °C and stirred for another 90 minutes. The magnetic decantation was used to separate the resulting black precipitation. Deionized water and ethanol used to rinse the precipitation. Finally, it was freeze-dried

The covalent functionalized Fe_3O_4 nanoparticles were characterized chemically and morphologically to investigate the degree of functionalization. Four different weight concentrations as presented above, were prepared for further investigation. Colloidal stability and thermophysical characteristics of the synthesized water-based Fe_3O_4-PEG nanofluids were carefully explored and reported.

3.5 Characterization

Various techniques include Fourier transform infrared spectroscopy (FTIR), energy-dispersive X-ray spectroscopy (EDS), Transmission Electron Microscopy (TEM), and the average partition size measurement was used to characterize the distinct nanomaterials and nanofluids produced in this research.

TEM is a handy tool to characterize the scattering, shape, and size of the nanomaterials. However, due to the use of dried samples in this method of characterization, the actual state of the nanomaterials in the nanofluid cannot be obtained (Ghadimi et al., 2011). In this method for microscopy, an ultra-thin specimen is used and interacts with a beam of electrons at it permits through it. The image formed from the contact is enlarged and focused onto an imaging device. In this study, two TEM devices were used: a high contrast/high-resolution digital TEM form Hitachi (HT7700) with an accelerating voltage of 120 kV and an LEO 912 AB electron microscope with an accelerating voltage of 100 kV. For preparing the specimen for TEM, a drop of dilute nanofluid with a ratio of (1:40) was placed onto a lacey carbon grid and oven-dried at 45 °C overnight.

FTIR is a method in which an infrared spectrum of absorption or emission can be obtained for a liquid, solid, or gas. In FTIR, when the infrared radiation permits through a sample, some is transmitted, and the sample absorbs the other. The spectrum obtained from this test represents the absorption and transmission of molecules, and thus generating a unique fingerprint for the molecules in the sample (Thermo, 2001). In this study, Bruker (IFS 66/S) was used for characterization with FTIR.

Energy-dispersive X-ray spectroscopy (EDS) is the process used for the elemental analysis or chemical characterization based on the interaction of a sample with a source of X-ray excitation. This characterization is based on the fundamental theory that every

element's distinctive atomic structure is unique in terms of its peak in the range of the X-ray emission spectrum (Goldstein et al., 2003). In this research, desktop scanning electron microscopes EDS was used (Phenom ProX, Netherlands).

3.6 Measurement devices

The two parts below are outlined the equipment used in stability assessment and measurement of the thermophysical properties.

3.6.1 Nanofluid stability

Long-term stability is important for the efficient use of nanofluids as operational fluids in heat transfer applications. Two techniques have been employed to evaluate the colloidal stability of water-based nanofluids synthesized in this study: UV–vis spectral analysis and zeta potential.

UV-vis spectroscopy can be used to calculate the quantitative characterization of the colloidal stability utilizing the concept of light absorption calculation of the suspension. Shimadzu UV-spectrometer was used in the 190-1100 nm range of wavelengths in the present study (UV-1800, Shimadzu Corporation, Kyoto, Japan). The light absorption data in all the samples were evaluated for a period of (60 days) using unique quartz cuvettes suited for the UV region at certain distinct intervals. All specimens were water-diluted with a 1:20 proportion to allow the correct propagation of light.(A Ghadimi, R Saidur, & HSC Metselaar, 2011a; Harish et al., 2012; Nanda et al., 2008; Vandsburger, 2009; W. Yu et al., 2010). In order to check the device's accuracy, every read of absorbance was replicated twice, where the peak gaps of 0.08% were noted.

The zeta potential measurement of a nanofluid is a process used by scientists to measure stability by assessing the degree of repulsion between the nearer particles of the

same charge (Lee et al., 2008; Vandsburger, 2009; H. Zhu et al., 2007). The zeta potential of the dilute nanofluids that were produced was evaluated with Zeta-sizer Nano ZS using the concept of electrophoretic light dispersion (ELS) (Malvern Instruments Ltd, Malvern, UK).

3.6.2 Thermophysical properties

In this section, measurement devices for thermophysical properties are presented, which was used in the present study.

3.6.2.1 Thermal conductivity

Approximately 5% accurate KD2 Pro (Decagon Geräte, Inc., USA) Thermal Properties analyzer was utilized to measure the thermal conductivity of the nanofluids synthesized in this study. KS-1 prob with diameter 1.3 mm and length 60 mm used as a needle sensor, and its working principle is based on the transient hot-wire method. Aligning the probe in the middle of the sample vial was the primary issue with low error measurement. Due to the dark colour of carbon nanostructures based nanofluid, this issue is more severe, which makes it hard to be visually aligned. A modified sample holder is therefore designed and constructed to guarantee the best alignment of the samples inside the vial without frequent alignment checking. The holder comprises two Teflon parts which are connected to the bottom part with the help of three nuts and bolts. The bottom portion of Teflon is linked to the sample vial by a thread, while the KD2 Pro is tucked between both parts of Teflon. During the readings, two water baths were used to maintain the samples at the required temperature. The "Wise Circu WCR-P6" (Daihan Scientific Co., Ltd, Korea) refrigerated bath circulator was used at or below 35 °C with 0.1 °C and 1.4 kW precision. Whereas, during a heating bath, "Lab. Cw-05 G Companion" (Jeiotech Co., Ltd., Seoul, Korea) has been used to achieve higher temperatures with a precision of

0.1 ° C and 1.04 kW. After the vial has been filled with the sample and the probe fixed with the modified holder, the vial has been positioned within a water bath for approximately 30 minutes prior to the measurement process in order to allow sample and needle temperatures to match the water bath temperature. Over 12 readings with a span of fifteen minutes between consecutive readings were taken at each measuring stage to enable the temperature of the sample to balance. Readings with errors less than 0.01 were taken into consideration, and average thermal conductivity was calculated of eight readings with the lowest error in the sample at each point.

3.6.2.2 Dynamic viscosity

The viscosity of any prepared nanofluid is an essential factor in determining the suitability as a heat transfer fluid because of its direct effect on pumping power and pressure drop. An Anton Paar rotation rheometer (Anton Paar GmbH, Physica MCR 301) was used to measure the viscosity of prepared nanofluid in this study. For testing at different temperatures, shear rates of 20-200 1/s were used.

3.6.2.3 Density

The density of prepared nanofluids was evaluated using a density meter Mettler Toledo (DM40) at different temperature and weight concentrations. The measurement range for this device is 0.0-3.0 $g/cm^{3,}$ with an accuracy of 0.1 mg/cm^3. The principle of measurement for this density meter is based on measuring the period of oscillation of a U-shaped glass tube containing the sample by a sensor. An electromagnetic transmitter induces the oscillations with a magnet attached to the U-shaped tube. Using a particular relation, the oscillation duration can be computed for the density. For individual samples, the measurement of density at each temperature was repeated three times, and the average value of them was considered as the density of the sample at this temperature.

3.6.2.4 Specific heat

The specific heat (Cp) is an intensive property of a substance and defined as “The energy required to raise the temperature of a unit mass of a substance by one degree” (Çengel, 2003). The differential calorimetry scanning (DSC) was used to measure the specific heat through a thermal analysis process that controls the difference between the heat flow supplied to the reference and the sample as a function of temperature. In this study, the specific heat of nanofluid prepared was evaluated by using (DSC-Q2000, TA Instruments) at distinct weight concentrations and temperatures.

3.7 Experimental test setup

Figure 3.2 presents the experimental setup for the thermal performance of the FPSC based on nanofluid used in this study. The main parts of the experimental setup are refrigerated water bath, flow loop, measurements and control devices, data logger, and flat-plate collector. The operational fluid in the forced convection system was circulated through an electric centrifugal pump. The test configuration was described in two parts, namely the flow circuit and the FPSC section.

3.7.1 Flat-plate solar collector section

Figure 3.3 represents that the materials used in the FPSC section are aluminum stand with T-slotted structure, sheet frame of polypropylene (PP), copper absorber plate of 2-mm thickness, riser, and header tubes (copper), glazing (glass), insulation, and base with adjustable angle. Table 3.2 represents the comprehensive specs of the FPSC used in this study. A ratio of Tin (Sn)/Silver (Ag) alloy (96.5/3.5) was used on both sides of each pipe to solder the copper absorber plate straight to the riser tubes. The choice of the copper absorber plate 2 mm rather than 1 mm thick for the dimension of 91.44 × 50.8 cm ensured that after implementation of the heat needed for soldering between the copper absorber

plate and riser pipes, the plate remains flat without corrugations. During the installation of a flexible adhesive heater, it is important to consider the flatness of the copper absorber plate for uniform distribution of heat flux along the surface (Figure 3.4). The insulation material used in this study was Isowool ceramic fiber, and it had 0.07 W/m K thermal conductivity at 400 °C. There are four copper risers 12.7-mm parallel attached with 22.2-mm copper header pipes on both ends. Digital AC-clamping-meters of Kyoritsu (model Kew Snap 2017) has been used to evaluate the alternating current and voltage values of the electric heater.

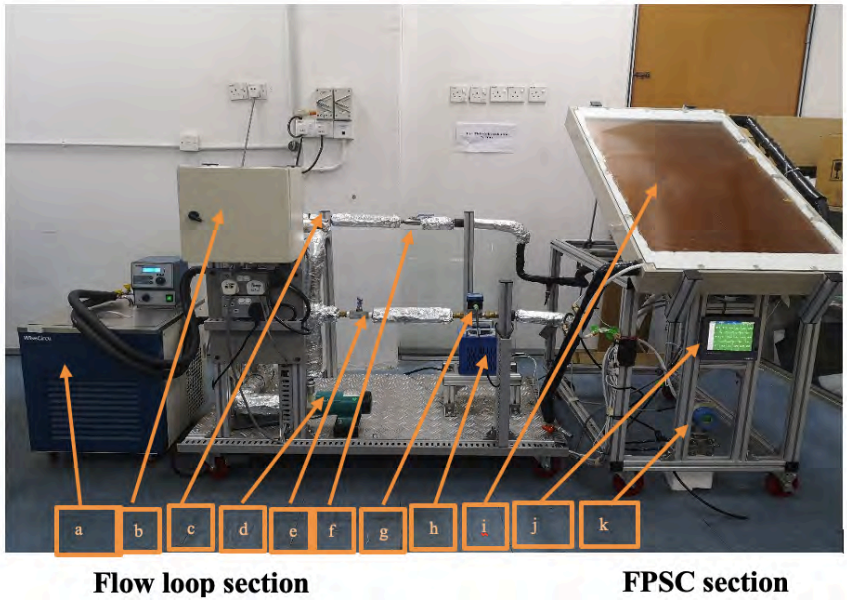

Figure 3.2 Photograph of experimental setup utilized in the present study, the parts of the setup are numbered as ; (a) Refrigerated bath, (b) Electricity control box, (c) Bypass valve, (d) Centrifugal pump, (e) Flowline valve, (f) Ball valve, (g) Flow meter, (h) Transformer (i) FPSC, (j) Data logger, (k) Pressure transducer.

The adhesive heater used to produce continuous heat flux similar to the solar radiation comprises six distinct 30.48 × 25.4 cm flexible insulated heaters, which are attached to a transformer of varying voltage. The heaters have been fitted with an adhesive layer, which

is pressure sensitive and provided by Omega USA (KH-1012/(2.5)-P). The thickness of the individual heater is about 0.14 mm and composed of an etched foil of approximately 0.015-mm thick, covered by two 0.05-mm Kapton Polyimide film and a single layer of fluorinated ethylene propylene with 0.025-mm thickness. Each heater has a total wattage of 300 W at 115 V and 0.39 W / cm^2 (2.5 W / in^2) watt density. The heater wattage, which presently used remains the minimum available on Omega's list; it is significantly higher than the necessary wattage density for this work. In addition, 115V is the highest voltage available of such type of heater, the voltage available in Malaysia is 230 V which is not compatible with available heater. Therefore, the heaters are attached through parallel and series so that the final wattage density reduced and working voltage increased. The last heater becomes with a maximum wattage of 800 W at 230 V. The production specifications showed that the measuring accuracy of the clamp meter for voltage and current is 1% and 1.5%, respectively. This study was carried out with T-type self-adhesive surface thermocouples (SA1 XL-T-72) with 2 m long cable insulated with fiberglass and imported from Omega, USA, these thermocouples were used to measure surface temperatures of riser tube and absorber plate. Four different axial spots, i.e., 11.4, 34.3, 57.2, 80.1 cm of two riser tubes, an absorber plate, were selected for the installation of 12 calibrated T-Type thermocouples.

Furthermore, to record the bulk temperature of the fluid flowing at the inlet and outlet pipe of the FPSC, two calibrated resistance (RTD-Type PT100) temperature sensors were mounted using copper tees and the compress fitting. The supplier data are indicating that the tolerances of RTDs and T-type thermocouples were (0.15 + 0.002* |T|) and 0.75% °C, respectively, for the temperature range used in experiments. Moreover, an adjustable 0 – 60 ° angle base was used to regulate the FPSC tilt angle, in the present study, the angle was fixed at 30 °.

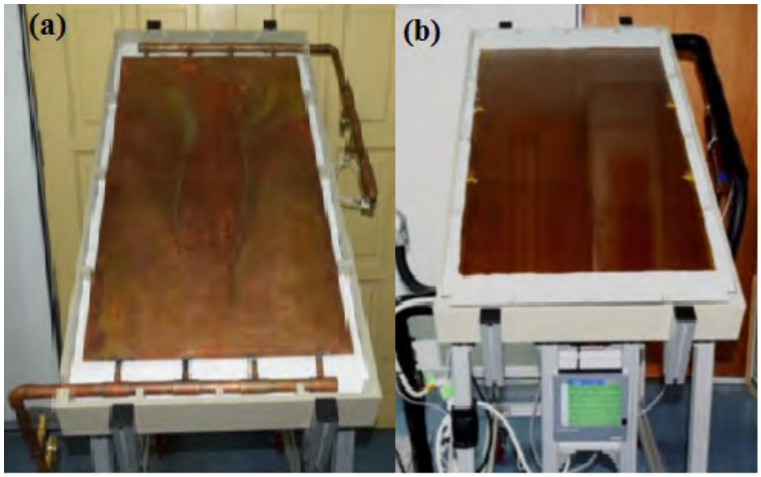

Figure 3.3 (a) During the fabrication phase of FPSC (b), the final look of FPSC after installation of the data logger, surface heater, insulation, glass cover, and thermocouple.

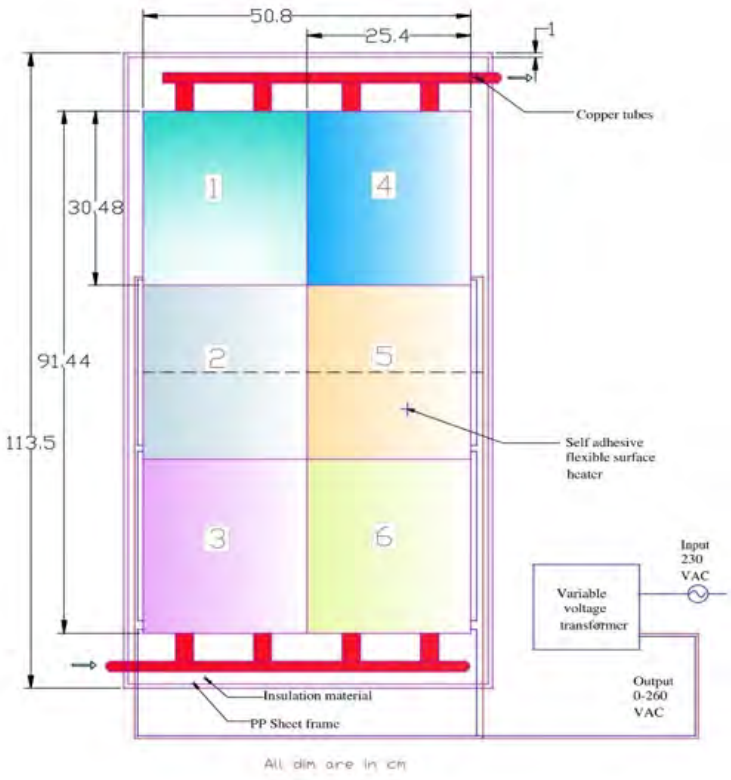

Figure 3.4 Absorber plate with electric heater configuration, variable voltage transformer, and wiring diagram.

An eighteen-channel data logger (EC18) was used to connect the DPT, RTD, flow meter, and all thermocouples and record the experimental data. Six universal cards were used in this data logger, and each card contains three channels. A half-inch silicon hose is used to connect the flow loop section to FPSC. As the diameter of the silicon hose is smaller than the header tube, the customized tapered cone made of copper is used for both headers to reduce the disturbance inflow. The pressure drop along the FPSC was measured by using differential pressure transmitter (DPT), the model used in this study is ADP9000-D5 imported from ALIA Group Inc. with the capacity of 0- 0.16 kPa and connected at inlet and outlet through tapping points (Figure 3.5). To minimize the fluid hammer effect, two pressure snubbers were introduced at both sides of DPT.

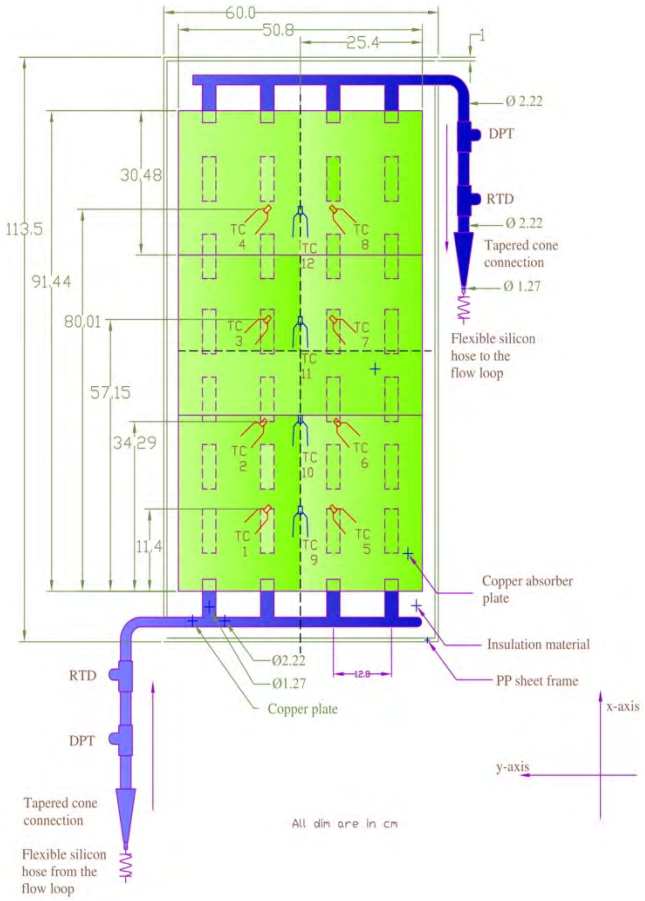

Figure 3.5 Schematic diagram of the flat-plate solar collector used in this study

Table 3.2 The detailed description of components and devices used for the fabrication of FPSC.

Name of component	Supplier/Material	Model/Capacity/Dimension	Units	No. of items
Stand for FPSC	Aluminum profile T-slotted structure	Profile 40 × 40	mm	1
Frame	PP sheet	Thickness (10)	mm	1
Absorber plate	Copper	L × W = 914.4 × 508 Thickness = 2		1
A compact insulated heater with pressurized adhesive	Kapton polyimide film isolation engraved foil feature	L × W = 30.48 × 25.4 Thickness = 0.14 Watt density = 0.39 Total Watt = 300	cm mm W/cm^2 W	6
Header	Copper	Thickness = 1.3 Length = 600 Outer dia. = 22.2	mm mm mm	2
Riser	Copper	Thickness = 1.1 Length = 1020 Outer dia. = 12.7 Spacing = 128	mm mm mm mm	4
Insulation	Ceramic fiber blanket	Side thickness = 30 Back thickness = 50	mm mm	-
Glazing	Glass	Thickness = 5	mm	1
Gap from the surface of glass to the absorbers	-	20	mm	-
T-type thermocouples	Omega SA1 XL with fiberglass insulated wires	Length of wire = 2	m	12
Wet/wet low DPT	ALIA Group	ADP9000-D5 (0-0.16)	kPa	1
Data logger	ECO LOG	EC18	-	1
Clamp meter for alternating current measurement	Kyoritsu	Kew Snap 2017	-	1
Tapered Cone	Copper	-	Custom machined	2
Tee (1/2″)	Copper	-	-	4

3.7.2 Flow loop section for FPSC

The flow loop parts are described in Figure 3.6 and includes electrical control box, refrigerated water bath, needle valves, ball valve, digital flow meter, thermally insulated stainless steel tubes, mechanical stirrer, tank with thermally insulated, and a centrifugal pump operated with electrically. Table 3.3 provides detailed specifications for the components used in this section. An electric centrifugal pump (Araki model EX-30R (M)) with a head and a maximum flow rate of 3.8 m, 32 l / min, respectively, have been used in the present study. To store the working fluid, a thermally insulated stainless steel jacketed tank with eight litter capacity was used. Moreover, in order to maintain the inlet temperature of FPSC, this tank behaves like a heat exchanger with a refrigerated bath. "WiseCircu WCR-P22" (Daihan Scientific Co., Ltd., Korea) was attached with an insulated jacketed tank and used as a refrigerated bath circulator to absorb the heat coming from FPSC and maintained the inlet temperature of FPSC section. The maximum capacity and accuracy of the refrigerated bath is 3.4 kW and 0.1°C, respectively. To improve the concentration of liquid within the storage tank and to improve heat exchange between cooler water circulating in the jacket and bulk operational liquid inside the storage tank, an overhead mechanical stirrer (model IKA RW 20 digital) was attached to the jacketed reservoir.

A needle valve with valve flow coefficient (C_v) 0.35 was mounted on the liquid flow line before the flow meter to ensure a reliable flow rate. After the pump, the diameter circuit was fitted with a needle valve with a larger C_v of 1.05 to achieve the minimum required flow rate of 0.6 kg/min by reduced the pump load. The flow rate of working fluid was measured by using a digital flow rate transmitter (Model SE32 PV, Burkert) and installed at the discharge line of the pump. A return flow line from the FPSC to a storage tank, a ball valve was introduced for the cleaning purpose of the line and removal of the air from

DPT. Two RTDs were used to measure the temperature of the bulk working fluid inside the jacketed tank and cooler inside the jacket and connected to the data logger.

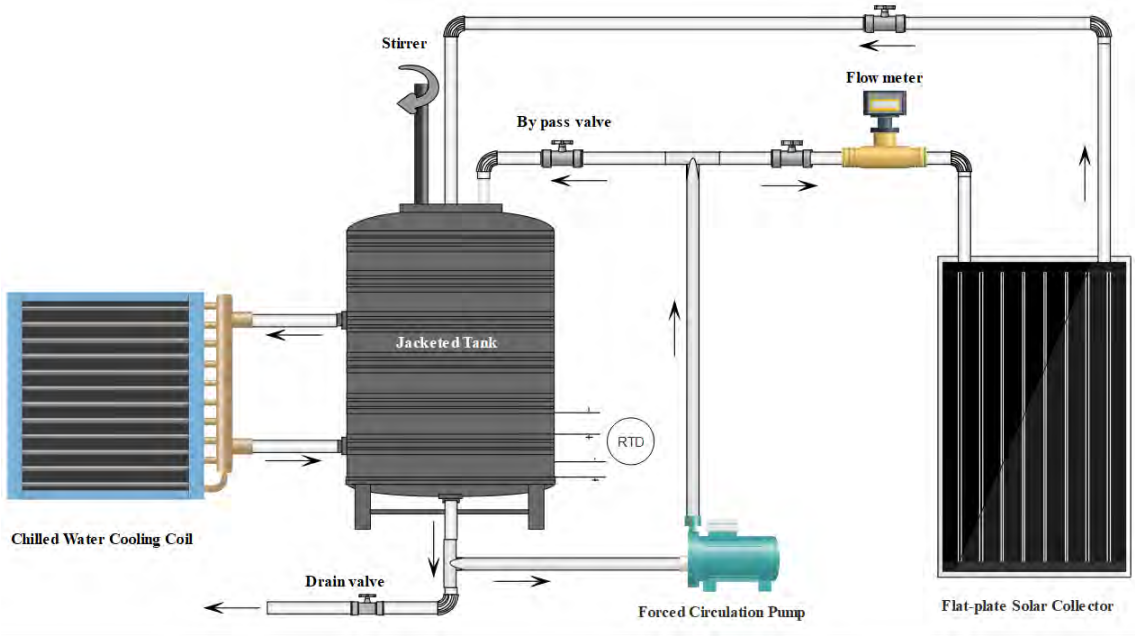

Figure 3.6 Schematic diagram of the flow loop section

Table 3.3 The detail description of components and devices used for the fabrication of flow loop section

Name of component	Supplier-Model	Category	Dimension/Units	No. of items
Pump	Araki (EX-30R)	Centrifugal magnetic driven	Speed = 2800 rpm Head = 3.8 m Flow rate = 32 L/min Operating voltage = 230V-50 Hz	1
Insulated tank	Locally made (Grade 316)	Stainless steel	Capacity = 8 L Height = 26 cm ID = 19.8 cm OD = 27.4 cm	1
Stirrer	IKA (RW 20 digital)	Overhead	72 W 220-240 V 50/60 Hz	1
Flowline valve	Parker (HNVS8FF)	316 stainless steel needle valves	Orifice = 4 mm Cv = 0.35 0.5-inch NPT (female)	1
Bypass line valve	Parker (8F-V12LN-B)	Brass material Needle valve	0.5-inch NPT (female) Orifice = 7.9 mm Cv = 1.05	1
Flow meter	Burkert (SE32PV)	Inline paddle wheel transmitter with display	0 – 8 L/min	1

Transformer	QPS (VT2-1)	Variable voltage	Input = 230 V Output = 0-260 V Capacity = 10A	1
Pipeline	Grade 316	Stainless steel	ID = 10.21 mm OD = 12.7 mm	-
Refrigerated water bath circulator	Daihan, Korea (WiseCircu WCR-P22)	Refrigerated	3.4 kW	1
Resistance temperature detector	Class A 3-wire	PT100	85 mm long sensor	2

3.8 Mathematical modeling and simulation implementation

Present study is based on Duffie & Beckman's HW model (2013), and some changes are made in the mathematical model for simulation of a FPSC's thermal efficiency by utilizing nanofluids for its operational fluids. In order to simplify the problem without impacting fundamental principles, the model is developed under certain assumptions. The following physical assumptions were taken:

1. FPSC has a uniform mass flow rate in all header and riser tubes, so the system work under steady-state condition.
2. The thermal transmission is perpendicular to the flow direction in one-dimensional layers, except for the heat which the flow takes.
3. Two edge-side insulation is regarded as perfect, so it is adiabatic. The heat flow is single-dimensional through the back.
4. At the front and behind of FPSC, the environmental temperature is the same.
5. The temperature is uniform around the raising tube wall.
6. Thermal-physical fluid characteristics depend on the temperature.
7. The used nanofluids are dispersed well and are very colloidally stable.
8. Nanofluid is treated as a single fluid phase.

Considering the assumptions mentioned above, dynamic CFD simulation of the temperature and the flow activity of various working fluids with various types of concentrations in FPSC was performed in ANSYS 16.1. Figure 3.7 represents the flowchart of the modeling. It concludes with the analysis of the efficiency of the flat solar collector under various conditions.

The total heat loss coefficient should be measured in a flat plate solar collector for measuring the overall heat loss, including the top, edge, and bottom heat loss coefficients.

$$U_L = U_t + U_b + U_e \tag{3.1}$$

To calculate the top heat loss coefficient (U_t) first, calculate the mean absorber plate temperature (T_{ap}) and then use the analytical equation of Klein (1379) as represented in equation 2.5 (Duffie & Beckman, 2013). The thermal conduction loss from the absorber plate to the atmosphere can be explained by the law of Fourier concerning the bottom heat loss coefficient (U_b).

$$Q_b = K_{ins,b} A_c \frac{(T_{ap} - T_a)}{thk_{ins,b}} = U_b A_c (T_{ap} - T_a) \tag{3.2}$$

$$\Longrightarrow U_b = \frac{K_{ins,b}}{thk_{ins,b}} \tag{3.3}$$

Where $K_{ins,b}$ is the thermal conductivity of bottom insulation and $thk_{ins,b}$ is the width of the insulation at the bottommost. In the same way, the FPSC's edge heat loss to the environment also occurs as:

$$Q_e = K_{ins,e} A_e \frac{(T_{ap} - T_a)}{thk_{ins,e}} \tag{3.4}$$

The equation (3.4) is revised because all heat loss parameters apply to the same field as the collector Area (A_c).

$$Q_e = \frac{K_{ins,e}A_e}{A_c}A_c\frac{(T_{ap}-T_a)}{thk_{ins,e}} = U_eA_c(T_{ap}-T_a) \quad (3.5)$$

$$\Longrightarrow U_e = \frac{K_{ins,e}A_e}{thk_{ins,b}A_c} \quad (3.6)$$

Where $K_{ins,e}$is the thermal conductivity of edge insulation and $thk_{ins,b}$is edge insulation thickness, A_e and A_c are edge area and collector area, respectively.

In the experimental set-up of this analysis, the FPSC's absorber plate is in contacted with four riser tubes. Just one tube has been considered in the mathematical model as all tubes work under parallel channel conditions, given the fluid flows uniformly through each upright tube of the collector. A range from the external diameter(d_o) of the rise tube to the centerline between the two rise tubes is known as a fin with a length [(W-d_o)/2]. The energy balance represented in Figure 3.8c will provide the following equation according to the first law of thermodynamics, which takes into account an aspect in that narrow width (Δy), an element length in the direction of flow, and a temperature (T_y):

$$S\Delta y - U_L\Delta y(T_y - T_a) + \left(-K_{ap}t_{ap}\frac{dT}{dy}\right)\Big|_y - \left(-K_{ap}t_{ap}\frac{dT}{dy}\right)\Big|_{y+\Delta y} = 0 \quad (3.7)$$

As (Δy) comes close to zero, it follows that the limit of the previous equation is:

$$\because \lim_{\Delta y\to 0}\frac{\frac{dT}{dy}\Big|_{y+\Delta y} - \frac{dT}{dy}\Big|_y}{\Delta y} = \frac{d^2T}{dy^2} \quad (3.8)$$

$$\therefore \frac{d^2T}{dy^2} = \frac{U_L}{K_{ap}t_{ap}}\left(T_y - T_a - \frac{S}{U_L}\right) \quad (3.9)$$

To solve the equation (3.9), which is the second-order differential equation: two boundary conditions (B.C.) should be given. The following two boundary conditions are introducing in the above equation.

$$B.C.1: \left.\frac{dT}{dy}\right|_{y=0} = 0 \tag{3.10}$$

$$B.C.2: T|_{y=(W-do)/2} = T_b \tag{3.11}$$

In order to solve this second-order differential equation, finite difference analysis was used. Figure 3.8d shows discretization and node structure. The fin has been split into (n) nodal sections. There should be three sets of equations, one for the internal nodal points start from 2 to n-1, and two for borders of nodes (1) and (n). First, we present the central finite difference approximation.

$$\frac{\left.\frac{dT}{dy}\right|_{y+\frac{\Delta y}{2}} - \left.\frac{dT}{dy}\right|_{y-\frac{\Delta y}{2}}}{\Delta y} = \frac{T_{y+1} - 2T_y + T_{y-1}}{\Delta y^2} = \frac{U_L}{K_{ap}t_{ap}}\left(T_y - T_a - \frac{S}{U_L}\right) \tag{3.12}$$

$$\Longrightarrow \left(\frac{K_{ap}t_{ap}}{U_L\Delta y^2}\right)T_{y-1} - \left(1 + \frac{2K_{ap}t_{ap}}{U_L\Delta y^2}\right)T_y + \left(\frac{K_{ap}t_{ap}}{U_L\Delta y^2}\right)T_{y+1} = \left(-\frac{S}{U_L} - T_a\right) \tag{3.13}$$

At point 1, the calculation of finite difference approximation using B.C. 1 results:

$$\frac{\left.\frac{dT}{dy}\right|_{y+\frac{\Delta y}{2}} - 0}{\frac{\Delta y}{2}} = \frac{2}{\Delta y^2}(T_2 - T_1) = \frac{U_L}{K_{ap}t_{ap}}\left(T_1 - T_a - \frac{S}{U_L}\right) \tag{3.14}$$

$$\Longrightarrow \left(1 + \frac{2K_{ap}t_{ap}}{U_L\Delta y^2}\right)T_1 + \left(\frac{2K_{ap}t_{ap}}{U_L\Delta y^2}\right)T_2 = \left(-\frac{S}{U_L} - T_a\right) \tag{3.15}$$

At point n, the calculation of finite difference approximation using B.C. 2 results in:

$$\frac{T_b - 2T_n + T_{n-1}}{\Delta y^2} = \frac{U_L}{K_{ap}t_{ap}}\left(T_n - T_a - \frac{S}{U_L}\right) \tag{3.16}$$

$$\Rightarrow \left(\frac{K_{ap}t_{ap}}{U_L\Delta y^2}\right)T_{n-1} - \left(1 + \frac{2K_{ap}t_{ap}}{U_L\Delta y^2}\right)T_n = \left(-\frac{S}{U_L} - T_a - \left(\frac{K_{ap}t_{ap}}{U_L\Delta y^2}\right)T_b\right) \quad (3.17)$$

The energy transmitted from fins on both sides by unit length to the riser tube has been computed according to the law of Fourier:

$$q_{rt}|_{fin} = 2K_{ap}thk_{ap}\frac{(T_n - T_b)}{\Delta y} \quad (3.18)$$

Energy is also obtained from the field above the riser tube and can be expressed in the following equation:

$$q_{rt}|_{top} = Sd_{o-}U_L d_o(T_b - T_a) \quad (3.19)$$

Therefore, the sum of equations (3.18) and (3.19) reflect the total heat gain from the absorber to the riser tube.

$$q_{rt}| = q_{rt}|_{top} + q_{rt}\big|_{fin} = Sd_{o-}U_L d_o(T_b - T_a) + 2K_{ap}thk_{ap}\frac{(T_n - T_b)}{\Delta y} \quad (3.20)$$

Finally, the useful heat gain was conveyed via the riser tube to the working fluid. The working fluid is passing through thermal resistance of riser tube wall thickness, convective coefficient of heat transfer, and bond, which hold the riser tube with an absorber plate. The final form of the equation to calculate the heat transfer of working fluid per unit length inside riser was expressed as:

$$q_{rt} = \frac{T_b - T_f}{\frac{\ln\left({}^{d_o}/_{d_i}\right)}{2\pi K_{rt}} + \frac{1}{C_b} + \frac{1}{\pi d_i h_i}} \quad (3.21)$$

Where, C_b is consider the conductance of bond material which is equal to:

$= K_b \times W_b/thk_b$

K_b is the thermal conductivity of bond material. W_b and thk_b are the width and thickness of bond material, respectively. Shah equation is used to measure the convective heat transfer under constant heat flux and laminar range of flow (Shah, 1975).

$$Nu_x = \frac{d_i h_{ix}}{K_f} \begin{cases} 4.364 + 0.0722\, Re\, Pr \frac{d_i}{x} \;\; Range\left(Re\, Pr \frac{d_i}{x}\right) < 33.3 \\ 1.953 \left(Re\, Pr \frac{d_i}{x}\right)^{\frac{1}{3}} \;\; Range\left(Re\, Pr \frac{d_i}{x}\right) \leq 33.3 \end{cases} \quad (3.22)$$

Where, x = Range in a fluid flow path

Pr = Prandtl number = $C_{pf}\mu_f / K_f$

Re = Reynolds number = $\rho_f V_f d_i / \mu_f$

The fluid temperature is known at the inlet (T_f) of each elementary tube length, but an iteration process in the form of equations (3.20) and (3.21) independently has been implemented for the calculation of the (T_b) value. The (T_b) value shall be changed until an equilibrium is achieved between the two (q_{rt}) values.

In the flow direction, the length of the riser tube of the collector was divided into (m) elements with each (Δx) element frequency. The energy balance shown in Figure 3.8f will give the following equation from the first law of thermodynamics:

$$\frac{\dot{m}}{n} C_p T_f\big|_x + q_{rt} \Delta y = \frac{\dot{m}}{n} C_p T_f\big|_{x+\Delta x} \quad (3.23)$$

Where the mass flow rate and the number of riser tubes are represented as $\dot{m}$ and n, respectively. As we know that $\Delta x \rightarrow 0$, the resultant equation of equation (3.23) is:

$$\dot{m}C_p \frac{dT_f}{dx} - nq_{rt} = 0 \tag{3.24}$$

In order to find the upstream fluid temperature along the riser tube, a forward finite difference method was used to solve this first-order differential equation at defined inlet fluid temperature (T_{in}).

$$T_{x+1} - T_x = \frac{nq_{rt}\Delta x}{\dot{m}C_p}, for\ x = 1\ to\ m \tag{3.25}$$

The selected part of the collector for ANSYS Fluent simulation is represented in Figure 3.8b. A 3-D model for the solar heater was built using the geometry module in the ANSYS workbench package v16 to evaluate the performance of the solar heat at different thermal and flow conditions. The model was constructed from a single tube with the connection to the heated surface of width equals to the pitch between two tubes and the same length of the physical solar heater. A quadrilateral meshes shown in Figure 3.9 was built using the Mesh module and tested at different mesh densities to ensure that the solution is mesh dependent. As the nanofluid samples are Newtonian fluids, all the nanofluid samples were considered as a homogenous single-phase fluid. To solve the governing equations (3.26), (3.27), and (3.28), the problem was recognized as a steady pressure-based problem with absolute velocity formulation (Blazek, 2015). According to the flow rates and pipe dimensions, all Reynolds numbers were under 5000, so; the laminar regime was selected for the viscous model and neglect all radiation effects. The flow boundary conditions were adjusted as in the experimental work for the flow inlet velocity, and the inlet flow temperature was fixed at 30 °C for all samples and then changed to 40 °C and 45°C and 50°C for the DW samples for more comparison. The outlet was adjusted as a pressure outlet with zero Pascal for the gauge pressure. The heated surface (solar plate) was defined as a constant heat flux surface for its top surface and completely insulated from

its bottom surface. The heat flux and inlet velocity were the same as in the experimental work.

Conservation of mass:

$$\nabla\left(\rho\vec{V}\right) = 0 \tag{3.26}$$

Conservation of momentum:

$$\nabla.\left(\rho\vec{V}\,\vec{V}\right) = -\nabla P + \mu\,\nabla^2\vec{V} + \rho\vec{g} \tag{3.27}$$

Conservation of energy:

$$\nabla.\left(\rho C_p\,\vec{V}T\right) = K_{eff}\nabla^2 T + \nabla(\tau_{eff}\vec{V}) \tag{3.28}$$

The effective surface temperature of a whole absorber plate is measured after it has reached the end of the riser tube and compared to the approximate temperature used to measure the coefficient of heat loss at the top surface (U_t). The estimated value will be corrected if the gap between them reaches a threshold, and the cumulative measurements will be repeated before equilibrium has been achieved.

The thermal efficiency of a solar flat-plate collector is measure as defined as (Duffie & Beckman, 2013). The ratio between useful heat gain Q_u and total energy received by absorber plate provides the effectiveness of collector and is calculated using equation (3.29).

$$\eta_c = \frac{Q_u}{A_c\,G_T} = \frac{Actual\ useful\ energy\ collected}{heat\ flux\ received\ at\ the\ surface\ of\ collector} \tag{3.29}$$

The equation (3.30) is used to calculate the useful heat gain energy, and it is calibrated by taking the difference between heat energy absorbed and heat energy loss by absorber plate as in equation (3.31)

$$Q_u = \dot{m}C_p(T_o - T_i) = \rho V C_p(T_o - T_i) \tag{3.30}$$

$$Q_u = A_c F_R[G_T(\tau\alpha) - U_L(T_i - T_a) \tag{3.31}$$

A lightweight adhesive electric heater is used in this study to create a continuous heat flux equivalent to solar radiation. The equation (3.32) can, therefore, be rewritten in an appropriate form using equation (2.3). The multiplication of the total area of solar collector and solar radiation absorbed at the surface of the collector represents the power taken from the adhesive heater in terms of current multiply by voltage.

$$\eta_c = \frac{Q_u}{A_c \dfrac{S}{\tau_g \alpha_{ap}}} = \frac{\dot{m}C_p(T_o - T_i)}{\dfrac{SA_c}{\tau_g \alpha_{ap}}} \tag{3.32}$$

Based on equation 3.31, collector efficiency can be represented as:

$$\eta_C = \frac{A_c F_R[G_T(\tau\alpha) - U_L(T_i - T_a)}{\dfrac{SA_c}{\tau_g \alpha_{ap}}} \tag{3.33}$$

Equation (3.32) can be rewritten, as shown in equation (3.33). Where F_R is known as heat removal factor according to the Hottel-Whillier equation, and it defines as the ratio between the actual useful heat gain to the useful heat gain if the whole collector surface is at fluid inlet temperature (Duffie & Beckman, 2013).

$$F_R = \frac{\dot{m}C_p(T_o - T_i)}{A_c[G_T(\tau_g \alpha_{ap}) - U_L(T_i - T_a)} \tag{3.34}$$

Based on equation 3.29 to 3.34, the final form of FPSC's thermal efficiency can be expressed as:

$$\eta_c = F_R(\tau_g \alpha_{ap}) - F_R U_L \frac{(T_i - T_a)}{G_T} = F_R(\tau_g \alpha_{ap}) - F_R U_L \frac{(T_i - T_a)}{\frac{S}{\tau_g \alpha_{ap}}} \quad (3.35)$$

The solar collector's thermal efficiency η_c is considered to plot a graph using equation (3.35) against reduced temperature parameter $\left(\frac{T_i - T_a}{G_T}\right)$, Providing a straight line. This straight-line intersects the thermal efficiency line (vertical axis line) at $F_R(\tau\alpha)$. At this point, the inlet temperature of the collector equal to the ambient temperature, and the thermal efficiency of the collector reach its highest value. This point is also known as the zero-loss efficiency point. On the other side, the thermal efficiency is zero when the straight line intersects the horizontal axis (reduced temperature line). The parameter $F_R(\tau\alpha)$ is known as absorbed energy parameter and $F_R U_L$ is known as removed energy parameter (H. K. Gupta, Das Agrawal, & Mathur, 2015; S. A. Kalogirou, (2009).; Sakhaei & Valipour, 2019; Stalin et al., 2019).

A performance index (PI) is chosen as an appropriate parameter to measure the effects and use of various nanofluids as working fluids in FPSCs. Based on the previous research (Alawi et al., 2019a; Amiri et al., 2015; Arzani et al., 2016; Sarsam et al., 2017; Sarsam, Amiri, Zubir, et al., 2016b), Performance Index can be described in a form which is suitable for thermal collector as follows:

$$PI = \frac{(\eta_c)_{nf} \Big/ (\eta_c)_{bf}}{(\Delta P)_{nf} \Big/ (\Delta P)_{bf}} = \frac{R_{\eta_c}}{R_{\Delta P}} \quad (3.36)$$

If the performance index is higher than 1, the nano-fluid can be consumed in the FPSC rather than the base-fluid for improved thermal efficiency. However, the nanofluid is not a suitable replacement if its output index is less than 1(Chaji et al., 2013; Razi et al., 2011; Sadri, Hosseini, Kazi, Bagheri, Abdelrazek, Ahmadi, Zubir, Ahmad, Abidin, et al., 2018).

The pressure drops over the FPSC can be accomplished through the operation of the energy balance equation between entry and exit of the tube where the DPT is connected (Cengel, 2006):

$$P_i + \frac{\rho {V_i}^2}{2} + \rho g Z_i = P_o + \frac{\rho {V_o}^2}{2} + \rho g Z_o + \Delta P_{loss} \quad (3.37)$$

Where, ΔP_{loss} is total pressure loss across the FPSC. Due to equal diameter of the header tubes, the velocity heads at inlet and outlet of the solar collector will be consider same, and expressing the vertical distance (Z_{out}-Z_{in}) as (L_{rt} Sinφ), the above equation can be reduced to the following equation for calculating the pressure drop across the FPSC;

$$\Delta P_{FPSC} = P_i - P_o = \rho g \, L_{rt} \, \text{Sin}\varphi + \Delta P_{loss} \quad (3.38)$$

The overall pressure loss (ΔP_{loss}) is the sum of all pressure losses in the riser tube, fittings, curves, tees, inlets, and outlets (Cengel, 2006).

$$\Delta P_{loss} = (\Delta P_{loss})_{riser\ tube} + (\Delta P_{loss})_{minor} = (\Delta P_{loss})_{riser\ tube} + \left(\frac{\rho V^2}{2} \sum K_L\right) \quad (3.39)$$

As the FPSC 's inlet tube and outlet tube are opposite and the elevated tubes parallel, the pressure drop of any rising tube will be the same, because fluid flows through each tube are uniform. The minor loss factor (K_L) has values of 0.5, 1.0, 0.2, 2.0, and 0.3 for the tube entrance (sharp-edged), tee (branch flow), tee (line flow), tube exit, and smooth bend (90°), respectively (Cengel & Cimbala, 2006). During the passage of fluid in the hydrodynamic input area of the conduit, the pressure is lost due to the friction of the fluid in addition to the shear of the surface.

The correlation proposed by (Bender, 1969) was therefore used for the measurement of pressure loss in the hydrodynamic laminar entry range (equation (3.41)). From the

following equation (Cengel & Cimbala, 2006), the length of the hydrodynamic entry length can be calculated (L_h):

$$L_h = Hydrodynamic\ entry\ length = 0.05Re\ d_i \tag{3.40}$$

$$(\Delta P_{loss})_{riser\ tube} = \frac{\rho V^2}{2}\left(13.74\sqrt{\frac{x}{d_i Re}} + \frac{1.25 + 64\frac{x}{d_i Re} - 13.74\sqrt{\frac{x}{d_i Re}}}{1 + 0.00018\left(\frac{x}{d_i Re}\right)^{-2}}\right) \tag{3.41}$$

The pressure drop, for the fully developed flow in a pipe, can be calculated as (Cengel, 2006);

$$(\Delta P_{loss})_{riser\ tube} = f\frac{L}{D}\frac{\rho V^2}{2} \tag{3.42}$$

Where, f =Darcy-Weisbach friction factor = $\frac{64}{Re}$

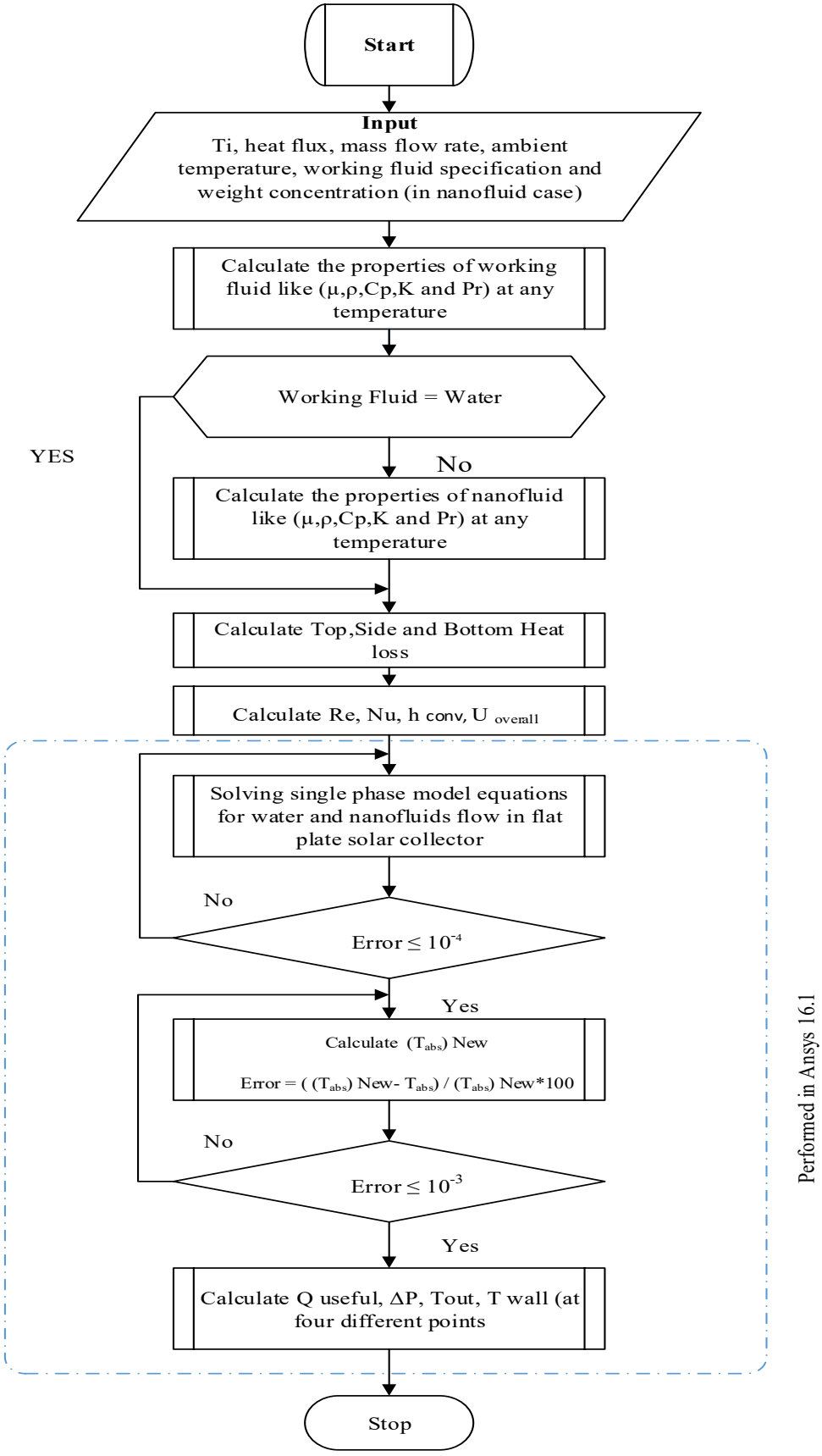

Figure 3.7 Flow-chart of mathematical modeling

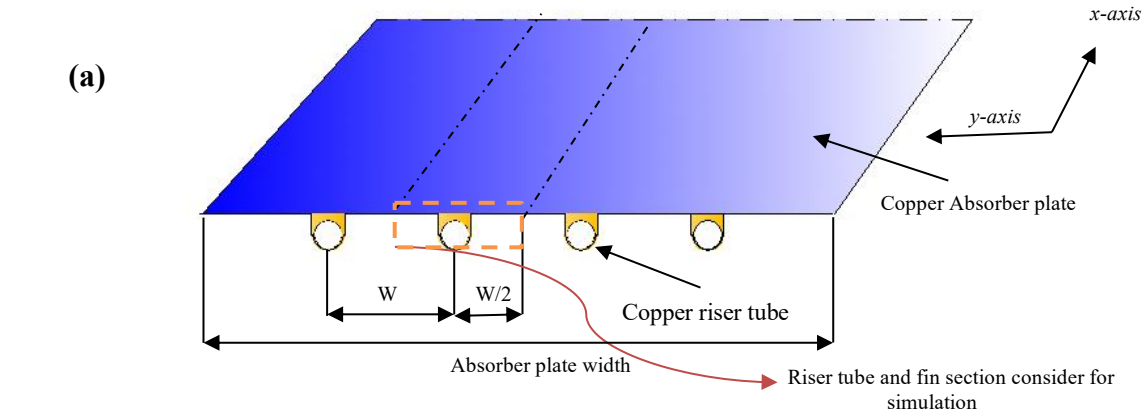
(a)
x-axis
y-axis
Copper Absorber plate
W
W/2
Copper riser tube
Absorber plate width
Riser tube and fin section consider for simulation

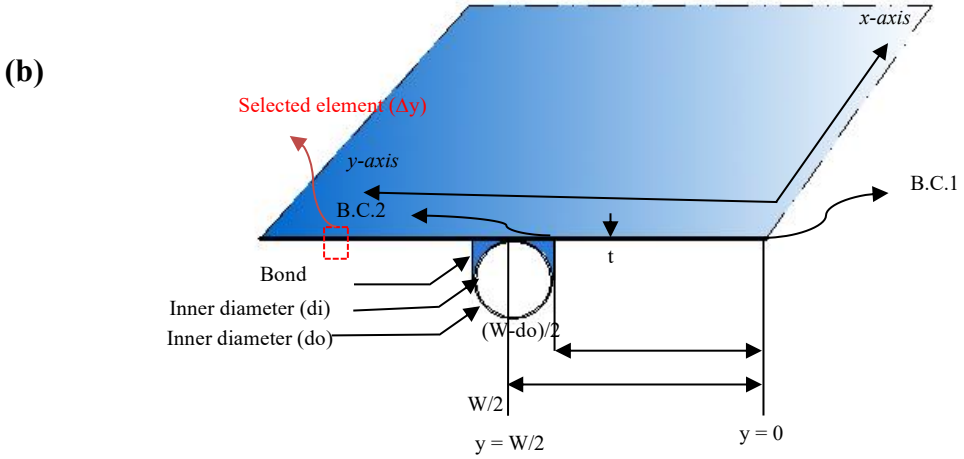
(b)
x-axis
Selected element (Δy)
y-axis
B.C.2
B.C.1
t
Bond
Inner diameter (di)
Inner diameter (do)
(W-do)/2
W/2
y = W/2
y = 0

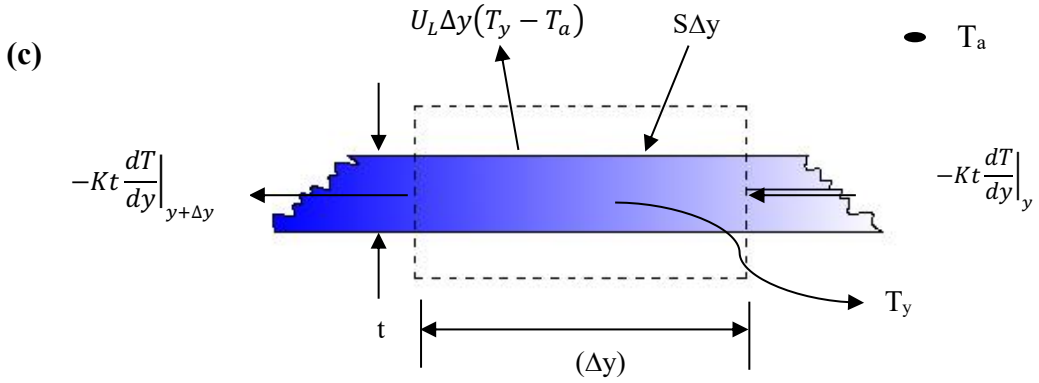
(c)
$U_L\Delta y(T_y - T_a)$
SΔy
T_a
$-Kt\frac{dT}{dy}\Big|_{y+\Delta y}$
$-Kt\frac{dT}{dy}\Big|_{y}$
T_y
t
(Δy)

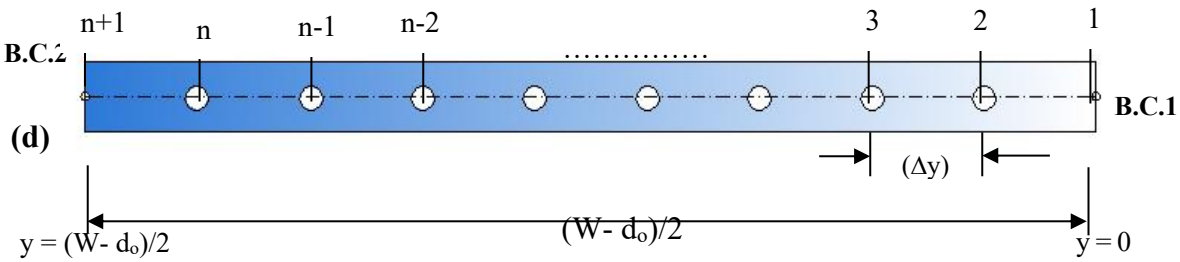
n+1
n
n-1
n-2
3
2
1
B.C.2
B.C.1
(d)
(Δy)
y = (W- do)/2
(W- do)/2
y = 0

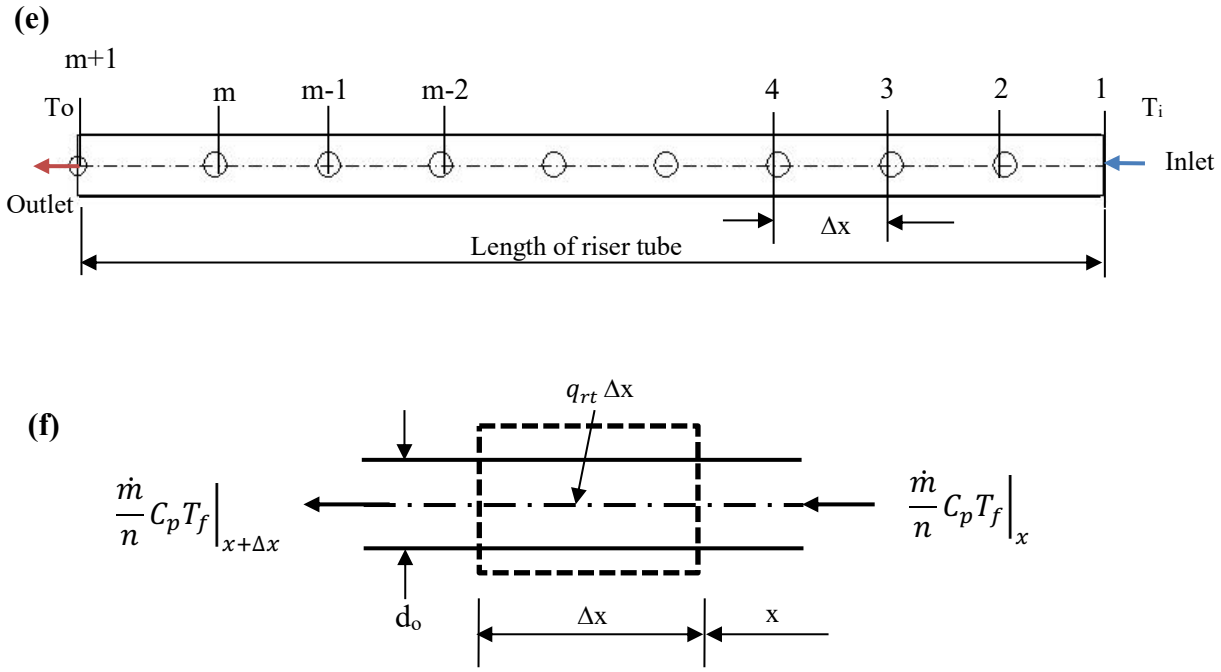

Figure 3.8 (a-f) Fin and tube section consider for mathematical modeling and simulation implementation

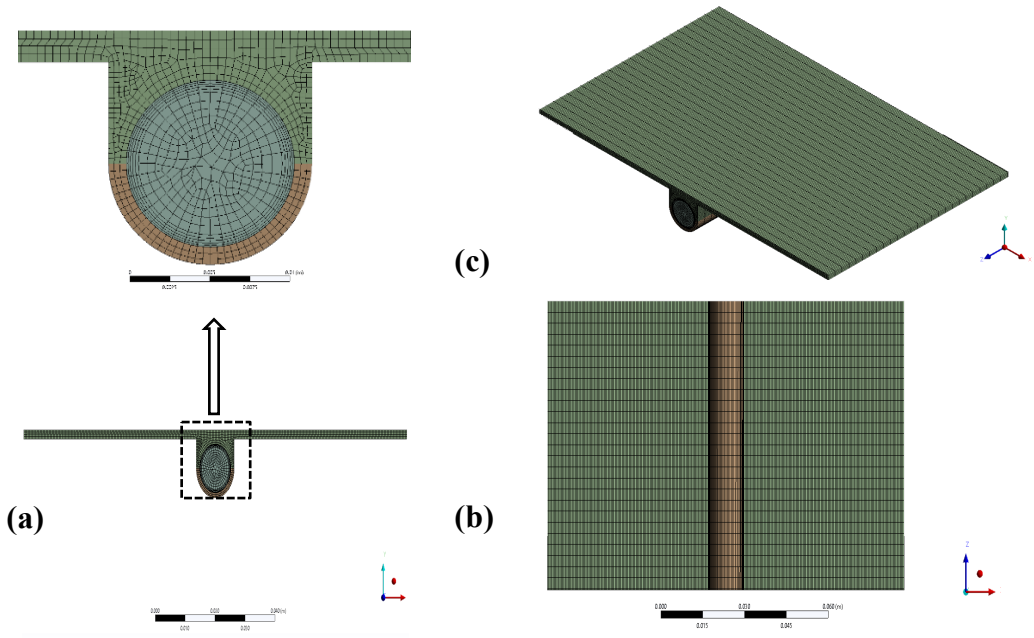

Figure 3.9 Side, bottom and top view of quadrilateral meshes of riser tube and heated plate

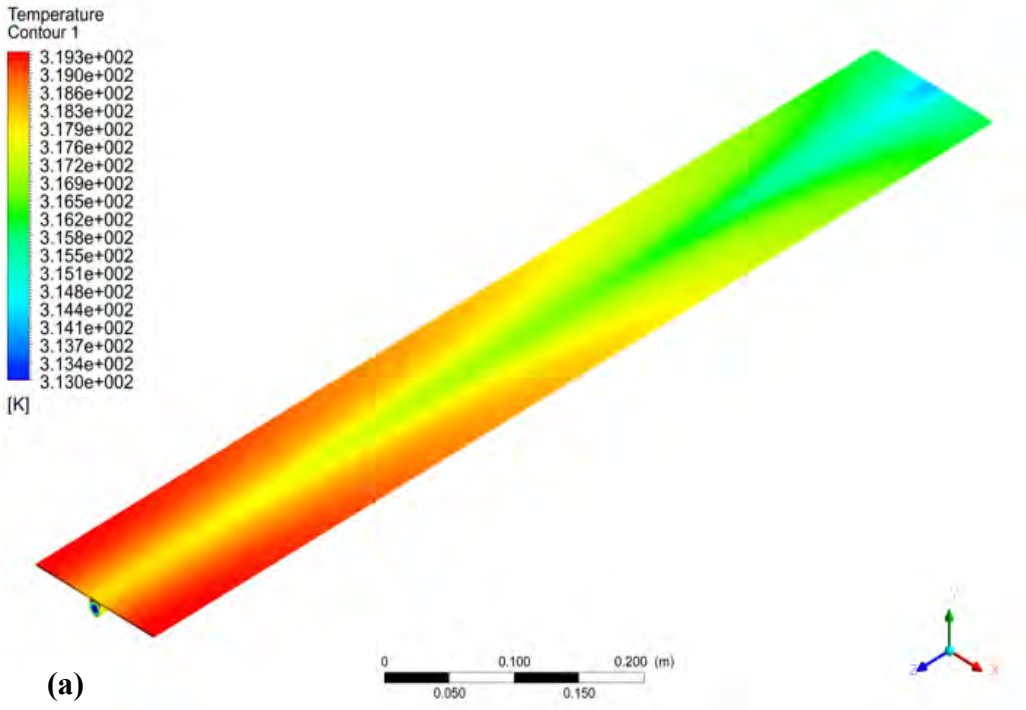
Temperature
Contour 1
3.193e+002
3.190e+002
3.186e+002
3.183e+002
3.179e+002
3.176e+002
3.172e+002
3.169e+002
3.165e+002
3.162e+002
3.158e+002
3.155e+002
3.151e+002
3.148e+002
3.144e+002
3.141e+002
3.137e+002
3.134e+002
3.130e+002
[K]
0
0.100
0.200 (m)
0.050
0.150

(a)

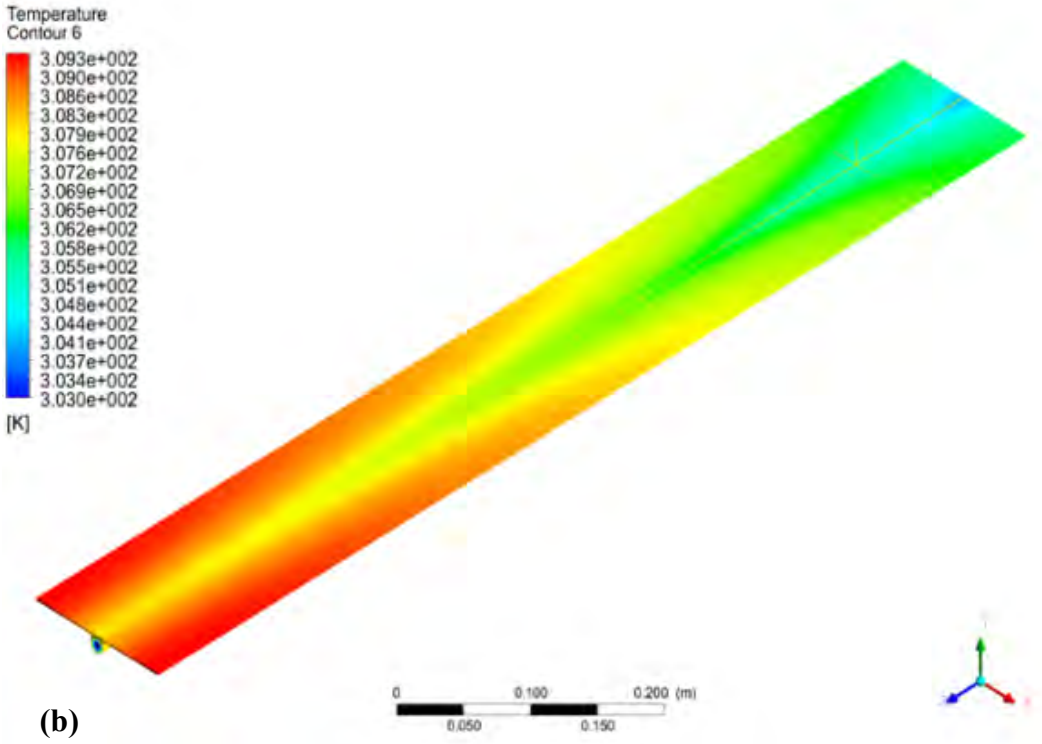
Temperature
Contour 6
3.093e+002
3.090e+002
3.086e+002
3.083e+002
3.079e+002
3.076e+002
3.072e+002
3.069e+002
3.065e+002
3.062e+002
3.058e+002
3.055e+002
3.051e+002
3.048e+002
3.044e+002
3.041e+002
3.037e+002
3.034e+002
3.030e+002
[K]
0
0.100
0.200 (m)
0.050
0.150

(b)

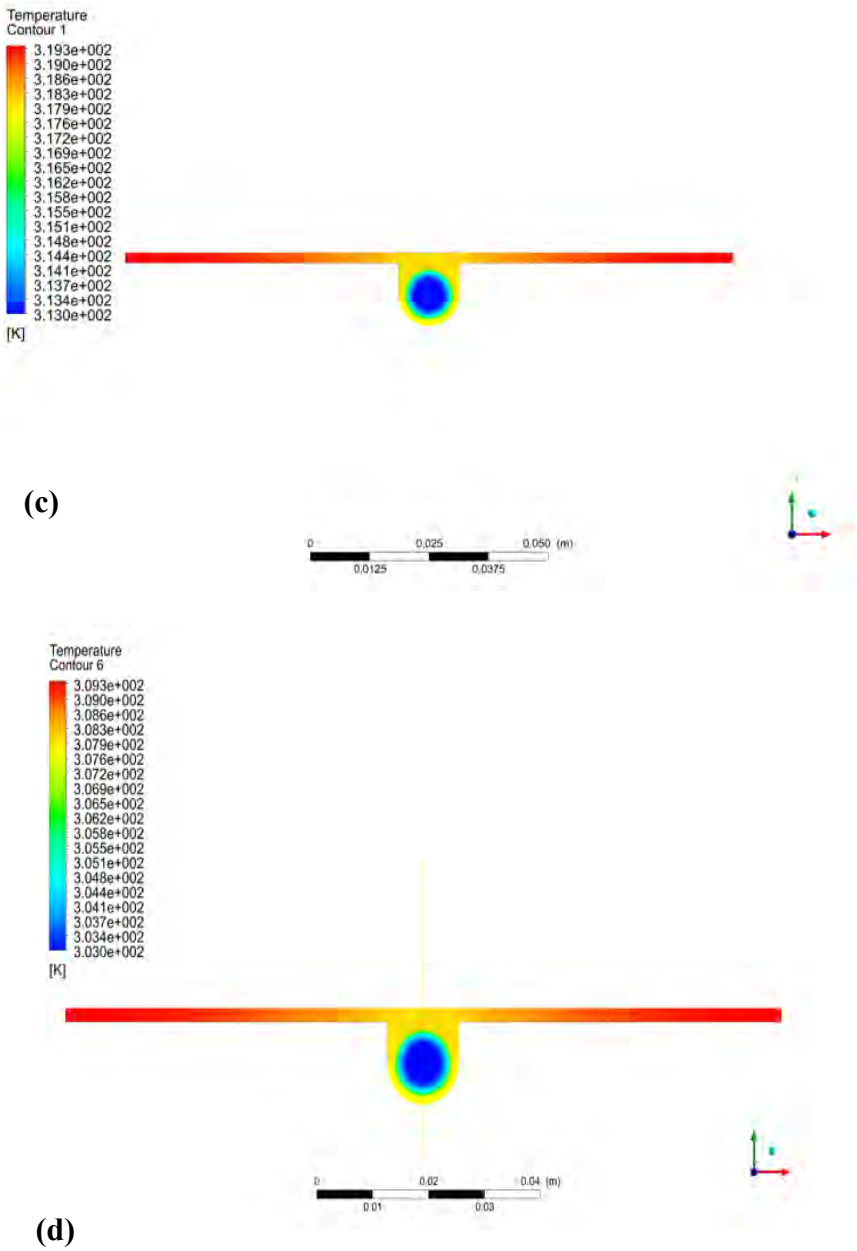

Figure 3.10 Temperature contour for absorber plate along a single riser tube for different reduced temperatures.

3.9 Uncertainty Analysis

In any experimental investigation, the collected data has few errors and inaccuracies which cannot be avoided, which creates uncertainty in the experimental data. Hence, in this investigation, the accuracy of thermal efficiency for flat plate solar collectors is calibrated from the collected experimental data, and it was calculated using uncertainty

analysis. The effectiveness of flat plate solar collector used in this study can be conveyed in a proportional form as:

$$\eta_c \propto \frac{Actual\ useful\ energy\ collected}{heat\ flux\ received\ at\ the\ surface\ of\ the\ collector} \propto \frac{\rho V C_p (T_o - T_i)}{\tilde{V} \times \tilde{I}} \tag{3.43}$$

$$\Longrightarrow \eta_c \propto \rho V C_p \left(\tilde{V} \times \tilde{I}\right)^{-1} (T_o - T_i) \propto \rho V C_p \, \tilde{V}^{-1} \, \tilde{I}^{-1} \Delta T \tag{3.44}$$

The uncertainty (ω) in the value of R can be expressed using the following relation (Holman (Holman, J. P. (2012).) and Kline & McClintock (Kline, 1953)), eq. (3.45).

$$\frac{\omega_R}{R} = \left[\sum_{i=1}^{n} \left(\frac{a_i \omega_{x_i}}{x_i}\right)^2\right]^{0.5} \tag{3.45}$$

Consequently, using Eq.12, the experimental data is used to find the uncertainty in the value of FPSC's efficiency using the following relation, eq. (3.46):

$$\frac{\omega_{\eta_c}}{\eta_c} = \left[\left(\frac{\omega_\rho}{\rho}\right)^2 + \left(\frac{\omega_V}{V}\right)^2 + \left(\frac{\omega_{C_p}}{c_p}\right)^2 + \left(\frac{\omega_{G_T}}{G_T}\right)^2 + \left(\frac{\omega_{\Delta T}}{\Delta T}\right)^2\right]^{0.5} \tag{3.46}$$

The uncertainty values of the five independent variables are 0.04%, 1.67%, 2.75%, 1.75%, and 0.67% respectively. Hence, the uncertainty in the measured efficiency of the FPSC was estimated to be 3.75%. The maximum variation in ambient temperature, inlet temperature, and radioactive flux in each test period was ± 0.5 °C, ± 0.1 °C, and ± 25 W/ m², respectively.

CHAPTER 4: RESULTS AND DISCUSSION

4.1 Introduction

In this chapter, the data collected in pictorial, graphical, and tabular formats from the different tests, measurements, and studies during this research have been clarified and compared for confirmation. The data extracted from nanofluid was compared with DI water as well as with different materials. Thermophysical properties' data were compare with correlation models and which can help to suggest new correlation.

4.2 Characterization of CGNPs (clove-treated graphene nanoplates)

To study the elemental composition of the graphene nanostructure before and after the functionalization, XPS are used. The binding energy of regular carbon (284.6 eV) has been connected to each edge. From the large spectra XPS-scans of GNPs and CGNPs (Figure 4.1a), it can be observed that the O 1s and C 1s peaks are clustered at 532.8 eV and 284.6eV, respectively. In comparison to GNPs, the clove-treated GNPs have a higher O 1s peak strength because the ratio between oxygen to carbon is improved by 0.247 for CGNPs from 0.029 (GNPs). This shows that numerous functional oxygen groups were successfully oxidized amorphous carbon impurities as well as free radical splicing onto CGNPs. The edges and surfaces of GNPs will be very likely to be bound to the oxygen containing groups such as COO (carboxylic acid), C=O (carbonyl derivatives), and C—O (in hydroxyls and epoxy). In order to test the contributions of these groups, conducted curve adaptation to the high-resolution C 1s and O 1s. The XPS distribution of the C 1s de-convoluted peak components for GNPs and CGNPs with high-resolution spectrums are presented in Figure 4.1(b) and (c). The findings demonstrate the existence of $\pi - \pi$ interaction, $O - C = O$ (carboxyl group), $C = O$ (carbonyl group), $C - O$ (hydroxyl and epoxy group), $C - C$ (aliphatic group) and $C = C$ (sp^2-hybridized structure) at 290.13, 289.02, 287.61, 286.27, 285.39, and 284.60 eV, respectively. The intensity of the

carboxyl group, carbonyl group, hydroxyl, and epoxy group, raised from 1.62,4.04, 5.75% (standard GNPs) to 4.7,5.95,13.04% (CGNPs), respectively, on the other side $\pi - \pi$ interaction bond disappeared completely. The enhanced peak strength in the spectrum of the O 1s at 530.7 and 533 eV (Figure 4.1d and e) indicates that significant percentages of oxygen atoms are present as stable $C = O$ and $C - O$ grouping for the CGNPs. Instead of this the pure GNPs reveal that structures such as the $C = O$ and $C - O$ are weak and generic (R. Das et al., 2015). Such dynamic groups have been produced inadvertently as natural oxidizing agents such as ozone and hydroxyl radicals when GNPs were environmentally exposed. In Table 4.1, the findings from XPS are summarized.

While TEM indicates that GNPs are surface degraded (morphology) and scratched, no knowledge about their functional groups comes from this technique. The TEM images for CGNPs and GNPs are shown in Figure 4.2(a) and (b), respectively. Figure 4.2a shows that GNPs are arranged in many layers and have a smooth surface and edges (low edge errors) with a higher aggregating effect. On the other hand, the CGNP exists on a surface which is very rugged and has higher defects and irregularities due to the covalent structure. The appearance of wrinkles and lines on the CGNPs surface is due to the inherent flaws of two-dimensional systems and the alterations for increased GNPs durability after intermolecular connectivity with cloves.

Figure 4.3a specifically shows that the FTIR spectrum of pristine and CGNPs give some apparent signs to the Clove molecule compared to the pristine GNP. The range of the CGNPs shows a broad peak at 3436 cm^{-1}, due to the O-H vibration. The simple vibrations of both symmetric and antisymmetric CH bonds for CGNPs are seen at 2849-2917cm^{-1}. Also, the peaks within the range 1577-1715 cm^{-1} have to do with the vibration

of the graphene flakes extending from the C=C following opening due to the electrophilic attach reaction of the main structure or edge of GNP with the Clove – OH band.

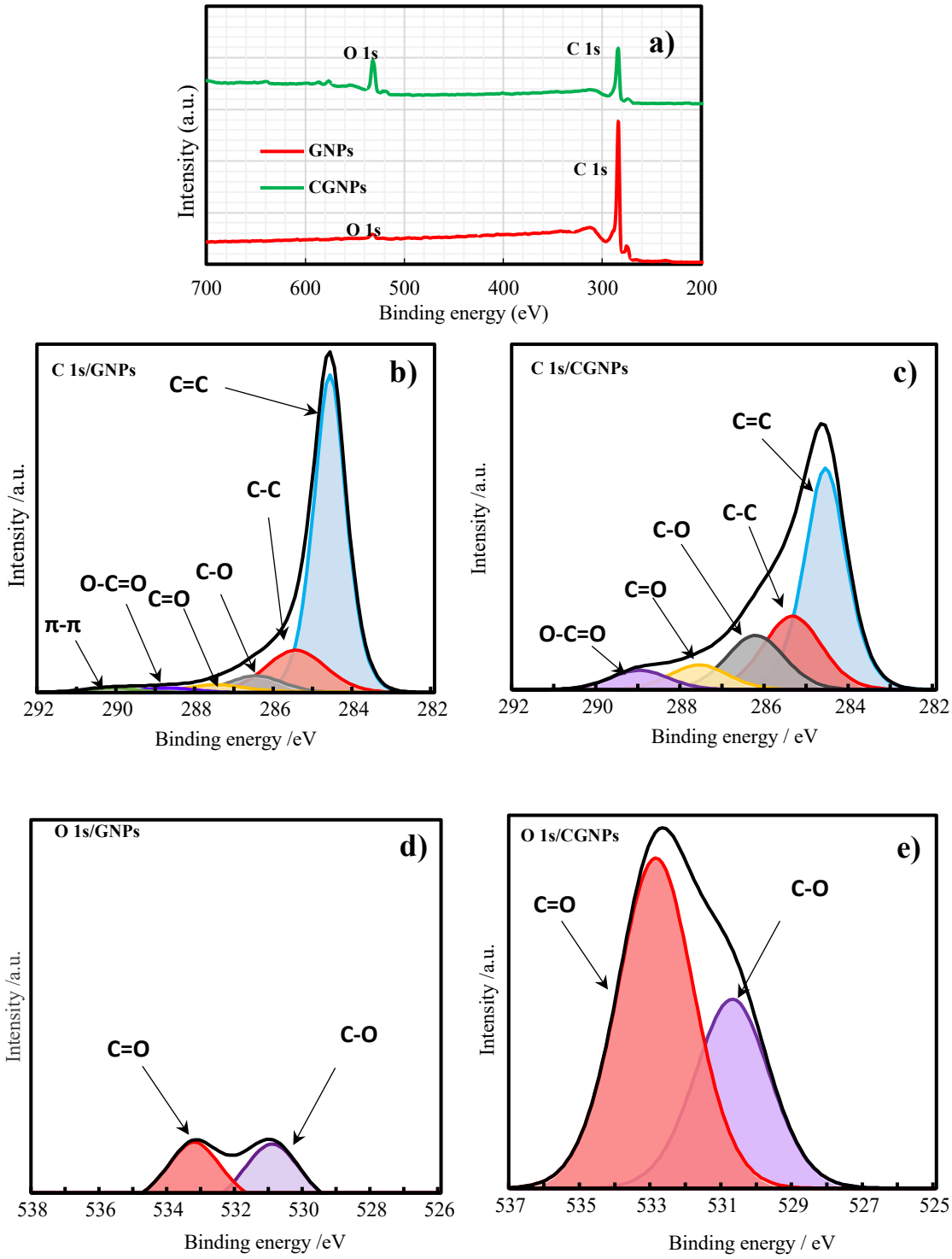

Figure 4.1 (a) The GNPs and CGNPs wide-scan XPS spectrums (b-c) XPS range with high resolution of the reduced C 1s components for GNPs and CGNPs (d-e) XPS range high-resolution of the deconvoluted O 1s peaks for GNPs and CGNPs

Table 4.1 The results of XPS analysis for pristine graphene and clove-treated graphene

Sample	Total atomic %		Basic component (atom %)							
			C 1s						O s1s	
	C 1s	O 1s	C = C	C – C	C – O	C = O	O – C = O	π – π	C – O	C = O
Pristine Graphene	97.09	2.91	68.15	16.19	5.75	4.04	1.62	1.52	1.32	1.41
Clove-treated Graphene	80.15	19.85	39.63	17.63	13.04	5.95	4.7	0	6.84	12.21

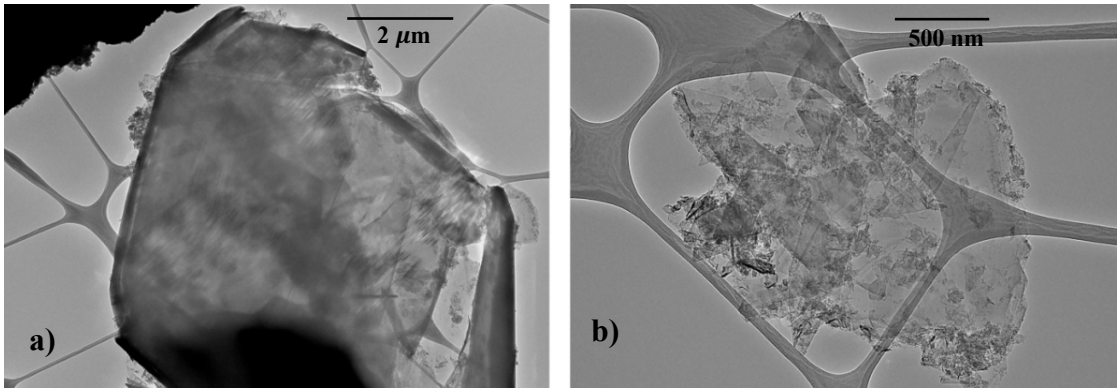

Figure 4.2 TEM image for (a) GNPs (b) Clove-treated GNPs

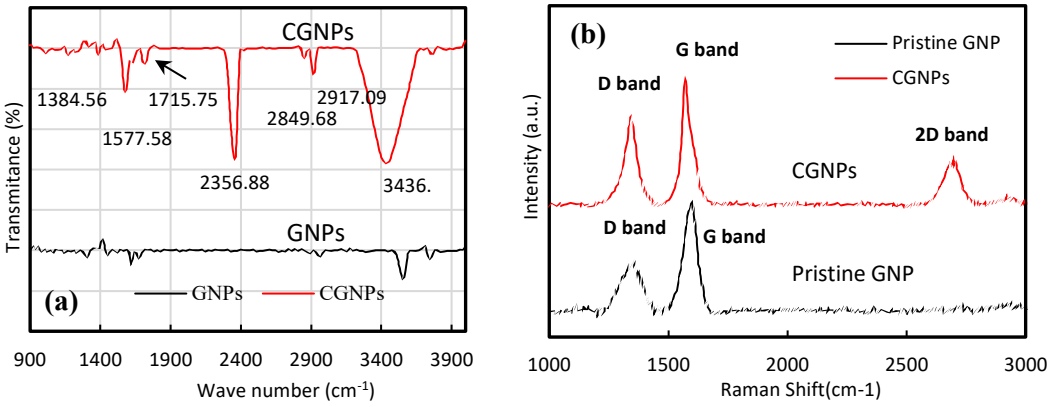

Figure 4.3 (a) FTIR spectra of pristine GNPs and CGNPs (b) Raman spectra of pristine GNPs and CGNPs

Figure 4.3b shows Raman's spectral study of pure GNPs and CGNPs. The Raman spectra of both samples indicate D and G bands at wavenumbers of 1346 and 1588 cm^{-1}, respectively. Both bands D and G are associated with sp^3 and sp^2 hybridization, respectively (Hodkiewicz & Scientific, 2010). The improvement in the Raman intensity ratio between these two bands means that the covalent functionality of certain hybridized carbons has improved from sp^2 to sp^3 (Jeon, Chang, Kumar, & Baek, 2011).

4.3 Characterization of Polyethylene glycol (PEG200) treated Fe_3O_4 nanoparticles

FTIR spectroscopy is used to extracts the surface properties of PEG functionalized iron nanoparticles. Figure 4.4a portrays IONP's FTIR spectra. The IONPs FTIR spectrum is dominated by a strong absorption band about 552 cm^{-1}, which in Fe_3O_4 nanoparticles can be related to Fe-O bonds (Liu et al., 2012; Mondini et al., 2008). It is indicated that the key phase of the synthesized IONPs is Fe_3O_4. The PEG200 FTIR spectrum has various bands of absorption within the 650–1450 cm−1 region (Figure 4.4a). A PEG200 absorption band that is visible in the FTIR Spectra (1062 cm^{-1}) of IONPs is the most extreme absorption band in this area, due to the Vibration Band of the C-O bond. Such experimental findings indicate that the surface of IONPs contains a very small amount of PEG 200.

Figure 4.4b shows the XRD peak patterns of the functional PEG-Fe_3O_4 nanoparticles. XRD reflections prove that nanoparticles are pure magnetite and cubic reverse backend (JCPDS No. 82-1533) (Dorniani et al., 2012). In addition, the lattice planes [311], [220], [400], [333] and [440] reflects the magnetite diffraction peaks at 2θ value of 31°, 36°, 43°, 57°, and 63, respectively. The nonappearance of [210], [213], and [300] superlattice diffractions supported the fact that maghemite is not found in the present study. In fact, the XRD evidence shows that the iron oxide phase was not impaired by functionalization.

High-resolution electron microscopy (HRTEM) was used to study the morphology of synthesized PEG-Fe_3O_4.The TEM image of PEG functionalized Fe_3O_4 nanoparticles distribution shows in Figure 4.5. The average size for PEG-Fe_3O_4 nanoparticles are 9.60nm (Figure 4.5c). 0.29 nm of crystal lattice length equivalent to planes of [220] lattice in nanoparticles with the use of cubic iron oxide (Iyengar et al., 2014). Nanoparticles are agglomerated due to the particle's magnetic behavior. The size of the In-Situ functionalized PEG-Fe_3O_4 is ultra-small, relative to the Fe_3O_4 nanoparticles synthesized using post functionalized method. This confirmation indicates the efficient and productive impact of in-situ functionalization in this analysis, which is considerably lower than other synthesis paths.

The hysteresis loops are shown in Figure 4.6 in conjunction with the magnetic field at normal temperatures. For PEG-Fe_3O_4, the value 53 emu g^{-1} was given. The synthesis of nanoparticles is superparamagnetic, with low magnetization rates as bulk magnetite around 92 emu g^{-1} (Cornell & Schwertmann, 2003).

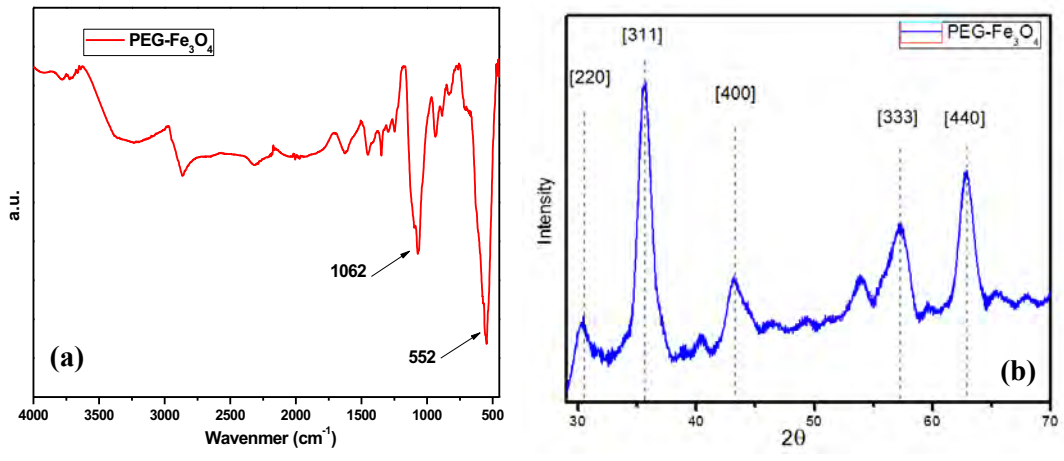

Figure 4.4 (a) FTIR spectra & (b) XRD spectra of functionalized PEG-Fe_3O_4 nanoparticles

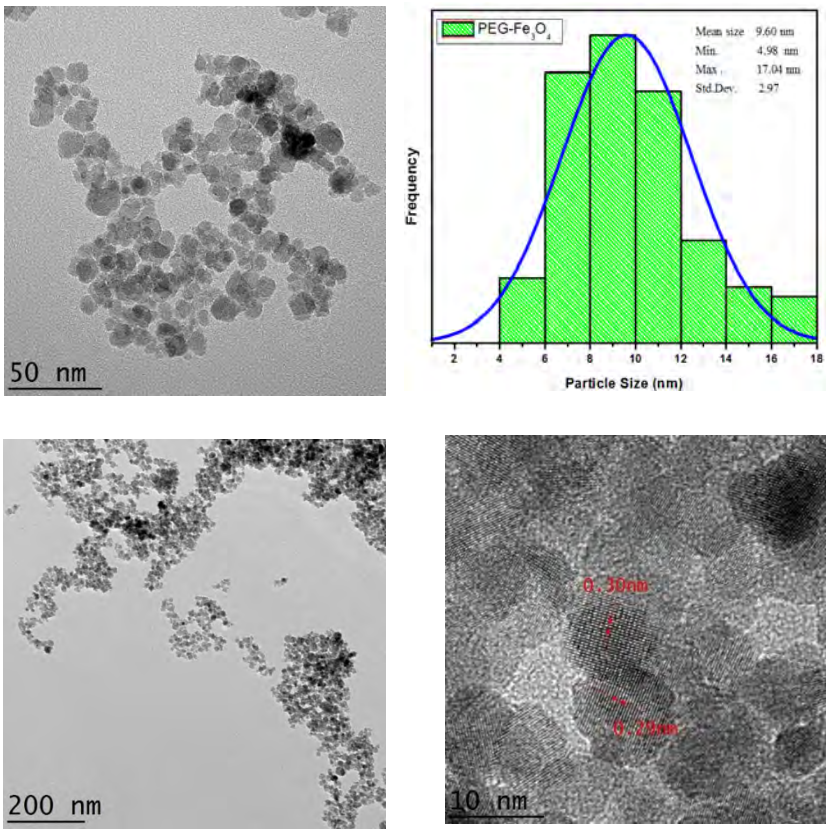

Figure 4.5 TEM images (a,b,c) and particle size distribution (d) of PEG-Fe_3O_4

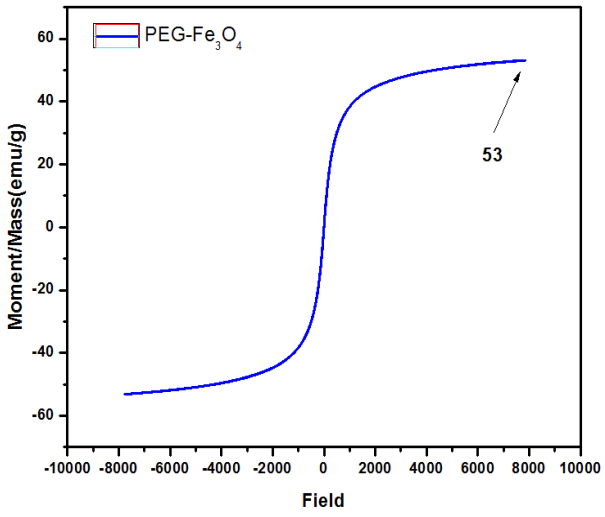

Figure 4.6 Magnetic hysteresis loops of PEG-Fe_3O_4

During the Energy Dispersive X-ray Spectroscopy (EDX) Analysis, Fe and O verified that the magnetite nanoparticles are present, while C signals originate from PEG (Figure 4.7). In the mapping pictures, the spatial dispersion of the iron atoms shows precisely the

uniform distribution of the atoms. In the EDX analysis, following functionalization, the percentage of iron, oxygen, and carbon rises are shown in Table 4.2, which could be closely due to OH radicals attached at PEG-Fe_3O_4 *the* surface, which is in line with the FTIR tests.

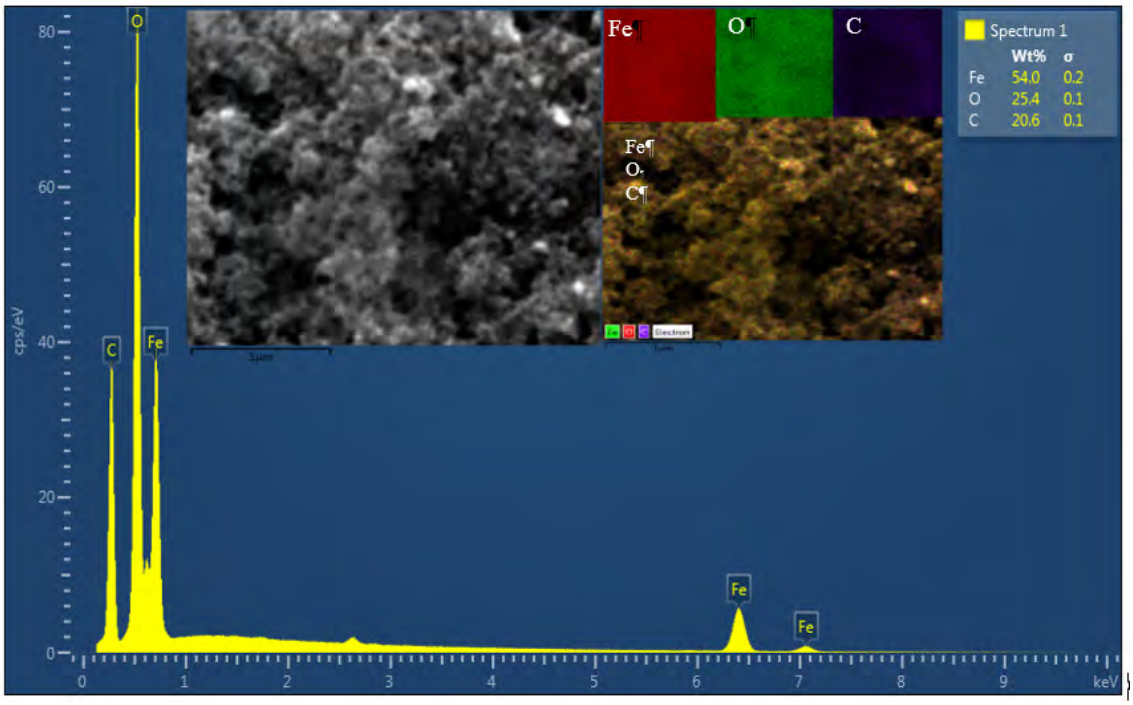

Figure 4.7 FESEM PEG- Fe_3O_4 image (inset: EDX elemental map of Fe, O, C)

Table 4.2 EDX element composition

Element	Line Type	Wt%	Wt% Sigma	Atomic%
C	K Series	20.60	0.12	40.19
O	K Series	25.36	0.12	37.14
Fe	K Series	54.04	0.20	22.67
Total		100		100

4.4 Stability of Synthesized nanofluids

In this research, all water-based nanofluids were prepared with a two-step method using various types of nanomaterials of different dimensions. Moreover, the colloidal stability

of the prepared nanofluids was improved by different functionalization processes. Colloidal stability for the various synthesized nanofluids has been provided in the flowing parts.

4.4.1 Colloidal stability of water based CGNPs nanofluids

The exact calculated amount of CGNPs was added to a specified volume of distilled water. The base fluid to prepare the water based CGNPs nanofluid, and the mixture was then sonicated for 60 minutes. This cycle time of sonication was chosen to make all (0.1 wt.%,0.075 wt.%,0.05 wt.%,0.025 wt.%) of the aqueous dispersions of the covalently functionalized nanomaterials; which was based on the previous analysis (Sarsam, Amiri, Zubir, et al., 2016b). The sonication cycle was conducted at a power output of 80% amplitude using a sequential mechanism of three seconds. Zeta-Potential measurement and UV-spectroscopy were used to check the stability of the synthesized nanofluids in this study.

In order to ensure that the visible UV-vis spectrometer wavelengths can move through the samples, the sample was diluted with DI water at a 1:20 dilution rate. Then, poured the samples into quartz cuvettes, which were particularly used to transmit UV wavelengths, and measured the absorption of the samples over 58 days at wavelengths of 265 nm at specified intervals. The photometric analysis was used to monitor the weight concentrations of all the samples after synthesis and at the specified time intervals for more than 58 days. The sample weight concentrations decreased at different rates with time, as seen in the figure due to sedimentation and agglomerations. It is easy to note that for all of the samples after sixty days, the remaining concentrations of weight were (0.0217 for 0.025 wt.%), (0.0461 for 0.05 wt.%), (0.062 for 0.075 wt.%), and (0.092 for 0.1 wt.%), respectively (Figure 4.8a). Therefore, the rate of sedimentation among the

samples differed at different weight concentrations. The results of previous researchers agree with these results (Behi & Mirmohammadi, 2012; Sarsam et al., 2017).

The relative concentration data assist in deciding the maximum stability of the sample from all the synthesized samples. The relative concentrations of the nanofluids were declined by increasing the number of days following the preparation of the sample. After fifty-eight days, In the corresponding estimates, the relative sample concentrations were 0.9195, 0.9078, 0.8960 and 0.8821, for 0.025 wt.%, 0.05 wt%,0.075 wt.% and 0.1 wt.%, respectively (Figure 4.8b). From these findings, the 0.025-wt.% CGNP assay with a relative concentration of 0.9195 was attained to the maximum colloidal stability, indicating 8.05% sedimentation after fifty-eight days.

Zeta potential analyzer was used for testing the stability of nanofluids. Figure 4.9 shows the measured zeta potential values as a function of pH for the CGNP aqueous suspension. It can be observed that the CGNP nanofluid has high negative values (–4.42 mV to –49.5 mV) within the pH variations from 1.84 to 10.55. More importantly, the zeta potential values for the CGNP nanofluids are far from the isoelectric point (i.e., point of zero charges), which indicates that this pH range (2.8–10.55) results in strong electric repulsion forces between the particles of CGNPs. It prevents aggregation of the CGNPs by non-covalent interactions such as π-π interactions. CGNP-water nanofluids were found stable for 58 days.

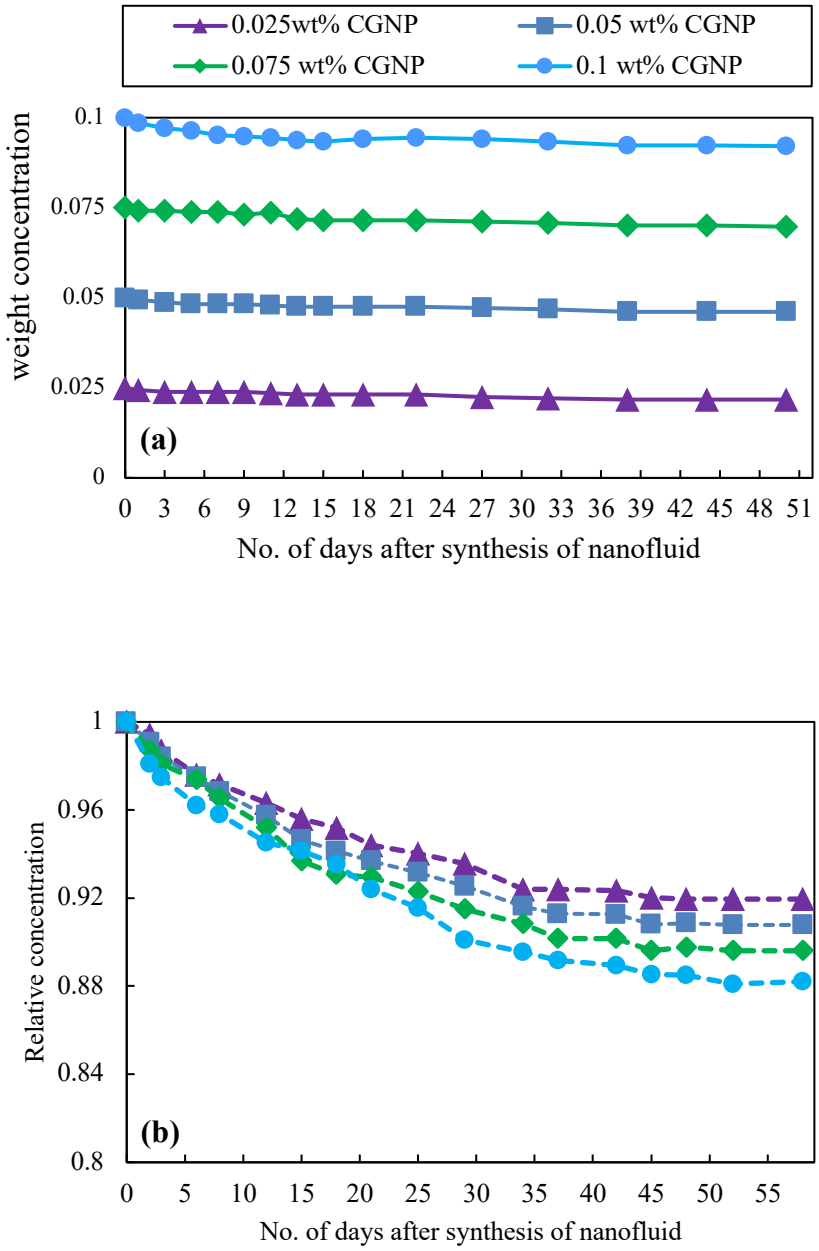

Figure 4.8 (a) Weight concentrations and (b) relative concentration of CGNP nanofluids against no. of days at different concentrations.

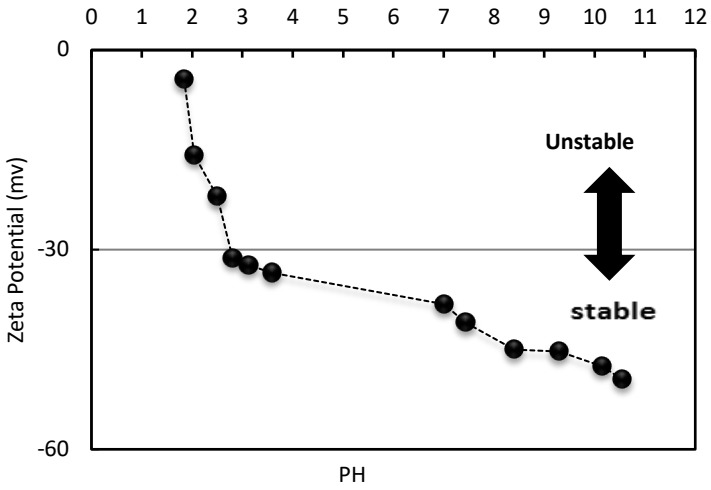

Figure 4.9 Zeta potential Values of CGNPs nanofluids at different pH

4.4.2 Colloidal stability of water-based PEG-Fe_3O_4 nanofluids

The specific amount of PEG-Fe_3O_4 was added to the base fluid for the processing of nanofluids on a defined quantity of distilled water, and the blend was sonicated over 60 minutes. A sequential three-second system was used for the sonication process at a power consumption of 60%. UV-spectroscopy is used to check the stability of synthesized nanofluids in this study. The sample was diluted at 1:20 with DI water to ensure that the samples will absorb detectable UV wavelengths. Then, poured the samples into quartz cuvettes, which were particularly used to transmit UV wavelengths, and measured the absorption of the samples over 50 days at wavelengths of 290-590 nm at specified intervals (Figure 4.10). The photometric study was carried out at various periods and was scheduled for more than 50 days to track the weight concentration of all the samples. The sample weight concentrations decreased at different rates with time, as seen in Figure 4.11a due to sedimentation and agglomerations. It is easy to note that for all of the samples after 50 days, the remaining concentrations of weight were (0.0221 for 0.025 wt.%), (0.0467 for 0.05 wt.%), (0.0713 for 0.075 wt.%), and (0.086 for 0.1 wt.%), respectively. The sedimentation intensity of the samples thus varied at various weight concentrations.

By increasing the number of days following sample preparation, the relative concentration of nanofluid decreased. After 50 days, In the corresponding estimates, the relative sample concentrations were 95.43, 93.61, 88.8, and 86.31% for 0.025 wt.%, 0.05 wt%,0.075 wt.% and 0.1 wt.%, respectively as represented in Figure 4.11b. From these findings, the 0.025-wt% PEG-Fe_3O_4 assay with a relative concentration of 95.43 was attained to the maximum colloidal stability, indicating 4.53% sedimentation after fifty days.

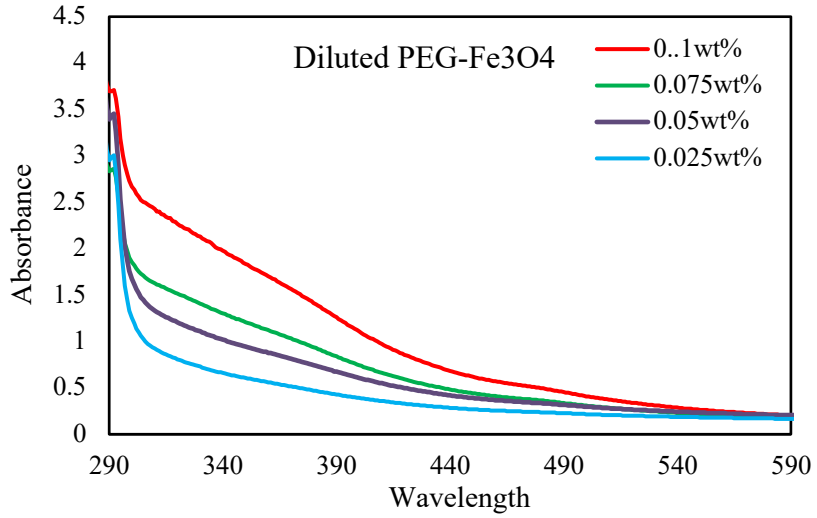

Figure 4.10 UV–Vis absorption, volume diluted at a ratio of 1:20 for the different concentration of PEG-Fe_3O_4 water-based nanofluids

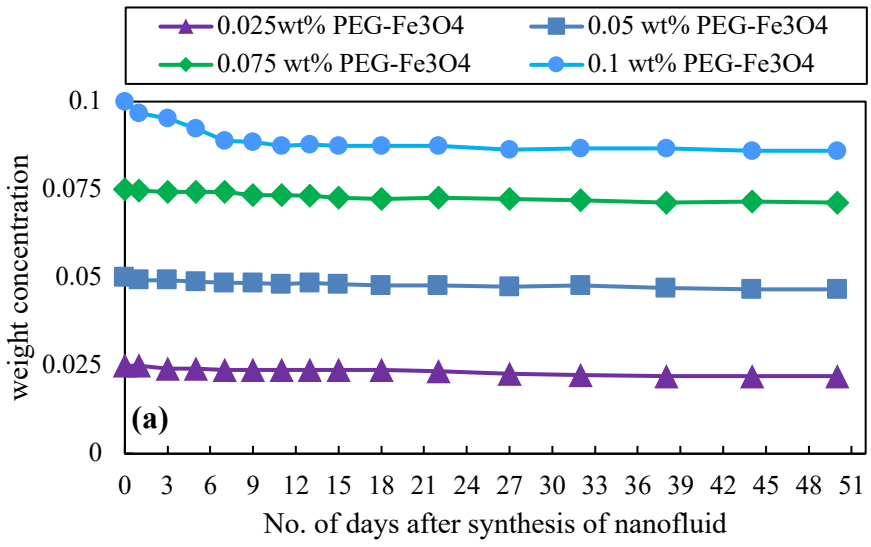

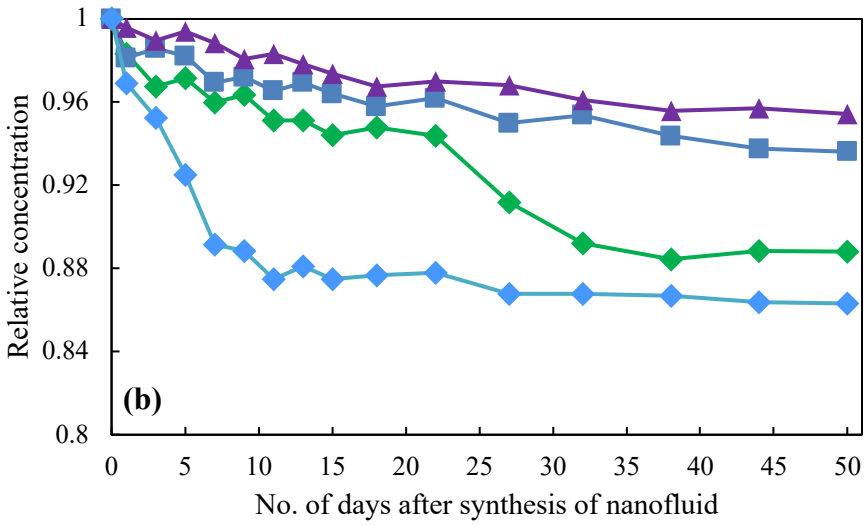

Figure 4.11 (a) Weight concentration and (b) relative concentration of PEG-Fe_3O_4 nanofluid against no. of days at different concentrations

4.4.3 Stability of metal oxide (ZnO and SiO_2) water-based nanofluids

Eight different samples of nanofluids were synthesized by following the two-step method. In this investigation ZnO and SiO_2, materials at four different concentrations of 0.015%,0.1%,0.15%, and 0.2% were prepared. A sequential three-second system was used for the sonication process at an amplitude of 70%, and 30 minutes ultrasonication time was selected for the preparation of nanofluids. The concentrations for ZnO and SiO_2 nanofluids were different from the Carbon and Iron-based nanofluids because the stabilities and thermophysical properties at lower concentrations were low. After the detailed study at the different concentrations, the optimal concentrations were selected with the common concentrations of 0.05% and 0.1% with carbon and Iron-based nanofluids. UV-vis spectroscopy was used to analyze the weight concentration of ZnO and SiO_2 nanofluids as the function of time for more than 30 days. The relative concentration helps the researchers to select the sample with maximum and minimum stability from the available samples. Figure 4.12 represents the relative concentrations of ZnO and SiO_2 at different concentrations. The results indicate that after 30 days, the

relative concentrations of 0.05 wt.%, 0.1 wt.%, 0.15.wt.%, and 0.2 wt.% fresh sample were (87.04, 86.660, 86.425 and 85.665) and (87.42, 86.66, 86.19 and 85.14) for ZnO and SiO_2, respectively. The maximum colloidal stability for both the materials were obtained at 0.05 wt.%, i.e., 87.04 and 87.42, which means that the rate of sedimentation and agglomeration of the particles were 12.96% and 12.56% for ZnO and SiO_2, respectively.

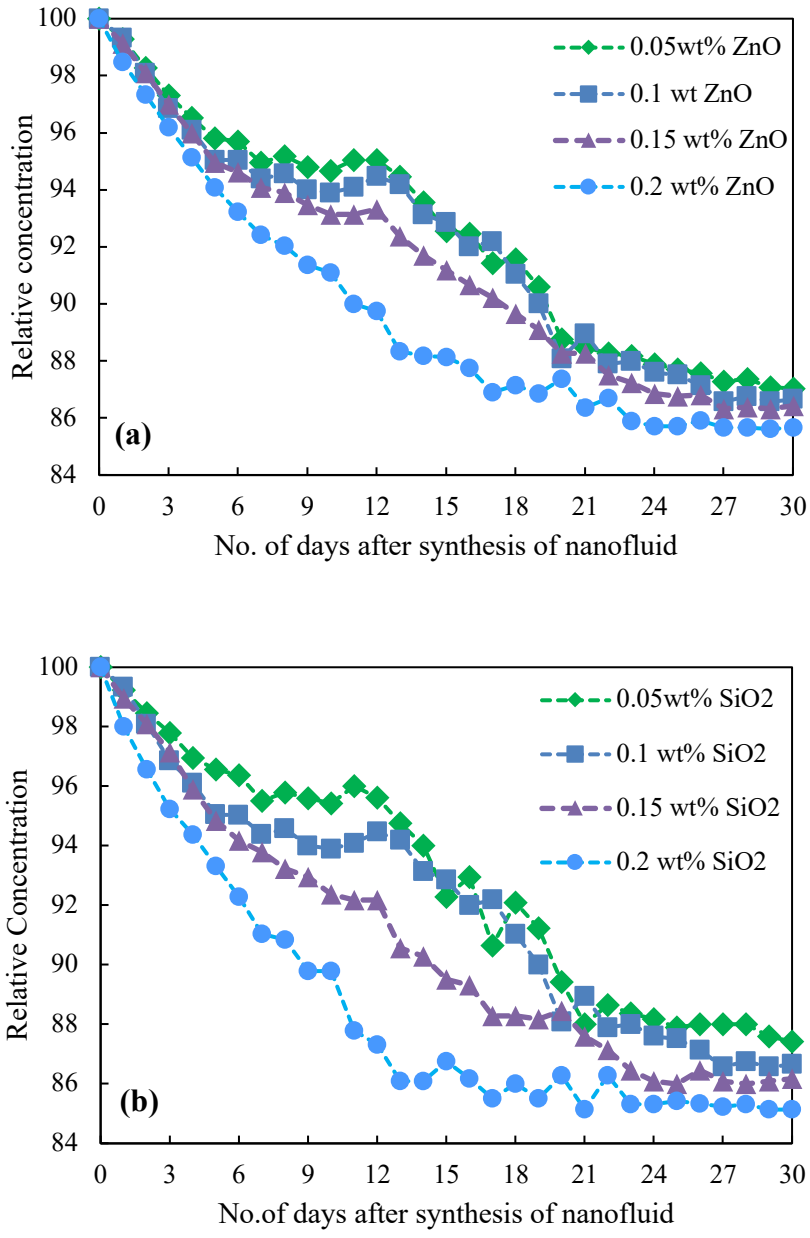

Figure 4.12 Relative concentration of nanofluid as a function of time (a) ZnO (b) SiO_2

4.5 Thermophysical properties of synthesized nanofluids

To precisely measure the thermophysical characteristics of the synthesized nanofluids, stability of the expected data for the thermophysical properties of the base fluid (water) is necessary. The standard thermophysical properties of water provided by Arnold (1970) in the defined temperature range used in the present study were regenerated by using the correlations mentioned in the prior chapter of this study. In this section, detailed information on the thermophysical properties of synthesized nanofluid has presented.

4.5.1 Nanofluids thermal conductivity

KD2 Pro thermal analyzer was used to measure the thermal conductivity of water and synthesized nanofluids in 20 to 45°C temperature range. The calculated data for distilled water has been compared with standard data provided by Arnold (1970) and NIST to verify that the KD2 Pro performs within the specified accuracy limits (Figure 4.13). As predicted, the trend of thermal conductivity of water increases with the increase in temperature was noted. With a maximum error of 4.32% and 3.74%, the KD2 Pro underestimated the standard thermal conductivity values, as presented by Arnold (1970) and NIST, respectively. Therefore, it can be stated that the designed precision level of data acquisition of KD2 Pro is satisfactory.

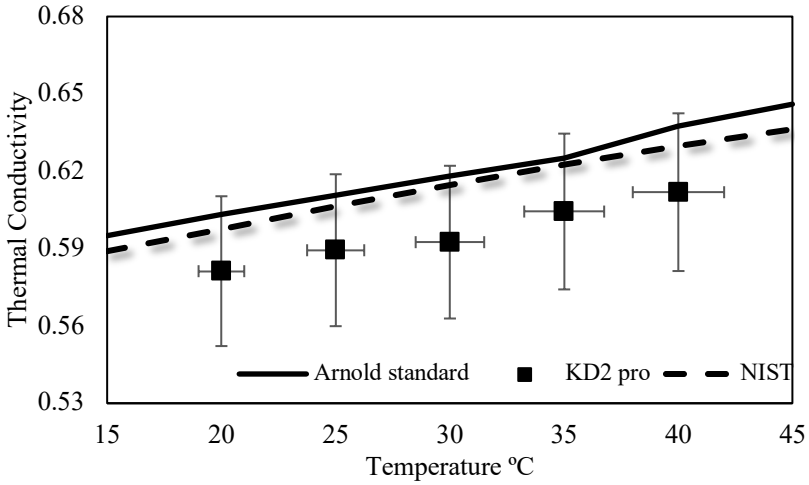

Figure 4.13 A comparison of thermal conductivity values of water measured with KD2 pro, Arnold (1970), and National Institute of Standards and Technology (NIST).

4.5.1.1 Thermal conductivity of clove-treated GNPs

Figure 4.14 showed the thermal conductivity of water and water-based CGNPs at four different concentrations in the temperature range of 20 – 45 ºC. Here, it can be noticed that the enhancement in thermal conductivity of CGNPs nanofluids in the above temperature range was from 0.6120 to 0.6730, 0.6271 to 0.6972, 0.6460 to 0.7380, 0.6690 to 0.7830 W/m K at weight concentration of 0.025% 0.05%, 0.075% and 0.1%, respectively. The resulting percentage improvements of nanofluids in thermal conductivity in comparison with water was from 5.29% to 8.02%, 7.9% to 11.91%, 11.13% to 18.45%, 15.1% to 25.68% at weight concentration of 0.025% 0.05%, 0.075% and 0.1%, respectively. From these outcomes, it can be concluded that the rise in weight concentration and temperature can cause the enhancement in thermal conductivity of CGNPs nanofluid, and the maximum improvement was noticed by 25.68% at 0.1 wt.%.

The experimental data obtained from the KD2 Pro device for CGNPs nanofluids at different weight concentrations and temperature range compared with the available

thermal conductivity models Maxwell (1881), Hamilton & Crosser (1962), Bruggeman, and Lu-Lin (1996) (Figure 4.15) as presented in chapter 2. From Figure 4.15, it can be represented that at a low concentration of 0.025 wt.% Maxwell (1881), Lu-Li (1996) and Bruggeman Model were well matched with the experimental data taken from KD2 Pro for CGNPs nanofluid. As concentration increases from 0.05 wt.% to 0.1 wt.%, only Lu-Li (1996) model was well-matched with experimental data taken from KD2 Pro; all three other models underestimated the experimental data at higher concentrations.

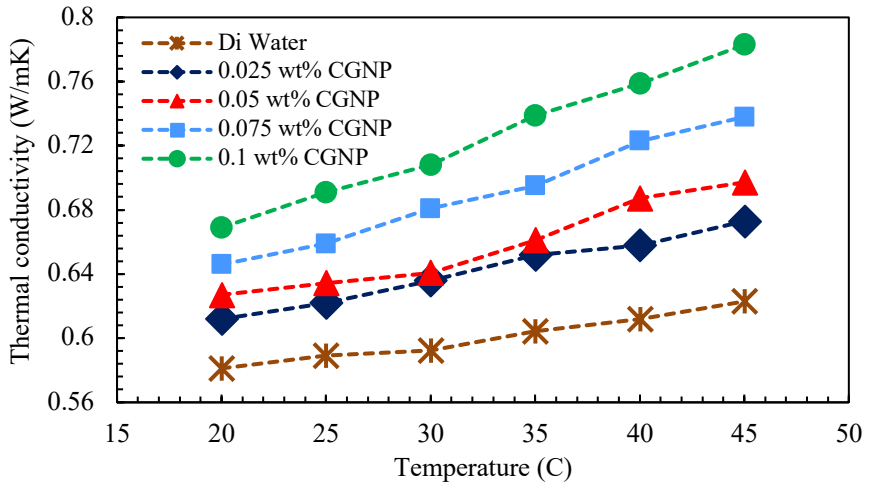

Figure 4.14 Thermal conductivity of CGNPs nanofluid and water at different temperatures and concentrations

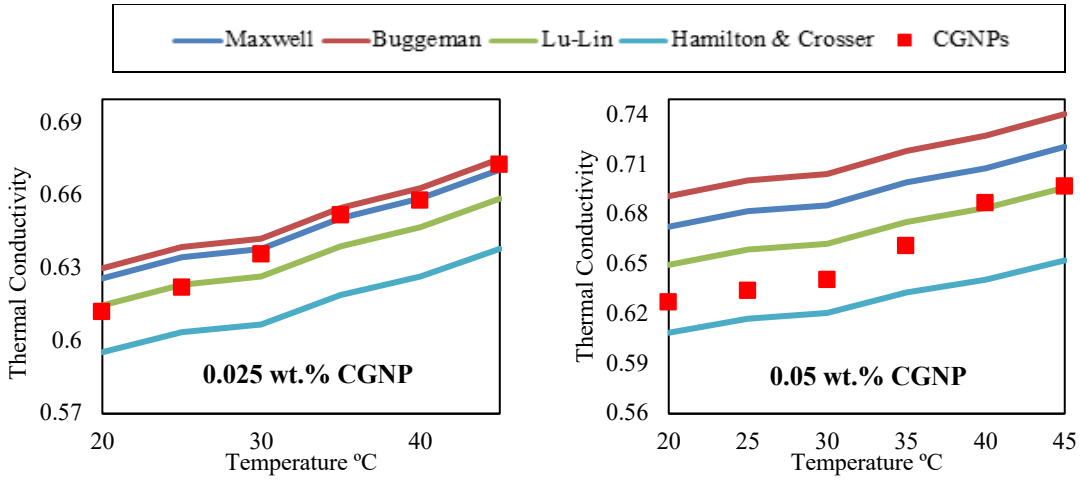

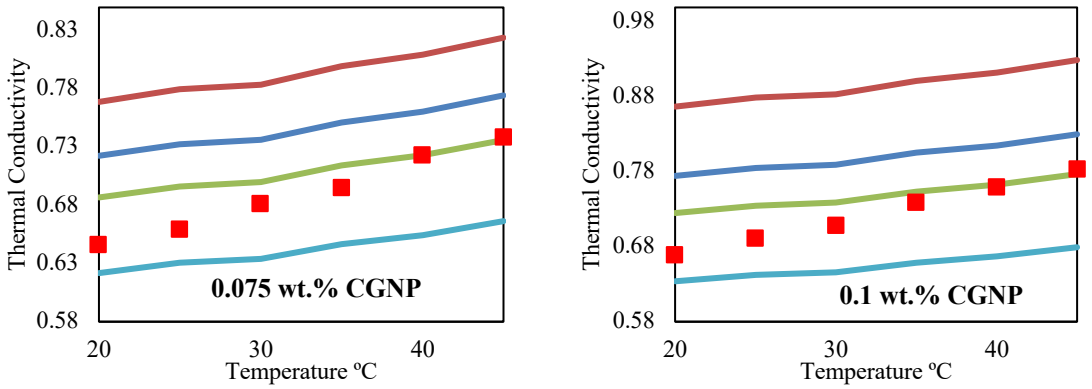

Figure 4.15 Comparison of thermal conductivity of CGNPs nanofluid measured with KD2 Pro at different concentrations with the available model of thermal conductivity

4.5.1.2 Thermal conductivity of PEG-Fe_3O_4 nanofluid

Thermal conductivity of $PEG-Fe_3O_4$ nanofluid with four different weight concentrations and temperature range of 25 to 45 ºC was presented in Figure 4.16. It was observed from Figure 4.16 that as temperature and weight concentration of nanofluids increases the thermal conductivity of nanofluids increases. For the weight concentration of 0.025%,0.05%,0.075% and 0.1% of $PEG-Fe_3O_4$ nanofluids the thermal conductivity of respective concentration in the temperature ranges from 25 to 45 ºC was 0.607 – 0.649, 0.620 – 0.669, 0.627-0.680, and 0.637-0.694 W/m K. Similarly, the percentage enhancement of thermal conductivity of $PEG-Fe_3O_4$ nanofluids in comparison with water for the same temperature range was 4.401% to 6.067%, 6.72% to 9.35%, 7.87% to 11.19% and 9.59% to 13.35% at of weight concentration of 0.025% 0.05%, 0.075% and 0.1%, respectively. Based on these results, it was concluded that the thermal conductivity of $PEG-Fe_3O_4$ nanofluids increase with an increase in concentration and temperature while the highest improvement was noticed at a weight concentration of 0.1%, i.e., 13.35%.

Four thermal conductivity models Maxwell (1881), Hamilton & Crosser (1962), Bruggeman, and Lu-Lin (1996), were used to compare the experimental data with available models. The graphical representation of experimental data, along with the selected models, was presented in Figure 4.17. Based on these selected models, it was observed that at low concentration Lu-Lin (1996) model was well matched with the experimental data taken from KD2 Pro. It may because Lu-Lin (1996) model considered the spherical and non-spherical particles separately. Also, the interactions between near and far-field pairs are considered. For a high concentration of nanofluid, i.e., 0.075% and 0.1%, the Hamilton & Crosser (1962) model give better agreement with experimental data taken from KD2 Pro, as shown in Figure 4.17.

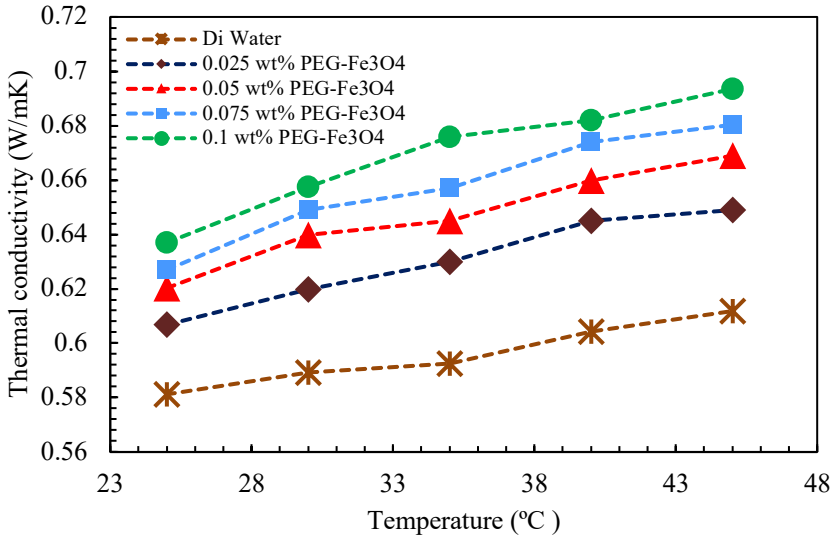

Figure 4.16 Thermal conductivity of PEG-Fe_3O_4 nanofluid and water at different temperature and concentrations.

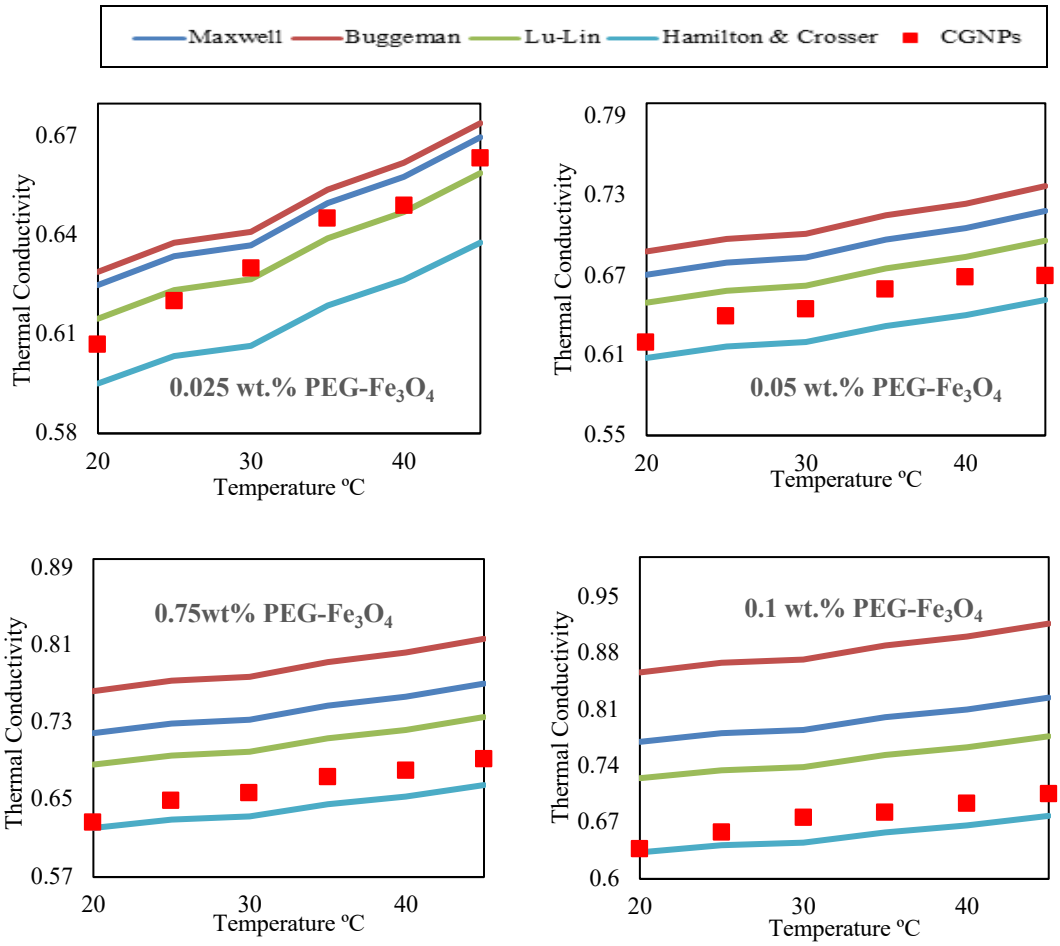

Figure 4.17 Comparison of thermal conductivity of PEG-Fe_3O_4 nanofluid measured with KD2 Pro at different concentration with the available model of thermal conductivity

4.5.1.3 Thermal conductivity of SiO_2 and ZnO nanofluids

The measured values of thermal conductivity of SiO_2 and ZnO in comparison with water data are presented in Figure 4.18 at different weight concentrations (0.05%,0.1%0.15%,0.2%) and temperature range (20-40 ºC). The general trend of increment of thermal conductivity of SiO_2 and ZnO samples were matched with the carbon and Iron-based nanofluids, i.e., an increase in thermal conductivity with an increase in weight concentration and temperature. The range of weight concentrations selected in the present study were 0.05%,0.1%0.15%, and 0.2% for SiO_2 and ZnO, which

was different from the range of weight concentrations of Carbon and Iron-based nanofluids (0.025%,0.05%,0.075%,0.1%). The main reason behind this difference is the low thermal conductivity behavior of SiO_2 and ZnO nanofluids at low concentrations. In order to compare the effect of all materials on thermophysical properties and thermal performance of FPSC, 0.05 wt.%, and 0.1 wt.% was chosen as common concentrations. From the Figure 4.18 (a) it was observed that thermal conductivity of SiO_2 improve from 0.613 to 0.640, 0.620 to 0.657, 0.638 to 0.661, and 0.644 to 0.678 W/m K for weight concentration of 0.05%,0.1%0.15%, and 0.2%, respectively. Similarly, for the ZnO nanofluid this enhancement was from 0.617 to 0.648, 0.625 to 0.660, 0.648 to 0.675 and 0.671 to 0.702 W/m K at weight concentrations of 0.05%,0.1%0.15%, and 0.2%, respectively as shown in Figure 4.18 (b). The percentage enhancement of SiO_2 and ZnO nanofluids in comparison with water for the temperature range of 20 to 40 ºC were 4.63% to 5.73%, 6.71% to 8.16%, 8.01% to 10.11%, 10.40% to 11.49%; and 5.93% to 6.36%, 7.53% to 9.09%, 10.32% to 12.58%,13.40% to 15.42% at of weight concentration of 0.05%,0.1%0.15%, and 0.2%, respectively. The main reason behind this increment in thermal conductivity is liquid molecular level layering at the interface between fluid and particles, Brownian motion, cluster impact, and nature of thermal transport.

A comparison of thermal conductivity of CGNPs, $PEG-Fe_3O_4$, SiO_2 and ZnO nanofluids at the weight concentrations of 0.05% and 0.1% with water are presented in Figure 4.19 (a-b). Thermal conductivity of all the samples improved in the compassion with water data. However, the thermal conductivity of CGNPs was dominant on other nonfluids at both the concentrations of 0.05% and 0.1% (Alawi et al., 2019a). The minimum thermal conductivity reported for SiO_2 at the concentration of 0.05% and 0.1% in comparison with other material's thermal conductivity. As a whole, it was concluded that all the selected materials improved the thermal conductivity of suspension when they

were dissolved in the base fluid (water) (Omer A Alawi, AR Mallah, SN Kazi, Nor Azwadi Che Sidik, & G Najafi, 2019b).

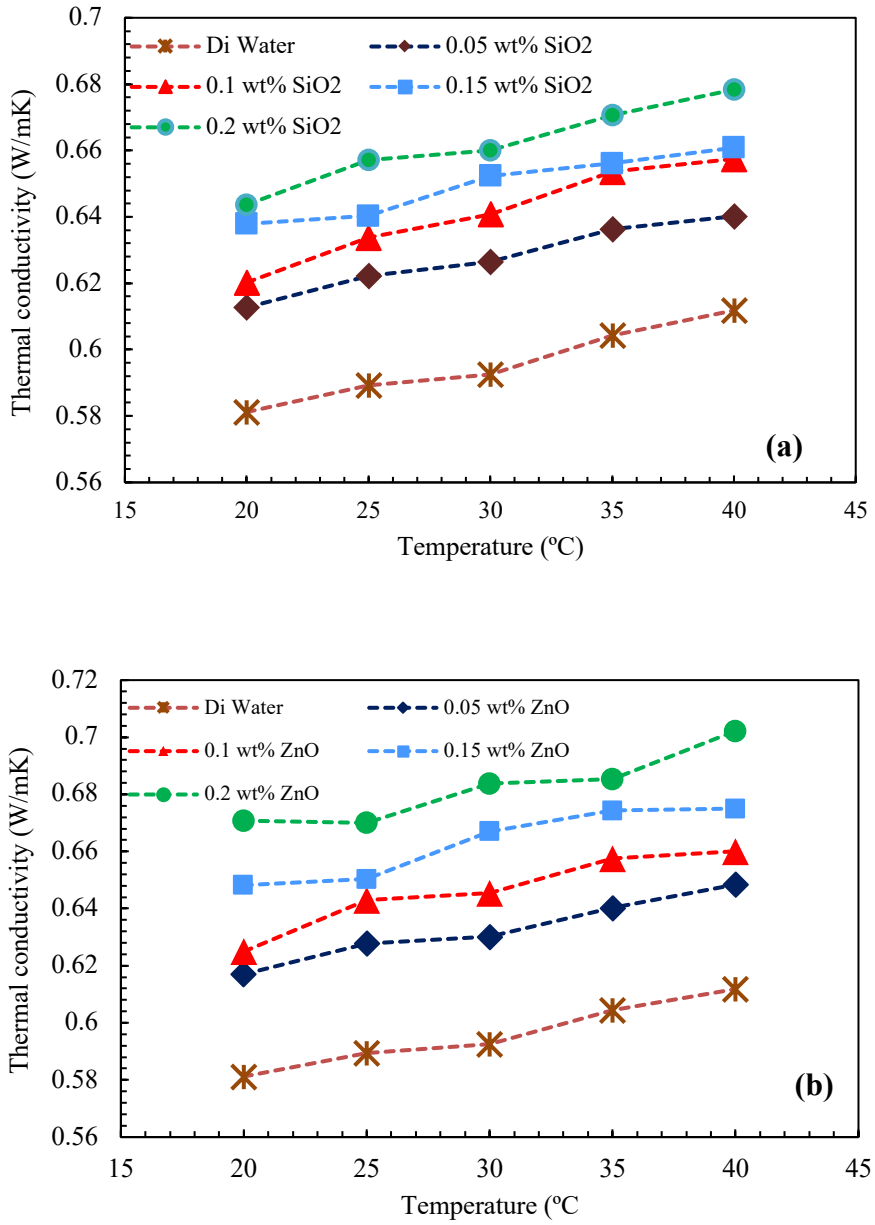

Figure 4.18 Thermal conductivity values at different temperature and concentrations for (a) SiO_2 (b) ZnO

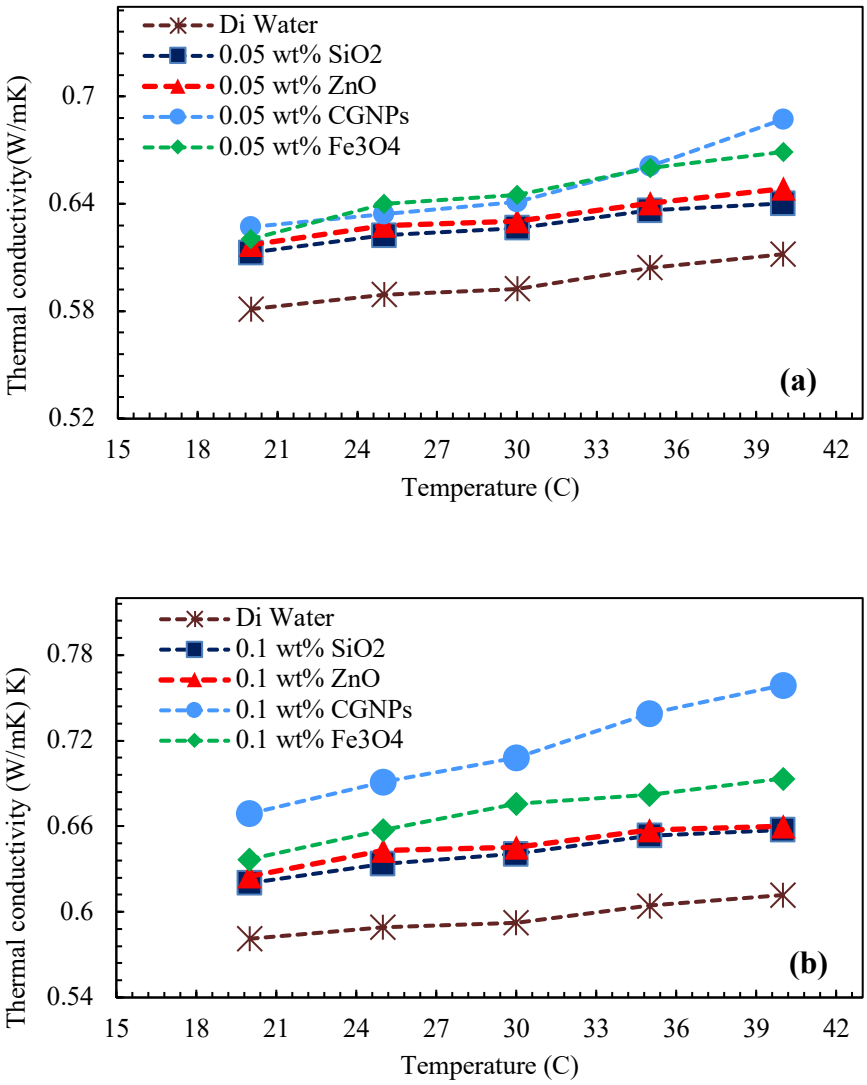

Figure 4.19 A comparison of thermal conductivity of different nanofluids and water at (a) 0.05 wt.% (b) 0.1 wt.%

4.5.2 Dynamic Viscosity of synthesized Nanofluids

By comparing the calculated viscosity values for distilled water at a shear rate of 200-1/s with the standard values of Arnold (1970), a maximum deviation of 0.47% was observed (Figure 4.20), the precision and reliability of the rheometer was checked. Therefore, a rheometer was found suitable as a measuring device for the viscosity of nanofluids.

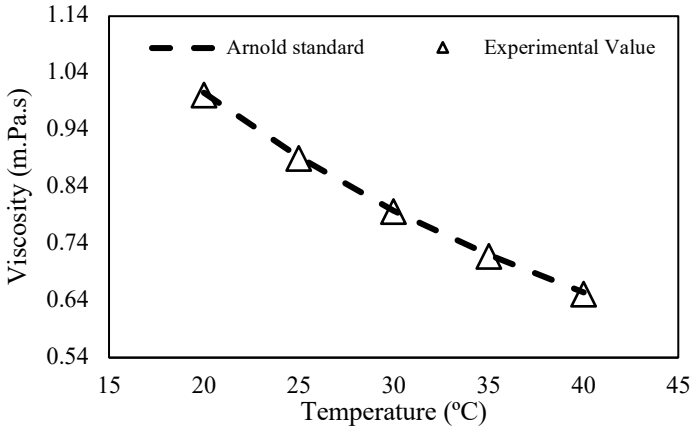

Figure 4.20 A comparison of measured viscosity versus standard values presented by Arnold (1970) for DI water at 200 1/s shear rate

4.5.2.1 Viscosity of clove-treated GNPs

A comparison of the dynamic viscosity against shear rate (20-200 1/s) of water-based CGNPs at the weight concentrations of 0.025%,0.05%,0.075%, and 0.1%; and temperature range of 20 - 40 °C is presented in Figure 4.21. As far as the shear rate increases, the value of viscosity remains almost the same at a specific temperature for CGNPs nanofluid, which proves that the nanofluid behaves as a Newtonian fluid. However, the value of viscosity decreases with an increase in temperature and increases with an increase in concentration. Figure 4.22 represents the measured values of the viscosity of DI water and water based CGNPs nanofluids versus temperature. The dynamic viscosity of CGNPs nanofluid is higher than that of DI water at every concentration. The percentage enhancement in viscosity of CGNPs nanofluids in comparison with water at the weight concentrations of 0.025%, 0.05%, 0.075% and 0.1% and temperature range of 20 - 40 °C were (6.3% - 6.5%), (6.9% - 7.6%), (10.1% - 13.7%) and (11.6% - 12%), respectively. The maximum percentage enhancement was noted at the weight concentration of 0.1% CGNPs nanofluid.

Furthermore, the dynamic viscosity of nanofluid was compared with three different classical models of viscosity (as presented in chapter 2) at two different temperature

values of 30 and 40 degrees (Figure 4.22). As shown in Figure 4.23, the measured values of nanofluid were well matched with the Einstein and Batchelor classical model with a maximum deviation of 6.3% and 6.1% at 30 °C; 7.3% and 7.1% at 40 °C, respectively. At the same time, the Brinkman model showed the under-predicted values of viscosity with a maximum deviation of 16.1% and 15.1% at 30°C and 40°C, respectively. High colloidal stability and low viscosity of nanofluid are the critical factors for the effective use of nanofluid as a working fluid in heat transfer applications. It was concluded that the CGNPs nanofluids at all the concentrations was suitable for the use of heat transfer applications (Behi & Mirmohammadi, 2012; Duangthongsuk & Wongwises, 2010).

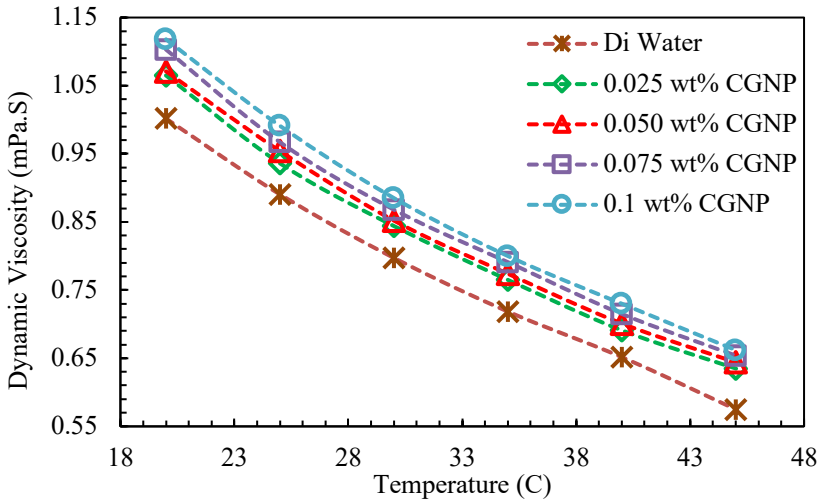

Figure 4.21 A comparison of the measured values of dynamic viscosity of CGNPs at different concentrations and temperatures with DI water

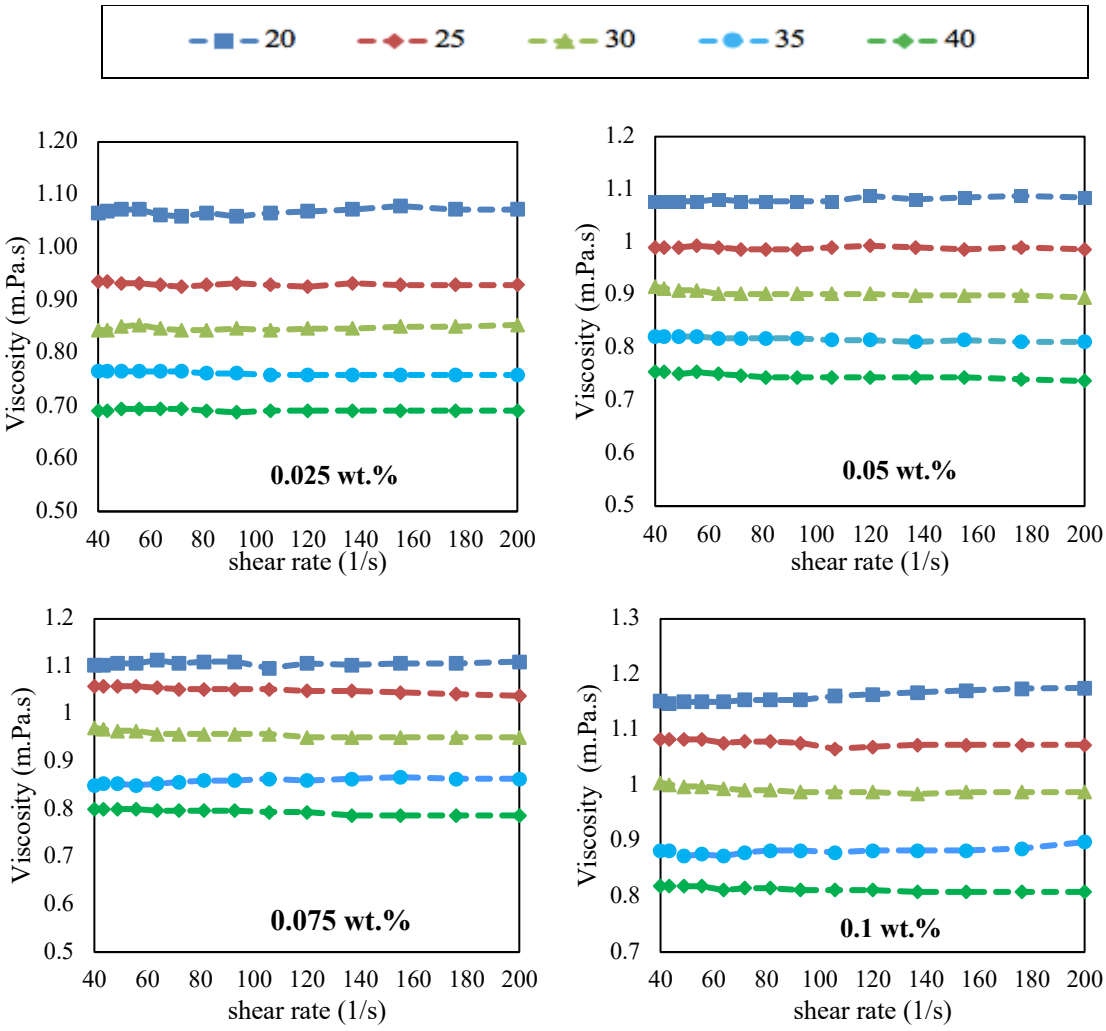

Figure 4.22 Experimental values of the viscosity of clove-treated GNPs against the shear rate at the weight concentrations of 0.025%,0.05%,0.075% and 0.1% of CGNPs nanofluids

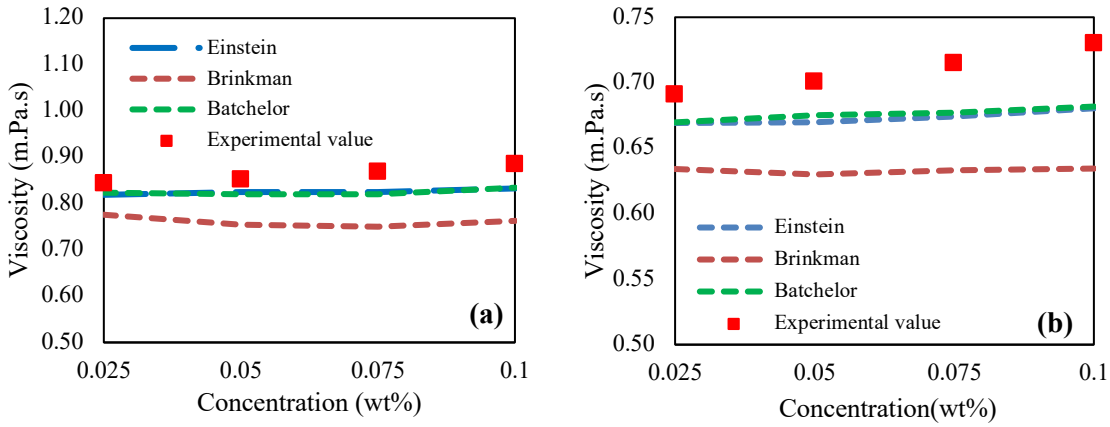

Figure 4.23 Plot of measured values of viscosity for clove-treated GNPs with the classical model (Brinkman, Batchelor, and Einstein) at (a) 30°C and (b) 40°C

4.5.2.2 Viscosity of PEG-Fe_3O_4 nanofluid

Figure 4.24 represents the comparison of experimental viscosity of DI water and water-based PEG-Fe_3O_4 nanofluids versus temperature at a shear rate of 200 1/s. The viscosity of PEG-Fe_3O_4 nanofluid is higher than that of DI water at each concentration, and the viscosity of nanofluid decreases with an increase in temperature. The enhancement in viscosity of PEG-Fe_3O_4 nanofluids in comparison of water at weight concentration of 0.025%, 0.05%, 0.075% and 0.1% and temperature range of 20 - 40 °C was (12.08% - 2.08%), (19.59% - 7.4%), (21.3% - 13.5%) and (22.41% - 20.9%), respectively. The highest percentage enhancement was noted at a weight concentration of 0.1% and 20°C. Figure 4.25 showed the viscosity of PEG-Fe_3O_4 nanofluids against the shear rate (20-200 1/s) at a weight concentration of 0.025%,0.05%,0.075%,0.1% and temperature range of 25-40 °C. From Figure 4.25, it can be observed that the viscosity of nanofluid at a fixed temperature was constant, which confirm the Newtonian behavior of nanofluid. Also, the viscosity of PEG-Fe_3O_4 nanofluid was compared with the three viscosity models, as presented in the previous section. Figure 4.26 represents the comparison of experimental viscosity of nanofluid with Einstein, Batchelor, and Brinkman classical model at 30°C and 40°C. From Figure 4.26, it was concluded that viscosities of all concentrations of nanofluids were well matched with Einstein and Batchelor classical model at 40°C. Based on the high stability and low viscosity of PEG-Fe_3O_4 nanofluid, it was concluded that PEG-Fe_3O_4 nanofluid could be used for the heat transfer applications.

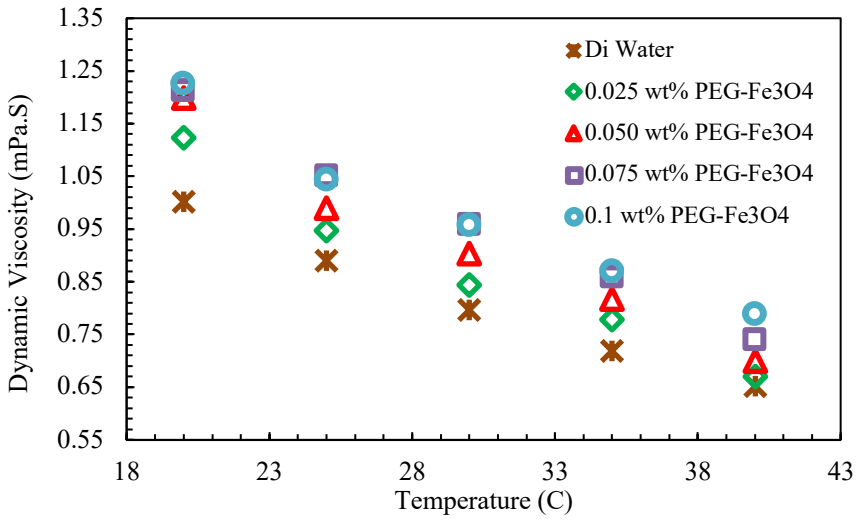

Figure 4.24 A comparison of measured values of dynamic viscosity of PEG- Fe_3O_4 at different concentration and temperature with DI water

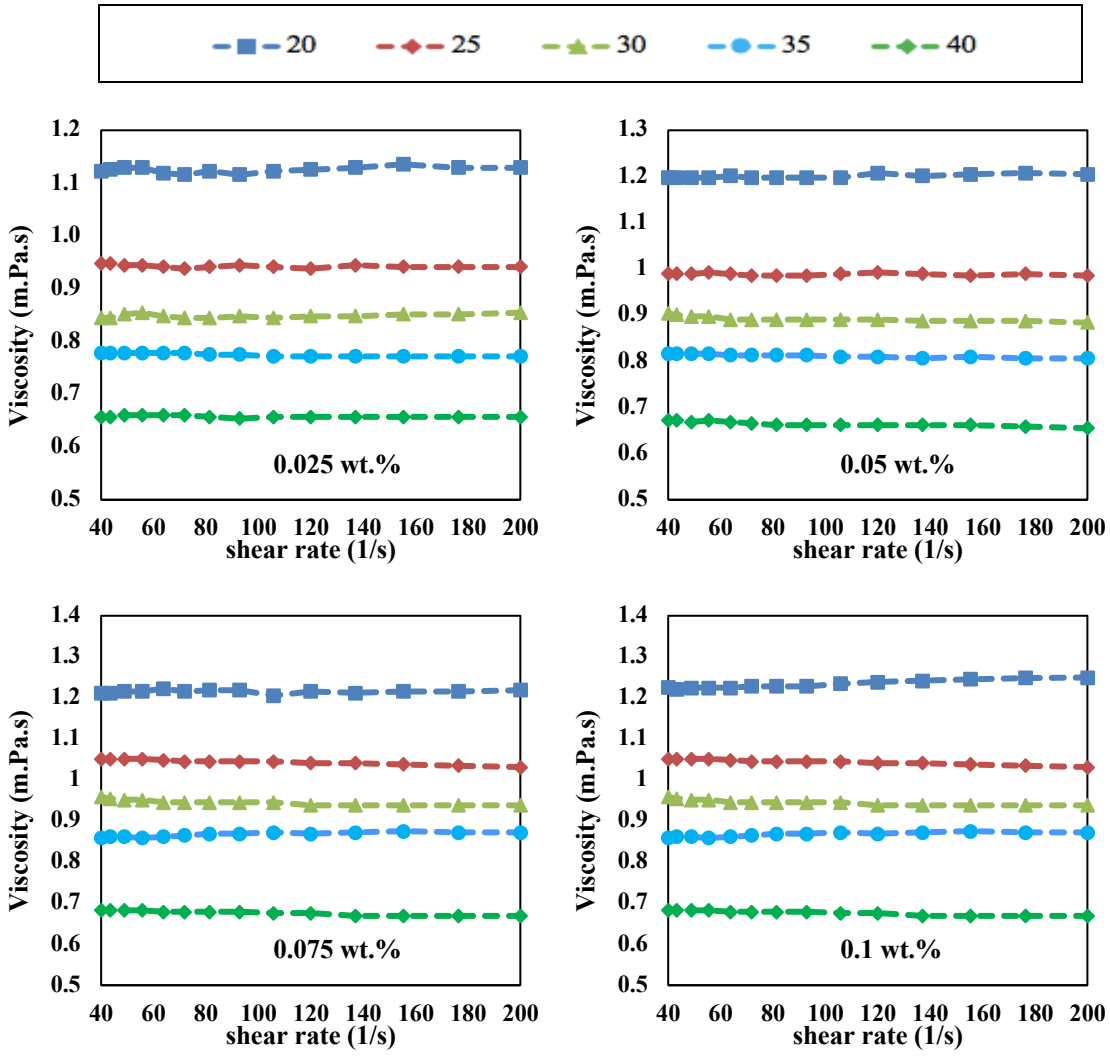

Figure 4.25 Experimental values of the viscosity of PEG- Fe_3O_4 against the shear rate at a weight concentration of 0.025%,0.05%,0.075% and 0.1% of PEG- Fe_3O_4 nanofluids

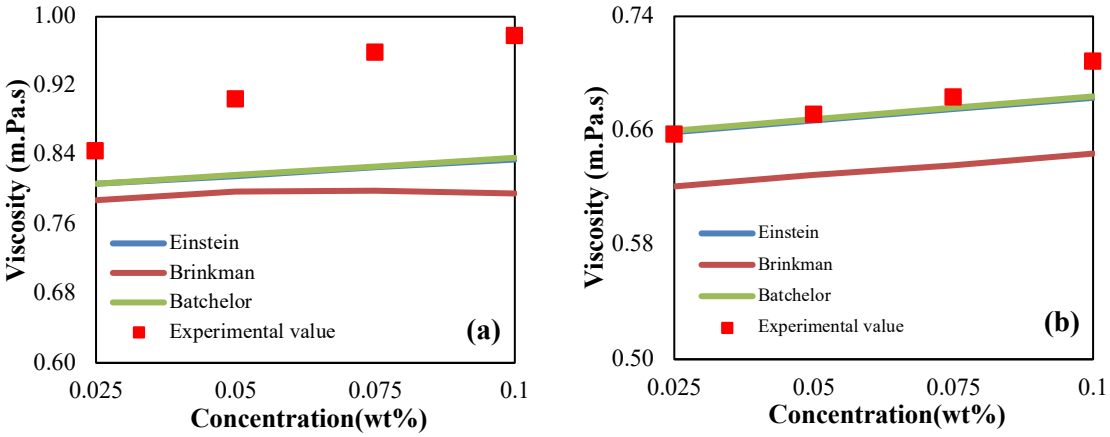

Figure 4.26 Plot of measured values of viscosity for PEG- Fe_3O_4 with the classical model (Brinkman, Batchelor, and Einstein) at (a) 30°C and (b) 40°C

4.5.2.3 Viscosity of metal oxide (SiO_2, ZnO) nanofluids

The viscosity of SiO_2 and ZnO nanofluids at a shear rate of 200-1/s, different temperatures, and weight concentrations are presented in Figure 4.27 (a-b). As presented in Figure 4.27 the viscosity of SiO_2 nanofluids at the weight concentrations of 0.05%, 0.1%, 0.15%, and 0.2% in the temperature range of 20 - 40°C was decreased with the increase of temperature and increased with the increase of concentration. The percentage enhancement in viscosity of SiO_2 nanofluids in comparison with water was (5.39% - 7.63%), (7.20% - 12.66%), (13.4% - 20.41%) and (18.23% - 24.05%) at the weight concentration of 0.05%, 0.1%, 0.15% and 0.2% in the temperature range of 20 - 40 °C, respectively. Similarly, Figure 4.27b represents the viscosity of ZnO nanofluids with the weight concentrations of 0.05%, 0.1%, 0.15%, and 0.2% in the temperature range of 20 - 40 °C. The percentage enhancement in viscosity of ZnO nanofluids in comparison with water at the weight concentration of 0.05%, 0.1%, 0.15%, and 0.2% at the said temperature range was (2.25% - 1.27%), (5.58% - 7.35%), (5.69% - 8.48%) and (7.44%

- 9.41%), respectively. The viscosity enhancement of ZnO was less as compared with SiO_2 nanofluids; it may happen due to the absence of surfactants required for the SiO_2 nanofluids synthesis and the particles might agglomerate sooner. Similarly, the higher viscosities of the SiO_2 and ZnO nanofluids were noticed at the higher weight concentrations range in comparison with the CGNPs and PEG-Fe_3O_4 nanofluids.

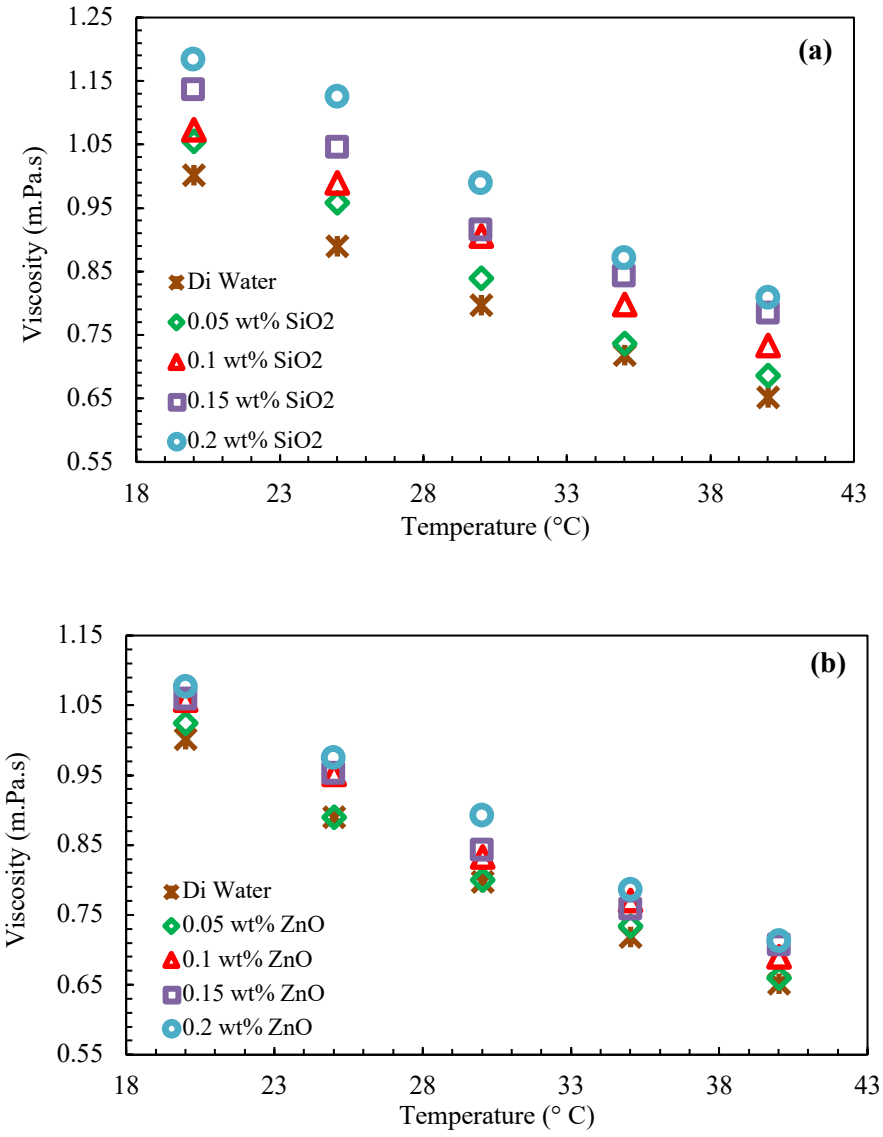

Figure 4.27 Comparison of measured values of viscosity against temperature at a shear rate of 200-1/s for water and different concentration of (a) SiO_2 (b) ZnO

4.5.3 Density of nanofluids

Due to the relatively higher density of the solid materials in comparison with liquid, the density of nanofluid increased as we add the nanomaterials were added in the base fluid, and it enhanced with the increase in weight concentrations. But the density of nanofluid decreased with the increase in temperature of the sample (Chandrasekar, Suresh, & Senthilkumar, 2012). The precision and reliability of density meter were verified through contrasting density calculation values for water at different temperatures with standard values of Arnold (1970), the maximum difference of 0.027% between experimental and standard values was noted (Figure 4.28). Therefore, it was concluded that the density meter could be a suitable instrument for evaluating the nanofluid density with very high precision.

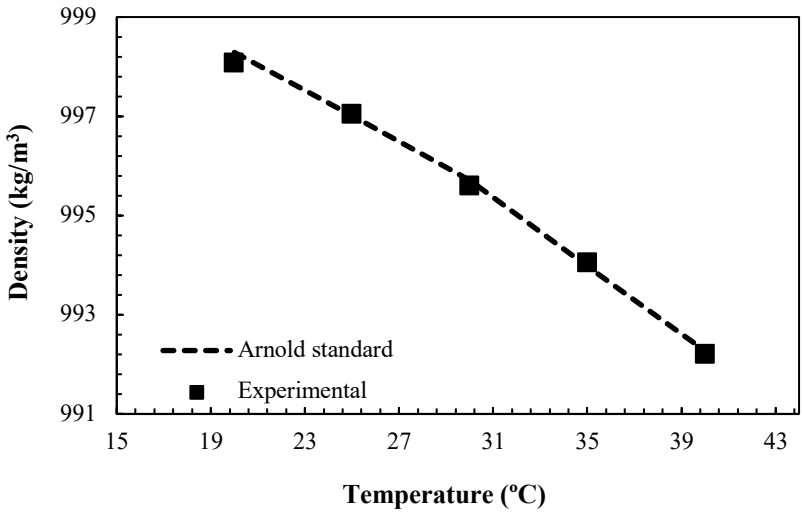

Figure 4.28 Comparison of the calculated density values at various temperatures for DI water with the reference values given by Arnold (1970).

4.5.3.1 Density of clove-treated GNPs

Figure 4.29 represents the measured values of the density of clove-treated GNPs at different weight concentrations and temperatures in comparison to the measured density of water. As described in Figure 4.29, the density of CGNPs nanofluid increases slightly

with weight concentration while it decreases as the temperature of nanofluid increases. The maximum increment noticed in the density of nanofluid was 0.08% in comparison to water. The experimental values of the density of nanofluid were compared with the calculated values of the Pak & Cho (1998) equation, as represented in Figure 4.30. The maximum difference of 0.12% was observed at a weight concentration of 0.1 wt.%. Thus, the Pak & Cho (1998) equation can be considered to be highly accurate for measuring the density values of water-based CGNPs nanofluids.

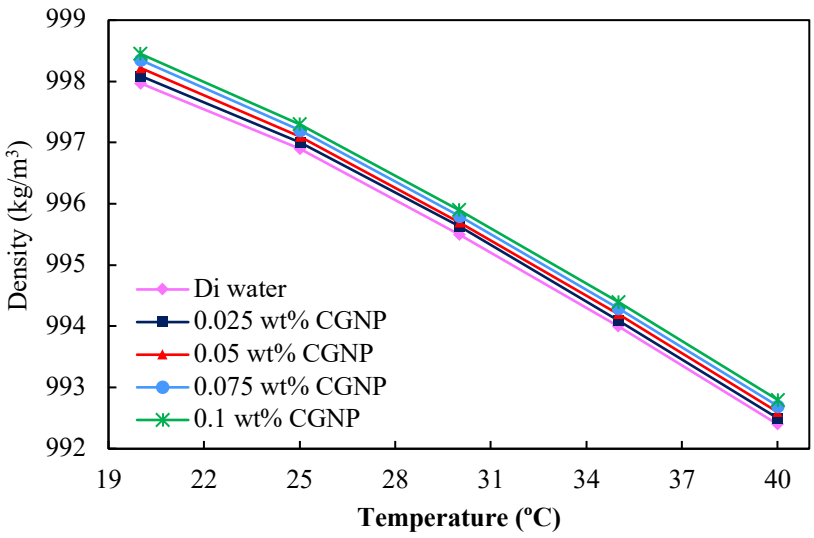

Figure 4.29 Experimental density values of DI water and clove-treated CGNPs nanofluid at different weight concentrations and temperatures.

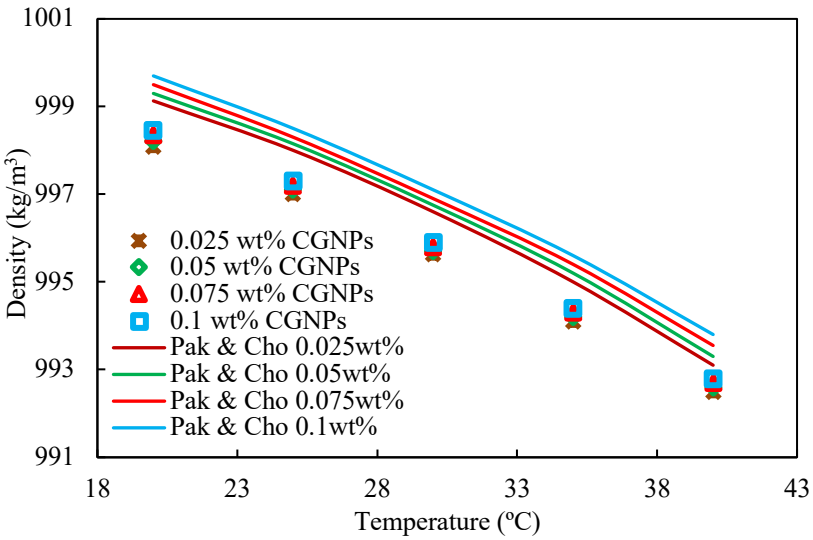

Figure 4.30 Comparison of experimental density values of CGNPs with Pak & Cho (1998) equation's values

4.5.3.2 Density of PEG-Fe_3O_4 nanofluid

The experimental values of density for PEG-Fe_3O_4 nanofluid and DI water at different weight concentrations and temperatures are shown in Figure 4.31. Due to the loading of nanoparticles form 0.025 wt.% to 0.1 wt.% causes an insignificant enhancement in the density of PEG-Fe_3O_4 nanofluid, up to 0.060% in comparison to water. The measured density of nanofluid decreases with increases in temperature. Figure 4.32 represents the comparison between the experimental values and calculated values (Pak & Cho (1998)) of density for water-based PEG-Fe_3O_4 nanofluids, which indicate outstanding agreements with a maximum difference of 0.10%. However, the Pak & Cho (1998) equation can be considered suitable to predict the density values of water-based PEG-Fe_3O_4 nanofluid.

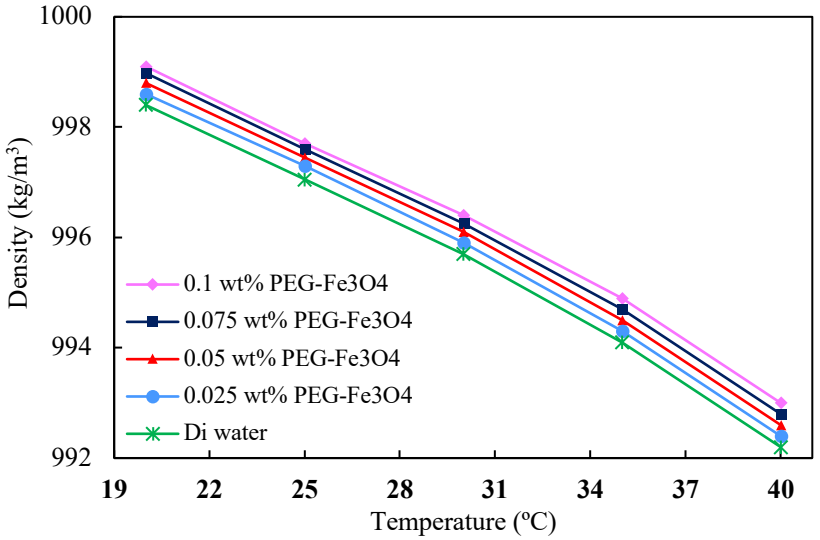

Figure 4.31 Experimental density values of DI water and PEG-Fe_3O_4 nanofluid at different weight concentrations and temperatures

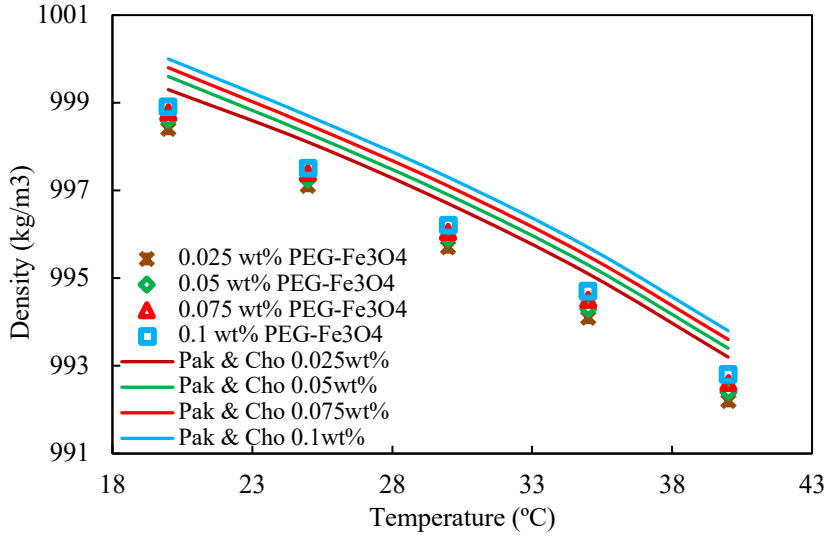

Figure 4.32 Comparison of experimental density values of PEG-Fe_3O_4 with Pak & Cho (1998) equation's values

4.5.3.3 Density of metal oxides (SiO_2, ZnO)

The measured density of SiO_2 and ZnO nanofluids at the weight concentrations of 0.05% - 0.2% and temperature range of 20-40 °C in comparison with water were presented in Figure 4.33 (a-b). The weight concentration ranges for SiO_2 and ZnO nanofluids was higher than that of CGNPs and PEG-Fe_3O_4 nanofluids. However, the

measured density values were high for SiO_2 and ZnO in comparison with other nanofluids. The maximum difference noticed between the density of DI water, SiO_2, and ZnO nanofluids was 0.12% and 0.22%, respectively. Furthermore, the measured values were compared with the calculated values of density for SiO_2 and ZnO nanofluids. Pak & Cho (1998) equation was used to calculate the density of SiO_2 and ZnO nanofluids (Figure 4.34, a-b). The highest difference between measured and calculated densities of SiO_2 and ZnO nanofluids were 0.11% and 0.12%, respectively. It can be observed that the density of nanofluid increased with weight concentration and decreased as temperature increased, but the difference between measured and calculated values of all the nanofluids were increased equally. Accordingly, it was decided that Pak and Cho equation is suitable for calculating the density of nanofluid.

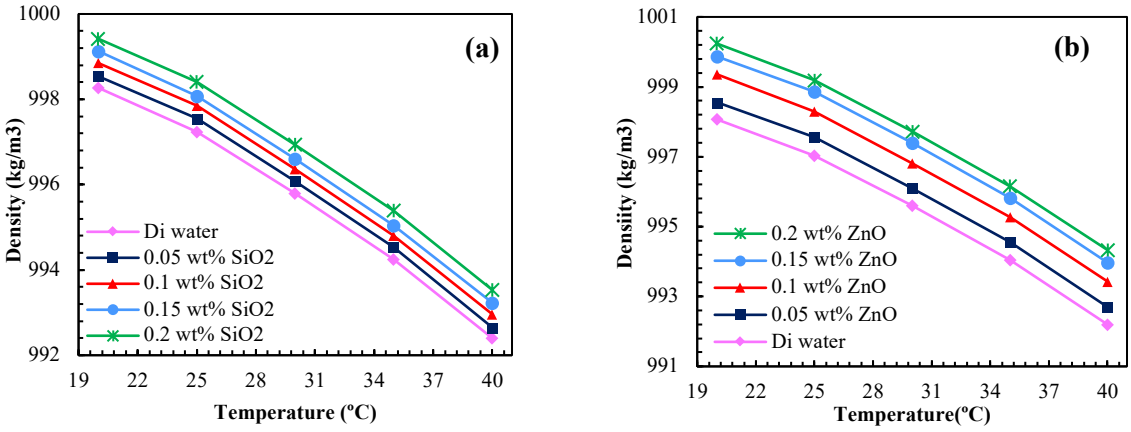

Figure 4.33 Comparison of experimental density values at different weight concentrations and temperatures of (a) SiO_2 (b) ZnO nanofluids with DI water.

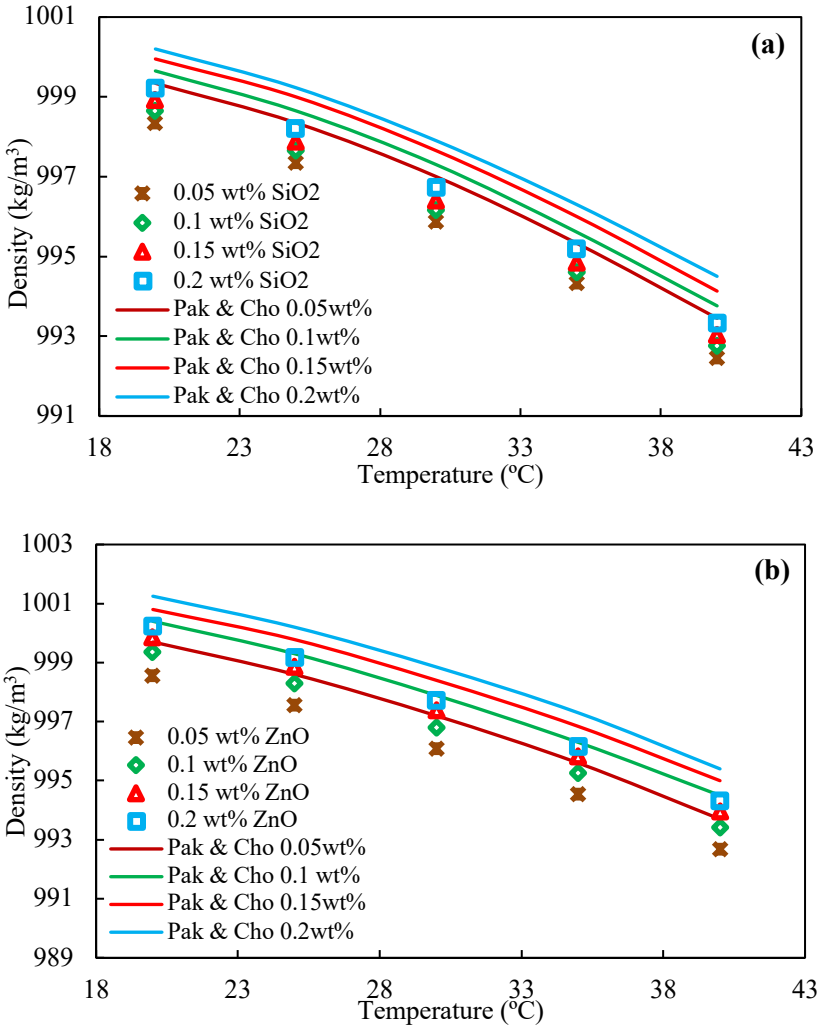

Figure 4.34 Comparison of experimental density values of (a) SiO_2 (b) ZnO with Pak & Cho (1998) equation's values

4.5.4 Specific heat of nanofluids

Figure 4.35 represents the comparison of measured specific heat capacity of DI water with standard values of NIST at different temperatures. The primary purpose of this comparison is to check the reliability and accuracy of the DSC device. The maximum difference between measured and standard values of specific heat was 0.86%, which reflects that the DSC device is reliable to measure the specific heat of nanofluid.

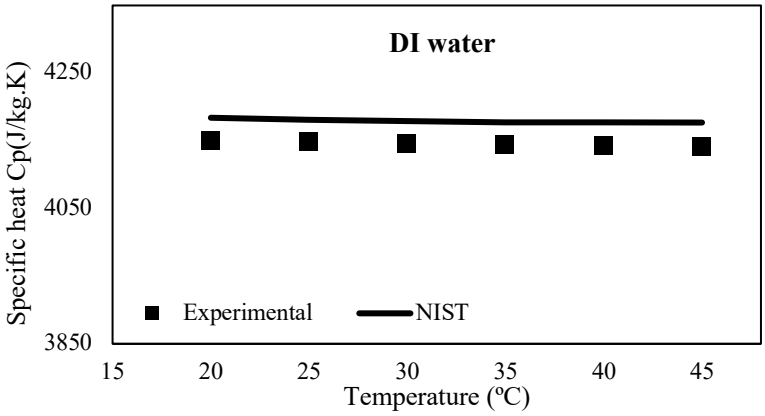

Figure 4.35 Comparison of measured specific heat values with NIST standard values at different temperature for DI water

4.5.4.1 Specific heat of clove-treated GNPs

The calculated specific heat capacity of CGNPs at different weight concentrations and temperatures are presented in Figure 4.36a along with the standard values of NIST and measured values of DI water. From Figure 4.36a, it can be noticed that the specific heat values decreases as the temperature of nanofluid increases. In comparison with water, the measured values of specific heat decreased as weight concentration increased. The maximum difference between the measured values of specific heat capacity of 0.025 wt.%, 0.05wt.%, 0.075wt.%, 0.1wt.% CGNPs nanofluid and DI water was 0.55%, 0.96%, 1.23% and 1.54%, respectively. This decline may be attributed to the fact that solid nanomaterials typically have a lower specific heat value than liquids.

The calculated values of specific heat using Pak & Cho (1998) and Xuan & Roetzel (2000) equations were compared with the experimental values of CGNPs nanofluid at different weight concentrations and temperatures. A sample of the comparison is presented in Figure 4.36b for the 0.1 wt.% CGNPs, which clearly shows that the experimental results are well matched with Xuan & Roetzel (2000) equation while equation Pak & Cho (1998) underestimate the experimentally measured values. The

maximum differences found for 0.1 wt.% CGNPs nanofluids were 0.19% and 1.24% for Xuan & Roetzel (2000) and Pak & Cho (1998), respectively.

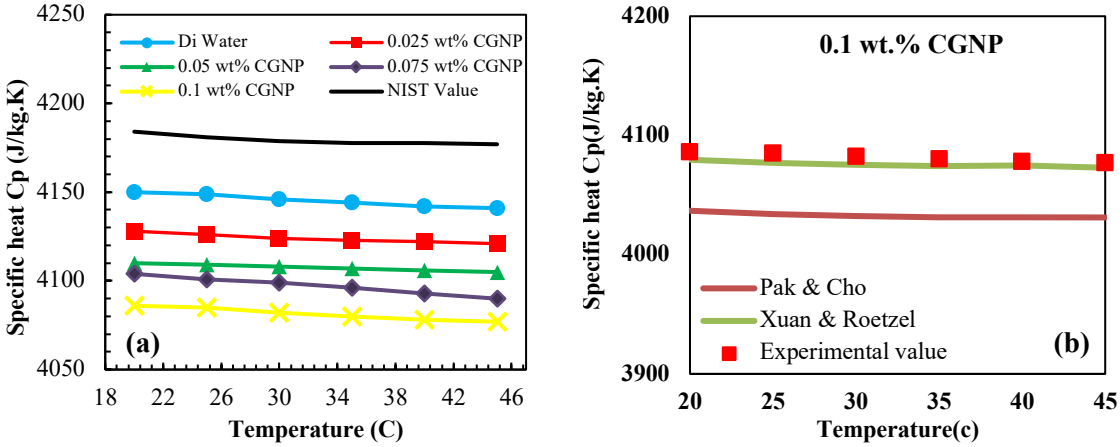

Figure 4.36 (a) Specific heat values of CGNPs nanofluid at different weight concentrations and temperature in comparison to DI water and NIST values (b) Comparison of specific heat capacity of CGNPs with an available correlation of Pak & Cho (1998) and Xuan & Roetzel (2000) at 0.1 wt.%

4.5.4.2 Specific heat of PEG-Fe_3O_4 nanofluid

Figure 4.37a represents the comparison of measured specific heat values of water and PEG-Fe_3O_4 nanofluid at different weight concentrations and temperatures. From Figure 4.37a, it is clear that measured specific heat of PEG-Fe_3O_4 nanofluid decreased in comparison to water, and it also decreased as weight concentration increased. Furthermore, the measured specific heat decreases as temperature increases. The maximum difference between the measured values of specific heat capacity of 0.025 wt.%, 0.05 wt.%, 0.075 wt.%, 0.1 wt.% PEG-Fe_3O_4 nanofluid and DI water was 0.10%, 0.19%, 0.28% and 0.37%, respectively. The experimental values of PEG-Fe_3O_4 nanofluid at 0.1 wt.% were compared with calculated values using Pak & Cho (1998) and Xuan & Roetzel (2000) equations as represented in Figure 4.37b. The maximum differences noticed for 0.1 wt.% PEG-Fe_3O_4 nanofluid were 0.15% and 1.33% for Xuan & Roetzel (2000) and Pak & Cho (1998), respectively.

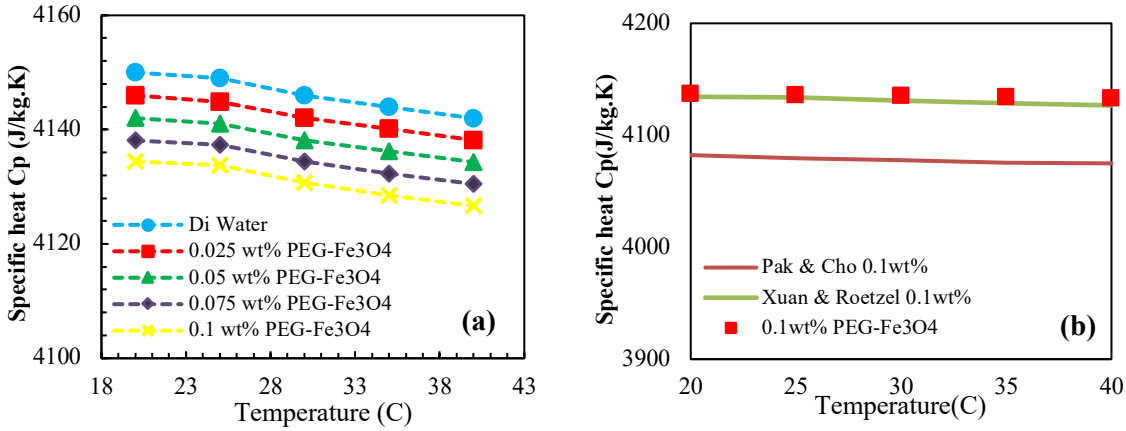

Figure 4.37 (a) Specific heat values of PEG-Fe_3O_4 nanofluid at different weight concentrations and temperature in comparison to DI water (b) Comparison of specific heat capacity of PEG-Fe_3O_4 with an available correlation of Pak & Cho (1998) and Xuan & Roetzel (2000) at 0.1 wt.%

4.5.4.3 Specific heat of SiO_2 and ZnO

The measured specific heat values of SiO_2 and ZnO at weight concentrations of 0.05%,0.1%,0.15%,0.2%, and temperatures range 20-40 °C are presented in Figure 4.38 (a-b) along with the standard values of NIST and measured values of DI water. In comparison with water and the standard values of NIST, the measured values of specific heat decreased as weight concentration increased. The maximum differences between the measured values of specific heat capacity of SiO_2 and ZnO nanofluid at the weight concentration of 0.05%,0.1%,0.15%,0.2% in comparison with DI water and NIST values were 0.55%, 0.96%, 1.23% 1.54% and 0.35%, 0.73%, 1.08% 1.43%, respectively. If the experimental values of specific heat of metal oxides based nanofluid were compared with graphene and iron-based nanofluids, then it was noticed that the decrement in specific heat values is higher than other nanofluids when compare with DI water, this may be attributed that the weight concentration is higher for metal oxides nanofluids.

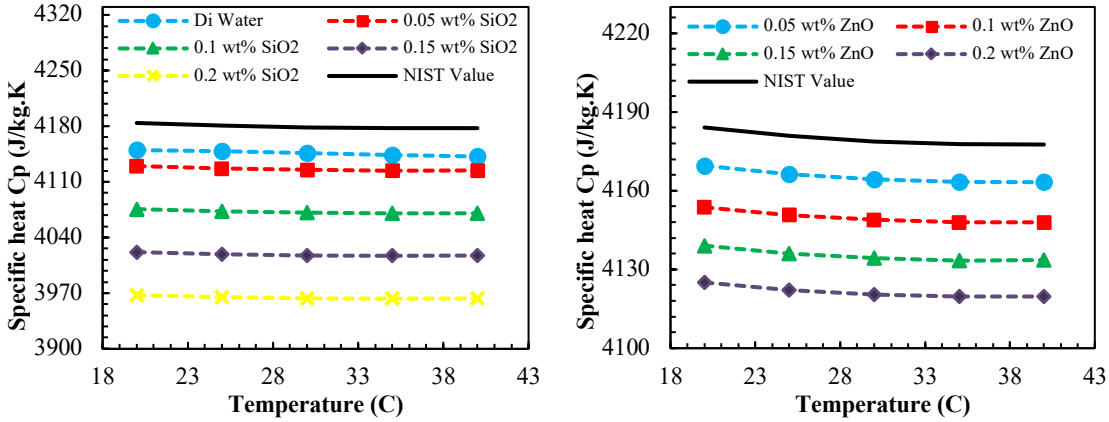

Figure 4.38 Specific heat values of (a) SiO_2 and (b) ZnO nanofluid at different weight concentrations and temperature in comparison to NIST values

4.6 The experimental thermal efficiency of FPSC

This segment includes a graphical description and analysis of the results from the experimental test runs and the ANSYS simulation on the thermal efficiency of the built FPSC test set-up. The working fluids used were DI water and five aqueous colloidal dispersal carbon and metal oxide-based nanofluids with weight concentrations of 0.025% to 0.2%. The environmental factors heat flux (597,775,988 W/m^2), ambient temperature, effect of different weight concentrations (0.025% - 0.2%), mass flow rates (0.8,1.0,1.2 kg/min), and inlet fluid temperature (30 – 50°C) were experimentally and numerically taken under consideration for investigation.

In four different positions along the x-axis, the exterior wall temperatures of the two middle riser tubes (TW) and central line temperature of absorber-plate (AP) were determined. It can be observed that the positions of thermocouples are at 11.4, 34.0, 57.2, 80.1 cm from the reference position of an absorber plate in the direction of the x-axis, it may call the dimensionless axial distance (x/d). The value of TW was taken by the averaged of two riser tubes at each position. The outlet, absorber plate (AP), tube wall (TW), and ambient temperature and pressure drop for each test run were recorded at

steady-state conditions as suggested by the ASHRAE Standard 93-2003 for indoor testing (A. Standard, 2003).

4.6.1 Water as a working fluid in FPSC

The experiments were carried out in the department of mechanical engineering at the University of Malaya, Malaysia, at a time interval of 9:00 to 16:00 h. All the experiments performed by following the ASHRAE Standard 93-2003 for indoor testing and DI water were initially used as the working fluid to check the accuracy, repeatability, and validity of the recorded data. The measured temperature of AP and TW versus dimensionless axial distance (x/d) in the flat-plate solar collector at different heat flux intensities, inlet temperature, and mass flow rate were presented in Figure 4.39, 4.40, and 4.41, respectively. It can be observed from these figures that values of AP and TW increase as the heat flux intensity (Figure 4.39) and fluid inlet temperature (Figure 4.40) increases and decrease as the mass flow rate increases (Figure 4.41). All the test runs were performed several times at different flow rates of 0.8, 1.2, and 1.6 kg/min, and the best data were chosen for presentation. The heat absorbed parameter $F_R(\tau\alpha)$, heat removed parameter $F_R U_L$ and thermal efficiency of flat plate solar collector against reduced temperature parameter for DI water are shown in Table 4.3 and Figure 4.42. From Table 4.3, it is demonstrated that the value of $F_R(\tau\alpha)$ and $F_R U_L$ increase as mass flow rate increase from 0.8 to 1.6 kg/min, so the thermal efficiency also increases with mass flow rate. All the data presented in Figure 4.42 are based on the fitted linear equation, and R^2 represents the root mean square error for these data points, which reflect that how close the data points are to the trend line. Through this, it is evident that the performance of the collector increases as the flow rate rises, which can be due to the decreased AP temperature (Figure 4.41), resulting in lower collector heat losses, i.e., improved collector output. Such a trend is verified by

Figure 4.43, which indicates variance in energy output overflow rate at various intensities of heat flux and fluid inlet temperatures. There it can also be inferred that the efficiency of the FPSC is in direct relation to the intensity of the heat flux (

Figure 4.43b) and inverse proportion to the temperature of the inlet fluid (

Figure 4.43a).

ANSYS simulation for the same defined values of mass flow rate, heat flow intensity, and liquid inlet temperature used in experimental test runs, plus the recorded ambient temperature, were carried out to measure the corresponding predicted values of AP, TW, pressure loss, and output temperature. Then, an experimental and simulated value comparison was made to validate the accuracy and reliability of the data obtained. The experimental and simulated values of AP and TW versus dimensionless axial distance (x/d) at heat flux 998 W/m^2 and inlet fluid temperature 30°C were presented in Figure 4.44, a very strong agreement between these values with a maximum difference of 2.21% and 2.48% were noticed for AP and TW, respectively. Moreover, a comparison is made between simulated and experimental thermal efficiency at a different mass flow rate, as shown in Figure 4.45, which reveals that both values are well-matched with a maximum difference of 3.22% at 1.6 kg/min. Therefore, it can be inferred that the data obtained from the experimental test run and ANSYS simulation is accurate and reliable.

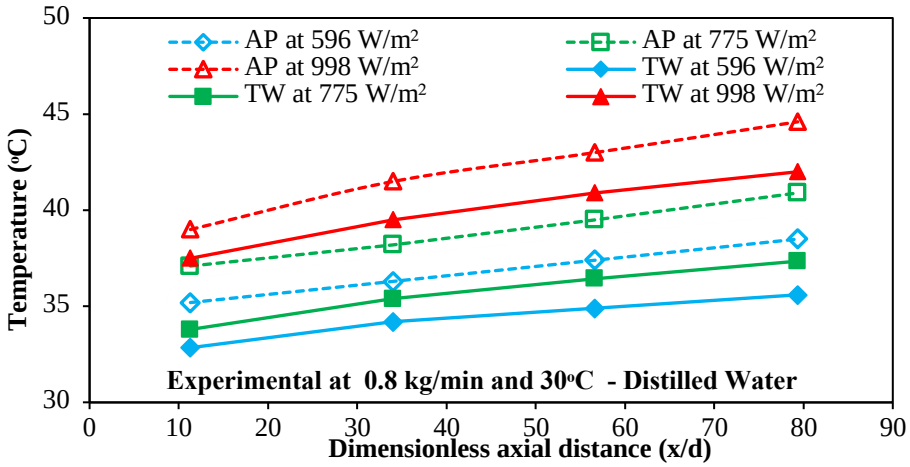

Figure 4.39 Variation in measured temperature of AP and TW versus axial distance along the FPSC using water as a working fluid at different heat flux intensities

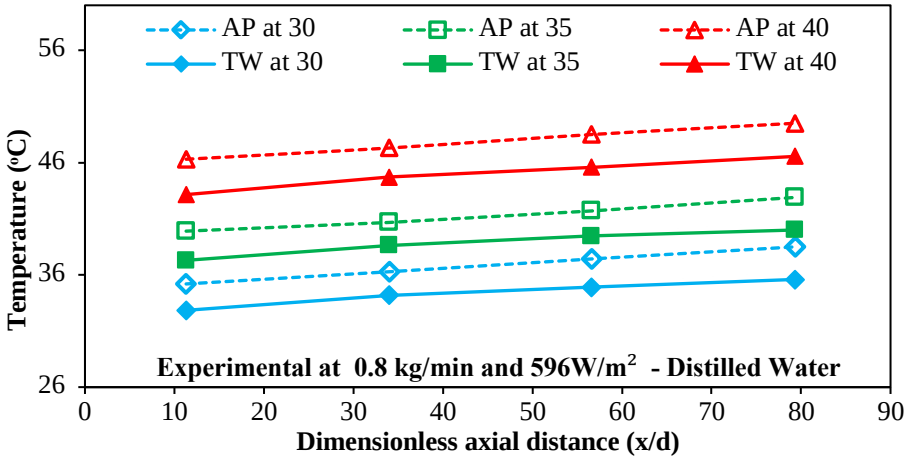

Figure 4.40 Variation in measured temperature of AP and TW versus axial distance along the FPSC using water as a working fluid at a different inlet temperature

Table 4.3 Heat absorbed factor and heat removal factor at a different flow rate for DI water

Mass flow rate (kg/min)	$F_R(\tau\alpha)$	$F_R U_L$	R^2
0.8	0.6120	4.8261	0.9684
1.2	0.6640	5.2561	0.9773
1.6	0.6829	5.2945	0.9739

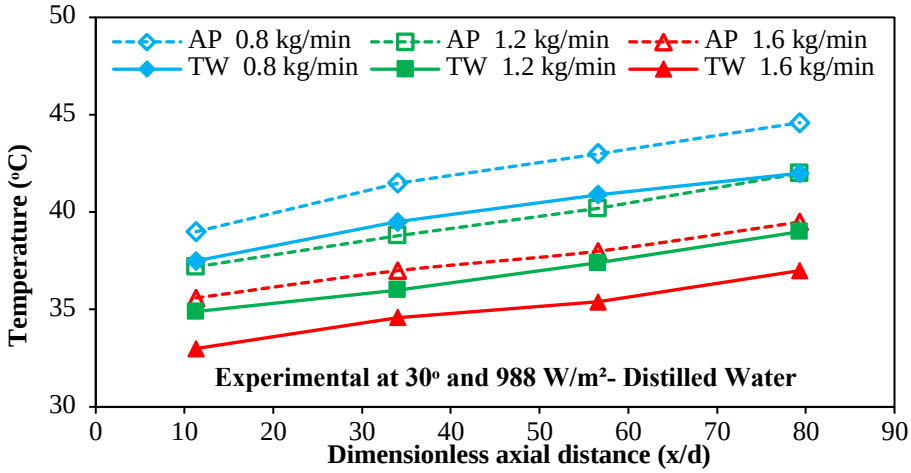

Figure 4.41 Variation in measured temperature of AP and TW versus axial distance along the FPSC using water as a working fluid at a different mass flow rate

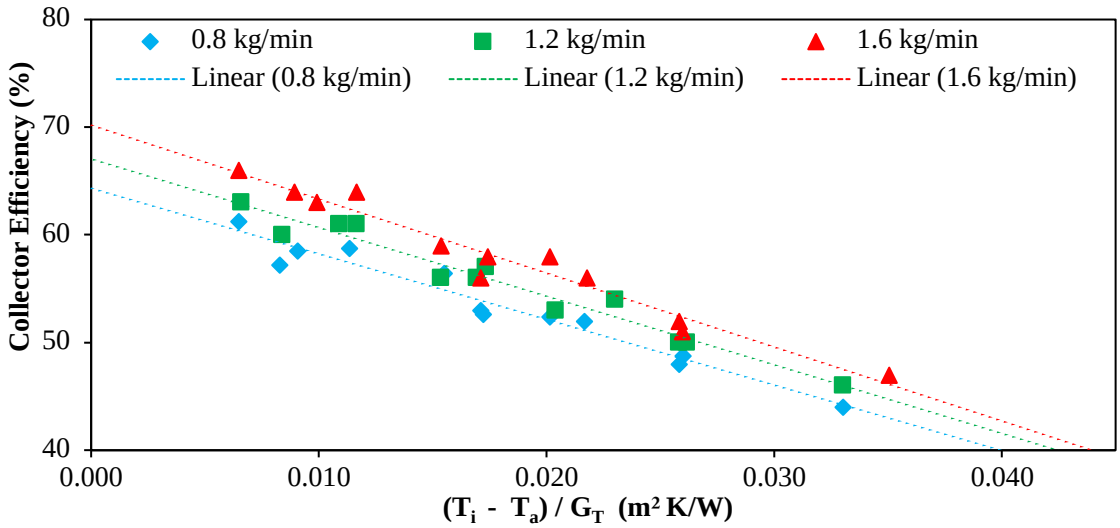

Figure 4.42 The experimental efficiency of FPSC versus reduced temperature parameter at different mass flow rate using DI water

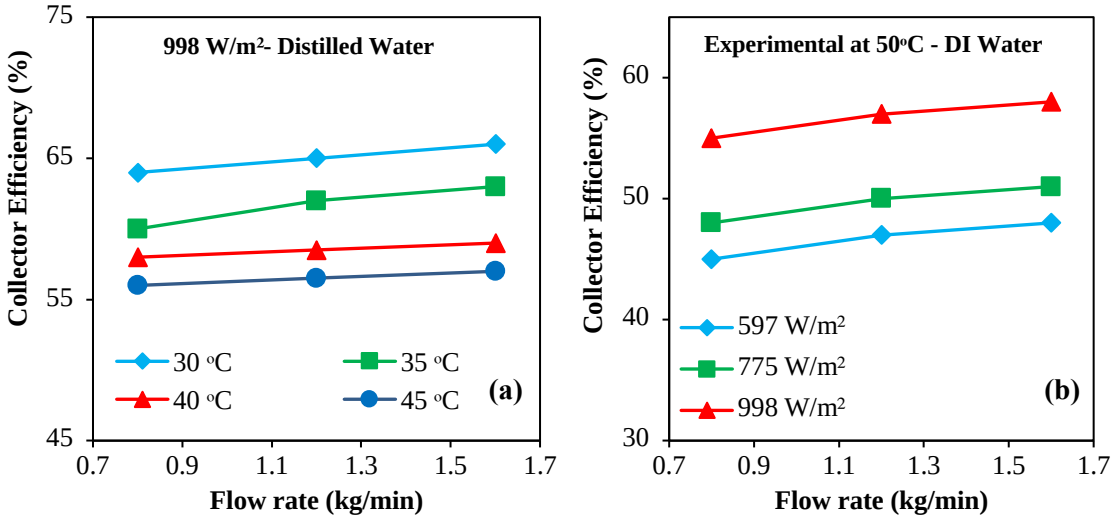

Figure 4.43 The experimental efficiency of FPSC versus mass flow rate at various (a) fluid inlet temperature and (b) heat flux intensities

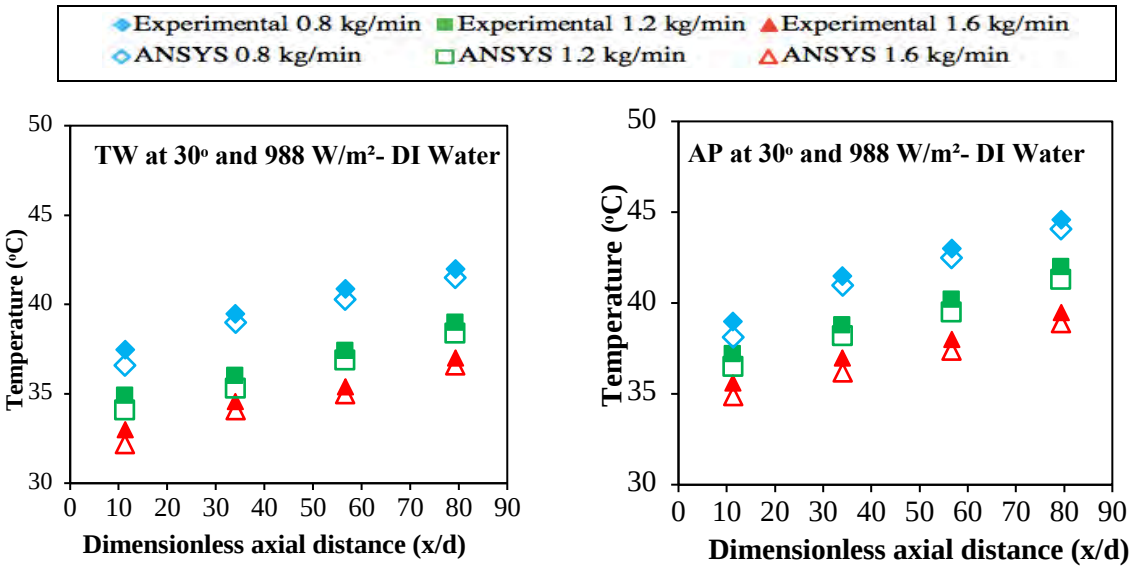

Figure 4.44 Comparison of experimental and ANSYS values of (a) TW and (b) AP for DI water at inlet temperature 30°C and heat flux 998 W/m^2 against dimensionless axial distance (x/d)

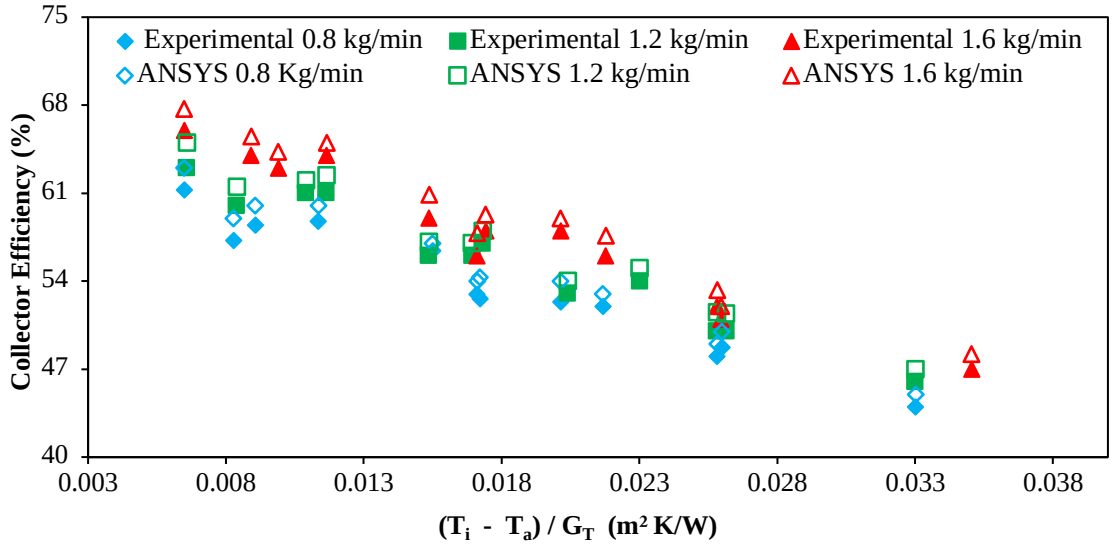

Figure 4.45 Comparison of thermal efficiency of experimental and ANSYS values for DI water against reduced temperature parameter

4.6.2 Thermal efficiency of FPSC using water-based nanofluid

The experiments were carried out with four different weight concentrations of water-based nanofluid which contain three covalently functionalized carbon and Iron nanostructures and two non-covalent metal oxide-based nanofluids; which have been prepared in this work to study the thermal efficiency of FPSCs as an alternative and improved work liquids instead of conventional heat transfer fluids. The subsequent parts present, describe and analyze the effects of the use of these water-based nanofluids on the AP, TW, pressure loss, efficiency, and performance index values of the experimental and simulated values of FPSC.

4.6.2.1 Bio-facial clove-treated GNPs nanofluid as working fluid in FPSC

The experimentally measured values of AP and TW versus x/d are shown in Figure 4.46 for DI water and CGNP nanofluids at weight concentrations (0.025%-0.1%), inlet fluid temperature 30°C, heat flux 998 W/m^2 and mass flow rate of 0.8 – 1.6 kg/min. Figure 4.46 clearly illustrates the reduction in the AP and TW values of CGNPs nanofluid at every weight concentration, the maximum reduction observed in AP, and TW value was

8.07% and 8.23% at 0.8 kg/min and 0.1 wt.%. The values of $F_R(\tau\alpha)$ and $F_R U_L$ for CGNP and water at different mass flow rates, and weight concentrations are presented in Table 4.4. It showed that the values of the heat removal factor for nanofluids were higher than that of water, and it goes on increasing as the flow rate increases. As already discussed, the thermal conductivity of nanofluid is higher than water data; the convective heat transfer coefficient was higher for CGNP than that of water alone. Therefore, the thermal performance of a solar collector could be enhanced by using CGNP/water nanofluid.

The efficiency of the solar collector is enhanced due to the convective heat transfer coefficient, and this value is directly related to the thermal conductivity of the heat transfer liquid or nanofluid used. The significant enhancement in convective heat transfer coefficient is mainly due to the thin thermal boundary layer formed at the riser tube walls resulting from the thermal conductivity enhancement of CGNP/water nanofluid as well as a decrease in thermal resistance between the nanofluid and inner wall surface of the riser tube. Also, carbon nanomaterials such as graphene and CNTs result in thinner thermal boundary layer thickness. The specific surface area and Brownian motion of the nanoparticles also play a role in influencing the convective heat transfer coefficient (Hosseini et al., 2018). It can be observed that there is an increment in the convective heat transfer coefficient when the *Re* is increased for the CGNP-water nanofluids and DI water.

Moreover, the concentration of nanoparticles has a pronounced effect on the convective heat transfer coefficient of the CGNP-water nano-coolants. We attribute this effect to the reduced thermal boundary layer thickness as well as the increased thermal conductivity in the presence of water-based CGNP nano-coolants. Furthermore, we believe that other factors such as the specific surface area and Brownian motion of the

CGNPs play a vital role in the convective heat transfer coefficient Several researchers gave reasons in the previous works (Alawi et al.; Chon & Kihm, 2005). Another factor that increases Brownian motion is forced circulation, which was implemented by the pump. The pump supplies energy to the operating working fluid. Due to this energy collision between liquid molecules and the solid particles, it improved the convective heat transfer coefficient and later thermal performance of the solar collector. Another factor that affects thermal performance is the reduced temperature parameter. Figure 4.47 (a-c) showed the efficiency of the solar collector against the reduced temperature parameter for water and nanofluid at different concentrations and flow rates. It could be seen that as the value of $\left(\frac{T_i - T_a}{G_T}\right)$ approach to zero, the efficiency of the collector rises to its highest point because at this point the trend line intersects y-axis and the value of $F_R(\tau\alpha)$ has become the maximum. The value of $F_R U_L$ is obtained from the slope of the trend line. On the other hand, the point at which trend line intersects x-axis is called the stagnation point, and at this point, the efficiency approaches zero and $\left(\frac{T_i - T_a}{G_T}\right)$ is showing the maximum. At a particular value of reduced temperature parameter, utilizing nanofluid as an alternative of water at a higher value of heat flux and low value of input temperature, the more useful performance is obtained according to the first law of thermodynamic (Stalin et al., 2019). Figure 4.47 (a-c) represents the effect of the weight fraction of CGNP on the thermal performance of solar collectors at weight fractions of 0.025, 0.075, and 0.1% and at several flow rates of 0.8, 1.20 and 1.2 kg/min. The thermal collector efficiency for CGNP against the reduced temperature parameter shows the weight fraction of nanoparticles has a significant effect on the thermal performance of a solar collector. From Figure 4.47a and Table 4.4, it is observed that at the flow rate of 0.8 kg/min and concentrations of 0.025, 0.075 and 0.1 wt.% the values of $F_R(\tau\alpha)$ increased compared to water data by 5.42%, 19.67%, and 21.51% respectively, while the corresponding value

of $F_R U_L$ has increased by 12.40%, 15.70% and 24.57%. Based on Figure 4.47b and Table 4.4 the enhancement in heat absorption factor and heat removal factor at the flow rate of 1.20 kg/min at the weight fractions of CGNP 0.025, 0.75 and 0.1 wt.% are 4.35, 18.56, 22.1 and 14.01, 18.57 and 21.82% respectively, compared to water data at the same flow rate. Figure 4.47c and Table 4.4 represents that the improvement in $F_R(\tau\alpha)$ are 4.87, 21.80, and 22.30% and $F_R U_L$ are 16.75, 25.09, and 32.49% at the flow rate of 1.60 kg/min at three concentrations of 0.025, 0.075 and 0.01 wt.% respectively.

As the reduced temperature parameter value increases, the efficiency line of water crosses the efficiency line of nanofluids at some point. The point of intersection of these efficiencies lines is called the critical point, which represents that before the intersection of lines, the efficiency of nanofluid is higher than that of water, but after the intersection point, water provides better output than nanofluid. Table 4.5 represents the values of the intersection point of the reduced temperature parameter against the different concentrations of CGNP.

Figure 4.48 (a-c) represents the thermal efficiency of solar collectors against reduced temperature parameters at the concentration of CGNP 0.025, 0.075, and 0.1 wt.% at the flow rates of 0.8, 1.2, and 1.6 kg/min. As visualized in Figure 4.48(a-c), the thermal efficiency of the solar collector increased with an increase in flow rate from 0.8 to 1.6 kg/min at each of the concentrations. The maximum enhancement in the thermal performance of solar collectors in a reduced temperature parameter was equal to 18.2%, at weight fraction 0.1 wt.%, and the flow rate was kept at 1.6 kg/min. The value of $F_R(\tau\alpha)$ and $F_R U_L$ was noticed also gradually increased with the flow rate. This is because of the enhancement in Brownian motion, which also refers increase of Reynold number, Nusselt

number, and also improvement of the convective heat transfer coefficient (Sadri, Hosseini, Kazi, Bagheri, Abdelrazek, Ahmadi, Zubir, Ahmad, & Abidin, 2018).

The heat removal factor F_R values are shown in Figure 4.49. The results showed that the removable heat factor for nanofluid is more than water. Also, it rises with the increasing mass flow rate. As the weight fraction of CGNP increases, the value of heat removable factor increases. Based on these results, the convective heat transfer coefficient was higher than that of water and both absorbed energy parameter, $F_R(\tau\alpha)$ and the removed energy parameter $F_R U_L$ for CGNP, nanofluid is increased. As a result of that, the performance of a solar collector is enhanced when using CGNP – nanofluid. Figure 4.50 represents the comparison of the thermal efficiency of FPSCs using three concentrations of CGNPs and DI water. It is evident from Figure 4.50 that the thermal efficiency of the collector increased by using CGNPs nanofluid.

A comparison was made between calculated and simulated values of AP and TW at the different mass flow rate, inlet temperature 30°C and heat flux 998 W/m2 for 0.1 wt.% CGNP nanofluid and presented in Figure 4.51. From which, it can be revealed that CFD simulation overestimates the measured values up to 2.70% and 1.88 % for AP and TW, respectively. Also, the comparison of experimental thermal efficiency of FPSCs and CFD predicted thermal efficiency were made at three different mass flow rate, inlet temperature rage 30-45°C and heat flux 998 W/m2 for 0.1 wt.% CGNP nanofluid and represented in Figure 4.52. From this figure, it can be observed that the CFD simulation over-estimated the experimental thermal efficiency values with a cumulative difference of 8.20% for 0.1 wt.% CGNPs nanofluid at a mass flow rate of 1.6 kg/min, fluid inlet temperature 45°C and heat flux intensity 988 W/m^2. Such discrepancy can be due to an ambiguity of the test values and also to errors in the CFD simulation, such as the reliance on the

correlations needed to measure some of the multiple variables, numerical errors, and the assumption that a mathematical model solution can be simplified. Therefore, it can be concluded that the established CFD simulation model is appropriate for the simulation of the thermal efficiency of FPSCs with adequate accuracy using water-based-CGNPs nanofluid as a working fluid.

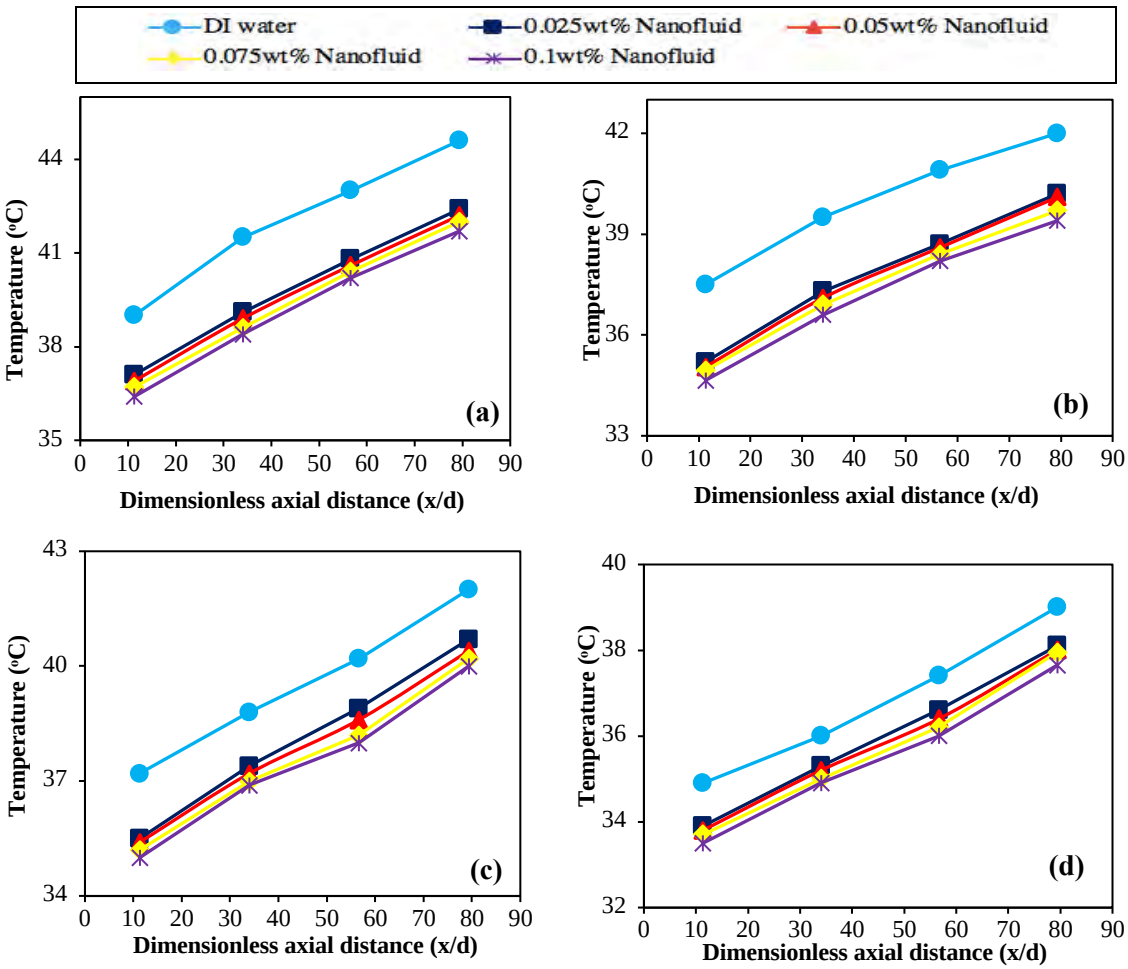

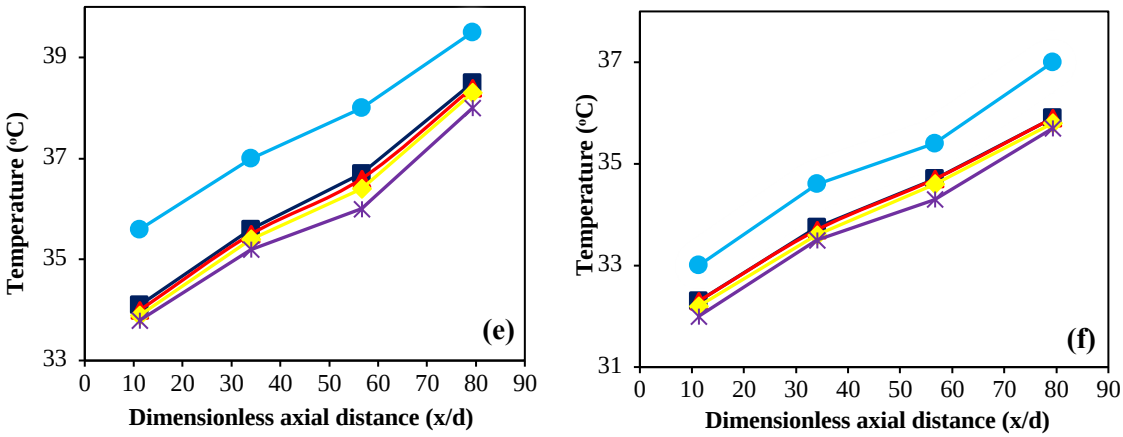

Figure 4.46 The experimental measured values of AP and TW at different weight concentrations (0.025%-0.1%) CGNP nanofluids, inlet fluid temperature 30°C, heat flux 998 W/m^2 and mass flow rate (a-b) 0.8 (c-d) 1.2 (e-f) 1.6 kg/min in comparison to DI water at same conditions

Table 4.4 Heat absorbed and Heat removal factor of CGNP at different weight concentrations and mass flow rate in comparison to DI water

Mass flow rate (kg/min)	Weight concentration (wt%)	$F_R(\tau\alpha)$	$F_R U_L$	R^2
0.8	0.1	0.7437	6.0120	0.9918
	0.075	0.7324	5.5838	0.9714
	0.025	0.6452	5.4250	0.9779
	DI Water	0.6120	4.8261	0.9684
1.2	0.1	0.8135	6.4032	0.9758
	0.075	0.7873	6.2325	0.9784
	0.025	0.6929	5.9928	0.9860
	DI Water	0.6640	5.2561	0.9773
1.6	0.1	0.8230	7.0131	0.9831
	0.075	0.8196	6.6232	0.9573
	0.025	0.7057	6.1816	0.9737
	DI water	0.6729	5.2945	0.9739

Table 4.5 The intersection of CGNP nanofluids, and the characteristics of water.

Mass flow rate (kg/min)	Weight concentration(wt%)	Intersection $(T_i-T_a)/G_T$
0.8	0.1	0.058
	0.075	0.037
	0.025	0.036
1.2	0.1	0.069
	0.075	0.035
	0.025	0.042
1.6	0.1	0.055
	0.075	0.037
	0.025	0.046

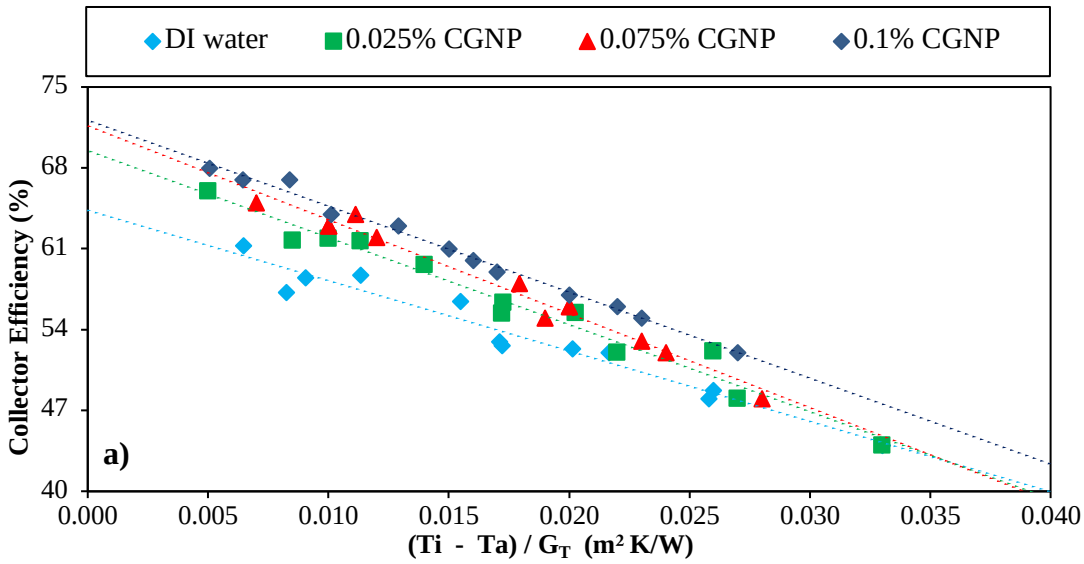

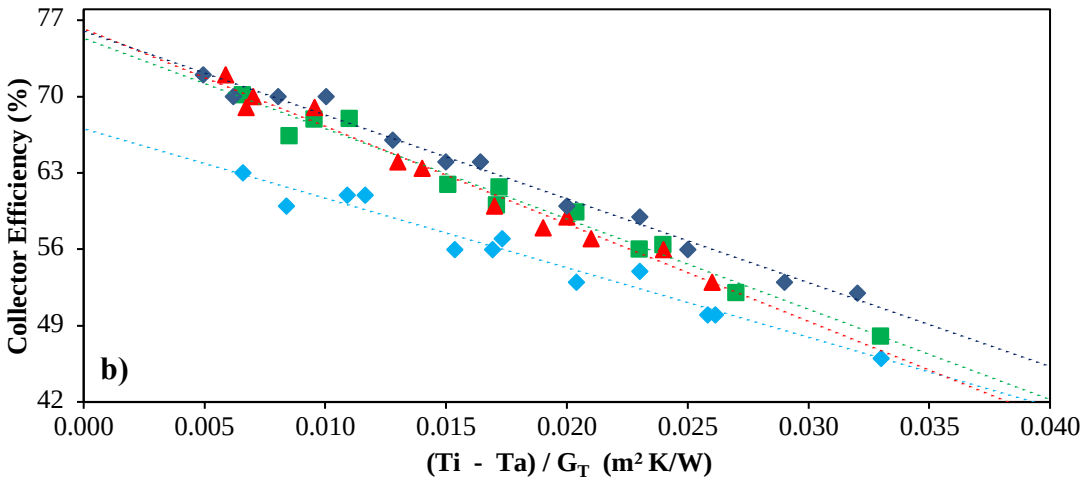

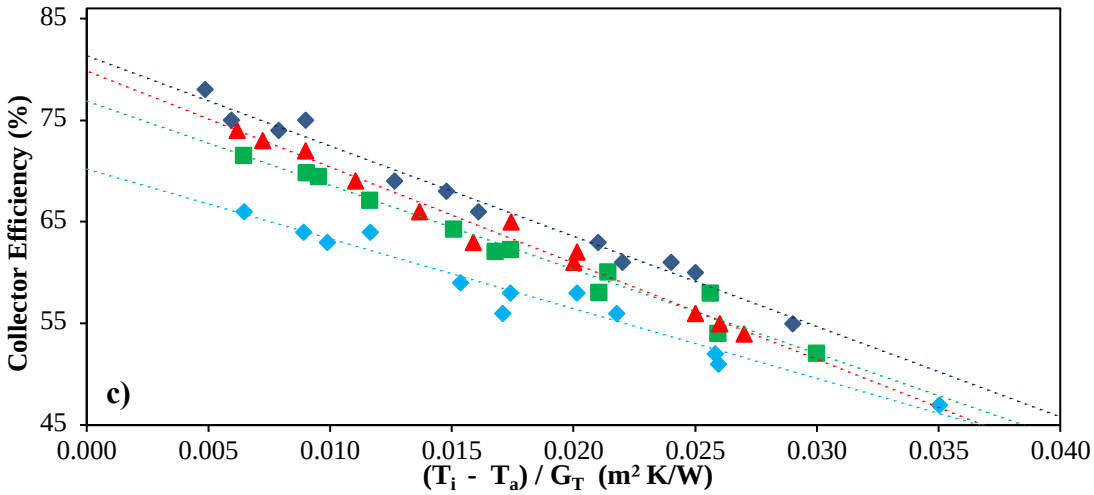

Figure 4.47 Thermal efficiency of FPSC using CGNP nanofluid with different weight concentration and mass flow rates a) 0.8, b) 1.20, c) 1.60 kg/min in comparison to DI water

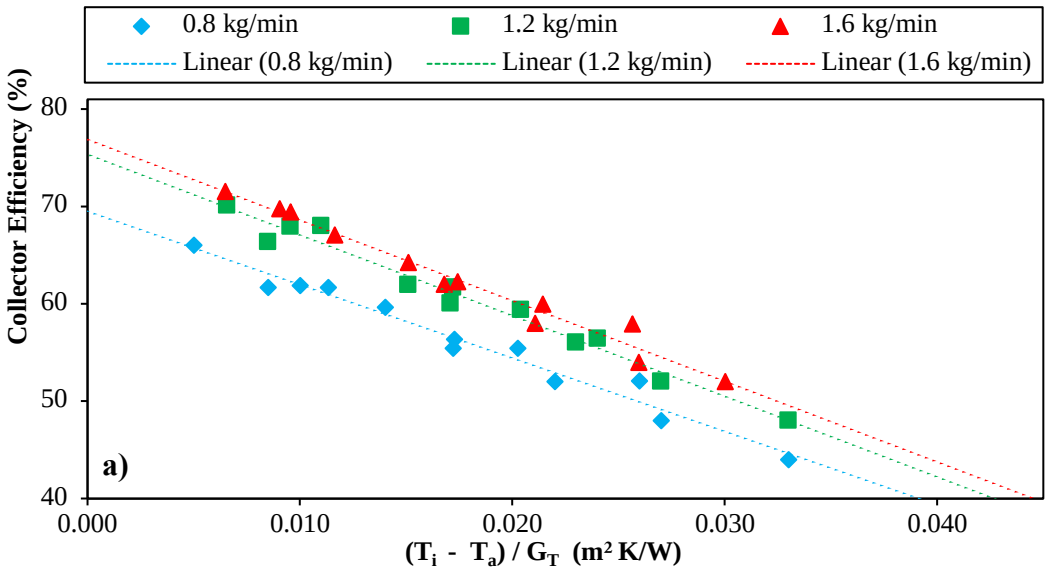

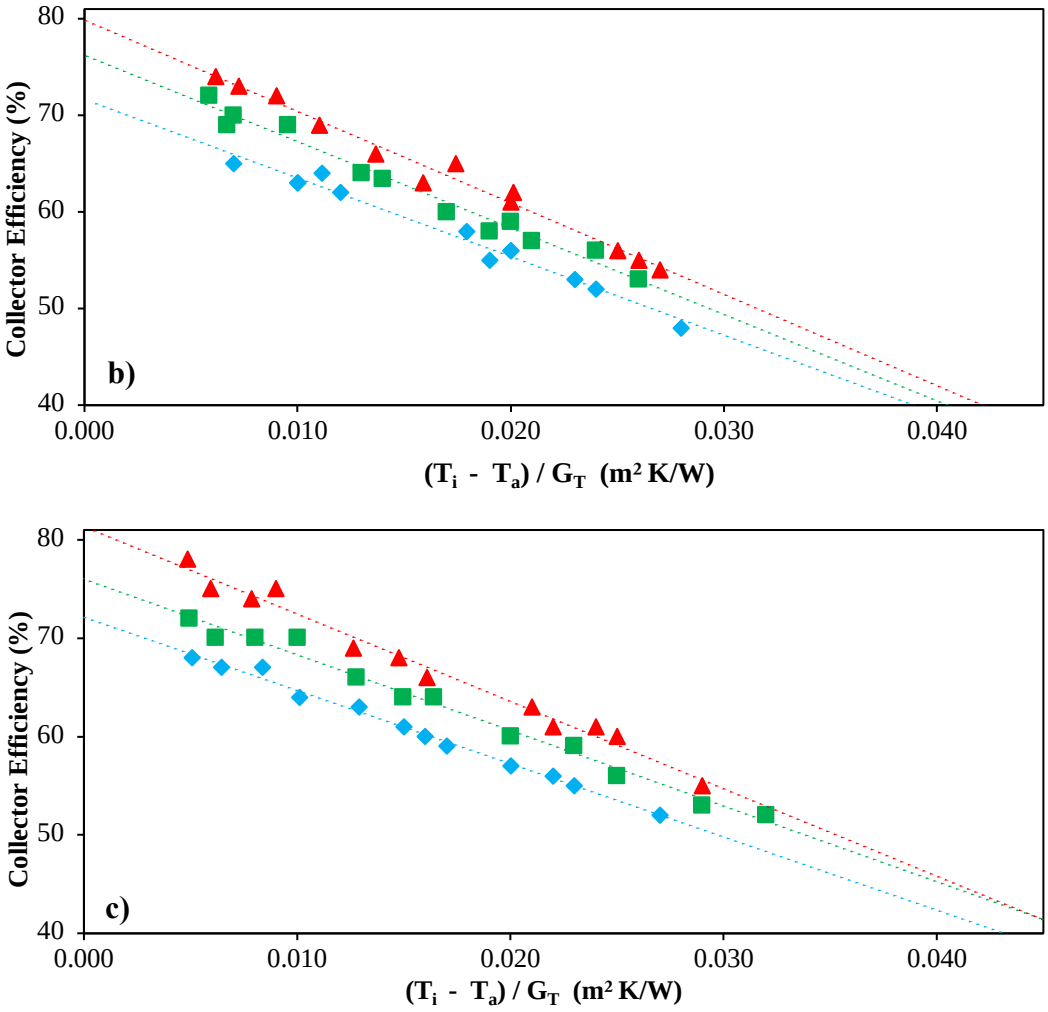

Figure 4.48 Thermal efficiency of FPSC using CGNP nanofluid with weight concentrations of (a) 0.025, (b) 0.075, and (c) 0.1 wt. % at different mass flow rates

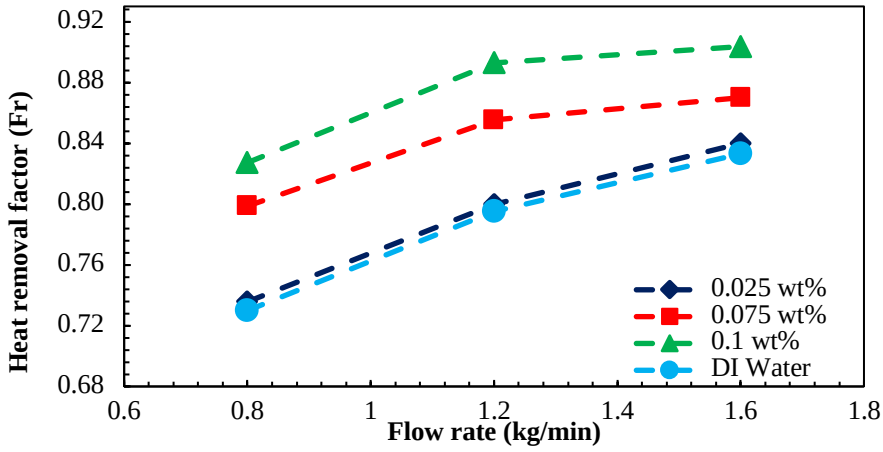

Figure 4.49 Heat Removal factor at different flow rates and different weight concentrations

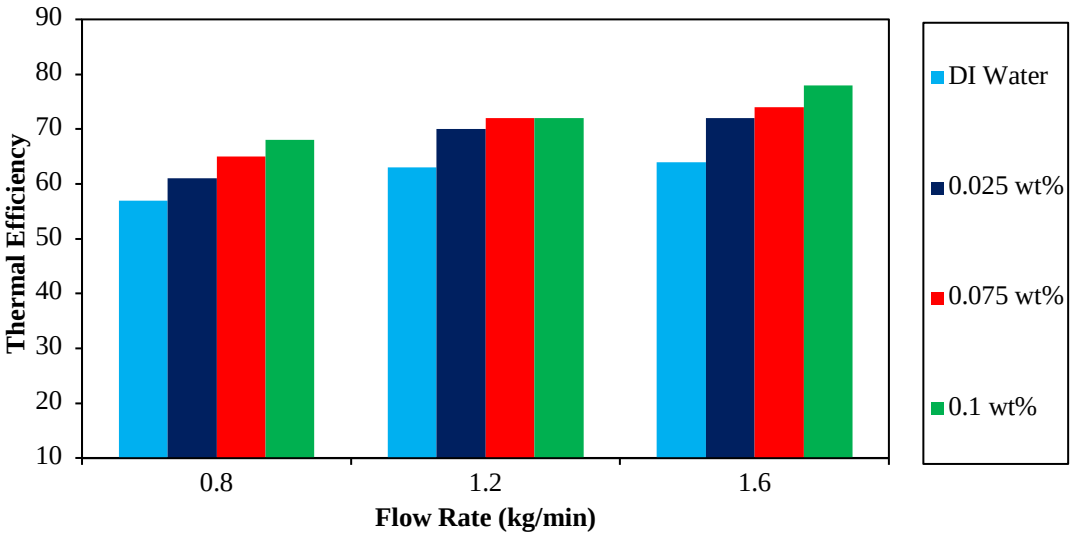

Figure 4.50 Comparison of thermal efficiency at various mass flow rates and weight concentration of CGNP nanofluids in comparison to DI water

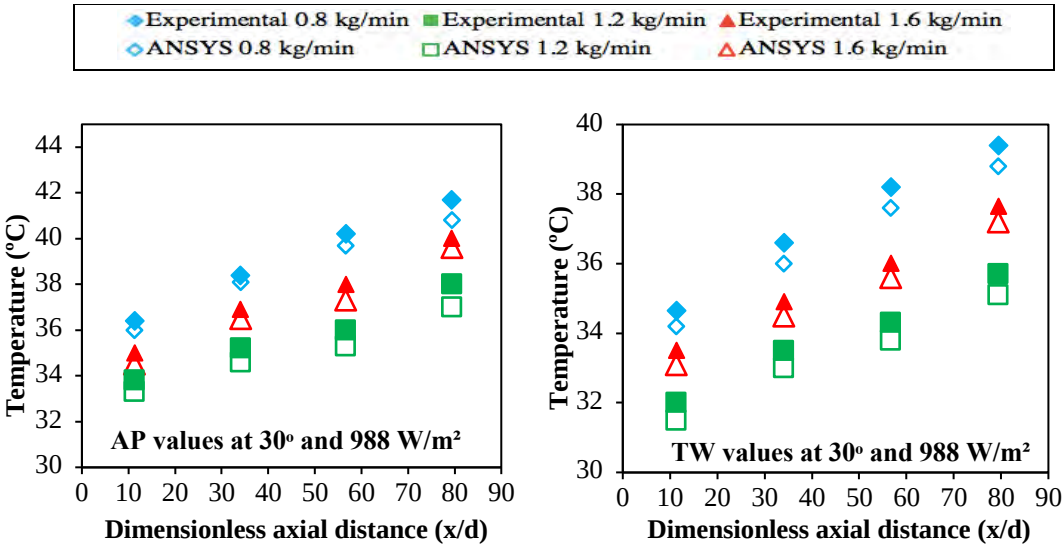

Figure 4.51 Experimental and ANSYS simulation values of AP and TW at the different flow rate, inlet temperature 30°C, heat flux 998 W/m^2 for 0.1 wt.% CGNP nanofluid

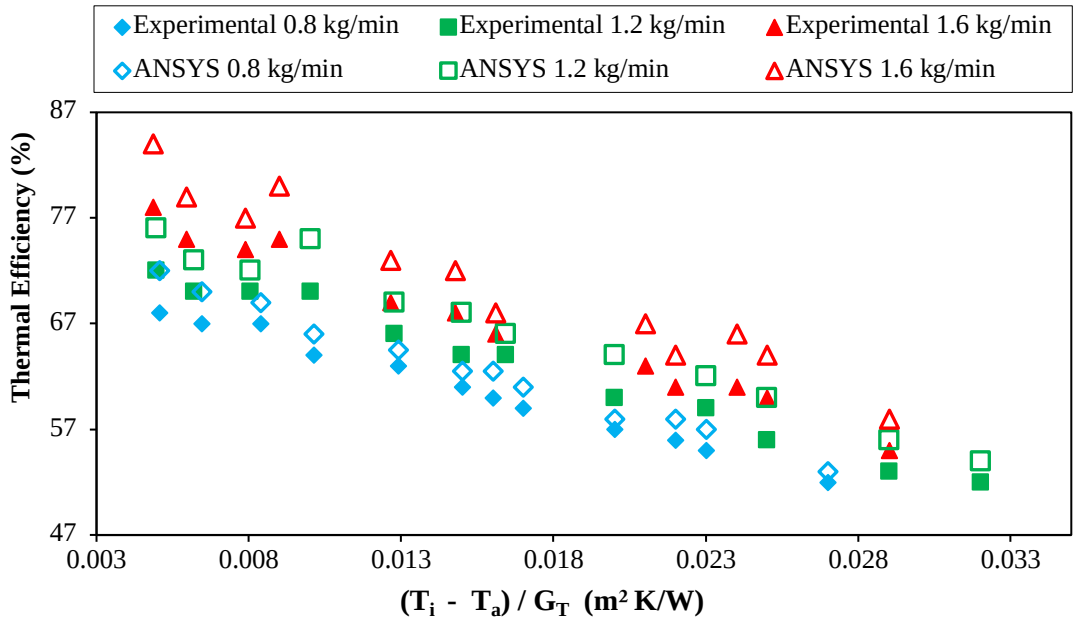

Figure 4.52 Comparison of the experimental and CFD simulated values of thermal efficiency of FPSC at a different flow rate and 0.1 wt.% CGNP nanofluid

4.6.2.2 PEG – Fe_3O_4 nanofluid as working fluid in FPSC

Figure 4.53 represents the experimentally measured values of AP and TW against the axial displacement at weight concentrations (0.025%-0.1%), inlet fluid temperature 30°C, heat flux 998 W/m^2 and mass flow rate of 0.8 – 1.6 kg/min for DI water and functionalized PEG – Fe_3O_4 nanofluid. From Figure 4.53, it was observed that the drop in the AP and TW values of PEG – Fe_3O_4 nanofluid at each concentration in comparison to DI water. The highest reduction of 5.93% and 4.80% was observed at 0.8 kg/min and 0.1 wt.% PEG – Fe_3O_4 nanofluid for AP and TW, respectively. This decrease will result in an increment in the heat transfer coefficient in the material due to the improvement in the thermal conductivity of PEG – Fe_3O_4 nanoparticles. In view of the fact that nanofluids with a greater thermal conductivity than their base fluids often have higher convective heat transfer coefficients in previous work as well as in laminar and turbulent regime (Sadri, Mallah, et al., 2018). A comparison between the experimentally and ANSYS simulated values of absorber plate and wall temperature at 30°C inlet fluid temperature and 998

W/m² heat flux intensity was executed at various mass flow rates for PEG – Fe_3O_4 nanofluids with 0.1-wt% and presented in Figure 4.57. From which, it can be revealed that the ANSYS simulated values overestimate the calculated values up to 2.61% and 2.42% for AP and TW, respectively.

The experimental thermal efficiency of collector against mass flow rate for 0.1-wt% PEG – Fe3O4 nanofluids is shown in

Figure 4.56 at various inlet fluid temperatures and heat flux intensities. This is a pattern similar to distilled water, which is to claim that efficiency increases as the intensity of heat transfer and mass flow rates rise and decline as fluid intake temperature increases. The effect of the weight concentration of PEG – Fe_3O_4 nanofluid on thermal performance against reduced temperature parameters at mass flow rates of 0.8, 1.20, and 1.2 kg/min in comparison to DI water was presented in Figure 4.54(a-c). It can be observed from the figure that the thermal efficiency enhanced with the loading of PEG – Fe_3O_4 nanoparticles with each concentration in comparison to water. However, the maximum thermal efficiency enhancement of 13.83% was noticed for 0.1 wt.% at 998 W/m² heat flux intensity and 1.6 kg/min mass flow rate. The effect of mass flow rate on thermal performance of collector was separately represented in Figure 4.55(a-d) at weight concentration of (a) 0.025, (b) 0.05 (c) 0.075, and (d) 0.10%. It is obvious from Figure 4.55 that as the mass flow rate increase from 0.8 to 1.6 kg/min, thermal efficiency enhanced for all weight concentration. Also, the experimentally measured thermal efficiency values of FPSC were compared with the ANSYS simulated efficiency values and shown in Figure 4.58. It may be noted that the ANSYS simulated thermal efficiency understated the experimental thermal efficiency with a maximum difference of 8.33% at 0.1 wt.% PEG – Fe_3O_4, 1.6 kg/min mass flow rate, 50°C of inlet fluid temperature, and

998 W/m² heat flux intensity. It may be due to the uncertainty of the calculated experimental values or error made in simulation, such as dependency on the correlations to quantify several required variables, numerical errors, and assumptions taken to simplify for the simulation model. It can, therefore, be inferred that the established ANSYS simulated model that has been established is suitable with acceptable accuracy for simulating the thermal performance of FPSC using PEG – Fe_3O_4 nanofluid as a working fluid.

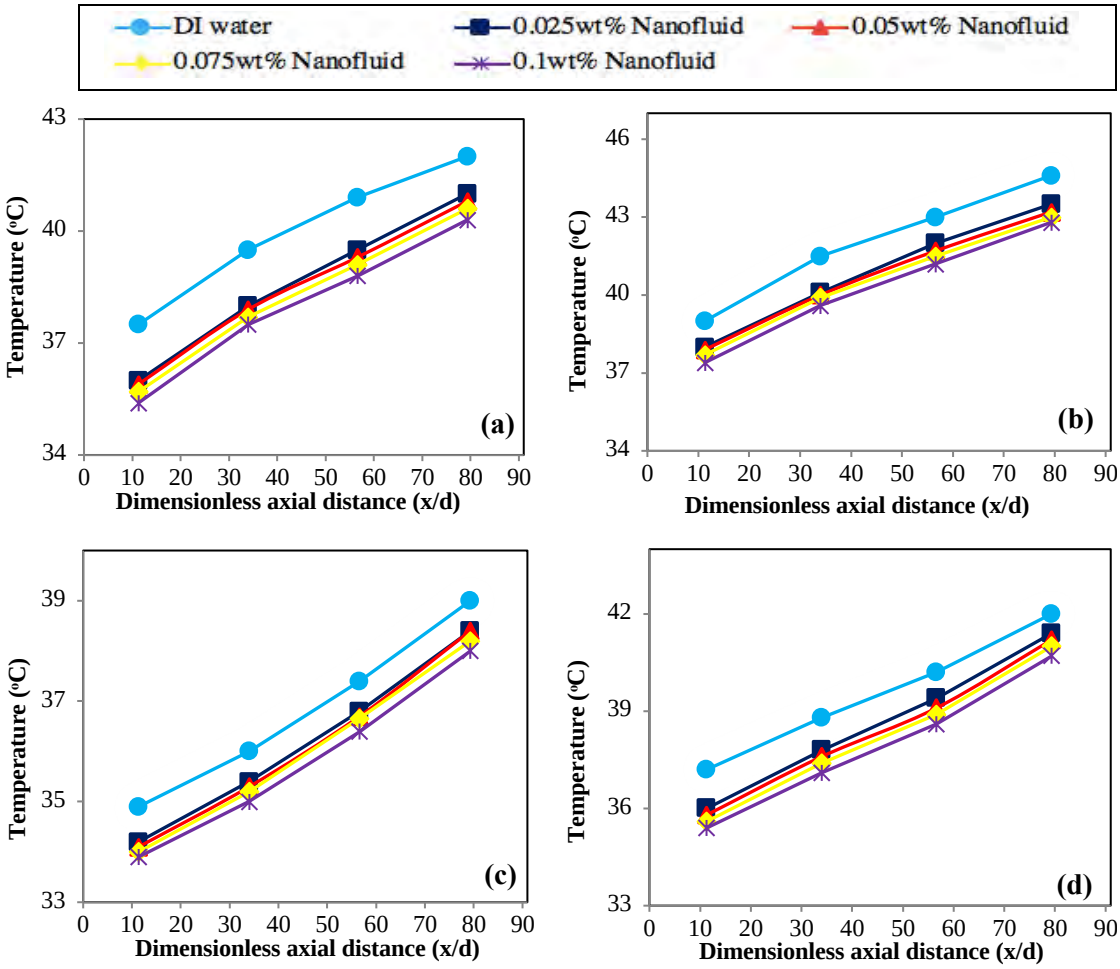

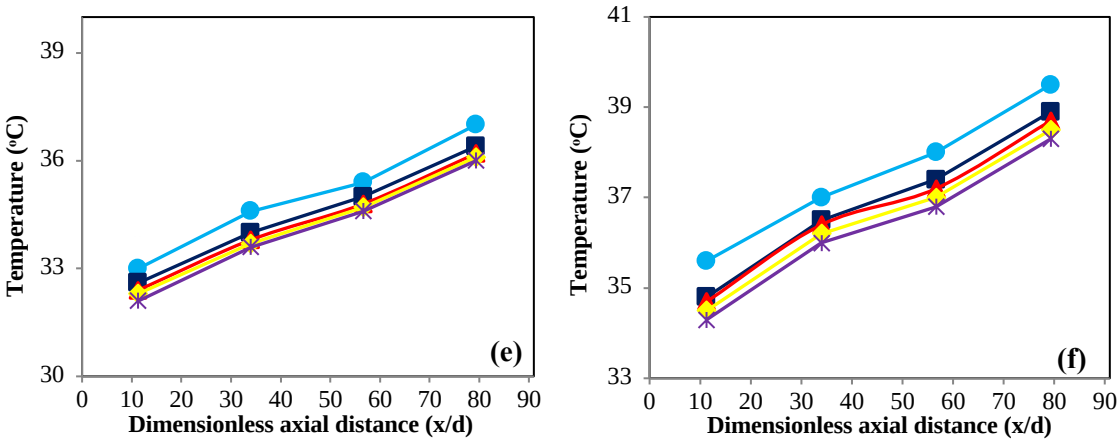

Figure 4.53 The experimentally measured values of AP and TW at different weight concentrations (0.025%-0.1%) PEG-Fe_3O_4 nanofluids, inlet fluid temperature 30°C, heat flux 998 W/m^2 and mass flow rate (a-b) 0.8 (c-d) 1.2 (e-f) 1.6 kg/min in comparison to DI water at same conditions

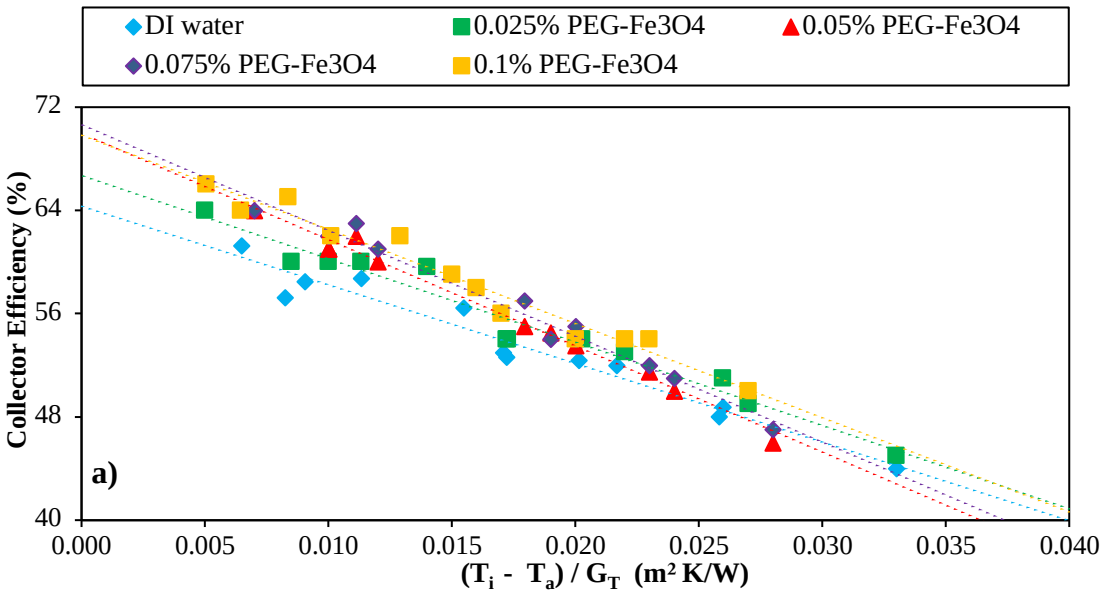

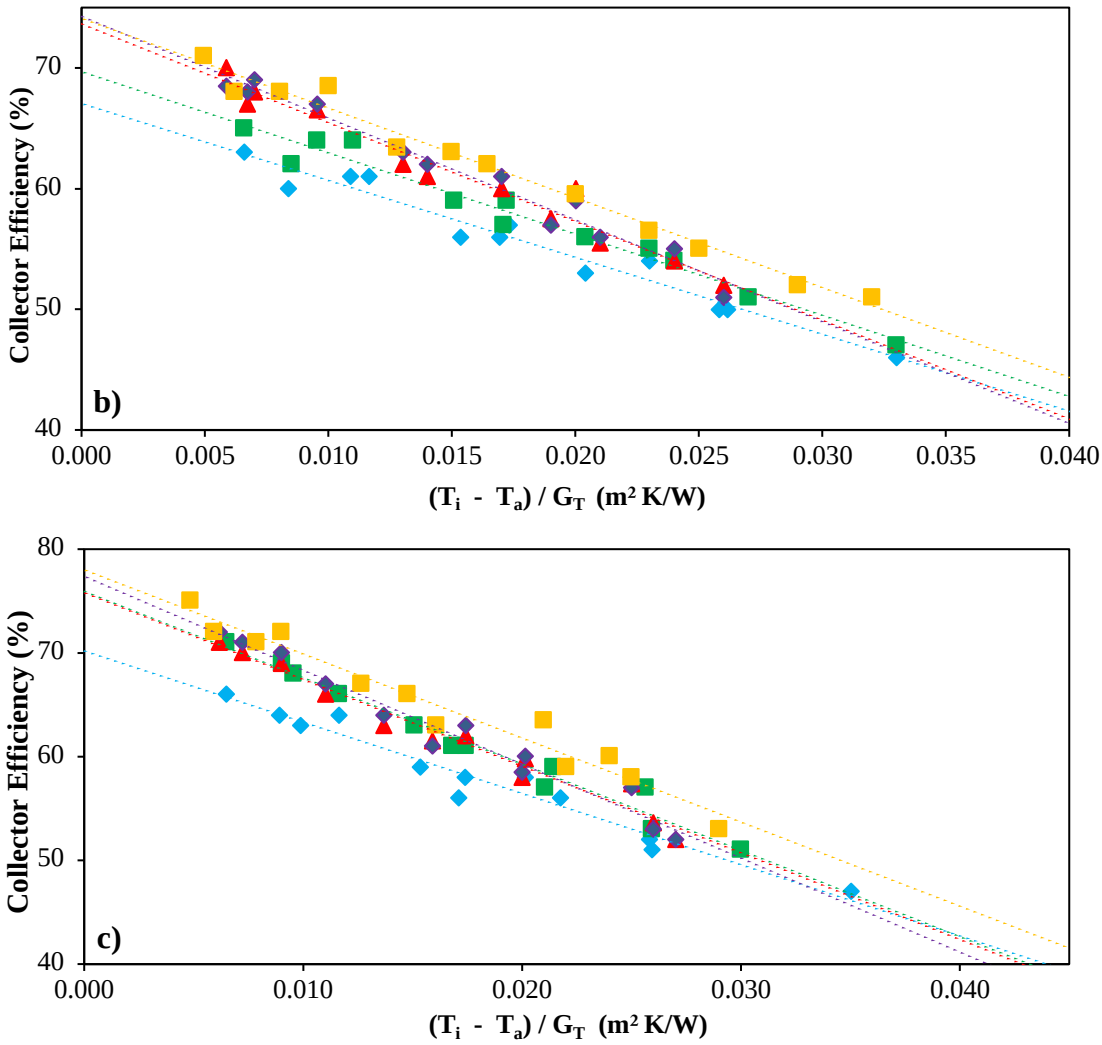

Figure 4.54 Thermal efficiency of FPSC using PEG-Fe_3O_4 nanofluids with different weight concentration and mass flow rates a) 0.8, b) 1.20, c) 1.60 kg/min in comparison to DI water

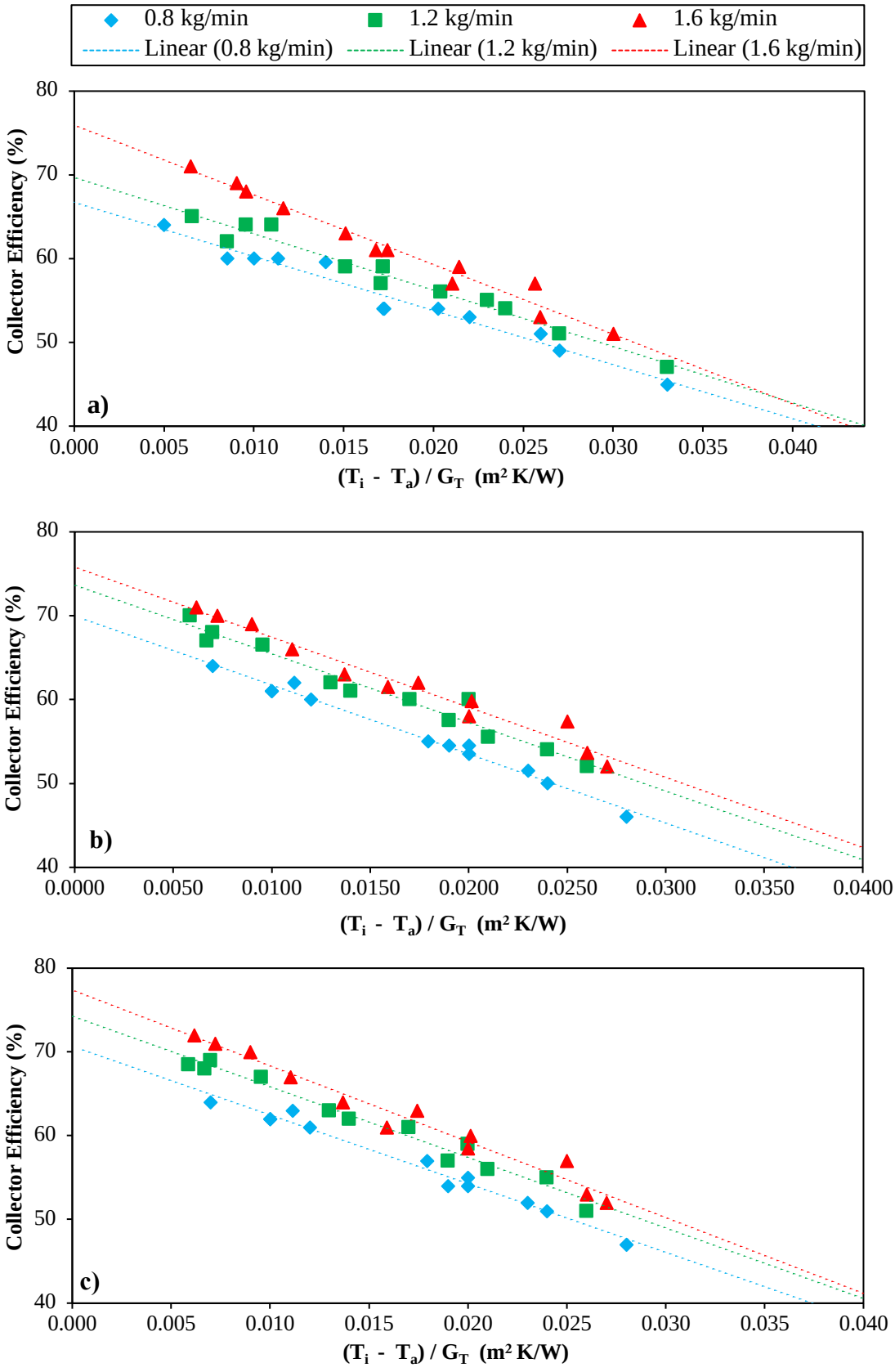
0.8 kg/min
1.2 kg/min
1.6 kg/min
Linear (0.8 kg/min)
Linear (1.2 kg/min)
Linear (1.6 kg/min)
Collector Efficiency (%)
80
70
60
50
40
a)
0.000
0.005
0.010
0.015
0.020
0.025
0.030
0.035
0.040
(T_i - T_a) / G_T (m² K/W)
Collector Efficiency (%)
80
70
60
50
40
b)
0.0000
0.0050
0.0100
0.0150
0.0200
0.0250
0.0300
0.0350
0.0400
(T_i - T_a) / G_T (m² K/W)
Collector Efficiency (%)
80
70
60
50
40
c)
0.000
0.005
0.010
0.015
0.020
0.025
0.030
0.035
0.040
(T_i - T_a) / G_T (m² K/W)

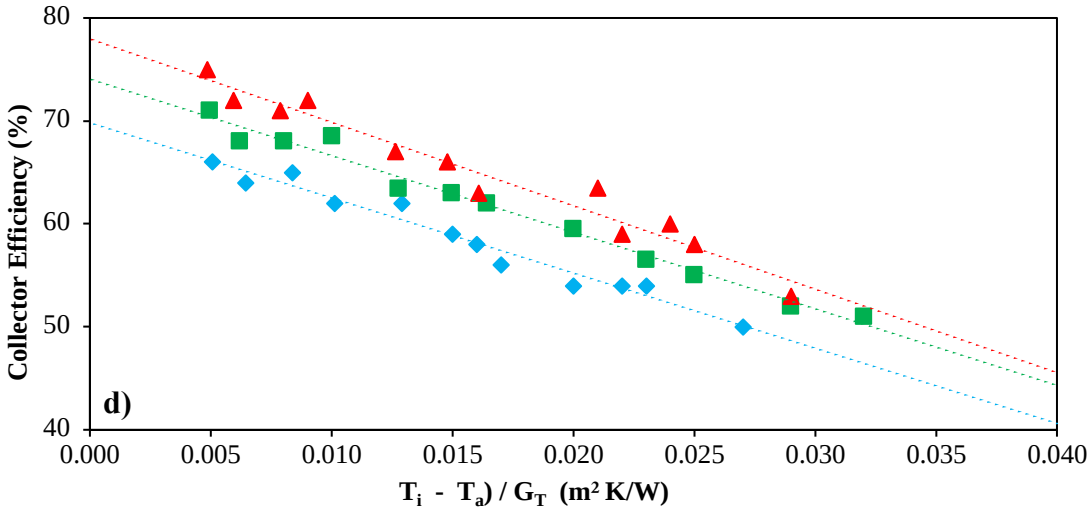

Figure 4.55 Thermal efficiency of FPSC using PEG-Fe_3O_4 nanofluids with the concentrations (a) 0.025, (b) 0.05 (c) 0.075, and (d) 0.1 wt. % at various mass flow rates

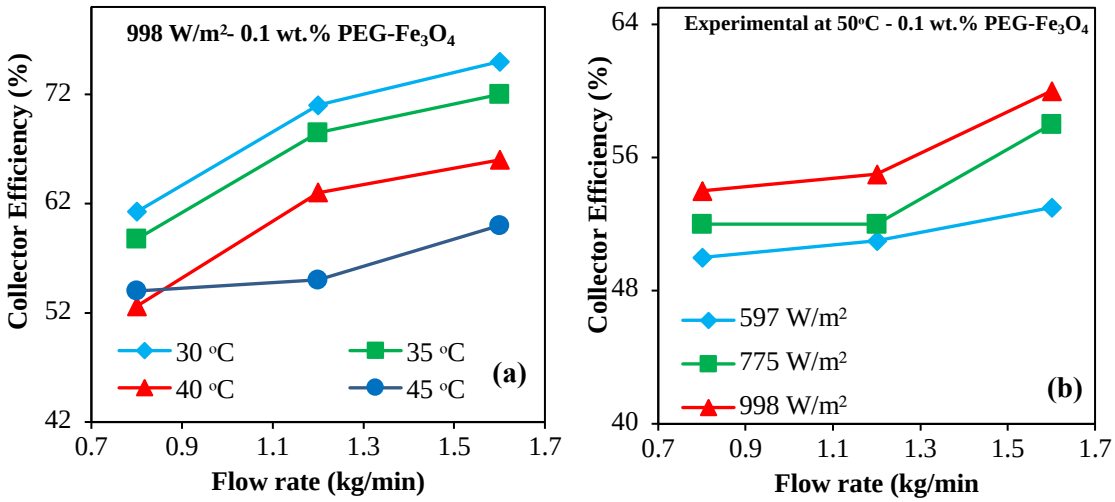

Figure 4.56 The experimental thermal efficiency of FPSC versus mass flow rate at various (a) inlet fluid temperature and (b) heat flux intensities using 0.1 wt.% PEG-Fe_3O_4 nanofluid as working fluid

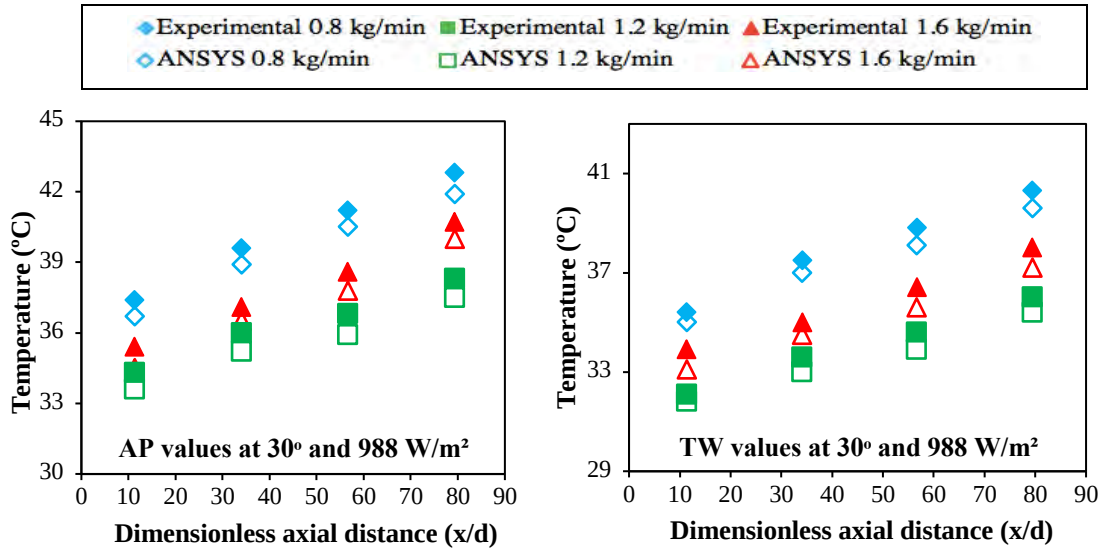

Figure 4.57 Experimental and ANSYS simulation values of AP and TW at the different flow rate, inlet temperature 30°C, heat flux 998 W/m^2 for 0.1 wt.% PEG-Fe_3O_4 nanofluid as working fluid

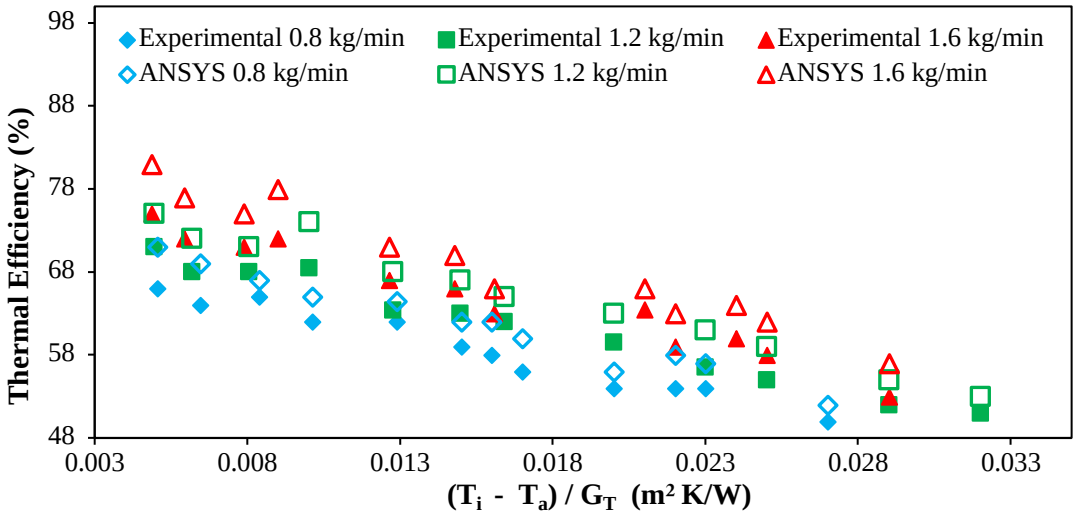

Figure 4.58 Comparison of the experimental and CFD simulated values of thermal efficiency of FPSC at a different flow rate and for 0.1 wt.% PEG-Fe_3O_4 nanofluid as working fluid

4.6.2.3 SiO_2 and ZnO nanofluids as working fluid in FPSC

In Figure 4.59, the variations of the calculated values of AP and TW against axial distance along the direction of flow in the collector for water and 0.1 wt.% water-based SiO_2 and ZnO nanofluids are shown at 998 W/m^2 heat flux strength and 30 °C fluid inlet

temperature. From this figure, it can be shown that the calculated values of TW and AP decline as the flow rate increases and their values for water-based SiO_2 and ZnO nanofluids are lower than their corresponding water values, down to 4.46% and 3.75%; 6.53% and 6.14% at 0.8 kg/min, respectively. In addition, experimental values of TW and AP at the fluid inlet temperature of 30°C and heat flux intensity 998 W/m^2 for DI water and at the different weight concentrations (0.05 wt.% - 0.2 wt.%) of SiO_2 and ZnO of nanofluids are presented in Figure 4.60. Here, in comparison with water, it can be recognized from this figure that the values of TW and AP for SiO_2 and ZnO decreased as weight concentrations increased, which can be justified in a similar way to that mentioned in the previous section. At 30 °C inlet fluid temperature and 998 W/m^2 heat flux intensity, the measured values of TW and AP along with ANSYS simulated values against axial distance along the direction of flow are displayed in Figure 4.61 for water-based 0.1 wt.% SiO_2 and ZnO nanofluids at various mass flow rates. From which, it can be seen that the measured values are always higher than the simulated values, down to 3.23% and 3.77%, 2.81%, and 2.37% for TW and AP, respectively, at 1.2 kg/min.

The experimental thermal efficiency of FPSC versus mass flow rate at different inlet fluid temperatures and heat flux intensities using 0.1 wt.% SiO_2 and ZnO nanofluid as working fluid are presented in Figure 4.62. This pattern is similar to that for distilled water discussed in a previous segment, from which it can be found that the efficiency increases as heat flux intensity and mass flow rate increases and decreases as inlet fluid temperature rises. Figure 4.63 displays the experimental thermal efficiency of FPSC against reduced temperature parameters at mass flow rate 1.60 kg/min and weight concentration range (0.05 - 0.2 wt%) for SiO_2 and ZnO nanofluid in comparison with DI water. From which it is obvious that the thermal efficiency of FPSC increases with the loading of nanoparticles in the base fluid. When compared with water, a maximum increase in

thermal efficiency of SiO_2 and ZnO nanofluid at 1.60 kg/min mass flow rate and weight concentrations of 0.05%,0.1%,0.15% and 0.2% were 8.0%, 10.7%, 12.96% and 13.21%; 9.30%, 11.14%, 13.75% and 14.21%, respectively. Also, the experimental thermal efficiency values of the collector along with their corresponding simulated values versus reduced temperature parameter at different mass flow rates and 0.1 wt.% weight concentration of SiO_2 and ZnO are shown in Figure 4.64(a-b). From these two figures, it can be observed that the expected thermal efficiency is higher than their corresponding experimental values with a maximum difference of 13.82% and 12.73% for SiO_2 and ZnO nanofluids, respectively. Therefore, it can be inferred that the ANSYS Fluent could be used to estimate the thermal efficiency of an FPSC using water-based SiO_2 and ZnO nanofluids as its working fluid with fair precision.

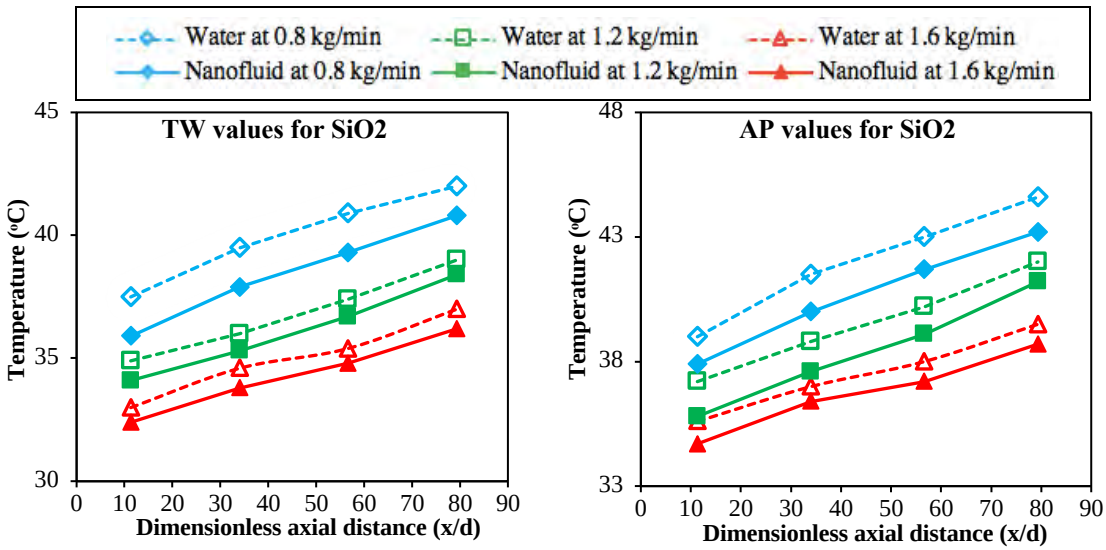

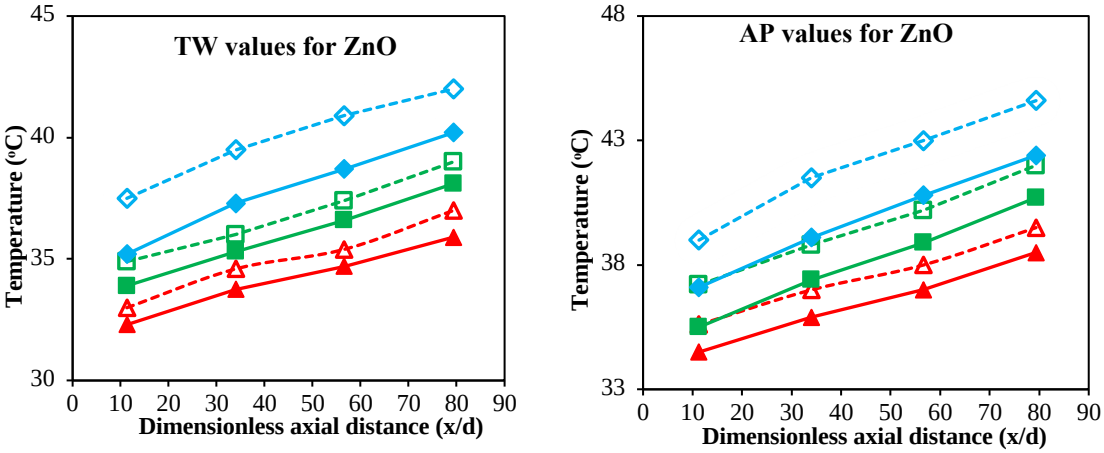

Figure 4.59 Experimentally measured values of TW and AP at the different mass flow rate, fluid inlet temperature 30°C and heat flux intensity 998 W/m^2 for DI water and 0.1 wt.% (a-b) SiO_2 and (c-d) ZnO nanofluids

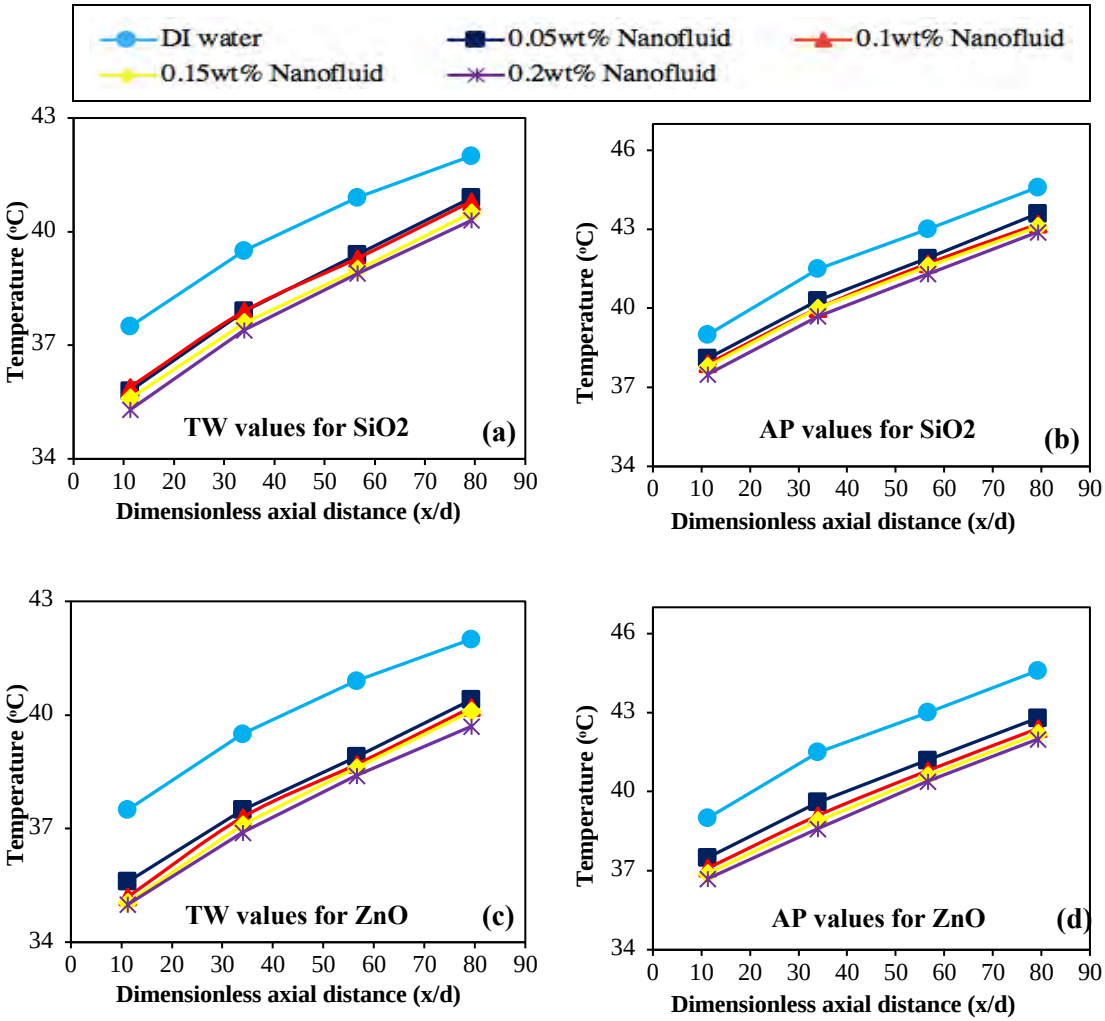

Figure 4.60 Experimentally measured values of TW and AP at a fluid inlet temperature 30°C and heat flux intensity 998 W/m^2 for DI water and different weight concentration of (a-b) SiO_2 and (c-d) ZnO nanofluids

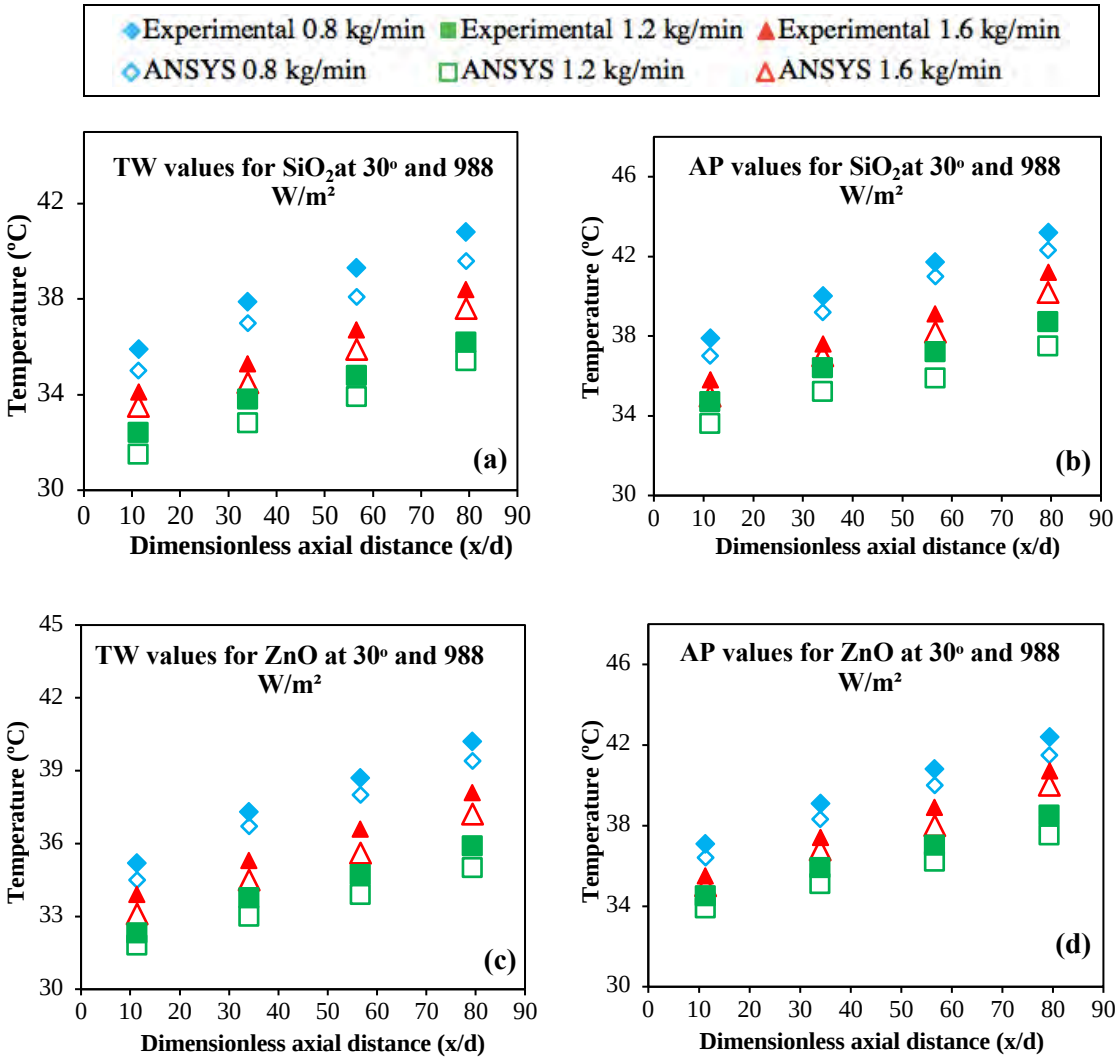

Figure 4.61 Experimentally measured values and ANSYS simulated values of TW and AP at a fluid inlet temperature 30°C, heat flux intensity 998 W/m^2 and different mass flow rates for 0.1 wt.% (a-b) SiO_2 and (c-d) ZnO nanofluids

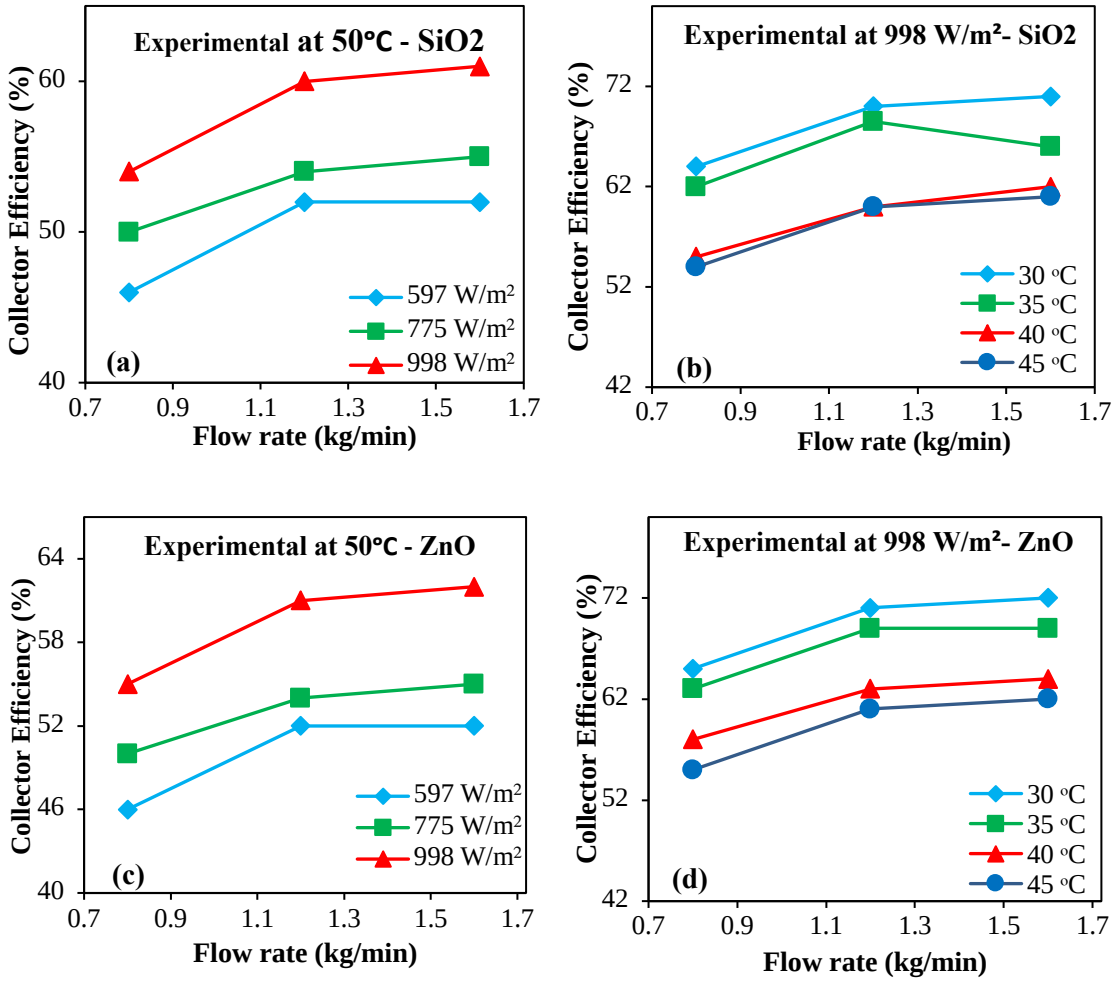

Figure 4.62 The experimental thermal efficiency of FPSC versus mass flow rate at various (a-c) fluid inlet temperature and (b-d) heat flux intensities using 0.1 wt.% SiO2 and ZnO nanofluid as working fluid

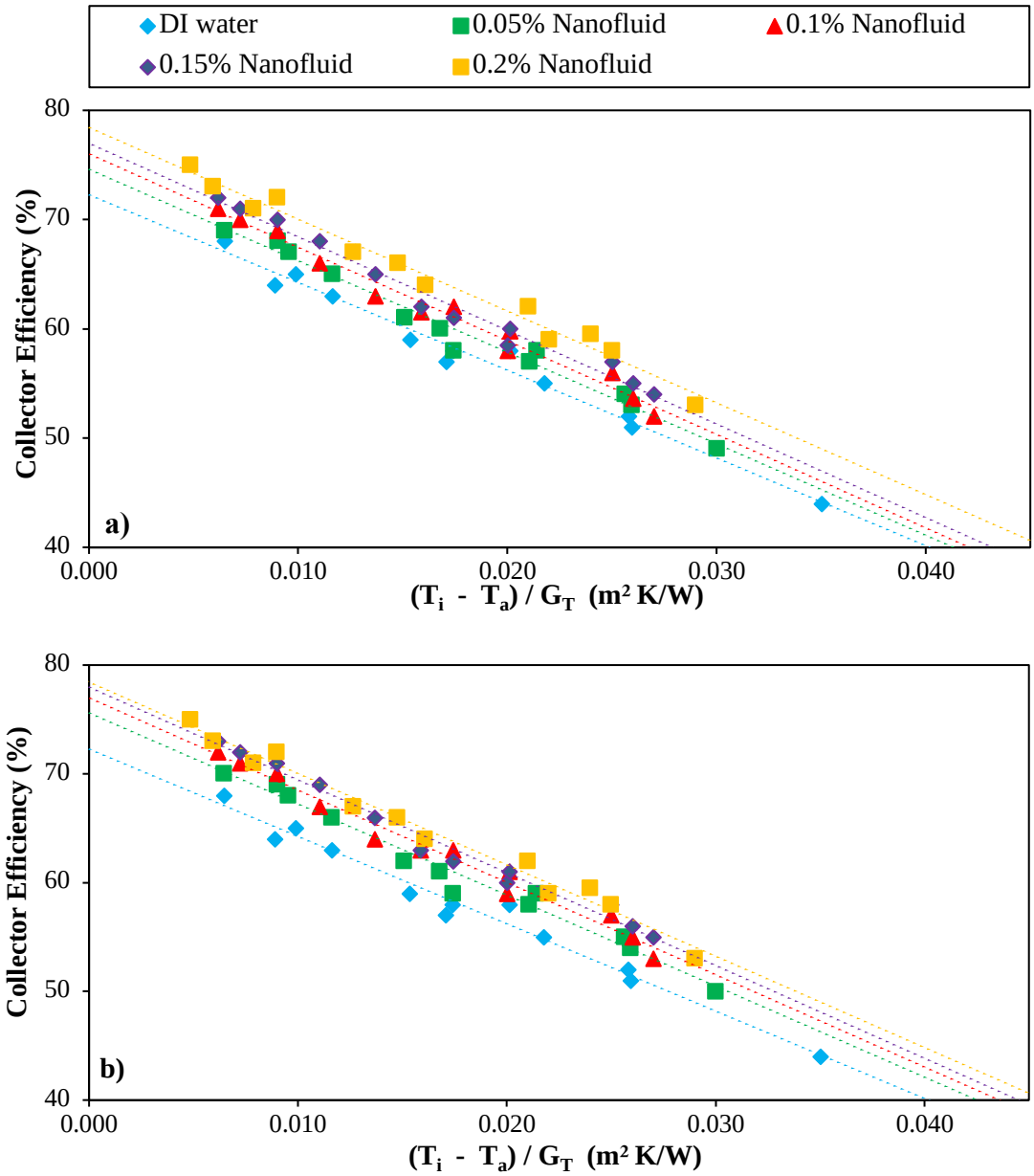

Figure 4.63 Thermal efficiency of FPSC using (a) SiO_2 and (b) ZnO nanofluids with different weight concentration at mass flow rates 1.60 kg/min in comparison to DI water

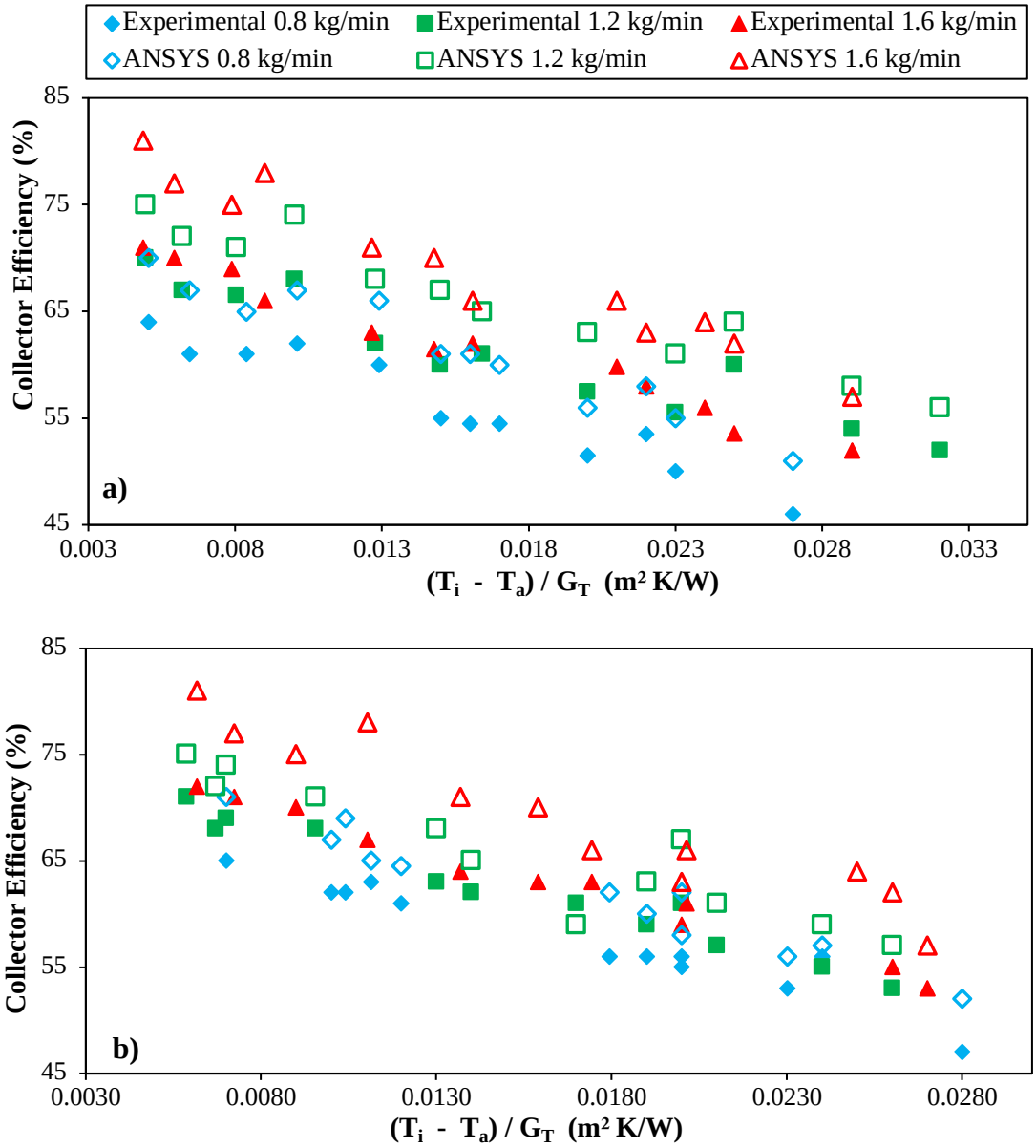

Figure 4.64 Comparison of the experimental and CFD simulated values of thermal efficiency of FPSC at different flow rate for 0.1 wt.% (a) SiO_2 and (b) ZnO nanofluid as working fluid

4.6.2.4 Comparison of metal oxides-based and carbon-based aqueous nanofluids

The previous sections have comprehensively addressed individual effects of covalently functionalized carbon/metal-based nanoparticles along with different weight concentrations as operational fluid on the thermal performance of FPSC. In this section, a final analysis has done between all of these five water-based nanofluids in terms of their positive effects on the thermal efficiency of FPSC, so that the best nanofluid can be

understood and chosen and that can be effectively used as an adequate alternative operating fluid in FPSC.

The influence of DI water and 0.1 wt.% nanofluids which were formulated in the present study on the values of TW and AP at 30°C inlet fluid temperature, 998 W/m^2 heat flux intensity and 1.6 kg/min mass flow rate along with the various locations of x/d in the direction of flow is shown in Figure 4.65. This figure shows that bio-facial clove-treated GNPs lead to the highest reduction in TW and AP compared to all other nanomaterials, including f-GNPs in comparison with DI water. It was noticed that the bio-facial clove treated GNPs showed better results than that of f-GNPs, which was prepared by the conventional functionalization method (acid-treated). This result is rational and agrees to with the fact that the same nanomaterial had previously demonstrated in this study, where the maximum rise in thermal conductivity of the base fluid was noticed. This has already been shown in previous sections that the convective heat transfer coefficient for nanofluids with the higher thermal conductivities is more significant relative to its pristine base fluid. Therefore, it can be inferred that the water-based CGNP nanofluids can reasonably be inferred that they have a comparatively higher coefficient of heat transfer and can achieve higher heat transfer efficiency.

The experimental thermal efficiency of FPSC against reduced temperature parameter at weight concentration 0.1% and different mass flow rates in comparison to DI water is presented in Figure 4.66. In contrast to that of water, it is clear that water based CGNP nanofluids again superior to all other nanofluids that were prepared in the present study. It shows the highest thermal performance of FPSC, up to 18.2% at 1.6 kg/min mass flow rate. Performances of 0.1 wt.% water based nanofluids can be sequenced as CGNPs > f-GNPs > PEG-Fe_3O_4 > ZnO > SiO_2 as result of the percentage improvement in FPSC's

thermal efficiencies obtain at the flow rate of 0.8 kg/min, with the corresponding values of 16.1% > 14.0% > 11.34% > 10.2% > 9.2%, respectively, in comparison with water data. The same sequence was found for the 1.2 kg/min and 1.6 kg/min mass flow rates but with the corresponding thermal efficiency values of 17.0% > 15.21% > 12.0% > 11.6% > 10.3% and 18.2% > 17.45% > 14.97% > 13.05% > 12.36%, respectively, in comparison with water data.

The change of performance index values versus a mass flow rate for the different water-based nanofluids that were prepared in the present study are shown in Figure 4.67 at the specific loadings of nanomaterials in the base fluid. It is remarkable that, regardless of weight concentrations and mass flow rates, all performance indexes are higher than 1, indicating that all water-based nanofluids that were prepared in the present study can be nominated as appropriate alternative working fluids in FPSCs. In this study, the 0.1 wt.% water-based nanofluids can be arranged in terms of the calculated values of performance index at a mass flow rate of 0.8 kg/min, as CGNPs > f-GNPs > PEG-Fe3O4 > ZnO > SiO_2 with the corresponding values of 1.125 > 1.115 > 1.098 > 1.067 > 1.063. Similar order was obtained for the 1.2 kg/min and 1.6 kg/min mass flow rates but with corresponding values of 1.140 > 1.130 > 1.105 > 1.104 > 1.08 and 1.142 > 1.110 > 1.105 > 1.096 > 1.087, respectively. In addition, the values of the performance index against weight concentrations are shown in Figure 4.68 at a mass flow rate of 1.6 kg/min. From this, it can easily be found that the performance index increases as the weight concentration of nanomaterials in the base fluid increases, indicating that the improvement in the thermal performance of the FPSC is higher than the rise in pressure drop. These results strengthened the concluding remarks that the aqueous colloidal dispersions of covalently functionalized carbon and iron-based nanomaterials that were prepared in this study have positive effects on the thermal performance of the FPSC and

superior to their negative effects on pressure drop. Thus, they can be used successfully in FPSCs or other related heat transfer applications as an exciting and innovative alternate working fluid. Based on the values as mentioned earlier for the improvement in thermal efficiency and performance index of the FPSC, it can be soundly decided that, among all the nanofluids that were prepared in the present study, the clove-treated GNPs is the most efficient nontraditional fluid that can be used for higher energy production in FPSCs or other machinery or engineering applications, instead of conventional work fluids.

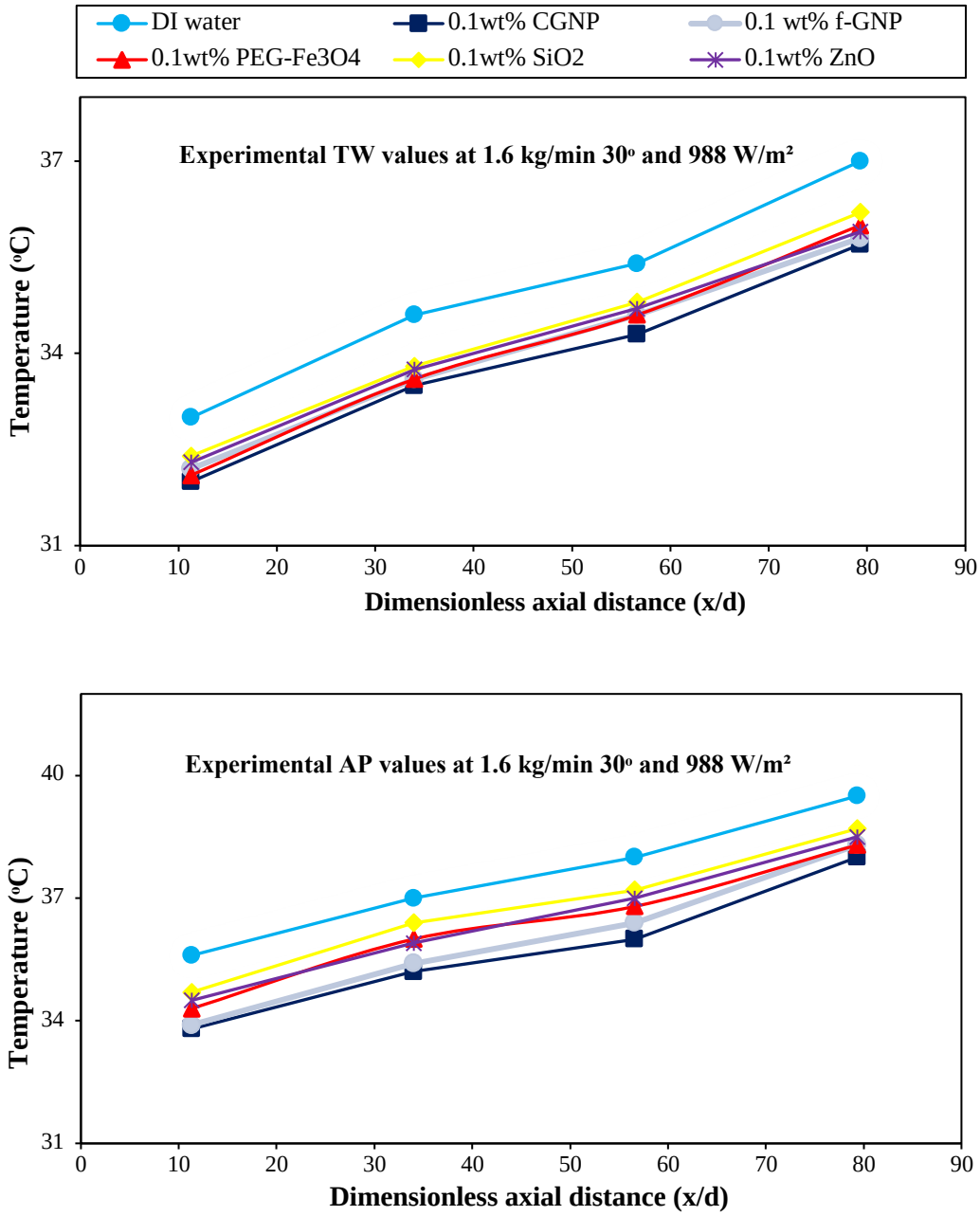

Figure 4.65 Experimental results of TW and AP for DI water and 0.1 wt.% carbon & metal-based nanofluids at inlet fluid temperature (30°C), heat flux intensity (998 W/m^2), and mass flow rate (1.6 kg/min).

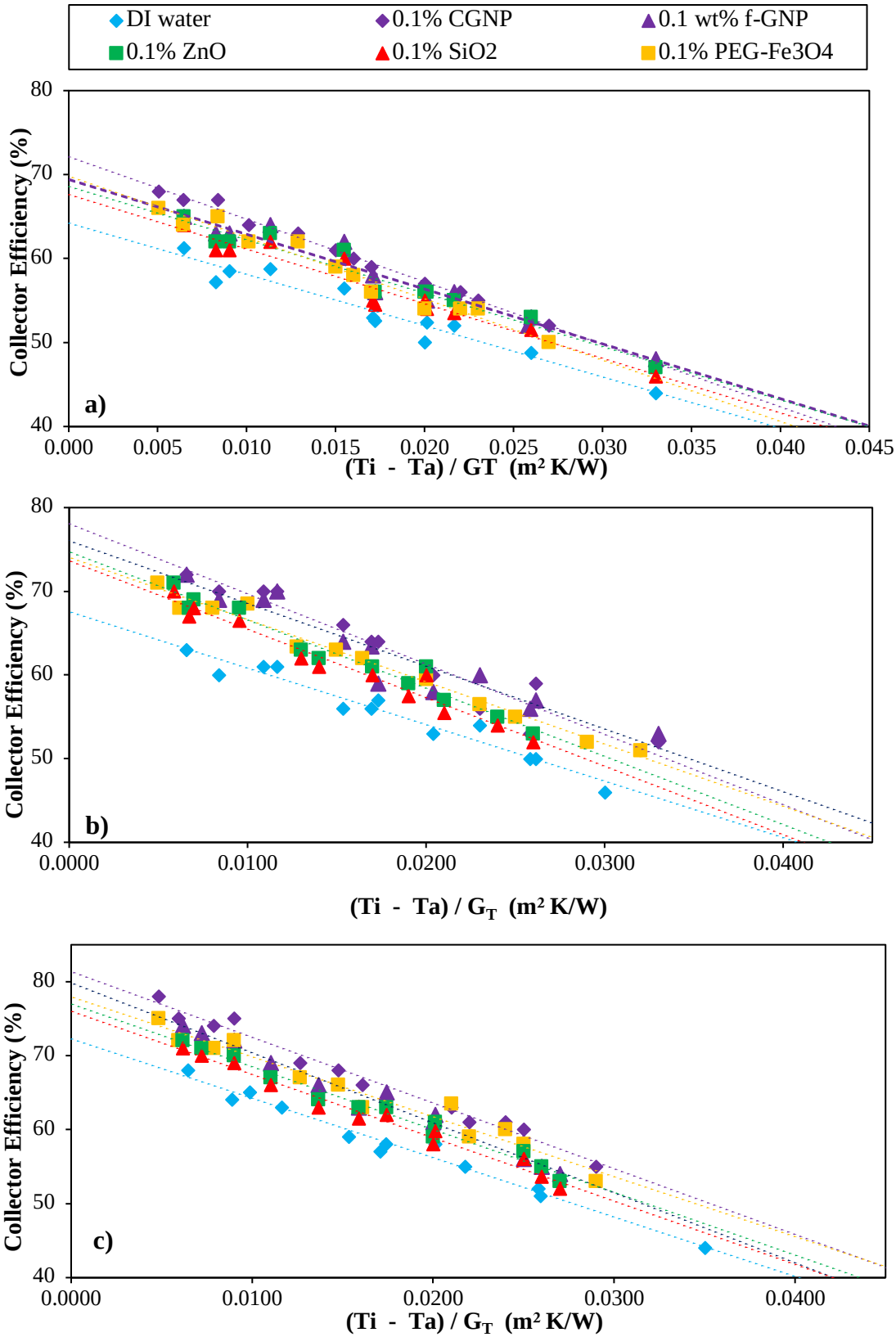

Figure 4.66 Comparison of the calculated thermal efficiency of FPSC for DI water and metal-based & carbon-based nanofluids at 0.1 wt.% concentration and mass flow rates of (a) 0.8 kg/min (b) 1.2 kg/min (c) 1.6 kg/min

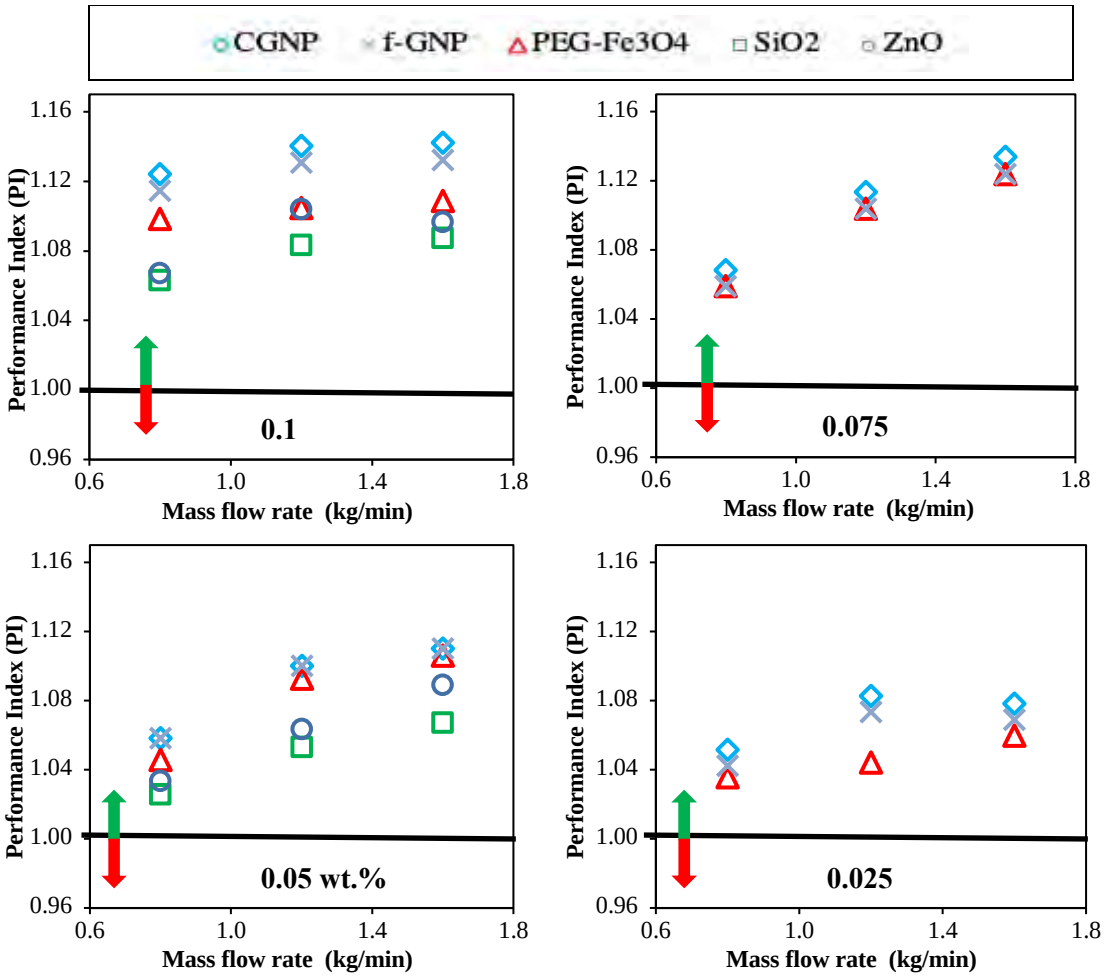

Figure 4.67 Performance index against flow rate for metal-based & carbon-based nanofluids at various weight concentrations

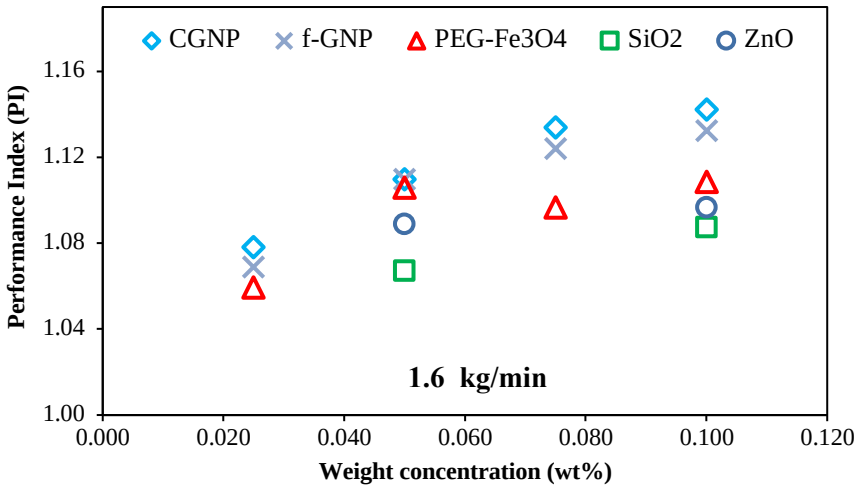

Figure 4.68 Variation of performance index with weight concentration for metal-based & carbon-based nanofluids at 1.6-kg/min mass flow rate

CHAPTER 5: CONCLUSION AND RECOMMENDATION

5.1 Introduction

The fundamental problems with the use of nanofluids in the flat-plate solar collector can be summarized by the high cost of nanomaterials, the long-term colloidal stability, and the increased viscosity which enhances the friction pressure drop and the pump power. Based on continued progress in the field of nanotechnology, all these problems can be solved soon.

The conclusions of the current research observations and the proposals for further work, which have not been carried out in this report due to lack of time, funding, materials, technology, and equipment restrictions etc. are presented in this chapter.

5.2 Conclusions

The present research aims to investigate, numerically and experimentally, the impact of using water-soluble carbon and metal oxides-based nanostructured nanofluids as the alternative working fluids on the performance of FPSC at various weight concentrations. The following conclusions could be drawn from all the results presented and discussions held in the previous chapters.

1. The maximum colloidal stability could be achieved with a period of 60 min ultrasonication, which could be concluded from stability data after various ultrasonication time of 15, 30, 60, and 90 min. For stable colloidal dispersion, covalent or non-covalent functionalization are therefore essential. The addition of sodium hexametaphosphate (SHMP) surfactant for non-covalent functionalization improved the stability up to a relative concentration of 0.87 for 0.05wt.% ZnO after 30 days. However, the covalent functionalization has been chosen due to excess foam and other adverse effects of surfactants on

nanofluid thermophysical properties. CGNPs, f-GNPs, and PEG- Fe_3O_4 were synthesized with covalent functionalization of pristine GNPs (SSA 750 m^2/g) and Iron nanoparticles (9 nm) respectively. Different characterization techniques have validated the success of the functionalization processes. Colloidal stability increased with covalent functionalization, and the rate of sedimentation depends upon the material type, specific area of material, and weight concentration of the materials. The colloidal stability of 0.025 wt.% PEG- Fe_3O_4 (9 nm) and the clove-treated GNPs (SSA 750 m^2/g) was substantially improved at the relative concentrations of 0.9543 and 0.9195, respectively.

2. Thermophysical properties like viscosity, density, and thermal conductivity were increased, while specific heat decreased with the weight concentrations of carbon and metal oxides-based nanofluids. The temperature was directly proportional to thermal conductivity and indirectly proportional to the viscosity, density, and specific heat of nanofluids. Experimental data of thermal conductivity of CGNPs showed good agreement with the model of Lu-Li (1996), While the model Maxwell (1881) is best for low weight concentration of CGNPs and PEG- Fe_3O_4. The maximum increment in viscosity of nanofluids was 24.05%, 22.4%, and 12% for SiO_2 (10-20 nm), PEG- Fe_3O_4 (9 nm), and CGNPs, respectively. The measured viscosity is well-matched with the Batchelor and Einstein model with a maximum deviation of 6.3% and 6.1% at 30 °C, respectively, for CGNPs nanofluids.
3. The Pak & Cho (1998) equation showed good agreement with measured value of density with maximum deviation of 0.12%, 0.10%, 0.11%, and 0.12%, respectively. The specific heat of nanofluids reduced by 1.54%, 1.23%, 1.08%,

and 0.37% for 0.1wt.% CGNPs, SiO_2 (10-20 nm), ZnO (< 50 nm), and PEG-Fe_3O_4 (9 nm), respectively. The Xuan & Roetzel (2000) and Pak & Cho (1998) equations are well-matched with the measured specific heat value with a maximum difference of 0.19% and 1.24%; 0.15% and 1.33% for CGNPs and PEG- Fe_3O_4 (9 nm), respectively.

4. A complete test rig was designed and fabricated for experimental analysis of the thermal efficiency of a FPSC. Distilled water and water-based nanofluids were used to conduct the tests. Values of AP and TW decreased with the increase in weight concentration and heat flux intensity. Similarly, the thermal efficiency of FPSC showed direct relation with the increase in heat flux intensity, weight concentration, and mass flow rate; and reverse relation with the fluid inlet temperature.
5. A decline in the AP and TW values and improved energy efficiency also resulted in the existence of each nanomaterial with any dimeter size, weight concentration, and SSA. In contrast to water, with rising weight concentration and SSA, and drop in diameter, the calculated values of AP and TW have reduced. The maximum reductions were 8.07% and 8.23% for CGNPs, and 5.93% and 4.80% for PEG-Fe_3O_4 (9 nm), respectively.
6. At 0.1 wt.% water-based nanofluids, the thermal efficiencies can be sequenced as CGNPs > f-GNPs > PEG-Fe_3O_4 (9 nm) > ZnO (< 50 nm) > SiO_2 (10-20 nm) as noticed from the results of the percentage improvement of the efficiencies in FPSC's at the flow rate of 0.8 kg/min. The thermal efficiencies of the FPSCs by using CGNPs, f-GNPs, PEG-Fe_3O_4 (9 nm), ZnO (< 50 nm) and SiO_2 were 16.1% > 14.0% > 11.34% > 10.2% > 9.2%, respectively in

comparison to the water data. Similar results trends were obtained at higher flow rates with enhanced efficiencies.

7. Thermal efficiency of FPSC and performance index, enhanced with the application of eco-friendly covalently functionalized GNPs (750 m^2/g) (CGNPs) based nanofluids. Thus, the explored alternative nanofluid could be a potential heat exchanging fluid for the next generation. On the other hand, the bio-facial synthesis method of CGNPs showed 0.75% improved thermal efficiency than the conventional functionalization method (acid-treated) of GNPs (f-GNPs), which further recommends the application of CGNPs and enhance environmental protection.
8. A mathematical model was set with some modifications and the ANSYS Fluent was used to simulate the thermal performance of the FPSC. This model was created according to certain assumptions to simplify the problem without affecting the fundamental principles. The correlations used for the thermophysical properties of nanofluids were chosen based on the various comparison of calculated and predicted data performed in this study. The experimental and simulation findings were verified with the available data. Experimental and simulated AP and TW values were well matched with a maximum difference of 2.21% and 2.48%, respectively.
9. Furthermore, the experimentally calculated thermal efficiency of FPSCs using water as a working fluid showed good agreement with predicted simulated values up to 3.22% accuracy which validated the experimental and ANSYS Fluent model data. The simulated thermal efficiency of FPSCs was higher than the experimental values with a maximum difference of 8.20% for CGNPs. Such variations between simulated and experimental results may appear from

numerous factors, including assumptions made for the mathematical model, correlation used for prediction of variable, numerical error as well as uncertainty in the experimental values. Consequently, the thermal efficiency of FPSC can be calculated using the ANSYS Fluent model by using water-based nanofluids within the acceptable accuracy level.

5.3 Recommendation for future work

In this work, the thermal performance of a FPSC was investigated with aqueous colloidal suspensions of covalently functionalized carbon and metal oxides-based nanofluids as its working fluids. The few generated research results in this area opened the option of a lot of work which could be done to enhance the performance of a FPSC. Based on the results of the present study, some specific subjects which may be considered in future research on nanofluids based FPSCs are enlisted below:

1. Researchers will, need to concentrate on preparing nanomaterials with higher SSA with their satisfactory colloidal stability, thermophysical properties, and thermal performance of the FPSCs.
2. The data obtained from the available correlations of thermophysical properties of nanofluids based on different materials were not in a regular manner when compared with measured data. Due to the unavailability of the correlations that can precisely calculate the thermophysical properties of any nanofluid, it is recommended to develop general correlations that can successfully predict the thermophysical properties of any nanofluid.
3. In the present work, five different nanomaterials at four different weight concentrations were used for the synthesis of water-based nanofluids. The thermal performance of FPSC was investigated using all the nanofluids at three

different mass flow rates, heat flux intensities, and inlet fluid temperatures. In the future, more research can be undertaken to explore thermal efficiency by increasing the mass flow rates and/or other types of nanoparticles that could provide a higher conductivity at lower weight concentrations, which can eventually generate higher thermal performance at less enhancement in viscosity of nanofluid based on water, i.e., higher levels of the performance index.

4. The current literature review on the nanofluid application in FPSCs revealed the lack of agreement in terms of thermophysical properties and thermal efficiency between the findings of the different researchers. More research is, therefore, necessary to determine the key causes of this difference in the experimental and theoretical results.
5. A crucial factor on selecting nanofluids as the heat transfer fluids is their stability in colloidal suspensions. Nanoparticles tend to agglomerate and settle in poorly prepared nanofluids, which can obstruct the flow channels and reduce their thermal conductivity. Therefore, researchers need to concentrate on synthesizing nanofluids with long colloidal stability in the suspension for their successful use in FSPCs or other applications in heat transfer equipment.

REFERENCES

Abdin, Z., Alim, M., Saidur, R., Islam, M., Rashmi, W., Mekhilef, S., & Wadi, A. (2013). Solar energy harvesting with the application of nanotechnology. *Renewable sustainable energy reviews, 26*, 837-852.

Ahmadi, A., Ganji, D. D., & Jafarkazemi, F. (2016). Analysis of utilizing Graphene nanoplatelets to enhance thermal performance of flat plate solar collectors. *Energy Conversion and Management, 126*, 1-11.

Ahuja, A. S. (1975). Augmentation of heat transport in laminar flow of polystyrene suspensions. II. Analysis of the data. *Journal of Applied Physics, 46*(8), 3417-3425.

Akhtar, N., & Mullick, S. (2007). Computation of glass-cover temperatures and top heat loss coefficient of flat-plate solar collectors with double glazing. *%J Energy, 32*(7), 1067-1074.

Alawi, O. A., Kamar, H. M., Mallah, A. R., Mohammed, H. A., Sabrudin, M. A. S., Newaz, K. M., . . . Yaseen, Z. M. (2021). Experimental and Theoretical Analysis of Energy Efficiency in a Flat Plate Solar Collector Using Monolayer Graphene Nanofluids. *Sustainability, 13*(10), 5416.

Alawi, O. A., Kamar, H. M., Mohammed, H. A., Mallah, A., & Hussein, O. A. (2020). Energy efficiency of a flat-plate solar collector using thermally treated graphene-based nanofluids: Experimental study. *Nanomaterials and Nanotechnology, 10*, 1847980420964618.

Alawi, O. A., Mallah, A., Kazi, S., Sidik, N. A. C., & Najafi, G. (2019a). Thermophysical properties and stability of carbon nanostructures and metallic oxides nanofluids. *Journal of Thermal Analysis Calorimetry, 135*(2), 1545-1562.

Alawi, O. A., Mallah, A., Kazi, S., Sidik, N. A. C., & Najafi, G. (2019b). Thermophysical properties and stability of carbon nanostructures and metallic oxides nanofluids. *Journal of Thermal Analysis and Calorimetry, 135*(2), 1545-1562.

Alawi, O. A., Mallah, A., Kazi, S., Sidik, N. A. C., Najafi, G. J. J. o. T. A., & Calorimetry. Thermophysical properties and stability of carbon nanostructures and metallic oxides nanofluids. *Journal of Thermal Analysis Calorimetry*, 1-18.

Alim, M., Abdin, Z., Saidur, R., Hepbasli, A., Khairul, M., & Rahim, N. (2013). Analyses of entropy generation and pressure drop for a conventional flat plate solar collector using different types of metal oxide nanofluids. *Energy and Buildings, 66*, 289-296.

Alper, A., & Oguz, O. (2016). The role of renewable energy consumption in economic growth: Evidence from asymmetric causality. *Renewable and Sustainable Energy Reviews, 60*, 953-959.

AlZaharani, A. A., Dincer, I., & Naterer, G. (2013). Performance evaluation of a geothermal based integrated system for power, hydrogen and heat generation. *International Journal of Hydrogen Energy, 38*(34), 14505-14511.

Amiri, A., Sadri, R., Shanbedi, M., Ahmadi, G., Chew, B., Kazi, S., . . . management. (2015). Performance dependence of thermosyphon on the functionalization approaches: an experimental study on thermo-physical properties of graphene nanoplatelet-based water nanofluids. *92*, 322-330.

Amrollahi, A., Rashidi, A., Emami Meibodi, M., & Kashefi, K. J. J. o. E. N. (2009). Conduction heat transfer characteristics and dispersion behaviour of carbon nanofluids as a function of different parameters. *4*(4), 347-363.

Amrutkar, S. K., Ghodke, S., & Patil, K. J. I. J. o. E. (2012). Solar flat plate collector analysis. *2*(2), 207-213.

Anderson, T. N., Duke, M., & Carson. (2010). The effect of colour on the thermal performance of building integrated solar collectors. *94*(2), 350-354.

Aravind, S. J., Baskar, P., Baby, T. T., Sabareesh, R. K., Das, S., & Ramaprabhu, S. (2011). Investigation of structural stability, dispersion, viscosity, and conductive heat transfer properties of functionalized carbon nanotube based nanofluids. *The Journal of Physical Chemistry C, 115*(34), 16737-16744.

Arzani, H. K., Amiri, A., Arzani, H. K., Rozali, S. B., Kazi, S., & Badarudin, A. (2016). Toward improved heat transfer performance of annular heat exchangers with water/ethylene glycol-based nanofluids containing graphene nanoplatelets. *Journal of Thermal Analysis Calorimetry, 126*(3), 1427-1436.

Assael, M., Metaxa, I., Arvanitidis, J., Christofilos, D., & Lioutas, C. (2005). Thermal conductivity enhancement in aqueous suspensions of carbon multi-walled and double-walled nanotubes in the presence of two different dispersants. *International Journal of Thermophysics, 26*(3), 647-664.

Azari, A., Kalbasi, M., Derakhshandeh, M., & Rahimi, M. (2013). An experimental study on nanofluids convective heat transfer through a straight tube under constant heat flux. *Chinese Journal of Chemical Engineering, 21*(10), 1082-1088.

Badran, A, A., Mustafa, F, M., Dawood, K, W., . . . K, Z. (2008). On the measurement of bond conductance in solar collector absorber plate. *J Energy Conversion Management, 49*(11), 3305-3310.

Badran, A. A., Mustafa, M. F., Dawood, W. K., & Ghazzawi, Z. K. (2008). On the measurement of bond conductance in solar collector absorber plate. *Energy Conversion Management, 49*(11), 3305-3310.

Bakari, R., Minja, R. J., & Njau, K. N. (2014). Effect of glass thickness on performance of flat plate solar collectors for fruits drying. *Journal of Energy, 2014*.

Balaji, K., Khan, A. I., Kumar, P. G., Iniyan, S., & Goic, R. (2019). Experimental analysis on free convection effect using two different thermal performance enhancers in absorber tube of a forced circulation flat plate solar water heater. *Solar Energy, 185*, 445-454.

Behi, M., & Mirmohammadi, S. A. (2012). Investigation on thermal conductivity, viscosity and stability of nanofluids. *Royal Institute of Technology (KTH) School of Industrial Engineering and Management, Stockholm, Sweden*.

Bender, E. J. C. I. T. (1969). Druckverlust bei laminarer Strömung im Rohreinlauf. *41*(11), 682-686.

Bhatt, M., Gaderia, S., & Channiwala, S. (2011). Experimental Investigations on Top Loss Coefficients of Solar Flat Plate Collector at Different Tilt Angle. *World Academy of Science, Engineering*.

Bisen, A., Dass, P., & Jain, R. (2011a). Parametric Studies of Top Heat Loss Coefficient of Double Glazed Flat Plate Solar Collectors. *MIT International Journal of Mechanical Engineering, 1*(2), 71-78.

Bisen, A., Dass, P., & Jain, R. (2011b). Parametric Studies of Top Heat Loss Coefficient of Double Glazed Flat Plate Solar Collectors. *J MIT International Journal of Mechanical Engineering, 1*(2), 71-78.

Blazek, J. (2015). *Computational fluid dynamics: principles and applications*: Butterworth-Heinemann.

Bogaerts, W. F., & Lampert, C. M. (1983). Materials for photothermal solar energy conversion. *Journal of Materials Science, 18*(10), 2847-2875.

Bourges, B., Rabl, A., Leide, B., Carvalho, M., & Collares-Pereira, M. J. S. E. (1991). Accuracy of the European solar water heater test procedure. Part 1: Measurement errors and parameter estimates. *47*(1), 1-16.

Cengel, Y. A., & Cimbala, J. M. (2006). *Fluid mechanics fundamentals and applications* (Vol. 2): McGraw-Hill Publication.

Chaji, H., Ajabshirchi, Y., Esmaeilzadeh, E., Heris, S. Z., Hedayatizadeh, M., & Kahani, M. (2013). Experimental study on thermal efficiency of flat plate solar collector using tio^ sub 2^/water nanofluid. *Modern Applied Science, 7*(10), 60.

Chandrasekar, M., Suresh, S., & Bose, A. C. (2010). Experimental investigations and theoretical determination of thermal conductivity and viscosity of Al2O3/water nanofluid. *Experimental Thermal Fluid Science, 34*(2), 210-216.

Chandrasekar, M., Suresh, S., & Senthilkumar, T. (2012). Mechanisms proposed through experimental investigations on thermophysical properties and forced convective heat transfer characteristics of various nanofluids–A review. *Renewable and Sustainable Energy Reviews, 16*(6), 3917-3938.

Chen, L., Xie, H., Li, Y., & Yu, W. (2008). Nanofluids containing carbon nanotubes treated by mechanochemical reaction. *Thermochimica acta, 477*(1-2), 21-24.

Chen, Z., Furbo, S., Perers, B., Fan, J., & Andersen, E. (2012). Efficiencies of flat plate solar collectors at different flow rates. *30*, 65-72.

Choi, S., Zhang, Z., Yu, W., Lockwood, F., & Grulke, E. (2001). Anomalous thermal conductivity enhancement in nanotube suspensions. *Applied physics letters, 79*(14), 2252-2254.

Choi, S. U., & Eastman, J. A. (1995). *Enhancing thermal conductivity of fluids with nanoparticles*. Retrieved from

Chon, C., & Kihm, K. J. T.-A. S. O. M. E. J. O. H. T. (2005). Thermal conductivity enhancement of nanofluids by Brownian motion. *Journal of Heat Transfer-Transactions of the Asme, 127*(8), 810. doi:Doi 10.1115/1.2033316

Chu, K., Li, W.-s., Dong, H.-f., & Tang, F.-l. (2012). Modeling the thermal conductivity of graphene nanoplatelets reinforced composites. *EPL, 100*(3), 36001.

Codd, D. S., Carlson, A., Rees, J., & Slocum, A. H. (2010). A low cost high flux solar simulator. *Solar Energy, 84*(12), 2202-2212.

Colangelo, G., Favale, E., De Risi, A., & Laforgia, D. (2013). A new solution for reduced sedimentation flat panel solar thermal collector using nanofluids. *Applied Energy, 111*, 80-93.

Corcione, M. J. E. C., & Management. (2011). Empirical correlating equations for predicting the effective thermal conductivity and dynamic viscosity of nanofluids. *Energy Conversion and Managment, 52*(1), 789-793.

Cornell, R. M., & Schwertmann, U. (2003). *The iron oxides: structure, properties, reactions, occurrences and uses*: John Wiley & Sons.

Coskun, C., Oktay, Z., & Dincer, I. (2012). Thermodynamic analyses and case studies of geothermal based multi-generation systems. *Journal of Cleaner Production, 32*, 71-80.

Das, R., Hamid, S. B. A., Ali, M., Annuar, M., Samsudin, E. M. B., & Bagheri, S. J. S. o. A. M. (2015). Covalent functionalization schemes for tailoring solubility of multi-walled carbon nanotubes in water and acetone solvents. *7*(12), 2726-2737.

Das, S. K., Choi, S. U., & Patel, H. E. (2006). Heat transfer in nanofluids—a review. *Heat transfer engineering, 27*(10), 3-19.

Das, S. K., Putra, N., Thiesen, P., & Roetzel, W. (2003). Temperature dependence of thermal conductivity enhancement for nanofluids. *Journal of Heat Transfer, 125*(4), 567-574.

Daungthongsuk, W., & Wongwises, S. (2007). A critical review of convective heat transfer of nanofluids. *Renewable and Sustainable Energy Reviews, 11*(5), 797-817.

Ding, Y., Chen, H., He, Y., Lapkin, A., Yeganeh, M., Šiller, L., & Butenko, Y. V. (2007). Forced convective heat transfer of nanofluids. *Advanced Powder Technology, 18*(6), 813-824.

Ding, Y., Wen, D., & Williams, R. (2004). *Nanofluids for heat transfer intensification–Where are we and where should we go?* Paper presented at the Proceedings of 6th International Symposium on Heat Transfer, Beijing.

Dorniani, D., Hussein, M. Z. B., Kura, A. U., Fakurazi, S., Shaari, A. H., & Ahmad, Z. (2012). Preparation of Fe3O4 magnetic nanoparticles coated with gallic acid for drug delivery. *International Journal of Nanomedicine, 7*, 5745.

Drzazga, M., Gierczycki, A., Dzido, G., & Lemanowicz, M. (2013). Influence of nonionic surfactant addition on drag reduction of water based nanofluid in a small diameter pipe. *Chinese Journal of Chemical Engineering, 21*(1), 104-108.

Duangthongsuk, W., & Wongwises, S. (2010). An experimental study on the heat transfer performance and pressure drop of TiO2-water nanofluids flowing under a turbulent flow regime. *International journal of Heat and Mass transfer, 53*(1-3), 334-344.

Duffie, J. A., & Beckman, W. (1980). Solar thermal engineering processes. In: Wiley, New York.

Duffie, J. A., & Beckman, W. A. (2013). *Solar engineering of thermal processes*: John Wiley & Sons.

Eastman, J. A., Choi, S., Li, S., Yu, W., & Thompson, L. (2001). Anomalously increased effective thermal conductivities of ethylene glycol-based nanofluids containing copper nanoparticles. *Applied Physics Letters, 78*(6), 718-720.

Efficiency, G. G. E. (2013). Retrieved from http://www.green-group.rs/index.php?r=1780

Esfe, M. H., Arani, A. A. A., Rezaie, M., Yan, W.-M., Karimipour, A. J. I. C. i. H., & Transfer, M. (2015). Experimental determination of thermal conductivity and dynamic viscosity of Ag–MgO/water hybrid nanofluid. *International Communications in Heat andMass transfer, 66*, 189-195.

Faizal, M., Saidur, R., & Mekhilef, S. (2013). *Potential of size reduction of flat-plate solar collectors when applying MWCNT nanofluid.* Paper presented at the IOP Conference Series: Earth and Environmental Science.

Faizal, M., Saidur, R., Mekhilef, S., & Alim, M. (2013). Energy, economic and environmental analysis of metal oxides nanofluid for flat-plate solar collector. *Energy Conversion and Management, 76*, 162-168.

Farajzadeh, E., Movahed, S., & Hosseini, R. (2018). Experimental and numerical investigations on the effect of Al2O3/TiO2H2O nanofluids on thermal efficiency of the flat plate solar collector. *Renewable Energy, 118*, 122-130.

Foster, R., Ghassemi, M., & Cota, A. (2009). *Solar energy: renewable energy and the environment*: CRC Press.

Garg, P., Alvarado, J. L., Marsh, C., Carlson, T. A., Kessler, D. A., & Annamalai, K. (2009). An experimental study on the effect of ultrasonication on viscosity and heat transfer performance of multi-wall carbon nanotube-based aqueous nanofluids. *International journal of Heat and Mass transfer, 52*(21-22), 5090-5101.

Garrido, J., Aichmayer, L., Wang, W., & Laumert, B. J. E. (2017). Characterization of the KTH high-flux solar simulator combining three measurement methods. *Energy, 141*, 2091-2099.

Ghadimi, A., & Metselaar, I. H. (2013). The influence of surfactant and ultrasonic processing on improvement of stability, thermal conductivity and viscosity of titania nanofluid. *Experimental Thermal and Fluid Science, 51*, 1-9.

Ghadimi, A., Saidur, R., & Metselaar, H. (2011a). A review of nanofluid stability properties and characterization in stationary conditions. *International journal of Heat and Mass transfer, 54*(17-18), 4051-4068.

Ghadimi, A., Saidur, R., & Metselaar, H. (2011b). A review of nanofluid stability properties and characterization in stationary conditions. *International journal of heat mass transfer, 54*(17-18), 4051-4068.

Gillett, W. B., & Moon, J. E. (1985). Test methods and design guidelines. Dordrecht, Holland: D. Reidel Pub. Co. for the Commission of the European Communities. *Solar collectors*.

Godson, L., Raja, B., Lal, D. M., & Wongwises, S. (2010). Experimental investigation on the thermal conductivity and viscosity of silver-deionized water nanofluid. *Experimental Heat Transfer, 23*(4), 317-332.

Goldstein, J. I., Newbury, D. E., Echlin, P., Joy, D. C., Lyman, C. E., Lifshin, E., . . . Michael, J. R. (2003). Special topics in electron beam x-ray microanalysis. In *Scanning Electron Microscopy and X-ray Microanalysis* (pp. 453-536): Springer.

Gong, F., Bui, K., Papavassiliou, D. V., & Duong, H. M. (2014). Thermal transport phenomena and limitations in heterogeneous polymer composites containing carbon nanotubes and inorganic nanoparticles. *Carbon, 78*, 305-316.

Goodwin, J. W. (2004). Colloids and Interfaces with Surfactants and Polymers - An Introduction (pp. i-ix). Retrieved from http://www.slideshare.net/ivancastaneda925/colloids-and-interfaces-with-surfactants-and-polymers-an-introduction. doi:doi:10.1002/0470093919

Gupta, H. K., Das Agrawal, G., & Mathur, J. (2015). An experimental investigation of a low temperature Al2O3-H2O nanofluid based direct absorption solar collector. *Solar Energy, 118*, 390-396. Retrieved from <Go to ISI>://WOS:000359166700037

Gupta, M., Singh, V., Kumar, R., & Said, Z. (2017). A review on thermophysical properties of nanofluids and heat transfer applications. *Renewable and Sustainable Energy Reviews, 74*, 638-670.

Hajabdollahi, F., & Premnath, K. (2017). Numerical study of the effect of nanoparticles on thermoeconomic improvement of a solar flat plate collector. *Applied Thermal Engineering, 127*, 390-401.

Halelfadl, S., Maré, T., & Estellé, P. (2014). Efficiency of carbon nanotubes water based nanofluids as coolants. *Experimental Thermal and Fluid Science, 53*, 104-110.

Harish, S., Ishikawa, K., Einarsson, E., Aikawa, S., Inoue, T., Zhao, P., . . . Maruyama, S. J. M. E. (2012). Temperature dependent thermal conductivity increase of aqueous nanofluid with single walled carbon nanotube inclusion. *Materials Express, 2*(3), 213-223.

Hawwash, A., Rahman, A. K. A., Nada, S., & Ookawara, S. (2018). Numerical Investigation and Experimental Verification of Performance Enhancement of Flat Plate Solar Collector Using Nanofluids. *Applied Thermal Engineering, 130*, 363-374.

He, Q., Wang, S., Zeng, S., & Zheng, Z. (2013). Experimental investigation on photothermal properties of nanofluids for direct absorption solar thermal energy systems. *%J Energy Conversion Management, 73*, 150-157.

He, Q., Zeng, S., & Wang, S. (2015). Experimental investigation on the efficiency of flat-plate solar collectors with nanofluids. *Applied Thermal Engineering, 88*, 165-171.

Ho, C., & Chen, T. (2006). The recycle effect on the collector efficiency improvement of double-pass sheet-and-tube solar water heaters with external recycle. *31*(7), 953-970.

Hodkiewicz, J., & Scientific, T. J. a. n. (2010). Characterizing carbon materials with Raman spectroscopy. *51946*.

Holman. (J. P. (2012).). Experimental methods for engineers (Eight ed.). . *New York: McGraw-Hill series in mechanical engineering.*

Hong, T.-K., Yang, H.-S., & Choi, C. (2005). Study of the enhanced thermal conductivity of Fe nanofluids. *Journal of Applied Physics, 97*(6), 064311.

Hood, T. G., & Meyer, S. F. (1994). Low transmission heat-reflective glazing materials. In: Google Patents.

Hordy, N., Rabilloud, D., Meunier, J.-L., & Coulombe, S. (2014). High temperature and long-term stability of carbon nanotube nanofluids for direct absorption solar thermal collectors. *Solar Energy, 105*, 82-90.

Hosseini, M., Abdelrazek, A. H., Sadri, R., Mallah, A., Kazi, S., Chew, B., . . . Yusoff, N. (2018). Numerical study of turbulent heat transfer of nanofluids containing eco-friendly treated carbon nanotubes through a concentric annular heat exchanger. *International journal of Heat and Mass transfer, 127*, 403-412.

Hottel, H., & Woertz, B. (1942). Performance of flat-plate solar-heat collectors. *Trans. ASME (Am. Soc. Mech. Eng.);(United States), 64*.

Hottel, H. C., & Whillier, A. (1958). Evaluation of flat-plate solar-collector performance. Paper presented at the Transactions of the conference on the use of solar energy,. *University of Arizona, Tucson, AZ.*

Huang, J., Wang, X., Long, Q., Wen, X., Zhou, Y., & Li, L. (2009). *Influence of pH on the stability characteristics of nanofluids.* Paper presented at the 2009 Symposium on Photonics and Optoelectronics.

Hussein, O. A., Habib, K., Muhsan, A. S., Saidur, R., Alawi, O. A., & Ibrahim, T. K. (2020). Thermal performance enhancement of a flat plate solar collector using hybrid nanofluid. *Solar Energy, 204*, 208-222.

Huxtable, S. T., Cahill, D. G., Shenogin, S., Xue, L., Ozisik, R., Barone, P., . . . Shim, M. (2003). Interfacial heat flow in carbon nanotube suspensions. *Nature materials, 2*(11), 731.

Hwang, Lee, J., Lee, C., Jung, Y., Cheong, S., Lee, C., . . . Jang, S. (2007). Stability and thermal conductivity characteristics of nanofluids. *Thermochimica Acta, 455*(1-2), 70-74.

Hwang, Y., Lee, J.-K., Lee, J.-K., Jeong, Y.-M., Cheong, S.-i., Ahn, Y.-C., & Kim, S. H. (2008). Production and dispersion stability of nanoparticles in nanofluids. *Powder technology, 186*(2), 145-153.

Hwang, Y., Park, H., Lee, J., & Jung, W. (2006). Thermal conductivity and lubrication characteristics of nanofluids. *Current Applied Physics, 6*, e67-e71.

Ibrahim, O., Fardoun, F., Younes, R., & Ibrahim, M. (2018). Improved model for calculating instantaneous efficiency of flat-plate solar thermal collector. *Journal of Heat Transfer, 140*(6), 062801.

Iyengar, S. J., Joy, M., Ghosh, C. K., Dey, S., Kotnala, R. K., & Ghosh, S. (2014). Magnetic, X-ray and Mössbauer studies on magnetite/maghemite core–shell nanostructures fabricated through an aqueous route. *Rsc Advances, 4*(110), 64919-64929.

Javadi, F., Saidur, R., & Kamalisarvestani, M. (2013a). Investigating performance improvement of solar collectors by using nanofluids. *Renewable and Sustainable Energy Reviews, 28*, 232-245.

Javadi, F., Saidur, R., & Kamalisarvestani, M. (2013b). Investigating performance improvement of solar collectors by using nanofluids. *Renewable Sustainable Energy Reviews, 28*, 232-245.

Jeon, I.-Y., Chang, D. W., Kumar, N. A., & Baek, J.-B. J. C. n.-p. n. (2011). Functionalization of carbon nanotubes. 91-110.

Jiang, L., Gao, L., & Sun, J. (2003a). Production of aqueous colloidal dispersions of carbon nanotubes. *Journal of colloid interface science, 260*(1), 89-94.

Jiang, L., Gao, L., & Sun, J. (2003b). Production of aqueous colloidal dispersions of carbon nanotubes. *Journal of Colloid and Interface Science, 260*(1), 89-94.

Jiaqiang, E., Liu, T., Yang, W., Li, J., Gong, J., & Deng, Y. (2016). Effects of fatty acid methyl esters proportion on combustion and emission characteristics of a biodiesel fueled diesel engine. *Energy Conversion and Management, 117*, 410-419.

Jouybari, H. J., Saedodin, S., Zamzamian, A., Nimvari, M. E., & Wongwises, S. (2017). Effects of porous material and nanoparticles on the thermal performance of a flat plate solar collector: An experimental study. *Renewable Energy, 114*, 1407-1418.

Kahani, M., Heris, S. Z., & Mousavi, S. M. (2013). Comparative study between metal oxide nanopowders on thermal characteristics of nanofluid flow through helical coils. *Powder Technology, 246*, 82-92.

Kalogirou, S. A. (2013). *Solar energy engineering: processes and systems*: Academic Press.

Kalogirou, S. A. ((2009).). Solar energy engineering - processes and systems (1st ed.): Academic Press.

Kang, H. U., Kim, S. H., & Oh, J. M. (2006). Estimation of thermal conductivity of nanofluid using experimental effective particle volume. *Experimental Heat Transfer, 19*(3), 181-191.

Kang, W., Shin, Y., & Cho, H. (2017). Economic Analysis of Flat-Plate and U-Tube Solar Collectors Using an Al2O3 Nanofluid. *Energies, 10*(11), 1911.

Keblinski, P., Eastman, J. A., & Cahill, D. G. (2005). Nanofluids for thermal transport. *Materials today, 8*(6), 36-44.

Khalifa, A. J. N., & Jabbar, R. A. A. (2010a). Conventional versus storage domestic solar hot water systems: A comparative performance study. *Energy Conversion Management, 51*(2), 265-270.

Khalifa, A. J. N., & Jabbar, R. A. A. (2010b). Conventional versus storage domestic solar hot water systems: A comparative performance study. *J Energy ConversionManagement, 51*(2), 265-270.

Khoukhi, M., & Maruyama, S. (2006). Theoretical approach of a flat-plate solar collector taking into account the absorption and emission within glass cover layer. *Solar Energy, 80*(7), 787-794.

Khullar, V., & Tyagi, H. (2010). *Application of nanofluids as the working fluid in concentrating parabolic solar collectors.* Paper presented at the 37th National & 4th International Conference on Fluid Mechanics & Fluid Power, IIT Madras, Chennai, India, Dec.

Khullar, V., Tyagi, H., Phelan, P. E., Otanicar, T. P., Singh, H., & Taylor, R. A. (2012). Solar energy harvesting using nanofluids-based concentrating solar collector. *Journal of Nanotechnology in Engineering and Medicine, 3*(3), 031003.

Kim, H., Kim, J., & Cho, H. (2017). Experimental study on performance improvement of U-tube solar collector depending on nanoparticle size and concentration of Al2O3 nanofluid. *Energy, 118*, 1304-1312.

Klein, S. (1975). Calculation of flat-plate collector loss coefficients. *Solar Energy, 17*, 79.

Kline, S. J. J. M. E. (1953). Describing uncertainty in single sample experiments. *75*, 3-8.

Köhl, M., Jorgensen, G., Brunold, S., Carlsson, B., Heck, M., & Möller, K. J. S. e. (2005). Durability of polymeric glazing materials for solar applications. *79*(6), 618-623.

Kumar, S. A., Meenakshi, K. S., Narashimhan, B., Srikanth, S., & Arthanareeswaran, G. (2009). Synthesis and characterization of copper nanofluid by a novel one-step method. *Materials Chemistry Physics Reports, 113*(1), 57-62.

Lee, G.-J., & Rhee, C. K. (2014). Enhanced thermal conductivity of nanofluids containing graphene nanoplatelets prepared by ultrasound irradiation. *Journal of Materials Science, 49*(4), 1506-1511.

Lee, G.-J., & Rhee, C. K. (2014). Enhanced thermal conductivity of nanofluids containing graphene nanoplatelets prepared by ultrasound irradiation. *Journal of materials science, 49*(4), 1506-1511.

Lee, J.-H., Hwang, K. S., Jang, S. P., Lee, B. H., Kim, J. H., Choi, S. U., & Choi, C. J. (2008). Effective viscosities and thermal conductivities of aqueous nanofluids containing low volume concentrations of Al2O3 nanoparticles. *International Journal of Heat Mass Transfer, 51*(11-12), 2651-2656.

Leon, O. (2010). Applications of nanofluids: current and future, Adv. *Mech. Eng, 519659*.

Li, J., Li, Z., & Wang, B. (2002). Experimental viscosity measurements for copper oxide nanoparticle suspensions. *Tsinghua Science and Technology, 7*(2), 198-201.

Li, X., Zhu, D., Wang, X., Wang, N., Gao, J., & Li, H. (2008). Thermal conductivity enhancement dependent pH and chemical surfactant for Cu-H2O nanofluids. *Thermochimica Acta, 469*(1-2), 98-103.

Li, Y., Tung, S., Schneider, E., & Xi, S. (2009). A review on development of nanofluid preparation and characterization. *Powder technology, 196*(2), 89-101.

Liu, X. L., Fan, H. M., Yi, J. B., Yang, Y., Choo, E. S. G., Xue, J. M., & Ding, J. (2012). Optimization of surface coating on Fe 3 O 4 nanoparticles for high performance magnetic hyperthermia agents. *Journal of Materials Chemistry, 22*(17), 8235-8244.

Mahbubul, I., Saidur, R., & Amalina, M. (2012). Latest developments on the viscosity of nanofluids. *International Journal of Heat Mass Transfer, 55*(4), 874-885.

Mahian, O., Kianifar, A., Kalogirou, S. A., Pop, I., & Wongwises, S. (2013). A review of the applications of nanofluids in solar energy. *International journal of Heat and Mass transfer, 57*(2), 582-594.

Mahian, O., Kianifar, A., Sahin, A. Z., & Wongwises, S. (2014). Performance analysis of a minichannel-based solar collector using different nanofluids. *Energy Conversion and Management, 88*, 129-138. Retrieved from <Go to ISI>://WOS:000345725400014

Mahian, O., Kianifar, A., Sahin, A. Z., & Wongwises, S. (2015). Heat transfer, pressure drop, and entropy generation in a solar collector using SiO2/water nanofluids: effects of nanoparticle size and pH. *Journal of Heat Transfer, 137*(6), 061011.

Mahmood, A. (2012). Numerical and analytical study of nanofluids thermal and hydrodynamic characteristics. (Doctoral dissertation),. *University of Sherbrooke Sherbrooke (Quebec), Canada.*

Maiga, S. E. B., Palm, S. J., Nguyen, C. T., Roy, G., & Galanis, N. (2005). Heat transfer enhancement by using nanofluids in forced convection flows. *International journal of heat and fluid flow, 26*(4), 530-546.

Marconnet, A. M., Panzer, M. A., & Goodson, K. E. (2013). Thermal conduction phenomena in carbon nanotubes and related nanostructured materials. *Reviews of Modern Physics, 85*(3), 1295.

Martín, R. H., Pinar, G. A., & García, J. P. (2011). *Experimental heat transfer research in enhanced flat-plate solar collectors.* Paper presented at the World Renewable Energy Congress-Sweden; 8-13 May; 2011; Linköping; Sweden.

Meibodi, M. E., Vafaie-Sefti, M., Rashidi, A. M., Amrollahi, A., Tabasi, M., & Kalal, H. S. (2010). The role of different parameters on the stability and thermal

conductivity of carbon nanotube/water nanofluids. *International Communications in Heat and Mass Transfer, 37*(3), 319-323.

Meibodi, S. S., Kianifar, A., Niazmand, H., Mahian, O., & Wongwises, S. (2015). Experimental investigation on the thermal efficiency and performance characteristics of a flat plate solar collector using SiO2/EG–water nanofluids. *International Communications in Heat and Mass Transfer, 65*, 71-75.

Michael, J. J., & Iniyan, S. (2015). Performance of copper oxide/water nanofluid in a flat plate solar water heater under natural and forced circulations. *Energy Conversion and Management, 95*, 160-169.

Minardi, J. E., & Chuang, H. N. (1975). Performance of a "black" liquid flat-plate solar collector. *Solar Energy, 17*(3), 179-183.

Mingzheng, Z., Guodong, X., Jian, L., Lei, C., & Lijun, Z. (2012). Analysis of factors influencing thermal conductivity and viscosity in different kinds of surfactant solutions. *Experimental Thermal and Fluid Science, 36*, 22-29.

Mirzaei, M., Hosseini, S. M. S., & Kashkooli, A. M. M. (2018). Assessment of Al2O3 nanoparticles for the optimal operation of the flat plate solar collector. *Applied Thermal Engineering, 134*, 68-77.

Moghadam, A. J., Farzane-Gord, M., Sajadi, M., & Hoseyn-Zadeh, M. (2014). Effects of CuO/water nanofluid on the efficiency of a flat-plate solar collector. *Experimental Thermal and Fluid Science, 58*, 9-14.

Moghadam, M. C., Edalatpour, M., & Solano, J. P. (2017). Numerical Study on Conjugated Laminar Mixed Convection of Alumina/Water Nanofluid Flow, Heat Transfer, and Entropy Generation Within a Tube-on-Sheet Flat Plate Solar Collector. *Journal of Solar Energy Engineering, 139*(4), 041011.

Mondini, S., Cenedese, S., Marinoni, G., Molteni, G., Santo, N., Bianchi, C. L., & Ponti, A. (2008). One-step synthesis and functionalization of hydroxyl-decorated magnetite nanoparticles. *Journal of Colloid and Interface Science, 322*(1), 173-179.

Munich, C. T. (2013). Modeling of the thermal output of a flat plate solar collector. (Master's thesis).The University of Arizona, Arizona. Retrieved from ProQuest Dissertations & Theses database. *(UMI No. 1537563)*.

Nan, C.-W., Shi, Z., & Lin, Y. (2003). A simple model for thermal conductivity of carbon nanotube-based composites. *Chemical Physics Letters, 375*(5-6), 666-669.

Nanda, J., Maranville, C., Bollin, S. C., Sawall, D., Ohtani, H., Remillard, J. T., & Ginder, J. (2008). Thermal conductivity of single-wall carbon nanotube dispersions: role of interfacial effects. *The Journal of Physical Chemistry C, 112*(3), 654-658.

Nawayseh, N. K., Farid, M. M., Omar, A. A., & Sabirin, A. (1999). Solar desalination based on humidification process—II. Computer simulation. *Energy conversion management, 40*(13), 1441-1461.

Nguyen, C., Desgranges, F., Roy, G., Galanis, N., Maré, T., Boucher, S., & Mintsa, H. A. (2007). Temperature and particle-size dependent viscosity data for water-based nanofluids–hysteresis phenomenon. *International Journal of Heat and Fluid Flow, 28*(6), 1492-1506.

Nieto de Castro, C., Li, S., Nagashima, A., Trengove, R., Wakeham, W. J. J. o. p., & data, c. r. (1986). Standard reference data for the thermal conductivity of liquids. *Journal of Physical and Chemical Reference Data, 15*(3), 1073-1086.

Noghrehabadi, A., Hajidavaloo, E., & Moravej, M. (2016). Experimental investigation of efficiency of square flat-plate solar collector using SiO2/water nanofluid. *Case Studies in Thermal Engineering, 8*, 378-386.

Ohler, A., & Fetters, I. (2014). The causal relationship between renewable electricity generation and GDP growth: A study of energy sources. *Energy economics, 43*, 125-139.

Oliva, A., Maldonado, R., Díaz, E., & Montalvo, A. (2013). *A high absorbance material for solar collectors' applications.* Paper presented at the IOP Conference Series: Materials Science and Engineering.

Ong. (1976). An improved computer program for the thermal performance of a solar water heater. *18*(3), 183-191.

Ong, K. J. S. E. (1974). A finite-difference method to evaluate the thermal performance of a solar water heater. *16*(3-4), 137-147.

Otanicar, T. P. (2009). *Direct absorption solar thermal collectors utilizing liquid-nanoparticle suspensions*: Arizona State University.

Otanicar, T. P., Phelan, P. E., Prasher, R. S., Rosengarten, G., & Taylor, R. A. (2010). Nanofluid-based direct absorption solar collector. *Journal of renewable and sustainable energy, 2*(3), 033102.

Pak, B. C., & Cho, Y. I. (1998). HYDRODYNAMIC AND HEAT TRANSFER STUDY OF DISPERSED FLUIDS WITH SUBMICRON METALLIC OXIDE PARTICLES. *Experimental Heat Transfer, 11*(2), 151-170. doi:10.1080/08916159808946559

Pantzali, M., Kanaris, A., Antoniadis, K., Mouza, A., & Paras, S. (2009). Effect of nanofluids on the performance of a miniature plate heat exchanger with modulated surface. *International Journal of Heat and Fluid Flow, 30*(4), 691-699.

Pantzali, M., Mouza, A., & Paras, S. (2009). Investigating the efficacy of nanofluids as coolants in plate heat exchangers (PHE). *Chemical Engineering Science, 64*(14), 3290-3300.

Parthasarathy, V. A., Chempakam, B., & Zachariah, T. J. (2008). *Chemistry of spices*: Cabi.

Phelan, P., Otanicar, T., Taylor, R., & Tyagi, H. (2013). Trends and opportunities in direct-absorption solar thermal collectors. *Journal of Thermal Science and Engineering Applications, 5*(2), 021003.

Prasher, R., Song, D., Wang, J., & Phelan, P. (2006). Measurements of nanofluid viscosity and its implications for thermal applications. *Applied Physics Letters, 89*(13), 133108.

Raj, P., & Subudhi, S. (2018). A review of studies using nanofluids in flat-plate and direct absorption solar collectors. *%J Renewable Sustainable Energy Reviews, 84*, 54-74.

Rashidi, S., Mahian, O., Languri, E. M. J. J. o. T. A., & Calorimetry. (2018). Applications of nanofluids in condensing and evaporating systems. *Journal of Thermal Analysis and Calorimetry, 131*(3), 2027-2039. doi:10.1007/s10973-017-6773-7

Razi, P., Akhavan-Behabadi, M., & Saeedinia, M. (2011). Pressure drop and thermal characteristics of CuO–base oil nanofluid laminar flow in flattened tubes under constant heat flux. *International Communications in Heat and Mass Transfer, 38*(7), 964-971.

Rubin, M. (1985). Optical properties of soda lime silica glasses. *Solar energy materials, 12*(4), 275-288.

Sadri, R., Hosseini, M., Kazi, S., Bagheri, S., Abdelrazek, A. H., Ahmadi, G., . . . Abidin, N. (2018). A facile, bio-based, novel approach for synthesis of covalently functionalized graphene nanoplatelet nano-coolants toward improved thermo-physical and heat transfer properties. *Journal of colloid and interface science, 509*, 140-152.

Sadri, R., Hosseini, M., Kazi, S., Bagheri, S., Abdelrazek, A. H., Ahmadi, G., . . . science, i. (2018). A facile, bio-based, novel approach for synthesis of covalently functionalized graphene nanoplatelet nano-coolants toward improved thermo-physical and heat transfer properties. *509*, 140-152.

Sadri, R., Hosseini, M., Kazi, S., Bagheri, S., Ahmed, S., Ahmadi, G., . . . Dahari, M. (2017). Study of environmentally friendly and facile functionalization of graphene nanoplatelet and its application in convective heat transfer. *Energy Conversion and Management, 150*, 26-36.

Sadri, R., Hosseini, M., Kazi, S., Bagheri, S., Zubir, N., Solangi, K., . . . Badarudin, A. (2017). A bio-based, facile approach for the preparation of covalently functionalized carbon nanotubes aqueous suspensions and their potential as heat transfer fluids. *Journal of colloid and interface science, 504*, 115-123.

Sadri, R., Mallah, A., Hosseini, M., Ahmadi, G., Kazi, S., Dabbagh, A., . . . Yaakup, N. (2018). CFD modeling of turbulent convection heat transfer of nanofluids

containing green functionalized graphene nanoplatelets flowing in a horizontal tube: Comparison with experimental data. *Journal of Molecular Liquids*.

Said, Z., Sabiha, M., Saidur, R., Hepbasli, A., Rahim, N., Mekhilef, S., & Ward, T. (2015). Performance enhancement of a flat plate solar collector using titanium dioxide nanofluid and polyethylene glycol dispersant. *Journal of Cleaner Production, 92*, 343-353.

Said, Z., Saidur, R., & Rahim, N. (2016b). Energy and exergy analysis of a flat plate solar collector using different sizes of aluminium oxide based nanofluid. *Journal of Cleaner Production, 133*, 518-530.

Said, Z., Saidur, R., Rahim, N., & Alim, M. (2014). Analyses of exergy efficiency and pumping power for a conventional flat plate solar collector using SWCNTs based nanofluid. *Energy and Buildings, 78*, 1-9.

Said, Z., Saidur, R., Sabiha, M., Hepbasli, A., & Rahim, N. (2016a). Energy and exergy efficiency of a flat plate solar collector using pH treated Al2O3 nanofluid. *Journal of Cleaner Production, 112*, 3915-3926.

Said, Z., Saidur, R., Sabiha, M. A., Rahim, N. A., & Anisur, M. R. (2015). Thermophysical properties of Single Wall Carbon Nanotubes and its effect on exergy efficiency of a flat plate solar collector. *Solar Energy, 115*, 757-769. Retrieved from <Go to ISI>://WOS:000355043600068

Saidur, R., Leong, K., & Mohammad, H. (2011). A review on applications and challenges of nanofluids. *Renewable and Sustainable Energy Reviews, 15*(3), 1646-1668.

Sakhaei, S. A., & Valipour, M. S. (2019). Performance enhancement analysis of The flat plate collectors: A comprehensive review. *Renewable & Sustainable Energy Reviews, 102*, 186-204. Retrieved from <Go to ISI>://WOS:000455404000016

Sani, E., Barison, S., Pagura, C., Mercatelli, L., Sansoni, P., Fontani, D., . . . Francini, F. (2010). Carbon nanohorns-based nanofluids as direct sunlight absorbers. *Optics Express, 18*(5), 5179-5187.

Sarsam, W. S., Amiri, A., Kazi, S., & Badarudin, A. (2016a). Stability and thermophysical properties of non-covalently functionalized graphene nanoplatelets nanofluids. *Energy Conversion and Management, 116*, 101-111.

Sarsam, W. S., Amiri, A., Kazi, S., & Badarudin, A. (2016b). Stability and thermophysical properties of non-covalently functionalized graphene nanoplatelets nanofluids. *Energy conversion management, 116*, 101-111.

Sarsam, W. S., Amiri, A., Shanbedi, M., Kazi, S., Badarudin, A., Yarmand, H., . . . Zaharinie, T. (2017). Synthesis, stability, and thermophysical properties of aqueous colloidal dispersions of multi-walled carbon nanotubes treated with beta-alanine. *International Communications in Heat Mass Transfer, 89*, 7-17.

Sarsam, W. S., Amiri, A., Zubir, M. N. M., Yarmand, H., Kazi, S., & Badarudin, A. (2016a). Stability and thermophysical properties of water-based nanofluids containing triethanolamine-treated graphene nanoplatelets with different specific surface areas. *Colloids and Surfaces A: Physicochemical and Engineering Aspects, 500*, 17-31.

Sarsam, W. S., Amiri, A., Zubir, M. N. M., Yarmand, H., Kazi, S., & Badarudin, A. (2016b). Stability and thermophysical properties of water-based nanofluids containing triethanolamine-treated graphene nanoplatelets with different specific surface areas. *Colloids Surfaces A: Physicochemical Engineering Aspects, 500*, 17-31.

Sekhar, Y. R., Sharma, K., & Rao, M. B. (2009). Evaluation of heat loss coefficients in solar flat plate collectors. *ARPN journal of engineering Applied Sciences, 4*(5), 15-19.

Shah, R. (1975). *Thermal entry length solutions for the circular tube and parallel plates.* Paper presented at the Proceedings of 3rd national heat and mass transfer conference.

Sharafeldin, M., & Gróf, G. (2018). Experimental investigation of flat plate solar collector using CeO 2-water nanofluid. *Energy Conversion and Management, 155*, 32-41.

Sharafeldin, M. A., Gróf, G., & Mahian, O. (2017). Experimental study on the performance of a flat-plate collector using WO3/Water nanofluids. *Energy, 141*, 2436-2444.

Shojaeizadeh, E., & Veysi, F. (2016). Development of a correlation for parameter controlling using exergy efficiency optimization of an Al2O3/water nanofluid based flat-plate solar collector. *Applied Thermal Engineering, 98*, 1116-1129.

Shojaeizadeh, E., Veysi, F., & Kamandi, A. (2015). Exergy efficiency investigation and optimization of an Al2O3–water nanofluid based Flat-plate solar collector. *Energy and Buildings, 101*, 12-23.

Skeiker, K. (2009). Optimum tilt angle and orientation for solar collectors in Syria. *J Energy Conversion Management , 50*(9), 2439-2448.

Sohn, C. W., & Chen, M. (1981). Microconvective thermal conductivity in disperse two-phase mixtures as observed in a low velocity Couette flow experiment. *Journal of Heat Transfer, 103*(1), 47-51.

Soudagar, M. E. M., Nik-Ghazali, N.-N., Kalam, M. A., Badruddin, I., Banapurmath, N., Akram, N. J. E. C., & Management. (2018). The effect of nano-additives in diesel-biodiesel fuel blends: A comprehensive review on stability, engine performance and emission characteristics. *Energy Conversion and Managment, 178*, 146-177.

Stalin, P. M. J., Arjunan, T. V., Matheswaran, M. M., & Sadanandam, N. (2019). Experimental and theoretical investigation on the effects of lower concentration CeO2/water nanofluid in flat-plate solar collector. *Journal of Thermal Analysis*

and Calorimetry, 135(1), 29-44. Retrieved from <Go to ISI>://WOS:000459206500003

Standard, A. (2003). Standard 93-2003. *Method of testing to determine the thermal performance of solar collector*.

Standard, A. J. A. S. o. H. (1977). Methods of testing to determine the thermal performance of solar collectors. 93-77.

Sundar, L. S., Singh, M. K., Punnaiah, V., & Sousa, A. C. M. (2018). Experimental investigation of Al2O3/water nanofluids on the effectiveness of solar flat-plate collectors with and without twisted tape inserts. *Renewable Energy, 119*, 820-833. Retrieved from <Go to ISI>://WOS:000423649700074

Sundar, L. S., Singh, M. K., & Sousa, A. C. (2014). Enhanced heat transfer and friction factor of MWCNT–Fe3O4/water hybrid nanofluids. *International Communications in Heat and Mass Transfer, 52*, 73-83. Taylor, R. (2011). *Thermal energy conversion in nanofluids* (Vol. 72).

Taylor, R. A. (2011). *Thermal energy conversion in nanofluids. (Doctoral dissertation), (UMI No. 3465706).* (Doctoral dissertation). Arizona State University, , Arizona.

Taylor, R. A., Phelan, P. E., Otanicar, T. P., Adrian, R., & Prasher, R. (2011). Nanofluid optical property characterization: towards efficient direct absorption solar collectors. *Nanoscale Research Letters, 6*(1), 225.

Teng, C.-C., Ma, C.-C. M., Lu, C.-H., Yang, S.-Y., Lee, S.-H., Hsiao, M.-C., . . . Lee, T.-M. (2011). Thermal conductivity and structure of non-covalent functionalized graphene/epoxy composites. *Carbon, 49*(15), 5107-5116.

Thirugnanasambandam, M., Iniyan, S., & Goic, R. (2010). A review of solar thermal technologies. *%J Renewable sustainable energy reviews, 14*(1), 312-322.

Timofeeva, E. V. (2011). Nanofluids for heat transfer–potential and engineering strategies. In *Two phase flow, phase change and numerical modeling*: IntechOpen.

Timofeeva, E. V., Gavrilov, A. N., McCloskey, J. M., Tolmachev, Y. V., Sprunt, S., Lopatina, L. M., & Selinger, J. V. (2007). Thermal conductivity and particle agglomeration in alumina nanofluids: experiment and theory. *Physical Review E, 76*(6), 061203.

Ting, K. (1981). SIMULATION AND SIZING OF FLAT PLATE SOLAR COLLECTORS FOR GRAIN DRYING.

Tugcu, C. T., Ozturk, I., & Aslan, A. (2012). Renewable and non-renewable energy consumption and economic growth relationship revisited: evidence from G7 countries. *Energy economics, 34*(6), 1942-1950.

Vajjha, R. S., & Das, D. K. (2009). Experimental determination of thermal conductivity of three nanofluids and development of new correlations. *International Journal of Heat Mass Transfer, 52*(21-22), 4675-4682.

Vakili, M., Hosseinalipour, S., Delfani, S., Khosrojerdi, S., & Karami, M. (2016). Experimental investigation of graphene nanoplatelets nanofluid-based volumetric solar collector for domestic hot water systems. *Solar Energy, 131*, 119-130.

Vandsburger, L. (2009). *Synthesis and covalent surface modification of carbon nanotubes for preparation of stabilized nanofluid suspensions.* McGill University,

Verma, S. K., Tiwari, A. K., & Chauhan, D. S. (2016). Performance augmentation in flat plate solar collector using MgO/water nanofluid. *Energy Conversion and Management, 124*, 607-617.

Verma, S. K., Tiwari, A. K., & Chauhan, D. S. (2017). Experimental evaluation of flat plate solar collector using nanofluids. *Energy Conversion and Management, 134*, 103-115.

Verma, V., & Kundan, L. (2013). Thermal performance evaluation of a direct absorption flat plate solar collector (DASC) using Al2O3-H2O based nanofluids. *ISOR Journal of Mechanical and Civil Engineering, 6*, 2320-3344.

Vijayakumaar, S., Shankar, R. L., & Babu, K. (2013). *Effect of CNT-H 2 O nanofluid on the performance of solar flat plate collector-an experimental investigation.* Paper presented at the Advanced Nanomaterials and Emerging Engineering Technologies (ICANMEET), 2013 International Conference on.

Vincely, D. A., & Natarajan, E. (2016). Experimental investigation of the solar FPC performance using graphene oxide nanofluid under forced circulation. *Energy Conversion and Management, 117*, 1-11. Retrieved from <Go to ISI>://WOS:000374616200001

Wang, B.-X., Zhou, L.-P., & Peng, X.-F. (2003). A fractal model for predicting the effective thermal conductivity of liquid with suspension of nanoparticles. *International Journal of Heat Mass Transfer, 46*(14), 2665-2672.

Wang, X.-j., & Zhu, D.-s. (2009). Investigation of pH and SDBS on enhancement of thermal conductivity in nanofluids. *Chemical Physics Letters, 470*(1-3), 107-111.

Wang, X.-Q., & Mujumdar, A. S. J. B. J. o. C. E. (2008). A review on nanofluids-part I: theoretical and numerical investigations. *Brazilian Journal of Chemical Engineering, 25*(4), 613-630.

Wen, D., & Ding, Y. (2005). Formulation of nanofluids for natural convective heat transfer applications. *International Journal of Heat Fluid Flow, 26*(6), 855-864.

Xiaowu, W., & Ben, H. (2005). Exergy analysis of domestic-scale solar water heaters. *Renewable and Sustainable Energy Reviews, 9*(6), 638-645.

Xuan, Y., Roetzel, W. J. I. J. o. h., & transfer, M. (2000). Conceptions for heat transfer correlation of nanofluids. *International journal of Heat and Mass transfer, 43*(19), 3701-3707.

Yarmand, H., Gharehkhani, S., Shirazi, S. F. S., Amiri, A., Alehashem, M. S., Dahari, M., & Kazi, S. (2016). Experimental investigation of thermo-physical properties, convective heat transfer and pressure drop of functionalized graphene nanoplatelets aqueous nanofluid in a square heated pipe. *Energy Conversion and Management, 114*, 38-49.

Yarmand, H., Gharehkhani, S., Shirazi, S. F. S., Amiri, A., Alehashem, M. S., Dahari, M., . . . Management. (2016). Experimental investigation of thermo-physical properties, convective heat transfer and pressure drop of functionalized graphene nanoplatelets aqueous nanofluid in a square heated pipe. *114*, 38-49.

Yousefi, T., Shojaeizadeh, E., Veysi, F., & Zinadini, S. (2012). An experimental investigation on the effect of pH variation of MWCNT–H2O nanofluid on the efficiency of a flat-plate solar collector. *Solar Energy, 86*(2), 771-779.

Yousefi, T., Shojaeizadeh, E., Veysi, F., & Zinadini, S. (2012a). An experimental investigation on the effect of pH variation of MWCNT–H2O nanofluid on the efficiency of a flat-plate solar collector. *Solar Energy, 86*(2), 771-779.

Yousefi, T., Veisy, F., Shojaeizadeh, E., & Zinadini, S. (2012). An experimental investigation on the effect of MWCNT-H2O nanofluid on the efficiency of flat-plate solar collectors. *Experimental Thermal and Fluid Science, 39*, 207-212. Retrieved from <Go to ISI>://WOS:000302667300021

Yousefi, T., Veisy, F., Shojaeizadeh, E., & Zinadini, S. (2012c). An experimental investigation on the effect of MWCNT-H2O nanofluid on the efficiency of flat-plate solar collectors. *Experimental Thermal and Fluid Science, 39*, 207-212.

Yousefi, T., Veysi, F., Shojaeizadeh, E., & Zinadini, S. (2012). An experimental investigation on the effect of Al2O3-H2O nanofluid on the efficiency of flat-plate solar collectors. *Renewable Energy, 39*(1), 293-298. Retrieved from <Go to ISI>://WOS:000296405600032

Yousefi, T., Veysi, F., Shojaeizadeh, E., & Zinadini, S. (2012b). An experimental investigation on the effect of Al2O3–H2O nanofluid on the efficiency of flat-plate solar collectors. *Renewable Energy, 39*(1), 293-298.

Yu, W., France, D. M., Routbort, J. L., & Choi, S. U. (2008a). Review and comparison of nanofluid thermal conductivity and heat transfer enhancements. *Heat Transfer Engineering, 29*(5), 432-460.

Yu, W., France, D. M., Routbort, J. L., & Choi, S. U. (2008b). Review and comparison of nanofluid thermal conductivity and heat transfer enhancements. *%J Heat transfer engineering, 29*(5), 432-460.

Yu, W., France, D. M., Routbort, J. L., & Choi, S. U. (2008c). Review and comparison of nanofluid thermal conductivity and heat transfer enhancements. *Heat transfer engineering, 29*(5), 432-460.

Yu, W., France, D. M., Singh, D., Timofeeva, E. V., Smith, D. S., & Routbort, J. L. (2010). Mechanisms and models of effective thermal conductivities of nanofluids. *Journal of Nanoscience Nanotechnology, 10*(8), 4824-4849.

Yu, W., & Xie, H. (2012). A review on nanofluids: preparation, stability mechanisms, and applications. *Journal of Nanomaterials, 2012*, 1.

Yu, W., Xie, H., Chen, L., & Li, Y. (2009). Investigation of thermal conductivity and viscosity of ethylene glycol based ZnO nanofluid. *Thermochimica Acta, 491*(1-2), 92-96.

Yu, W., Xie, H., & Chen, L. (2012). Nanofluids. In Dr Abbass Hashim (Ed.), Smart Nanoparticles Technology. 497-518. doi:10.5772/32854

Zamzamian, A., KeyanpourRad, M., KianiNeyestani, M., & Jamal-Abad, M. T. (2014). An experimental study on the effect of Cu-synthesized/EG nanofluid on the efficiency of flat-plate solar collectors. *Renewable Energy, 71*, 658-664.

Zanuttigh, B., Angelelli, E., & Kofoed, J. P. (2013). Effects of mooring systems on the performance of a wave activated body energy converter. *Renewable Energy, 57*, 422-431.

Zhang, X., Gu, H., Fujii, M. J. E. T., & Science, F. (2007). Effective thermal conductivity and thermal diffusivity of nanofluids containing spherical and cylindrical nanoparticles. *Experimental Thermal and Fluid Science, 31*(6), 593-599.

Zhu, D., Li, X., Wang, N., Wang, X., Gao, J., & Li, H. (2009). Dispersion behavior and thermal conductivity characteristics of Al2O3–H2O nanofluids. *%J Current Applied Physics, 9*(1), 131-139.

Zhu, H., Zhang, C., Tang, Y., Wang, J., Ren, B., & Yin, Y. (2007). Preparation and thermal conductivity of suspensions of graphite nanoparticles. *Carbon, 45*(1), 226-228.

Zhu, H.-t., Lin, Y.-s., & Yin, Y.-s. (2004). A novel one-step chemical method for preparation of copper nanofluids. *Journal of colloid interface science, 277*(1), 100-103.

Zubir, M. N. M., Muhamad, M. R., Amiri, A., Badarudin, A., Kazi, S. N., Oon, C. S., . . . Yarmand, H. (2016). Heat transfer performance of closed conduit turbulent flow: Constant mean velocity and temperature do matter! *Journal of the Taiwan Institute of Chemical Engineers, 64*, 285-298.